

# Spectro-Electrochemical Investigations on Immobilised Heme Proteins

vorgelegt von  
Diplom Chemiker  
**Murat Sezer**  
aus Berlin

von der Fakultät II – Mathematik und Naturwissenschaften  
der Technischen Universität Berlin  
zur Erlangung des Akademischen Grades  
Doktor der Naturwissenschaften  
Dr. rer. nat.

genehmigte Dissertation

Promotionsausschuss:

Vorsitzender:	Prof. Dr. Andreas Grohmann
Berichter:	Prof. Dr. Peter Hildebrandt
Berichterin:	Prof. Dr. Ulla Wollenberger

Tag der wissenschaftlichen Aussprache: 20. Juli 2011

Berlin 2011

D83



### **Note**

**Except for chapter 7.3, this thesis is written in British English. Chapter 7.3 is written in American English since it is a manuscript that has been accepted for publication in an American journal (*J. Phys. Chem. B.*). Moreover, the references in chapter 7.3 are listed separately in the end of chapter 7.3. Chapters 5.4 and 6.3 have been published in *Phys. Chem. Chem. Phys.* The references in chapters 5.4 and 6.4 are also listed separately in the end of the respective chapters. All other references are listed in chapter 10.**



## Table of Contents

Abbreviations .....	I
Symbols .....	II
Physical constants .....	III
Abstract.....	V
Zusammenfassung .....	IX
<b>1 Introduction.....</b>	<b>1</b>
<b>2 Theoretical Background.....</b>	<b>5</b>
2.1 Raman Spectroscopy .....	5
2.1.1 Normal Modes.....	5
2.1.2 Raman Scattering .....	6
2.1.3 Raman Signal Intensity.....	7
2.1.4 Polarisability Tensor Components.....	8
2.2 Resonance Raman Effect.....	9
2.3 Surface Enhanced Raman Spectroscopy .....	12
2.4 Electrochemical Interface at the Bare Silver Electrode .....	14
2.5 Self Assembled Monolayers of Alkanethiol Derivatives.....	15
2.6 Electron Transfer Theory.....	17
2.6.1 Homogeneous Electron Transfer.....	18
2.6.2 Heterogeneous Electron Transfer.....	21
2.7 Heme Proteins .....	23
<b>3 Instrumentation.....</b>	<b>25</b>
3.1 Excitation Source .....	25
3.2 Sample Arrangement.....	26
3.3 Electrochemical Setup.....	28
3.4 Spectroscopic and Spectro-Electrochemical Setup.....	28
<b>4 Methods .....</b>	<b>31</b>
4.1 Resonance Raman Spectroscopy of Heme Proteins .....	31
4.2 Surface Enhanced Resonance Raman Spectroscopy of Heme Proteins .....	34
4.2.1 Electrode preparation.....	34
4.2.3 Time Resolved Potential Controlled Measurements.....	36
4.2.4 SERR Spectroscopic Study of Catalytic Oxidation Processes .....	37
4.3 Component Fit Analysis.....	38
4.4 Protein Film Voltammetry .....	40
4.4.1 Protein Film Voltammetry under non-Turnover Conditions.....	41
4.4.2 Protein Film Voltammetry under Turnover Conditions .....	44
4.5 Computational Chemistry .....	45
<b>5 Silver-Gold Hybrid Devices for Spectro-Electrochemistry.....</b>	<b>47</b>
5.1 Analytical Model for the Optical Performance .....	48
5.2 Cytochrome <i>c</i> .....	51
5.3 Overpotential Dependence of Heterogeneous Electron Transfer Rates.....	52
5.4 Multi-layer electron transfer across nanostructured Ag-SAM-Au-SAM junctions probed by surface enhanced Raman spectroscopy.....	<b>55</b>

<b>6 Human Sulphite Oxidase</b> .....	<b>65</b>
6.1 Structure of Human Sulphite Oxidase.....	66
6.2 Catalytic Mechanism of Sulphite Oxidases.....	66
6.3 Redox properties and catalytic activity of surface-bound human sulfite oxidase studied by a combined surface enhanced resonance Raman spectroscopic and electrochemical approach.....	<b>69</b>
<b>7 Membrane Bound Hydrogenase from <i>Ralstonia eutropha</i> H16</b> .....	<b>85</b>
7.1 Structure of the Membrane Bound Hydrogenase from <i>Ralstonia eutropha</i> H16.....	86
7.2 Redox Chemistry and Catalytic Cycle.....	88
7.3 Role of the HoxZ subunit in the electron transfer pathway of the membrane-bound [NiFe]-hydrogenase from <i>Ralstonia eutropha</i> H16 immobilized on electrodes.....	<b>91</b>
<b>8 Other Projects</b> .....	<b>115</b>
8.1 Surface Enhanced Resonance Raman Spectroscopic Investigations on Xenobiotic Reductase A.....	115
8.1.1 RR and SERR Spectra Using 8-Aminooctanethiol Coating.....	116
8.1.2 SERR Spectra Using 6-Aminohexanethiol Coating .....	118
8.2 Resonance Raman Spectroscopic Investigations of Mitochondria Preparations from Mouse Pancreas.....	120
<b>9 Conclusion and Outlook</b> .....	<b>123</b>
9.1 Silver-Gold Hybrid Devices.....	123
9.2 Human Sulphite Oxidase.....	124
9.3 Membrane Bound Hydrogenase from <i>Ralstonia eutropha</i> H16.....	125
<b>10 References</b> .....	<b>127</b>
<b>11 List of Publications</b> .....	<b>137</b>
Danksagung.....	<b>141</b>

## Abbreviations

5c, 6c	five-coordinated, six-coordinated
AHT	6-aminohexanethiol
AOT	8-aminooctanethiol
AUT	11- aminoundecanethiol
CCD	charge coupled device
clSO	chicken liver sulphite oxidase
CV	cyclic voltammetry
cw	continuous wave
Cyt <i>b</i>	(di-heme) cytochrome <i>b</i> (domain of the membrane bound hydrogenase from <i>Ralstonia eutropha</i> H16)
Cyt <i>b</i> 5	cytochrome <i>b</i> 5 (domain of human sulphite oxidase)
Cyt <i>c</i>	cytochrome <i>c</i>
EPR	electron paramagnetic resonance
ET	electron transfer
FC	Franck-Condon
FMN	flavin-mononucleotide
HS, LS	high spin, low spin
hSO	human sulphite oxidase
HHCyt <i>c</i>	horse heart cytochrome <i>c</i>
IET	intramolecular electron transfer
IR	infrared
MBH	membrane bound hydrogenase from <i>Ralstonia eutropha</i> H16
MDHA	16-mercaptohexadecanoic acid
moco	molybdopterin cofactor (of human sulphite oxidase)
MUA	11-mercaptoundecanoic acid
[NiFe]	nickel iron (metal ions of the active site of certain hydrogenases)
PFV	protein film voltammetry
RR	resonance Raman
SAM	self assembled monolayer
SHE	standard hydrogen electrode (-0.210 V vs. Ag/AgCl)
SE(R)R	surface enhanced (resonance) Raman
Tris	tris(hydroxymethyl)aminomethane
TR-SERR	time resolved surface enhanced resonance Raman
UV-Vis	ultra violet – visible
XenA	xenobiotic reductase A from <i>Pseudomonas Putida</i> 86
YCyt <i>c</i>	iso-1-cytochrome <i>c</i> from yeast

## Symbols

symbol	unit	signification
$A$	[cm <sup>2</sup> ]	real electrode surface area
$c$	[mol · cm <sup>-2</sup> ]	surface concentration
$E$	[V]	potential
$E$	[eV]	energy
$\vec{E}$	$\left[ \frac{kg \cdot m}{A \cdot s^3} \right]$	electric field vector
$F(\nu)$		wavelength dependent electric field enhancement factor
$H_{RP}$	[eV]	electronic coupling
$\hat{H}_{el}$		Born-Oppenheimer electronic Hamiltonian
$I$	[eV, or a.u.]	intensity
$I$	[A]	current
$k$	[s <sup>-1</sup> ]	electron transfer rate constant
$M$		electron position operator
$M$		electronic transition moment
$n$		number of transferred electrons
$n$		number of repetitions
$pH$		negative logarithmic value of the H <sup>+</sup> concentration
$P(E_i)$		Boltzmann probability of state $i$ with energy $E_i$
$pK_A$		negative logarithmic value of the acid dissociation constant
$Q_k$	[kg <sup>1/2</sup> · m]	mass-weighted coordinates of the normal mode $k$
$R, r$	[nm]	radius
$t$	[s]	time
$T$	[K]	temperature
$\alpha$	[A <sup>2</sup> · s <sup>4</sup> · kg <sup>-1</sup> ]	molecular polarisability
$\alpha$	[°]	tilt angle of self assembled monolayers with respect to the surface normal
$\beta$		tunelling decay parameter
$\Gamma$	[cm <sup>-1</sup> ]	bandwidth at half height
$\Gamma$	[mol]	amount of electro-active protein on an electrode surface
$\Gamma_{Rr}$		damping constant related to the lifetime of the vibronic state $Rr$

$\delta$		Dirac delta function
$\delta$	[s]	delay time
$\varepsilon$		dielectric constant or dielectric function
$\eta$	[V]	overpotential
$\kappa_{el}$		electron transmission coefficient
$\lambda$	[nm]	wavelength
$\lambda$	[eV]	reorganisation free energy
$\bar{\mu}$	[debye]	dipole moment
$\nu$	[s <sup>-1</sup> ]	frequency
$\tilde{\nu}$	[cm <sup>-1</sup> ]	wavenumber
$\nu_{scan}$	[V·s <sup>-1</sup> ]	scan rate
$\nu_{el}$	[rpm]	rotation speed of the working electrode
$\rho$		density of states of a solid metal electrode
$\tau_D$	[s]	dielectric relaxation time
$\sigma$		resonance Raman cross section parameter
$\Phi$		quantum yield
$\Phi$	$\left[ \frac{kg \cdot m}{A \cdot s^3} \right]$	local electric field
$\Phi_{IF}$	[A·s·cm <sup>-2</sup> ]	surface charge density
$\psi$		dimensionless electric potential
$\psi$		electronic wave function

## Physical constants

$c$	speed of light	$c = 299792.458 km \cdot s^{-1}$
$e$	elementary charge	$e = 1.602 \cdot 10^{-19} As$
$F$	Faraday constant	$F = 96485.339 As \cdot mol^{-1}$
$h$	Planck constant	$h = 6.626 \cdot 10^{-34} J \cdot s$
$\hbar$	reduced Planck constant	$\hbar = 1.055 \cdot 10^{-34} J \cdot s$
$k_B$	Boltzmann constant	$k_B = 1.3806504 \cdot 10^{-23} J \cdot K^{-1}$
$R$	universal gas constant	$R = 8.314 J \cdot mol^{-1} \cdot K^{-1}$
$\varepsilon_0$	vacuum permittivity	$\varepsilon_0 = 8.854187 \cdot 10^{-12} C \cdot V^{-1} m^{-1}$



## Abstract

In this thesis, different aspects of spectro-electrochemical research on chromophore containing redox-active proteins were addressed. On the one hand, this work is related to the development of novel functional materials as substrates for surface enhanced resonance Raman (SERR) spectro-electrochemistry, on the other hand, electron transfer processes of immobilised enzymes were investigated.

The optical and electronic performance of novel silver-gold hybrid devices as support materials for SERR spectro-electrochemistry was explored using horse heart cytochrome *c* (HHCyt *c*) and yeast iso-1-cytochrome *c* (YCyt *c*) as model proteins. In these devices a thin gold island film, which can be further functionalised, is separated by amino-terminated self assembled monolayers (spacer SAMs) from an electrochemically roughened silver support. Comparable Raman signal intensity was observed for electrostatically immobilised HHCyt *c* on SAM-coated silver and silver-gold hybrid devices, respectively. The native heme conformation of HHCyt *c* was preserved upon electrostatic immobilisation and interfacial electron transfer (ET) between the protein and the silver-gold multilayer device occurred with an almost Nernstian behaviour with an apparent number of transferred electrons close to one ( $n = 0.8 - 0.9$ ). Interfacial ET rates were found to be limited either by electron tunnelling through the outer SAM on the gold layer or the spacer SAM between the metal layers, and impurities or defects in the spacer SAM. Fastest rates were obtained using 11-aminoundecanethiol (AUT) as spacer, shorter spacer SAMs yielded lower ET rates, most likely due to impurities or defects. The potential of zero charge of a Ag-AUT-Au-MDHA device (MDHA – 16-Mercaptohexadecanethiol) was determined to be  $E_{pzc} = -0.2$  V (vs. Ag/AgCl, 3M KCl), which is in between of the respective values for Ag-MDHA ( $E_{pzc} = -0.45$  V) and Au-MDHA ( $E_{pzc} = -0.03$  V). Also the overpotential dependence of heterogeneous reduction rate of HHCyt *c* on this particular hybrid device was found to lie in between of the respective silver and gold supports. YCyt *c* was covalently attached via Cys102 to the bare gold surface of the hybrid device, yielding 25 times higher SERR signal intensity as compared to the bare silver surface. The covalently attached YCyt *c* partially converted into a non-native species and exhibited a broad interfacial redox transition ( $n = 0.3$ ). It was shown that the hybrid device provides similar Raman signal enhancements as pure silver supports, exhibit the surface chemistry and biocompatibility of gold and efficient interfacial ET.

Human sulphite oxidase (hSO) was electrostatically immobilised on SAM-coated silver electrodes and studied by protein film voltammetry (PFV) and (time-resolved) potential controlled SERR spectroscopy. The heme pocket structure in the cytochrome *b5* (Cyt *b5*) domain and functionality of the enzyme were preserved upon immobilisation. It was shown that the

heterogeneous ET rate of the Cyt *b*5 domain and catalytic activity of hSO dramatically increase upon increasing the ionic strength of the buffer solution. Upon increasing the concentration of a Tris-acetate buffer from 5 mM to 750 mM, heterogeneous ET rates for the Cyt *b*5 domain of hSO increase from  $17\text{ s}^{-1}$  to  $440\text{ s}^{-1}$  and the apparent number of transferred electrons increases from  $n = 0.74$  to  $n = 0.96$  as obtained by SERR spectroscopy. PFV measurements demonstrated an increase of the apparent turnover rate of the immobilised hSO from  $0.85\text{ s}^{-1}$  in 100 mM to  $5.26\text{ s}^{-1}$  in 750 mM Tris-acetate buffer. These effects result from increased mobility of the enzyme with increasing buffer concentration due to a weakening of electrostatic interaction forces. Comparative studies with the isolated Cyt *b*5 domain and calculations on the surface potential distribution suggest that the entire hSO is most likely immobilised via its dimerisation domain to the SAM. The flexible loop region connecting the molybdopterin cofactor (Moco) containing domain, where the catalytic reaction takes place, and the Cyt *b*5 domain allows alternating contact of the Cyt *b*5 with the Moco domain interaction site and the SAM surface. This movement enables sequential intramolecular and heterogeneous ET from Moco via the Cyt *b*5 to the electrode. At higher ionic strength, the contact time of the Cyt *b*5 domain with both the Moco domain and the SAM surface, respectively, is shorter, corresponding to a faster overall ET process.

The entire HoxGKZ hetero-trimer and the isolated HoxZ domain of the membrane bound [NiFe] hydrogenase from *Ralstonia eutropha* H16 (MBH) were studied with PFV and potential controlled SERR spectroscopy. The role of the HoxZ domain, which is a di-heme cytochrome *b* (Cyt *b*) unit, in the electron transfer pathway of the immobilised HoxGKZ hetero-trimer from was investigated. Experimental conditions were optimised for the isolated Cyt *b* unit with regard to structural integrity and electronic communication with the electrode. Best results within this study were obtained using carboxyl-terminated SAMs and 100 mM phosphate buffer at pH 5.5. Under these conditions the heme pocket structure was preserved and a single broad heterogeneous electron transition between the heme cofactor(s) and the silver electrode was clearly observed with potential controlled SERR spectroscopy. The apparent number of transferred electrons of this redox transition is  $n \approx 0.5$ , the midpoint potential is similar to the value in solution ( $E_{m,sol} = -0.09\text{ V}$ , vs. SHE) and the heterogeneous ET kinetics were found to be rather slow ( $k = 0.24\text{ s}^{-1}$ ). The native six-coordinated low spin (6cLS) heme state and a non-native five-coordinated high spin (5cHS) state were found to be in an equilibrium that depends on experimental conditions. Experimental conditions at which the heme pocket structure is preserved were adopted for the study of the entire hetero-trimer. As observed with PFV, the immobilised HoxGKZ shows enzymatic activity in both directions, whereby the hydrogen splitting under hydrogen supply is much more efficient than hydrogen evolution under inert gas atmosphere. It was shown with SERR spectroscopy that electrons from enzymatic hydrogen oxidation are transferred to hemes of the HoxZ domain. The apparent rate of the catalytic heme reduction is low ( $k = 0.15\text{ s}^{-1}$ ) and includes transport of hydrogen to the electrode, reductive activation of the enzyme and intramolecular electron transfer.

The shape of the cyclic voltammograms resembles those previously reported for the HoxGK hetero-dimer. The immobilised HoxGKZ hetero-trimer exhibits similar anaerobic inactivation and reactivation behaviour with similar switch potential  $E_{switch} = 0.09$  V (vs. SHE). Also in this work, similar catalytic currents were observed for the HoxGK hetero-dimer, however, with much lower current intensity. On the basis of the experimental findings, we conclude that the HoxZ subunit is not primarily involved in the electron transfer of the immobilised HoxGKZ to the electrode but plays a crucial role in stabilising the enzyme on the electrode.



## Zusammenfassung

Diese Arbeit behandelt zwei Aspekte innerhalb des Forschungsgebiets der Spektro-Elektrochemie an chromophorhaltigen redox-aktiven Proteinen. Zum einen ging es um die Entwicklung neuartiger Materialien als Plattform für oberflächenverstärkte Resonanz Raman (SERR) Spektro-Elektrochemie, zum anderen um die Aufklärung von Elektronentransferprozessen immobilisierter Proteine.

Die optischen und elektronischen Eigenschaften von neuartigen Silber-Gold Hybrid Materialien als Substrate für SERR Spektro-Elektrochemie wurden untersucht, wobei Cytochrom *c* vom Pferdeherzen (HHCyt *c*) und iso-1-Cytochrom *c* aus Hefe (YCyt *c*) als Modellproteine verwendet wurden. In diesen Hybrid-Materialien ist eine dünne Inselfschicht aus Gold, welche noch weiter funktionalisiert werden kann, von einer elektrochemisch aufgerauten Silberoberfläche durch Amino-terminierte selbstorganisierte Monoschichten (Spacer-SAMs) separiert. Vergleichbare Raman Signalintensitäten für elektrostatisch gebundenes HHCyt *c* wurden auf SAM-beschichteten Silber beziehungsweise Silber-Gold Hybrid-Materialien beobachtet. Die natürliche Konformation des HHCyt *c* blieb bei der Immobilisierung erhalten und heterogener Elektronentransfer (ET) zwischen dem Protein und dem Silber-Gold Multischicht-Material entsprach nahezu idealem Nernstschen Verhalten. Die apparente Anzahl übertragener Elektronen lag nahe bei eins ( $n = 0,8 - 0,9$ ). Es hat sich heraus gestellt, dass der limitierende Faktor für den heterogenen ET entweder durch Elektronentunneln über die Spacer-SAM zwischen den Metallschichten beziehungsweise die äußere SAM auf der Goldschicht und durch Verunreinigungen oder Defekte in der Spacer-SAM gegeben ist. Die höchste ET-Geschwindigkeit wurde bei Verwendung von 11-Aminoundekanthiol (AUT) als Spacer-SAM beobachtet, die Verwendung von kürzeren Spacer-SAMs führte zu niedrigeren Geschwindigkeiten, vermutlich aufgrund von Verunreinigungen oder Defekten. Das Nullladungspotenzial einer Ag-Au-Au-MDHA (MDHA – 16-Mercaptohexadekanthiol) wurde mit  $E_{pzc} = -0,2$  V (vs. Ag/AgCl, 3M KCl) ermittelt. Dieser Wert liegt zwischen den entsprechenden Werten für Ag-MDHA ( $E_{pzc} = -0,45$  V) und Au-MDHA ( $E_{pzc} = -0,03$  V). Auch die Überpotentialabhängigkeit der heterogenen Reduktionsgeschwindigkeit von HHCyt *c* auf dieser speziellen Hybrid-Elektrode liegt zwischen denen auf reinem Silber beziehungsweise reinem Gold. YCyt *c* wurde kovalent über Cys102 an die Goldoberfläche der Hybrid-Elektrode gebunden. Die SERR Signalintensität war für dieses System 25 Mal höher im Vergleich zur Silberelektrode. Ein Teil des kovalent gebundenen YCyt *c* ging in einen nicht-nativen Konformationszustand über und es wurde ein sehr breiter heterogener ET ( $n = 0,3$ ) beobachtet. Dadurch wurde gezeigt, dass das Hybrid-Material die chemischen Oberflächeneigenschaften und die Biokompatibilität von Gold aufweist. Außerdem bietet es eine Verstärkung von Ramansignalen, die mit der von reinen

Silberoberflächen vergleichbar ist und zeigt einen effizienten heterogenen ET.

Menschliche Sulfid-Oxidase (hSO) wurde elektrostatisch auf SAM-beschichteten Silber-Elektroden immobilisiert und mit Proteinfilm Voltammetrie (PFV) und (zeitaufgelöster) Potential-kontrollierter oberflächenverstärkter Resonanz Raman (SERR) Spektroskopie untersucht. Die native Struktur der Häm-Bindungstasche in der Cytochrom *b5* (Cyt *b5*) Domäne und die Funktionalität des Enzyms blieben nach der Immobilisierung erhalten. Es wurde gezeigt, dass die heterogene ET-Geschwindigkeit der Cyt *b5* Domäne und die katalytische Aktivität des hSO durch eine Erhöhung der Ionenstärke der Pufferlösung sehr stark ansteigen. Durch eine Erhöhung der Konzentration eines Tris-Acetat Puffers von 5 mM auf 750 mM wurde mit SERR-Spektroskopie ein Anstieg der heterogenen ET-Geschwindigkeit für die Cyt *b5* Domäne der hSO von  $17 \text{ s}^{-1}$  auf  $440 \text{ s}^{-1}$  gemessen, wobei auch die apparente Anzahl übertragener Elektronen von  $n = 0,74$  auf  $n = 0,96$  angestiegen ist. PFV Messungen haben gezeigt, dass die apparente Umsatzrate der immobilisierten hSO von  $0,85 \text{ s}^{-1}$  in 100 mM auf  $5,26 \text{ s}^{-1}$  in 750 mM Tris-Acetat Puffer ansteigt. Beide Effekte resultieren von einer erhöhten Beweglichkeit des Enzyms mit steigender Pufferkonzentration aufgrund einer Schwächung elektrostatischer Wechselwirkungen. Vergleichende Studien zur isolierten Cyt *b5* Domäne und theoretische Berechnungen zur Verteilung des Oberflächenpotentials deuten darauf hin, dass die gesamte hSO vor allem über die Dimerisierungs-Domäne an die SAM gebunden ist. Die flexible Loop-Region, welche die Molybdopterin Kofaktor (Moco) enthaltende Domäne (in der die katalytische Reaktion stattfindet) mit der Cyt *b5* Domäne verbindet, erlaubt abwechselnden Kontakt der Cyt *b5* Domäne mit der Bindungstasche der Moco Domäne und der SAM-Oberfläche. Diese Bewegung ermöglicht aufeinanderfolgenden intramolekularen und heterogenen ET vom Moco über das Cyt *b5* zur Elektrode. Bei höheren Ionenstärken ist die Kontaktzeit der Cyt *b5* Domäne sowohl mit der Moco Domäne als auch mit der SAM-Oberfläche kürzer, was zu einem schnelleren ET Gesamtprozess führt.

Das gesamte HoxGKZ hetero-Trimer und die isolierte HoxZ Domäne der Membran-gebundenen [NiFe] Hydrogenase von *Ralstonia eutropha* H16 (MBH) wurden mit kombinierter Proteinfilm Voltammetrie und Potential-kontrollierter SERR Spektroskopie untersucht. Die Rolle der HoxZ Domäne, welches eine di-Häm Cytochrom *b* (Cyt *b*) Einheit ist, beim heterogenen Elektronentransfer des immobilisierten HoxGKZ hetero-Trimers wurde untersucht. Die experimentellen Bedingungen wurden zunächst für das isolierte Cyt *b* hinsichtlich struktureller Integrität und elektronischer Kommunikation mit der Elektrode optimiert. Innerhalb dieser Arbeit wurden die besten Ergebnisse bei der Verwendung von Carboxyl-terminierten SAMs und 100 mM Phosphat-Puffer mit einem pH von 5,5 erzielt. Unter diesen Bedingungen blieb die natürliche Konformation der Häm-Bindungstasche erhalten und ein einzelner, breiter heterogener Redoxübergang zwischen dem/den Häm Kofaktor(en) und der Elektrode wurde mit Potential-

kontrollierter SERR Spektroskopie beobachtet. Die apparente Anzahl übertragener Elektronen für diesen Elektronenübergang beträgt  $n \approx 0.5$  und liegt bei einem Potential, der dem Wert entspricht, der bei Messungen in Lösung ermittelt wurde ( $E_{m,sol} = -0.09$  V, vs. SHE). Die heterogene ET-Geschwindigkeit dieses Übergangs liegt bei  $k = 0.24$  s<sup>-1</sup>. Die native sechsfach-koordinierte low-spin (6cLS) Häm-Koordination liegt mit einem fünffach-koordinierten low-spin (5cHS) Zustand in einem Gleichgewicht, das von experimentellen Bedingungen abhängt. Die experimentellen Bedingungen, bei denen die native Struktur der Häm-Bindungstasche erhalten bleibt, wurden für die Untersuchung des gesamten hetero-Trimers übernommen. Mit PFV konnte gezeigt werden, dass das immobilisierte HoxGKZ in zwei Richtungen katalytisch aktiv ist, wobei die Wasserstoffspaltung unter Wasserstoffgaszufuhr wesentlich effizienter ist als die Wasserstoffproduktion unter Inertgas-Atmosphäre. Es wurde mit SERR Spektroskopie gezeigt, dass Elektronen, die dem Wasserstoff bei der enzymatischen Spaltung entzogen werden, zu den Häm-Gruppen der HoxZ Domäne übertragen werden. Die apparente Geschwindigkeit dieser katalytischen Häm-Reduktion ist niedrig ( $k = 0,15$  s<sup>-1</sup>) und beinhaltet den Transport von Wasserstoff zur Elektrode, reduktive Aktivierung des Enzyms und intramolekularen Elektronentransfer. Die Form der zyklischen Voltammogramme gleichen denen, die in früheren Arbeiten zum HoxGK hetero-Dimer berichtet wurden. Das immobilisierte HoxGKZ hetero-Trimer zeigt gleiches anaerobes Inaktivierungs- und Reaktivierungsverhalten mit gleichem switch-Potential  $E_{switch} = 0,09$  V (vs. SHE). Auch in dieser Arbeit wurde das HoxGK hetero-Dimer untersucht und es wurden ähnliche Ergebnisse erzielt, allerdings ist die Intensität des katalytischen Stromes im Falle des hetero-Dimers sehr viel geringer. Auf Basis der Ergebnisse schließen wir, dass die HoxZ Domäne nicht primär in den heterogenen Elektronentransfer des immobilisierten HoxGKZ involviert ist, allerdings eine wichtige Rolle bei der Stabilisierung des Enzyms auf der Elektrode spielt.



## 1 Introduction

The main motivation of this work was to gain insight into structural and mechanistic properties of selected chromophore containing enzymes immobilised on conductive support devices. Immobilisation of enzymes onto conductive supports is one of the main strategies in the design of bioelectronic devices such as biofuel cells [95] and biosensors [72, 78, 79]. The performance of these devices is determined by the catalytic activity and stability of the immobilised enzyme and the efficiency of its electronic communication with the conductive support. Moreover, biocompatibly coated conductive supports may represent model systems for mimicking membranes [1, 3]. In their natural environment, many enzymes exert their function at membranes under the influence of high electric fields. Since conductive supports allow for electrochemical potential and electric field control, they may provide a more realistic platform for the study of enzymes [3, 191, 198].

Electrochemical methods that monitor the integrated electronic response of immobilised species to changes of experimental parameters are being employed in the study and optimisation of support/enzyme devices [72, 95]. The membrane bound hydrogenase from *Ralstonia eutropha* H16 (MBH) [6, 18, 19, 21, 24, 97] and human sulphite oxidase (hSO) [72, 78, 79] represent two prominent examples of enzymes that have been extensively studied with electrochemical methods. However, these techniques do not provide structural information and do not give insight into molecular processes that are associated with the electron transfer. In this respect, surface enhanced vibrational spectroscopy represents an increasingly important technique complementing electrochemical methods [1, 3]. Moreover, surface enhanced spectroscopic techniques can be employed simultaneously with electrochemical methods [1-3, 5, 8, 68, 112] such as protein film voltammetry (PFV), which is a standard technique in the study of catalytic processes of immobilised proteins [6].

A combined surface enhanced resonance Raman (SERR) spectroscopic and protein film voltammetric (PFV) approach was employed in this work for the study of the heme containing enzymes hSO (chapter 6) [5] and MBH (chapter 7) [8]. The MBH is an oxygen tolerant [NiFe] hydrogenase consisting of three subunits HoxG, HoxK and the di-heme cytochrome *b* subunit HoxZ [23, 24, 103]. It is able to catalyse the reversible splitting of hydrogen into protons and electrons even in the presence of atmospheric oxygen concentrations [21]. In view of decreasing fossil resources there is the need of developing hydrogen-based energy conversion technologies [20, 95]. Therefore, research efforts have been made in order to explore the possibilities of MBH for application in bioelectronic devices [19, 21, 95] and examine its extraordinary oxygen tolerance [103]. However, research on MBH was mainly focussed so far on the HoxGK hetero-dimer [6, 18, 19, 21, 25-27]. In this work, the role of the HoxZ subunit in the electron transfer pathway of

immobilised MBH was explored [8] (chapter 7.3).

The homo-dimeric hSO contains a molybdopterin cofactor (moco) domain and a mono-heme cytochrome *b5* (Cyt *b5*) domain per monomer [73]. While catalytic oxidation of sulphite to sulphate takes place at the moco, the Cyt *b5* was shown to function as an electron shuttling unit that exhibits large translational reorientation between electron uptake from the moco domain and electron release to an external redox partner [13, 80 - 84]. HSO has been considered for application in sulphite biosensor devices [72, 78, 79]. Since sulphites may bear health risks [88, 89] but are widely used in food and pharmaceutical industries [85-87], there is a demand for low cost quantitative sulphite sensing devices. The rational design of a hSO based biosensor in particular and support/enzyme systems in general would benefit from a better understanding of the molecular processes at the support/protein interface. The aim of the SERR spectroscopic and electrochemical study of hSO presented in chapter 6.3 [5] was to examine the adsorption process of the enzyme and the role of the cytochrome *b5* subunit during catalysis in the immobilised state. A brief introduction into the current state of electrochemical and spectroscopic research and related issues on hSO and MBH is given in the respective chapters.

The main principles of SERR spectroscopy and PFV are presented in chapter 2.1 – 2.3 and chapter 4.4, respectively. SERR spectroscopy provides dynamic structural information with enormous sensitivity and a two-fold selectivity, because only the chromophore region of adsorbed molecules is probed [1, 3, 7]. However, the incident radiation needs to be in resonance with both the plasmon frequencies of an surface enhanced Raman (SER) active metal support material and an electronic transition of the adsorbed probe molecule, respectively [1, 7]. For the study of heme cofactors immobilised on sub-microscopically rough silver surfaces both resonance conditions are particularly well matched upon 413 nm excitation. Silver provides by far the highest signal enhancements throughout the visible and near-infrared region and is therefore best suited for SERR spectroscopy from the optical point of view [4]. However, the electrochemical applicability and biocompatibility of silver is poor [11, 156, 161] as compared to gold, which is more commonly used in electrochemistry [176-180]. Silver supports can still be employed in the study of biomolecules by using biocompatible electrode coating materials [1-3, 5, 7, 8, 67]. Self assembled monolayers (SAM) of  $\omega$ -functionalised alkanethiols represent the most versatile biocompatible coating materials [9] and were used throughout this work. They are presented in chapter 2.5.

There are also other approaches to improve the performance of silver-based SER-active support materials. A novel gold-silver-hybrid electrode for SER spectro-electrochemistry that aims at combining the electrochemical properties and chemical stability of gold with the optical properties of silver is introduced in chapter 5 [11, 12]. In this work, the performance of this hybrid device was explored (chapters 5.3 and 5.4) [12].

Finally, two more projects that were carried out in this work are briefly presented in chapter 8. These projects were the SERR spectroscopic study of the flavin containing xenobiotic reductase A from *Pseudomonas Putida* 86 and the resonance Raman spectroscopic study of mitochondria sample preparations from mouse pancreas.



## 2 Theoretical Background

### 2.1 Raman Spectroscopy

In this work, Raman spectroscopic techniques were employed for the study of chromophore containing proteins. For a better understanding, the theory and main principles of Raman spectroscopic techniques are briefly presented in the following chapters.

#### 2.1.1 Normal Modes

Each atom within a molecule has three degrees of freedom, hence an  $N$ -atomic molecule has  $3N$  degrees of freedom. For a non-linear (linear) molecule three of them refer to translations and three (two) to rotations of the molecule. The remaining  $3N - 6$  ( $3N - 5$ ) degrees of freedom are precisely defined periodic oscillations of the atoms. These oscillations can be described by displacements ( $\Delta x_\gamma$ ,  $\Delta y_\gamma$ ,  $\Delta z_\gamma$ ) of each individual atom  $\gamma$  within the Cartesian coordinates  $x$ ,  $y$  and  $z$ . They are the vibrations of the molecule, the so-called normal modes, which may also be described by normal mode coordinates,  $Q_k$  [ $kg^{1/2} \cdot m$ ]. For a given normal mode  $k$  (which has the frequency  $\nu_k$ ), the normal coordinates are  $Q_{k'} = 0$  for all  $k' \neq k$  and the movement of all atoms can be described in terms of a single scalar  $Q_k(t)$  oscillating at  $\nu_k$ . The normal coordinates  $Q_k$  are therefore a measure for the amplitude of the deformation according to the pattern of a given normal mode  $k$ .

Transitions between energy levels, i.e. oscillation frequencies, of normal modes are probed by vibrational spectroscopy. Normal mode frequencies lie in the range of 0.5 to 0.005 eV, which corresponds to electromagnetic radiation in the infrared region (wavelengths between 2.5 and 50  $\mu\text{m}$ ). For historical reasons the frequencies of normal modes are expressed in wavenumbers  $\tilde{\nu}$  [ $\text{cm}^{-1}$ ], defined according to

$$\{2.1.1\} \quad \tilde{\nu} = \frac{\nu}{c},$$

with  $\nu$  being the frequency of the normal mode and  $c$  the speed of light. In each normal mode each atom oscillates in-phase and with the same frequency. The amplitude of oscillation, however, may be different for each atom, such that the contribution of the oscillation of each individual atom to a particular normal mode may vary significantly. In many instances it is a reasonable

approximation to ascribe a certain normal mode to the oscillation of a group of few atoms within the whole molecule. Weighted by their contribution, the energies of a particular normal mode sensitively depend on (a) the masses of the individual atoms and (b) the forces acting on them. These forces do not only include chemical bonds of the individual atoms, but also non-bonding interactions within the molecule and with the environment of the molecule. Therefore, vibrational spectra are signatures of the chemical constitution, the structure, electron density distribution and chemical environment of the molecule.

### 2.1.2 Raman Scattering

The two main techniques to obtain vibrational spectra are infrared absorption (IR) and Raman spectroscopy, which are based on different physical mechanisms. In IR-absorption spectroscopy the molecule is exposed to a continuous IR radiation source and normal modes are excited directly into higher vibrational energy levels through the absorption of infrared radiation. In Raman spectroscopy vibrational transitions are induced via inelastic scattering of monochromatic light (figure 2.1.2). The light is usually in the visible region and can be provided by commercially available lasers. The inelastic scattering of light by matter is named after the Indian scientist C. V. Raman who was the first to observe this effect in 1928.

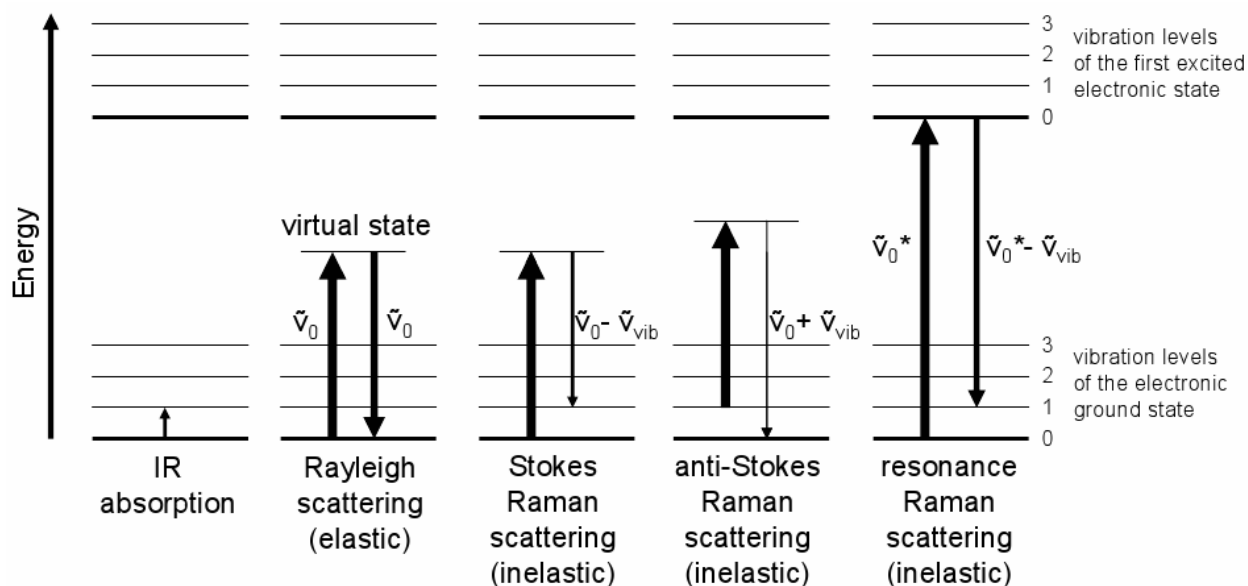


Figure 2.1.2: Energy transitions in vibrational spectroscopy.

The scattering process can be described with classical physics in terms of an interaction of the electric field vector of the incident light with the electron cloud of the molecule. As a response to the nuclear motions also the molecular electron cloud is vibrating with the normal mode frequency  $\tilde{\nu}_k$ . In a quantum mechanical picture an incident photon with the frequency  $\tilde{\nu}_0$  (whereby  $\tilde{\nu}_0 \gg \tilde{\nu}_k$ )

is scattered by the molecule to produce a phonon, corresponding to a normal mode with  $\tilde{\nu}_k$  and a scattered photon with  $\tilde{\nu}_0 - \tilde{\nu}_k$  (Stokes Raman scattering). In case of anti-Stokes Raman scattering ( $\tilde{\nu}_0 + \tilde{\nu}_k$ ) a phonon is annihilated whereas in Rayleigh scattering (elastic scattering) the frequency of the incident and the scattered light is the same. In inelastic scattering the frequencies are shifted with respect to the incident light and are associated with a transition from a lower into a higher vibration level ( $\tilde{\nu}_0 - \tilde{\nu}_k$ ) and vice versa ( $\tilde{\nu}_0 + \tilde{\nu}_k$ ). The wavenumbers of Raman bands are quoted as Raman shifts  $\Delta\tilde{\nu}$  and are defined according to  $\Delta\tilde{\nu} = \tilde{\nu}_0 - (\tilde{\nu}_0 \pm \tilde{\nu}_k)$ .

The frequencies obtained with Raman spectroscopy are in principle equivalent to the ones probed from IR absorption. However, due to different physical mechanisms, the probability for a certain vibrational transition is different for both techniques resulting in different relative and absolute intensities of absorbed (IR) and inelastically scattered (Raman) radiation. Therefore IR and Raman spectroscopy are commonly referred to as complementary techniques.

### 2.1.3 Raman Signal Intensity

Raman band intensities are proportional to the square of the induced dipole moment  $\vec{\mu}_{ind}$ , which results from the interaction of the molecular electron cloud with the electric field vector  $\vec{E}_0$  of the incident light. The induced dipole moment depends on the square root of the incident light intensity  $I_0 \sim (\vec{E}_0)^2$  and the polarisability  $[\alpha]$  of the molecule. It can be shown that the Raman scattering intensity for a fundamental transition from vibrational state  $|i\rangle$  to  $|f\rangle$  is proportional to the variation of the polarisability with respect to the motion along the normal mode coordinate  $Q_k$  of this vibrational mode according to:

$$\{2.1.3.1\} \quad \alpha_{if} \sim \left( \frac{d\alpha}{dQ_k} \right)_0 \delta \langle i | Q_k | f \rangle.$$

Only vibrational modes for which  $\alpha_{if}$  is non-zero are observable with Raman spectroscopy. This general selection rule for Raman scattering is different to the IR absorption selection rules, where the permanent dipole moment of the molecule must change upon nuclear motion along the normal mode coordinate. To account for its anisotropy, the molecular polarisability  $[\alpha]$  has to be expressed as a tensor containing nine elements  $\alpha_{\rho\sigma}$  with  $\rho$  and  $\sigma$  denoting the molecule fixed x, y and z coordinates.

The occupation of vibrational states is given by the Boltzmann distribution. Accordingly, the occupation of the vibrational ground state is always higher than for excited vibrational states. It should also be noted that, according to Rayleigh's  $\nu^4$ -law, the intensity of scattered light is proportional to the fourth power of its frequency ( $I_{sc} \sim \nu_{sc}^4$ ). Since light of shorter wavelengths is scattered with much higher intensity this law has also strong relevance for the choice of the excitation source, i.e. the frequency of the incident light beam.

All these considerations are summed up in the following expression for Raman band intensities  $I_{if}$  at the Raman band frequency  $\nu_k$ :

$$\{2.1.3.2\} \quad I_{if} \sim I_0 \cdot e^{\left(\frac{E_i}{k_B T}\right)} \cdot \underbrace{(\nu_0 \pm \nu_k)^4 \cdot \sum_{\rho, \sigma=x,y,z} (\alpha_{\rho\sigma})_{if}^2}_{\sim \sigma_{if} \text{ (Raman cross section)}}$$

$E_i$  denotes the energy of the initial vibrational state  $|i\rangle$ ,  $T$  the temperature and  $k_B$  the Boltzmann constant. It is useful to introduce the Raman cross section for this transition,  $\sigma_{if}$ , which is a quantity to define the inelastic scattering efficiency. It is proportional to the indicated terms of equation {2.1.3.2}.

According to the Boltzmann distribution, the intensity of Stokes scattering is always higher than anti-Stokes scattering, however, their intensity ratio is temperature dependent. The temperature dependence can, in turn, be utilised for the determination of local sample temperatures [39]. According to Rayleigh's  $\nu^4$ -law, also relative intensities of Stokes and anti-Stokes signals are different.

#### 2.1.4 Polarisability Tensor Components

A comprehensive description of the polarisability tensor components is only possible with quantum mechanics, also taking into account that vibrational modes may be coupled to electronic transitions. Since two photons are involved in the scattering process second order perturbation theory has to be applied. On the basis of Kramers-Heisenberg-Dirac's dispersion theory [33-36], the components of the polarisability tensor for a transition between the vibrational states  $|i\rangle$  and  $|f\rangle$  in the electronic ground state  $G$  can then be expressed as [1, 37-40]:

$$\{2.1.4\} \quad (\alpha_{\rho\sigma})_{if} = \frac{1}{\hbar} \sum_{R,r \neq i,f} \left( \frac{\langle iG|M_{\rho}|Rr\rangle \langle rR|M_{\sigma}|Gf\rangle}{\nu_{Rr} - \nu_k - \nu_0 + i\Gamma_{Rr}} + \frac{\langle rR|M_{\sigma}|Gf\rangle \langle iG|M_{\rho}|Rr\rangle}{\nu_{Rr} - \nu_k + \nu_0 + i\Gamma_{Rr}} \right).$$

Here  $\rho$ ,  $\sigma = x, y, z$  independently refer to the axes of the molecule-fixed non-rotating Cartesian coordinate system [39]. The indices  $R$  and  $r$  refer to the excited electronic states and the vibrational (vibronic) states of these excited electronic states of the molecule, respectively.  $M_{\rho}$  and  $M_{\sigma}$  are  $\rho$ - and  $\sigma$ -components of the respective electron position operator, referring to the polarisation of the incident ( $\rho$ ) and scattered ( $\sigma$ ) light. The frequency of the vibronic state  $Rr$  is denoted as  $\nu_{Rr}$  and  $\Gamma_{Rr}$  is a damping constant that is related to its lifetime. Under non-resonant conditions where  $\nu_0$  is far below any electronic transition, the denominators of both terms in the brackets at the right side of equation {2.1.4} are large resulting in low values for the polarisability.

In general, only a small fraction of light that passes through a sample is scattered. Moreover, most of the scattered light is scattered elastically and has therefore the same frequency as the incident light beam (Rayleigh scattering). The quantum yield of Raman scattering is very low ( $\Phi_{\text{Raman}} \sim 10^{-9}$ ).

## 2.2 Resonance Raman Effect

If the frequency of the monochromatic light source  $\nu_0$  is in resonance or pre-resonance with an electronic transition of the molecule ( $G \rightarrow R$ ), this will result in an up to  $10^6$ -fold amplification of the signals of vibrational modes. However, only the signals of those vibrational modes that are coupled to this specific electronic transition are enhanced. The selective signal amplification is a result of increased polarisability of these modes and can be readily explained with equation {2.1.4}. Under resonance conditions, the summation of vibrational states can be approximately restricted only to the one resonant excited electronic state  $R$ . This simplifies equation {2.1.4}. Also the summation term in brackets can be simplified. When  $\nu_0$  is close to the frequency of the electronic state  $R$ , hence also  $\nu_{Rr}$ , the denominator of the right handed expression ( $\nu_{Rr} - \nu_k + \nu_0 + i\Gamma_{Rr}$ ) is very high as compared to the left handed expression ( $\nu_{Rr} - \nu_k - \nu_0 + i\Gamma_{Rr}$ ). Hence, the right handed expression can be neglected. The integrals  $\langle iG|M_{\rho}|Rr\rangle$  and  $\langle rR|M_{\sigma}|Gf\rangle$  represent vibronic transition dipole moments that depend on both the nuclear and electronic coordinates. According to the Born-Oppenheimer approximation these can be separated leading to  $\langle ir\rangle M_{GR,\rho}$  and

$\langle rf \rangle M_{GR,\sigma}$ , respectively (Franck-Condon principle). The overlap integrals  $\langle ir \rangle$  and  $\langle rf \rangle$  of the vibrational wavefunctions  $i$ ,  $r$  and  $f$  are the Franck-Condon factors and  $M_{GR,\rho}$  and  $M_{GR,\sigma}$  are the  $\rho$ - and  $\sigma$ -components of the electronic transition moment. These considerations lead to the following simplified expression of equation {2.1.4} under resonance conditions:

$$\{2.2.1\} \quad (\alpha_{\rho\sigma})_{if} \approx \frac{1}{\hbar} \sum_{r \neq i,f} \frac{\langle ir \rangle \langle rf \rangle M_{GR,\rho} M_{GR,\sigma}}{\nu_{Rr} - \nu_k - \nu_0 + i\Gamma_{Rr}}.$$

If the Born-Oppenheimer approximation is valid, the dependence of the electronic transition moment on the internal normal mode coordinates  $Q_k$  is small. Therefore,  $M_{GR,\rho}$  and  $M_{GR,\sigma}$  can be expanded in a Taylor series with respect to  $Q_k$ .

$$\{2.2.2\} \quad \begin{aligned} M_{GR,\rho}(Q_k) &= M_{GR,\rho}(Q_k^{(0)}) + \sum_k \left( \frac{\partial M_{GR,\rho}}{\partial Q_k} \right)_0 Q_k + \dots \\ &= M_{GR,\rho}^0 + \sum_k M'_{GR,\rho} Q_k + \dots \end{aligned}$$

$M_{GR,\sigma}$  is expanded in a similar manner. The combination of equations {2.2.1} and {2.2.2} leads to an infinite number of terms, however, within the harmonic approximation only the first and second terms of the Taylor series are considered. With this, the  $\rho\sigma$ -components of the polarisability tensor can be expressed as the sum of two so-called Albrecht's A- and B-terms:

$$\{2.2.3\} \quad (\alpha_{\rho\sigma})_{if} \approx A_{\rho\sigma} + B_{\rho\sigma},$$

$$\{2.2.3a\} \quad A_{\rho\sigma} \approx \frac{1}{\hbar} M_{GR,\rho}^0 M_{GR,\sigma}^0 \sum_{r \neq i,f} \frac{\langle ir \rangle \langle rf \rangle}{\nu_{Rr} - \nu_k - \nu_0 + i\Gamma_{Rr}},$$

$$\{2.2.3b\} \quad B_{\rho\sigma} \approx \frac{1}{\hbar} \left( M'_{GR,\rho} M_{GR,\sigma}^0 \sum_{r \neq i,f} \frac{\langle i|Q_k|r\rangle \langle rf \rangle}{\nu_{Rr} - \nu_k - \nu_0 + i\Gamma_{Rr}} + M_{GR,\sigma} M'_{GR,\rho} \sum_{r \neq i,f} \frac{\langle ir \rangle \langle r|Q_k|f \rangle}{\nu_{Rr} - \nu_k - \nu_0 + i\Gamma_{Rr}} \right).$$

The  $A_{\rho\sigma}$  – and  $B_{\rho\sigma}$  – terms represent the two major enhancement mechanisms in RR spectroscopy. They are referred to as Franck-Condon (FC) ( $A_{\rho\sigma}$  – term) and Herzberg-Teller vibronic coupling (HT) ( $B_{\rho\sigma}$  – term) scattering. In both cases, the denominators ( $\nu_{Rr} - \nu_k - \nu_0 + \Gamma_{Rr}$ ) decrease rapidly when  $\nu_0$  approaches the frequency of the electronic state  $R$  leading to increased polarisability and thus an increased RR signal. The contribution of each of the mechanisms to the

overall enhancement, however, may be different for different vibrational modes and electronic transitions, respectively.

The  $A_{\rho\sigma}$  – term will contribute to the resonance enhancement, when the product of the FC factors  $\langle ir \rangle \langle rf \rangle$  is non-zero. Hence, for FC scattering the vibrational wavefunctions have to be non-orthogonal, which may arise in two ways. Either the shape of the electronic potential in the ground and excited state is different or there is a displacement of the electronic potential energy minima along the normal coordinate  $Q_k$ . In practice, a changed excited state potential shape only occurs if there is also a displacement of its energy minimum  $\Delta Q_k$  with respect to the ground state potential. Symmetry considerations require that such a displacement can occur only for totally symmetric modes (unless the molecular symmetry is changed in the excited state). The larger the displacement  $\Delta Q_k$  is the higher the non-orthogonality and hence the  $A_{\rho\sigma}$  – term contribution will be. On the other hand, FC scattering intensity is also strongly dependent on the product of the  $\rho$  - and  $\sigma$  -components of the electronic transition moment in the vibrational equilibrium position  $M_{GR,\rho}^0 M_{GR,\sigma}^0$ . In summary, the FC scattering mechanism particularly accounts for totally symmetric vibrational modes (non-orthogonality of wavefunctions) that are coupled to electric-dipole allowed electronic transitions (high values for  $M_{GR,\rho}^0 M_{GR,\sigma}^0$ ).

In equations {2.2.1} and {2.2.3} the summation of vibrational states is only restricted to the one resonant excited electronic state  $R$ . In  $B_{\rho\sigma}$  – term scattering, however, coupling to another electronic transition is involved. The crucial parameters here are the first derivatives of the  $\rho$  - and  $\sigma$  -components of the electronic transition moment  $M'_{GR,\rho}$  and  $M'_{GR,\sigma}$ . Their values may exceed those of  $M_{GR,\rho}^0$  and  $M_{GR,\sigma}^0$  if the resonant electronic state  $R$  can gain absorption strength from another electronic state  $S$  via  $Q_k$  by so-called Herzberg-Teller vibronic coupling. The stronger the transition to the state  $S$  is and the closer the energies of states  $R$  and  $S$  are the larger  $M'_{GR,\rho}$  and  $M'_{GR,\sigma}$  will be.  $B_{\rho\sigma}$  – term scattering may occur for both totally and non-totally symmetric vibrational modes. However, it can be shown that the  $B_{\rho\sigma}$  – term is only non-zero for totally symmetric modes, if the states  $R$  and  $S$  are of the same symmetry. This is usually not the case for two energetically nearby electronic states [40]. Therefore, the  $B_{\rho\sigma}$  – term particularly accounts for non-totally symmetric vibrational modes and weak electronic transitions that may couple to a nearby strong one.

## 2.3 Surface Enhanced Raman Spectroscopy

In the 1970ies it was discovered that molecules exhibit greatly enhanced Raman scattering if adsorbed on rough surfaces of certain metals. Other photophysical and photochemical processes are enhanced as well albeit to a different extent [45]. The so-called surface enhancement that can be of several orders of magnitude, is metal- and wavelength-specific and also closely related to the morphology of the metal surfaces [4, 44]. Even though surface enhanced Raman (SER) spectroscopy could be demonstrated using transition metals [125-127, 187], it mainly relies on the coinage metals gold, silver and copper, which exhibit the best performance as optically active support materials [128, 187]. Among them, silver support materials provide by far the highest plasmonic electromagnetic field enhancements throughout the visible and near-infrared region and are therefore best suited for SER spectroscopy from the optical point of view [4]. Gold and copper substrates only provide surface enhancement above 520 nm [4].

There are several methods for the preparation of a roughness in the nm-scale (10 – 100 nm), which was found to be necessary. In this work, a standard electrochemical roughening procedure of solid ring shaped silver electrodes was employed, other methods include chemical or vapour deposition on appropriate solid support materials [41, 42]. The SER effect is also observed upon adsorption on silver and gold nanoparticles in colloidal solutions [43, 184]. The application of rough solid silver electrodes, however, allows potential-dependent SER-spectroscopic studies by controlling the electrode potential. Due to its much lower oxidation potential, the applicable potential range is quite narrow for silver as compared to gold electrodes, which are more commonly used for electrochemistry [176-180]. Moreover, the intrinsic biocompatibility of silver is lower than of gold as  $\text{Ag}^+$  ions that can harm immobilised biomolecules are formed at the metal-solution interface [11, 156, 161]. In this respect, the properties of silver supports can be significantly improved with biocompatible coating materials, enabling the application of these devices also in the study of biomolecules [1-3, 5, 7, 8, 67] (see chapter 2.4).

Electrochemically roughened silver electrodes represent excellent platforms for SER spectroscopy and provide control of electrode potential. With respect to colloidal solutions this represents an important advantage for the study of redox processes. For the description of the SER effect, however, it is useful to consider a colloidal metal particle first.

The SER effect can be understood on the basis of classical electromagnetic theory [45]. If the radius  $r_0$  of a sphere-shaped metal particle is small with respect to the wavelength of the incident light  $\lambda_0$  (Rayleigh limit), the electric field of the incident light  $\vec{E}_0(\nu_0)$  can induce an electric dipole moment in the sphere and excite the surface plasmons, which are the collective vibrations of the free electrons of the metal particle. This induced dipole moment causes an additional induced

electric field component  $\vec{E}_{ind}(\nu_0)$ , which is normal to the surface in the near-field of the sphere. The induced electric field component is given by:

$$\{2.3.1\} \quad \vec{E}_{ind}(\nu_0) = \vec{E}_0(\nu_0) \cdot 2 \left( \frac{\tilde{\epsilon}_r(\nu_0) - 1}{\tilde{\epsilon}_r(\nu_0) + 2} \right).$$

The quantity  $\tilde{\epsilon}_r(\nu_0)$  is the frequency dependent dielectric constant of the metal divided by the square of the refractive index of the surrounding medium  $n_{solv}$ :

$$\{2.3.1a\} \quad \tilde{\epsilon}_r(\nu_0) = \frac{\epsilon_{re}(\nu_0) + i\epsilon_{im}(\nu_0)}{n_{solv}^2}.$$

The total electric field  $\vec{E}_{tot}(\nu_0)$ , which is the sum of the incident and induced electric field, can be expressed by:

$$\{2.3.2\} \quad \vec{E}_{tot}(\nu_0) = \vec{E}_0(\nu_0) + \vec{E}_{ind}(\nu_0) = \vec{E}_0(\nu_0) \cdot F_E(\nu_0).$$

It can be easily seen from equation {2.3.1} and {2.3.1a} that the enhancement factor  $F_E(\nu_0)$ , becomes large when the real part of the frequency dependent dielectric constant  $\epsilon_{re}(\nu_0)$  approaches -2 and the imaginary part  $i\epsilon_{im}(\nu_0)$ , which is a measure for losses in the solid related to absorption, is small. These conditions are particularly well matched for silver around 400 nm. The considerations for the enhancement of the electric field of the incident light may also account for the electric field of the Raman scattered light  $\vec{E}_{Ra}(\nu_0 \pm \nu_k)$ , which is proportional to  $\vec{E}_{tot}(\nu_0)$ . Due to shifted frequencies, however, the magnitude of the field enhancement  $F_E(\nu_0 \pm \nu_k)$  may be different from  $F_E(\nu_0)$ . Because both the electric field of the incident and Raman scattered light are enhanced and the intensity of light scattering is proportional to the square of the electric field, the SER effect may yield enormous signal enhancements. The enhanced electric field vector is directed normal to the metal plane. Since the metal plane is a particle or a rough surface, all possible directions are included on the macroscopic view. Therefore, SER signals are always depolarised.

The considerations for small colloidal particles can be principally adopted for the description of other surface morphologies including electrochemically roughened silver surfaces used in this work (see chapter 3.2). The morphology of an electrochemically roughened silver surface can be

approximately modelled by connected semi-spheres with a broad distribution of radii in the range between 20 – 200 nm. It was shown that the plasmon resonance frequency of particles with radii above the Rayleigh-limit ( $r_0 \ll \lambda_0$ ) is shifted to the red with increasing radii [181-183]. Therefore, the experimentally observed wavelength dependent surface enhancement for such a device is very broad and may cover the whole spectral range between the UV and IR region [4].

The electromagnetic theory implies that the surface enhancement is not restricted to directly adsorbed molecules. In fact, molecules that are not adsorbed but situated in close proximity of SER-active surfaces also experience the enhancement effect. The magnitude of surface enhancement of Raman scattering, expressed by the enhancement factor  $F_{SER}$ , decays with the distance dependence of dipole-dipole interactions. The enhancement  $F_{SER}(d)$  that a molecule at a distance  $d$  from a spherical particle with the radius  $r_0$  experiences can be expressed by

$$\{2.3.2\} F_{SER}(d) = F_{SER}(0) \cdot \left( \frac{r_0}{r_0 + d} \right)^{12},$$

with  $F_{SER}(0)$  representing the enhancement factor when directly adsorbed on the surface. The distance dependence is especially important for the study of biological molecules. In these studies SER-active metal surfaces are often covered by biocompatible coatings to prevent denaturation and/or inactivation of the biomolecule in the adsorbed state. The thickness of these coatings is typically between 1 and 5 nm. At these distances the surface enhancement from particles with radii in the range 20 – 100 nm is significantly decreased but still sufficiently strong to be utilised.

It should be noted that also in surface enhanced Raman spectroscopic experiments the resonance Raman effect may apply. If the exciting radiation is in resonance with an electronic transition of the molecule and the surface plasmons of the SER substrate, the molecular (RR) and surface plasmon (SER) resonance enhancement mechanisms will sum up resulting in very high sensitivity and a two-fold selectivity, because only the cofactor of only the adsorbed proteins are probed with surface enhanced resonance Raman (SERR) spectroscopy [43, 172].

## 2.4 Electrochemical Interface at the Bare Silver Electrode

A bare silver surface has a highly negative potential of zero charge ( $E_{pzc}$  around -0.7 V vs. SHE [195, 196]) and is therefore positively charged in aqueous electrolyte solutions. The positive charge is overcompensated by anions from the electrolyte solution that bind to the silver forming an

electric double layer on the surface (figure 2.4). Especially chloride, sulphate and phosphate ions are known to have a high tendency for specific binding on silver.

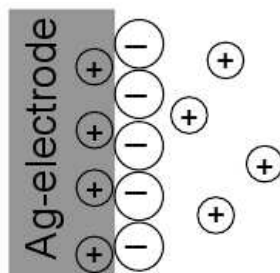


Figure 2.4: A) Representation of the Helmholtz electric double layer at the bare silver/electrolyte interface.

Proteins can bind electrostatically to the positively charged silver surface or to the compact anion-layer, respectively. However, most biomolecules will experience severe structural changes upon adsorption and may lose their functionality [156, 163]. Here, the crucial parameter is the surface charge density  $\Phi_{IF}$ , which is very high at the electrochemical interface of the bare silver electrode. Moreover, chemical reactions between silver ions and the adsorbate can not be excluded [156, 161]. These problems can be solved by using self assembled monolayers (SAMs) that separate the biomolecule from the silver surface.

## 2.5 Self Assembled Monolayers of Alkanethiol Derivatives

Alkanethiole derivatives attach spontaneously from solution to silver and gold surfaces via formation of strong covalent metal-sulphur bonds [9, 46]. This process can be described by the Langmuir or Frumkin adsorption isotherm and takes place within millisecond to few minutes, resulting in a monolayer of chemisorbed organic molecules on the metal surface. In a second step, the monolayer reorganises to form a compact monolayer [46]. This formation of a so-called self assembled monolayer (SAM) takes place within several hours. The driving force for the reorganisation is thermodynamic energy optimisation by hydrophobic interactions between the alkyl-chains [9]. The alkanethiol molecules can have an additional functional group X (e.g. X = -NH<sub>2</sub>, -COOH, -OH) in the terminal  $\omega$ -position.

It was shown that SAMs may facilitate immobilisation of proteins under preservation of their native structure and functionality [3]. The rational choice of a certain type of SAM can facilitate the adsorption of a particular biomolecule in the desired manner. The surface charge density  $\Phi_{IF}$  may be strongly decreased on a SAM with respect to the bare electrode. Carboxyl-terminated SAMs (X = -COOH), for instance, are mostly protonated at pH 7.0 (vide supra) and provide, therefore, a slightly negatively charged biocompatible surface. This may facilitate the immobilisation of cationic

proteins under preservation of their native structure and functionality [3]. A slightly positively charged biocompatible interface can be created by using amino-terminated SAMs ( $X = -NH_2$ ), facilitating the immobilisation of anionic proteins [5]. Methyl-terminated SAMs may be used for hydrophobic immobilisation while hydroxyl-terminated SAMs provide a polar but uncharged surface for immobilisation via dipole-dipole interactions.

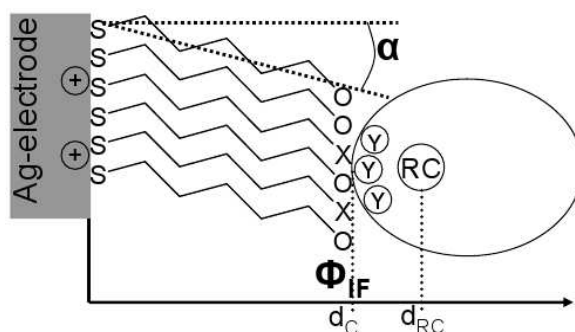


Figure 2.5.1: Schematic representation of a protein immobilised on a SAM-coated silver electrode. O and X represent the same functional group in the uncharged and charged state, respectively. Y represents a functional group of an amino acid side chain with a charge opposite to the charge of X. RC denotes the reaction center of the protein.

Also mixed SAMs with different functionalisation and/or chain length can be formed on silver surfaces, most easily by co-adsorption from a solution containing the different alkanethiols in a desired concentration ratio [176-179]. Here, it should be noted that the molar composition of the SAM does not necessarily correspond to concentration ratio of alkanethiols in the incubation solution [9]. The elucidation of the best suited SAM and other immobilisation conditions aiming at preserving the natural structure and functionality represents a new challenge for each biomolecule.

The SAM layer thickness  $d_C$  depends on the chain length of the SAM and the tilt angle of the SAM molecules with respect to the metal surface normal  $\alpha$ . The tilt angle may be different for alkanethiols adsorbed on different metals. There is evidence for a higher tilt angle on smooth gold surfaces ( $\sim 30^\circ$ ) with respect to smooth silver surfaces ( $\sim 15^\circ$ ) [47]. This would lead to differing distances of reaction centers of adsorbed proteins  $d_{RC}$  and has to be considered in the comparison of heterogeneous electron transfer rates obtained on both metals (see chapter 2.6.2).

In this work, SAMs of carboxyl-, amino- and hydroxyl-functionalised alkanethiols were employed. Due to repulsive interactions between functional groups of adjacent SAM molecules  $pK_A$  values of carboxyl- and amino-functionalised alkanethiol molecules are significantly shifted in the monolayer with respect to the  $pK_A$  of the monomers in solution. In general, it is less favourable for functional groups in the monolayer to carry charges. Therefore, the  $pK_A$  values of carboxyl-terminated alkanethiols are significantly up-shifted and those of amino-terminated

alkanethiols are significantly down-shifted upon formation of a monolayer [144, 145-150]. For example the  $pK_A$  of a mercaptoundecanoic acid SAM on a gold electrode is  $\sim 5.5$ , which is about two units higher than for the molecules in solution. Moreover, it should be noted that  $pK_A$  shifts are larger with increasing chain lengths [145] and strongly depend on the applied electrode potential [146].

Repulsive interactions between charged functional groups of adjacent SAM molecules may disturb the highly aligned structure. In fact, the SAM structure is not uniform in many instances. Two main SAM conformers, which are referred to as trans and gauche, may coexist on the same metal surface. Especially relatively short SAMs with a low number of methylene groups ( $n = 1$  to 5), and hence only weak hydrophobic interactions, exhibit high fractions of the less ordered gauche conformer (figure 2.5.2).

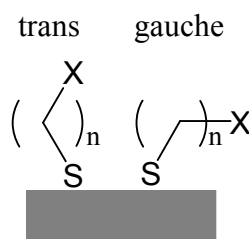


Figure 2.5.2: Cartoon of  $\omega$ -functionalised alkanethiol SAMs in trans- and gauche conformation.

If adsorbed on a SER-active substrate, trans and gauche conformers can be easily distinguished due to different frequencies of the prominent C-S stretching mode. Besides the chain-lengths the ratio between gauche- and trans-fractions also depends on the morphology of the solid support. The gauche to trans ratio is generally higher on SER-active sub-microscopically roughened silver surfaces as compared to flat surfaces.

## 2.6 Electron Transfer Theory

A unified theory for the treatment of both homogeneous and heterogeneous electron transfer processes was introduced by Marcus and adopted by other authors [3, 51, 138, 190, 191]. In order to describe heterogeneous electron transfer it is useful to introduce some basic concepts of homogeneous ET theory first [48-50]. This is done in the following chapter 2.6.1, which is mainly based on the overview on basic electron transfer theory provided by Bolton and Archer [54]. In chapter 2.6.2 simple expressions for the description of heterogeneous electron transfer processes are presented [1].



with  $\lambda$  being the reorganisation free energy, which is defined as the change in Gibbs energy of the reactant state upon distorting its configuration in order to adopt the equilibrium configuration of the product state (figure 2.6.1). The reorganisation free energy can be divided into an inner and an outer part ( $\lambda = \lambda_{in} + \lambda_{out}$ ). The inner part  $\lambda_{in}$  is related to free energy changes due to structural changes within the molecule. In the outer part  $\lambda_{out}$  free energy changes due to reorganisation and changes in the polarisation of the surrounding solvent molecules are considered. In polar solvents  $\lambda_{out}$  is usually much higher than  $\lambda_{in}$ .

The classical Marcus equation is given by

$$\{2.6.1.2\} \quad k_{ET} = \kappa_{el} \cdot \nu_n \cdot \exp\left[-\frac{(\lambda + \Delta G^0)^2}{4\lambda \cdot k_B T}\right].$$

Here,  $\nu_n$  is the frequency of passage through the transition state (intersection point). It is intimately related to the nuclear motions of the reactant state. The quantity  $\kappa_{el}$  is the so-called electron transmission coefficient at the intersection point. In adiabatic ET reactions  $\kappa_{el}$  is close to unity ( $\approx 1$ ), which means that ET will occur almost each time when the  $D/A$  complex reaches the transition state. Adiabatic ET is described well with classical Marcus theory. It generally occurs if  $D$  and  $A$  in the  $D/A$  complex are relatively close together. In diabatic ET processes, however,  $\kappa_{el}$  is much smaller ( $\ll 1$ ), resulting in low ET rates. In these cases, ET not necessarily occurs once the intersection point is reached. The system will more likely relax back to equilibrium configuration of the reactant state.

Adiabatic and diabatic ET represent the two main types of ET reactions. With classical physics different transmission coefficients can not be explained. For this, a quantum mechanical description is needed. The crucial parameter in this context is the electronic coupling  $H_{RP}$  between (Gibbs energy profiles of) reactant and product states:

$$\{2.6.1.3\} \quad H_{RP} = \langle \psi_R^0 | \hat{H}_{el} | \psi_P^0 \rangle,$$

with  $\psi_R^0$  and  $\psi_P^0$  being the electronic wave functions of the reactant and product state in the equilibrium conformation and  $\hat{H}_{el}$  is the Born-Oppenheimer electronic Hamiltonian for the system. The electronic transmission factor  $\kappa_{el}$  strongly depends on the magnitude of  $H_{RP}$ , which is

relatively large in adiabatic ET processes ( $>0.025$  eV) [52]. In these cases the Gibbs energy surfaces of reactant and product states interact as indicated in figure 2.6.1 (left) and electrons can be readily transferred. The gap in the intersection region that arises from the coupling corresponds to  $2H_{RP}$ . The electronic coupling reaches a maximum value  $H_{RP}^0$  at the so-called van der Waals donor-acceptor distance  $d_0$ . In case of diabatic ET, however,  $H_{RP}$  is small and depends exponentially on the donor-acceptor distance ( $d_{DA}$ ):

$$\{2.6.1.4\} \quad H_{RP}(d_{DA}) \approx H_{RP}^0 \cdot \exp\left[-\frac{\beta(d_{DA} - d_0)}{2}\right].$$

The parameter  $\beta$  is referred to as the tunnelling decay parameter (see also equation {2.6.2.1}). As a result of equation {2.6.1.4} an exponential dependence of  $k_{ET}$  on  $d_{DA}$  is observed.

In the quantum mechanical treatment, the electron transition probabilities from all reactant to all product vibrational states have to be considered for the determination of  $k_{ET}$ . Here, the Franck Condon principle for vibronic transitions applies. The overlap of certain vibrational wavefunctions  $j$  and  $i$  of reactant and product states (including solvent vibrational modes), respectively, determines the probability of this particular ET process. The Franck Condon factors  $(FC)_{ij} = \langle ij \rangle$  have to be weighted by their particular Boltzmann probability  $P(E_{Rj})$ , where  $E_{Rj}$  is the energy of the vibrational state  $j$  of the reactant state. These considerations are reflected in Fermi's 'Golden Rule' [34, 53], which is derived from time-dependent second order perturbation theory. Applied for the description of an electron transfer in the  $D/A$  complex it leads to the following expression:

$$\{2.6.1.5\} \quad k_{ET} = \frac{2\pi}{\hbar} (H_{RP})^2 \sum_{ij} [(FC)_{ij}]^2 P(E_{Rj}) \delta(E_{Pi} - E_{Rj}),$$

where  $\hbar$  is the reduced Planck constant and  $\delta$  is a Dirac delta function that needs to be included in order to ensure energy conservation (i.e.  $\delta = 0$  if  $E_{Pi} \neq E_{Rj}$ ;  $\delta = 1$  if  $E_{Pi} = E_{Rj}$ ). Some reasonable approximations can be made in order to simplify the expression in equation {2.6.1.5}. Since solvent vibrational modes usually have low energies, they are often treated classically, which leads to the so-called semi-classical Marcus equation [49]. Moreover, the relevant high frequency vibrational modes of the molecule can be represented by a single averaged mode with the frequency  $\nu$  leading to the following expression [50]:

$$\{2.6.1.6\} \quad k_{ET} = \frac{2\pi}{\hbar} (H_{RP})^2 (4\pi\lambda_{out}k_B T)^{-1/2} \sum_{m=0}^{\infty} \left[ \frac{e^{-S} S^m}{m!} \right] \exp \left[ -\frac{(\lambda_{out} + \Delta G^0 + m\hbar\nu)^2}{4\pi\lambda_{out}k_B T} \right],$$

with  $m$  being an integer and  $S = \lambda_{in}(\hbar\nu)^{-1}$ . For ET reactions, in which  $-\Delta G^0 < \lambda$  (which corresponds to the so-called normal ET region), equation {2.6.1.6} can be simplified to the “high-temperature limit” of the semi-classical Marcus expression:

$$\{2.6.1.7\} \quad k_{ET} = \frac{2\pi}{\hbar} (H_{RP})^2 (4\pi\lambda k_B T)^{-1/2} \exp \left[ -\frac{(\lambda + \Delta G^0)^2}{4\lambda k_B T} \right].$$

Fast ET reactions may be limited by solvent dynamics. To account for this possibility, the expression in equation {2.6.1.7} can be modified by multiplication with the factor [57]:

$$\{2.6.1.8\} \quad \left[ \frac{1}{1+g} \right],$$

where  $g$  is an adiabaticity factor, which is defined as  $g = k_{ET}^D F \tau_D (\varepsilon_{op} / \varepsilon_s)$ . Here,  $k_{ET}^D$  corresponds to the diabatic ET rate constant at  $g = 0$  and  $F$  is a function of the ratios of  $\lambda_{in} / \lambda_{out}$  and  $\Delta G^* / k_B T$ . The quantity  $\tau_D$  is the constant field dielectric relaxation time of the solvent and  $\varepsilon_{op}$  and  $\varepsilon_s$  are its optical and static dielectric constant. It should be noted that  $\tau_D$ , and hence the ET rate, is solvent viscosity dependent.

## 2.6.2 Heterogeneous Electron Transfer

An expression for electron tunnelling between an electrode and an adsorbed redox site, i. e. diabatic heterogeneous ET, can be formulated as [138, 190, 191]:

$$\{2.6.2.1\} \quad k_{ET}(\eta) \approx \frac{\pi}{\hbar} \cdot \rho \cdot (H_{RP}^0)^2 \cdot \exp(-\beta \cdot d_{RC}) \cdot \operatorname{erfc} \left( \frac{\lambda + e\eta}{\sqrt{4\lambda k_B T}} \right),$$

where  $\eta$  is the overpotential,  $k_B$  is the Boltzmann constant,  $e$  is the elementary charge and  $d_{RC}$  is the distance between the redox-center (RC) of the biomolecule and the electrode surface (see figure 2.6.2). The parameter  $\rho$  is the density of states of the solid (metal) electrode, since, unlike isolated systems like atoms or molecules, the density distributions of solid (metal) electrodes are

not discrete but continuous.

The complementary error function  $erfc$  is defined as:

$$\{2.6.2.1\ a\} \quad erfc(x) = \frac{2}{\sqrt{\pi}} \int_x^{\infty} \exp(-t^2) dt .$$

The overpotential  $\eta$  is defined as the difference between the applied electrode potential  $E$  and the midpoint potential of the adsorbate  $E_m$ ,  $\eta = E - E_m$ . It corresponds to the driving force of the heterogeneous ET process and thus replaces  $\Delta G^0$  in the expressions for homogeneous ET.

Electron transfer between electrodes and redox-active biomolecules that are separated by relatively long ( $\geq 10$  methylene units in the alkyl-chain) insulating SAMs has diabatic character. As outlined in the previous chapter, diabatic ET occurs via electron tunnelling and shows exponential distance dependence. In case of heterogeneous ET between a SAM-coated silver electrode and an adsorbed biomolecule the electron tunnels across the SAM (see figure 2.5.1). The distance between the electrode and the reaction center in the protein,  $d_{RC}$ , depends on the properties of the adsorbed biomolecule and its orientation with respect to the surface and the SAM layer thickness. Here, it should be noted that electron transfer between the reaction center of the protein and the binding region at the protein surface may take place according to a mechanism other than electron tunneling.

It should be further noted that heterogeneous electron transfer of heme proteins may be coupled to various other processes such as proton transfer, conformational transitions, ligand exchange at the heme cofactor or rearrangement of the donor-acceptor complex, respectively [3, 67, 191]. Only if it can be excluded that other processes than the actual electron tunnelling process are rate limiting, diabatic heterogeneous ET is described well with equation {2.6.2.1} [1, 3, 138, 190, 191]. A simplified expression for the ET rate at zero driving force ( $\eta = 0$ ) is given by [1]:

$$\{2.6.2.2\} \quad k_{ET}(0) = A \cdot \exp(-\beta \cdot d_{RC}) .$$

Here, the electronic coupling, density of states and other parameter are considered in a single pre-exponential factor  $A$ . Relating the ET rate at a given overpotential to the rate at zero driving force yields [1, 191]:

$$\{2.6.2.3\} \quad \frac{k_{ET}(\eta)}{k_{ET}(0)} = \frac{\operatorname{erfc}\left(\frac{\lambda + e\eta}{\sqrt{4\lambda k_B T}}\right)}{\operatorname{erfc}\left(\frac{\lambda}{\sqrt{4\lambda k_B T}}\right)}$$

From the measurement of diabatic ET rates at varying values of  $\eta$  the reorganisation energy  $\lambda$  for the ET can be obtained [56].

## 2.7 Heme Proteins

Hemes are iron coordinating protoporphyrins that play a pivotal role for life as being cofactors of a huge variety of different proteins. Heme proteins can be classified according to their biological function, the chemical constitution of the heme cofactors and the axial ligation pattern of the central iron. Chemically different heme cofactors are classified into *a*, *b*, *c* and *d* hemes. In this work, *b*- and *c*-type heme proteins were investigated.

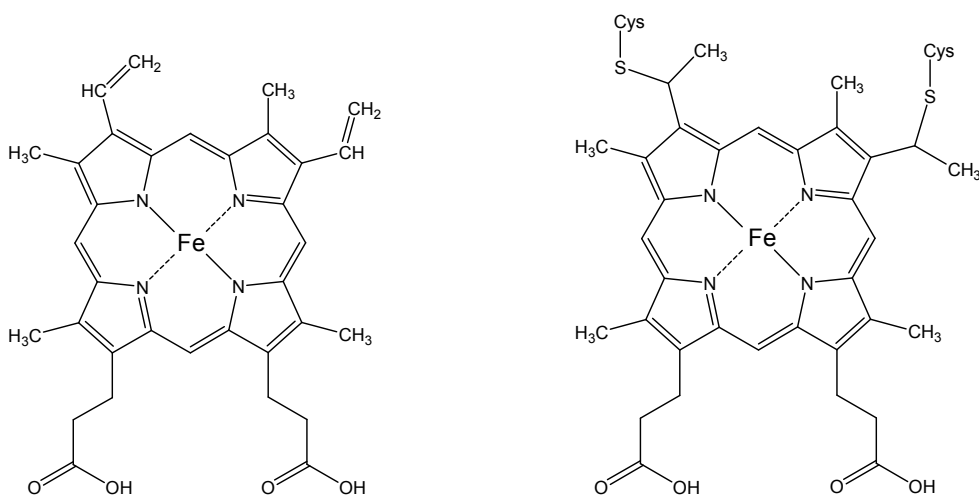


Figure 2.7: Chemical formulae of the *b*- (left) and *c*-type (right) heme cofactors.

*B*- and *c*-type hemes chemically differ inasmuch as the *c*-type heme is covalently bound to the protein moiety by forming two thioether bridges to cysteine residues. The *b*-type heme is bound to the protein moiety via non-covalent interactions, such as electrostatic interactions, coordinative bonding to the central iron, hydrogen bonds and other. These non-covalent interactions certainly play a role also in the binding of the *c*-type heme. Instead of the thioether linkages of the *c*-type heme, the *b*-type heme has vinyl groups (figure 2.7). In both cases the central iron is coordinated by the four pyrrole nitrogens. One or two axial binding sites may be occupied by amino acid side chains, leading to five- (5c) or six-coordinated (6c) iron, respectively. In some proteins such as

peroxidases, an axial iron coordination site represents the binding site for target molecules. In *b*-type heme proteins, both axial positions are usually occupied by nitrogens from histidine side chains of the protein matrix. The axial positions of the heme iron of cytochrome *c* in its native coordination, however, are occupied by a nitrogen atom of a histidine and a sulphur atom of a methionine residue.

In general, the heme iron may

1. have different coordination pattern,
2. be in high- (HS) or low-spin (LS) state,
3. be in the oxidation state  $\text{Fe}^{2+}$  (reduced) or  $\text{Fe}^{3+}$  (oxidised) and
4. undergo changes in its coordination pattern, spin and oxidation state, respectively.

Structural and associated electronic properties of the heme cofactor are closely related to the functioning of the protein and can be studied by RR and surface enhanced RR spectroscopy. Different heme proteins were investigated in this work, two of which are the human sulphite oxidase (chapter 6) and the membrane bound hydrogenase from *Ralstonia eutropha* H16 (chapter 7). Cytochrome *c*, which was used as a model protein in the study of silver-gold hybrid devices for spectro-electrochemistry, is briefly presented in chapter 5.2 and chapter 8.2.

### 3 Instrumentation

An experimental setup for Raman spectroscopy contains basic elements, which are the monochromatic radiation source (usually a laser), the sample arrangement, a unit for analysing the scattered radiation, an electronic detector unit (nowadays usually a charge coupled device camera, CCD camera) and a control unit for data acquisition (computer) (figure 3.4) [1]. Additional optical and/or electronic equipment may be required for specific Raman experiments. The experimental setup that was used for Raman spectroscopic and electrochemical experiments is described in this chapter.

#### 3.1 Excitation Source

Lasers are powerful sources for monochromatic radiation and, therefore, they are suited as excitation sources in Raman spectroscopy. Both pulsed and continuous wave (cw) lasers can be used. Pulsed lasers provide a photon flux per pulse that is several orders of magnitude higher than the photon flux of a cw-laser [1]. Since a high photon flux may induce unwanted photochemical reactions and/or degradation of biomolecules, the use of cw-lasers is better suited for studying proteins. Using cw-lasers may also be advantageous for certain time resolved spectroscopic experiments (see chapter 4.2.3), because laser pulses with defined and adjustable duration and repetition time can be created by gating the beam, e.g. with pockels cells. A pockels cell is a versatile electro-optical device that contains a voltage-controlled birefringent crystal of well chosen dimension and orientation [60]. The direction, to where an incident laser beam that passes through a pockels cell is refracted, changes as a function of applied voltage. As a consequence, for a given laser polarisation a voltage of minimum and maximum light throughput in the direction of the optical pathway of the Raman setup can be set, respectively. By switching between these two voltages laser pulses down to the nanosecond time scale can be created out of a cw-laser source.

Noble gas ion lasers emit a large number of discrete cw-laser lines that are appropriate for Raman spectroscopic studies. The emitted laser light is highly polarised perpendicular to its propagation direction [1]. In this study, mainly the 413 nm line a  $\text{Kr}^+$ -ion cw-laser (Coherent Innova 400c, Coherent Innova 300c) was used as excitation source. Additionally, the 514 nm line of  $\text{Ar}^+$ -ion cw-lasers (Coherent Innova 400c and Coherent Innova 70c) was used in some experiments.

### 3.2 Sample Arrangement

For resonance Raman experiments in the solution phase cylindrical quartz cuvettes provided by Hellma® were used (figure 3.2.1 a). The sample solution (and additional reducing or oxidising agents) was placed into the cuvette, which was mounted onto a rotating holder. Due to the rotation, the liquid sample was pressed to the wall of the cuvette, where the laser beam is focussed on. The volume of this cuvette is 500  $\mu\text{L}$ , however, a sample volume of 200  $\mu\text{L}$  was sufficient for operation.

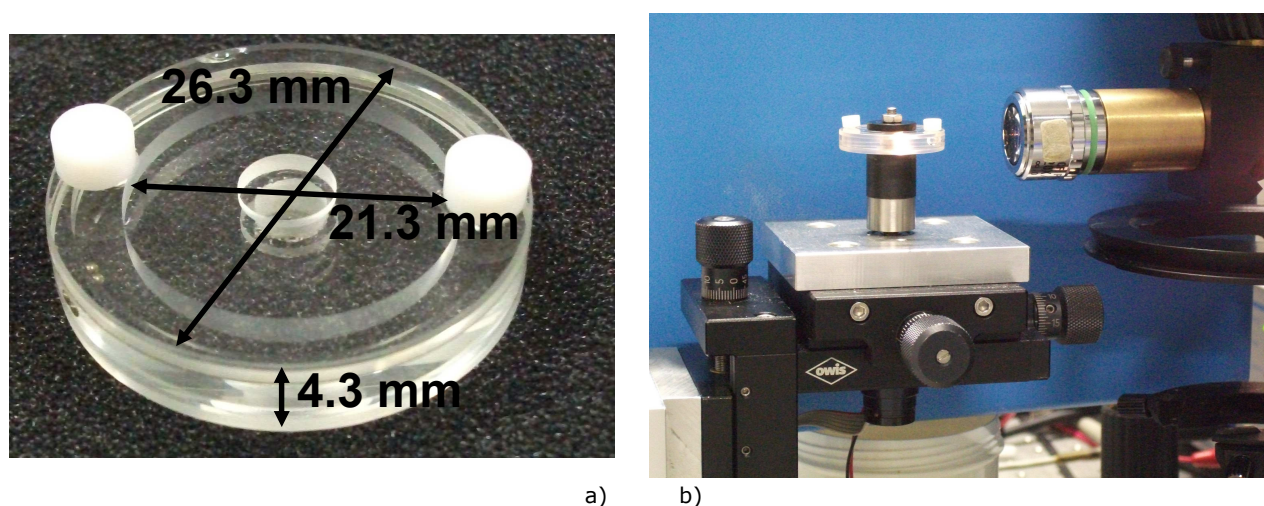


Figure 3.2.1: a) Cylindrical quartz cuvette and b) sample arrangement for resonance Raman experiments of samples in the solution phase.

For electrochemical and surface enhanced Raman spectroscopic measurements a homemade spectro-electrochemical cell was used. In these studies, silver ring electrodes served as SER-active substrates and working electrodes. The electrodes, shown in figure 3.2.2, were prepared in the workshop from a cylindrical silver block with 99.9 % purity provided by R. Götze GmbH & Co. KG.

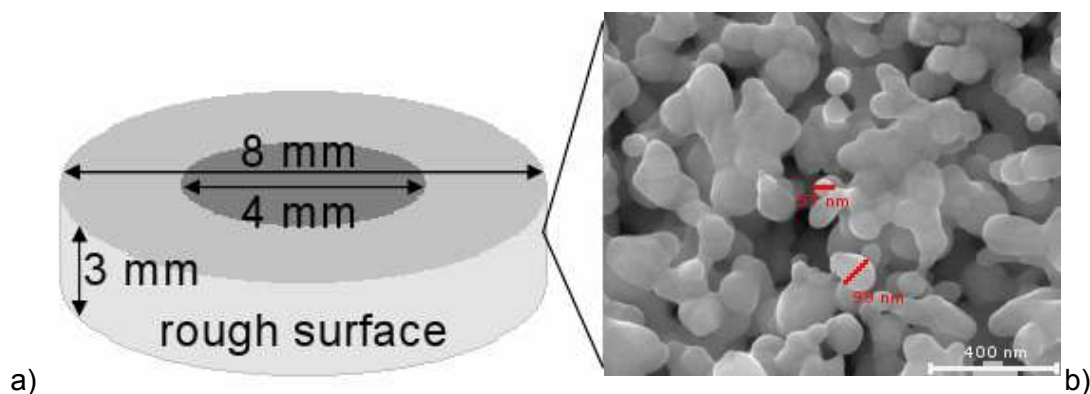


Figure 3.2.2 [65]: a) Cartoon of the silver ring electrode and b) scanning electron microscope image of the silver surface after roughening. The scale bar at the bottom right represents 400 nm.

The modified electrodes were mounted onto the rotating shaft of a homemade electrode holder. The lateral surface of the electrode, which is exposed to the electrolyte solution, is rough, chemically modified and used for protein immobilisation. The laser light is focussed on the lateral surface of the electrode with a long working distance objective. The smooth upper surface of the ring electrode is used for electrical contact with the holder. Constant rotation of the electrode ensures that individual proteins are not exposed for too long to the harmful laser light.

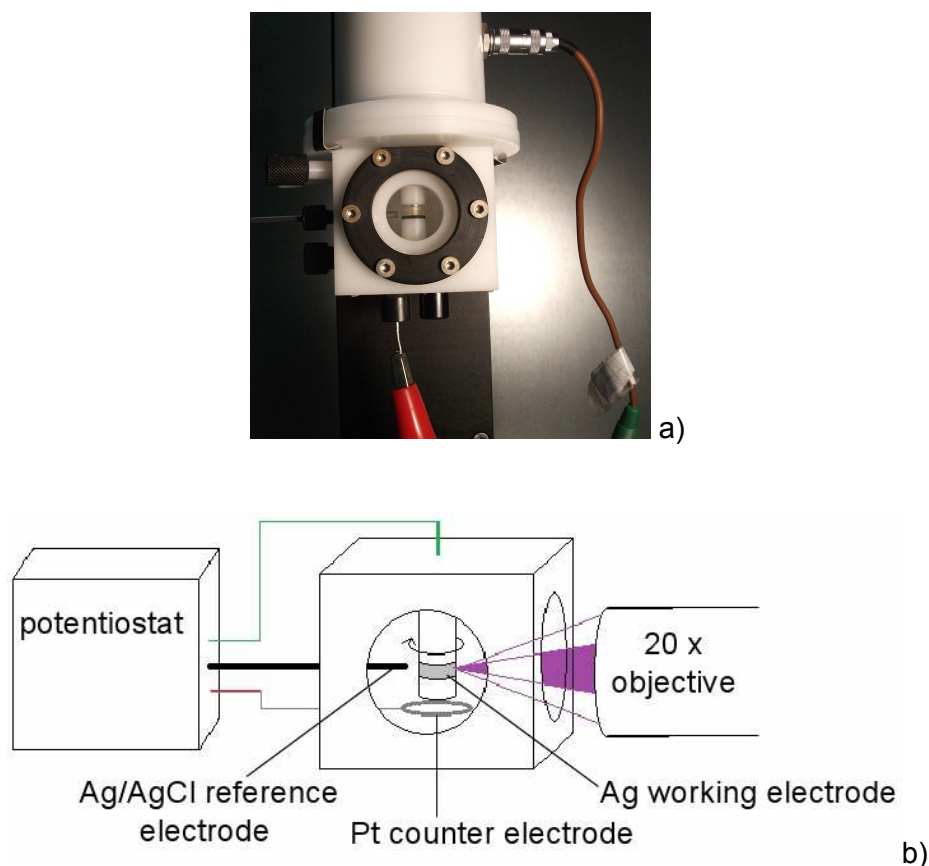


Figure 3.2.3: a) Front view picture of the spectro-electrochemical cell. b) Schematic representation of the electrochemical cell.

Spectro-electrochemical cells with a volume of about 10 mL can be mounted onto the holder as shown in figure 3.2.3a. The cell contained the modified Ag ring as the working electrode, a Ag/AgCl 3 M KCl reference electrode (Dri-Ref 2 from World Precision Instruments, +210 mV vs. standard hydrogen electrode), and a platinum ring shaped counter electrode. The applied electrode potential is controlled by a potentiostat (EG&G 273 and 263A). The spectro-electrochemical cell has additional entrances, which allow for purging the electrolyte solution with gases and filling of chemicals (e.g. the substrate of an immobilised enzyme). The presence of oxygen could disturb the measurements, especially since oxygen is reduced at the electrode at potentials  $< -0.25$  V (vs. Ag/AgCl 3M KCl). Therefore, the spectro-electrochemical cell was de-aerated with highly purified argon in most cases.

### 3.3 Electrochemical Setup

For the roughening of the silver ring electrodes a computer controlled CH instrument 660 C (Austin, USA) was used. A special homemade electrochemical cell containing a cylindrical Pt counter electrode with a high surface area was used for homogeneous roughening of the solution exposed silver surface. A stirring bar was placed on the bottom of the electrochemical roughening cell.

With the computer controlled potentiostat various electrochemical techniques can be employed. Since it is possible to connect not only the roughening cell but also the spectro-electrochemical measuring cell to the computer controlled potentiostat, electrochemical (CH instrument 660 C, Austin, USA) and spectro-electrochemical (EG&G 273 and 263A) experiments were performed subsequently on the same system with different potentiostats.

### 3.4 Spectroscopic and Spectro-Electrochemical Setup

Both SER- and RR spectra were measured with confocal Raman microscopes in backscattering geometry (LabRam HR-800, Jobin Yvon) equipped with liquid nitrogen cooled back-illuminated charged coupled device (CCD) detectors. The setup of spectroscopic and spectro-electrochemical experiments is depicted in figure 3.4.

The laser passes through two synchronised pockels cells (p.cell, Linos LM 0202) before it hits the sample. The pockels cells and the potentiostat are controlled by a homemade electronic 4-channel pulse delay generator. In this way defined laser pulses and potential jumps can be employed as needed in time resolved potential controlled spectroscopic measurements (see chapter 4.2.3). The laser is highly focussed onto the sample by the objective (O) of the microscope (Mic). The scattered light is collected by the same objective in 180° backscattering geometry. Due to focussing of the light onto a very tiny area and the resultant high local photon flux, relatively low laser powers have to be used. A Nikon 20 x objective with a working distance of 20.5 mm and a numeric aperture of 0.35 was used throughout all Raman spectroscopic experiments. The laser power on the sample was typically 1 – 2 mW.

Notch filters (NF) only reflect light in a narrow wavelength range and are transmissive for all other wavelengths. They have to be selected for the respective wavelength of the incident laser. With the appropriate choice of filter, inelastically scattered radiation passes through the filter and

the strong Rayleigh scattering is filtered out. The confocal pinhole (CP) ensures that only the scattered radiation at the focus of the objective passes to the lens (L), which focuses the light through the entrance slit (S) of the Czerny-Turner type monochromator.

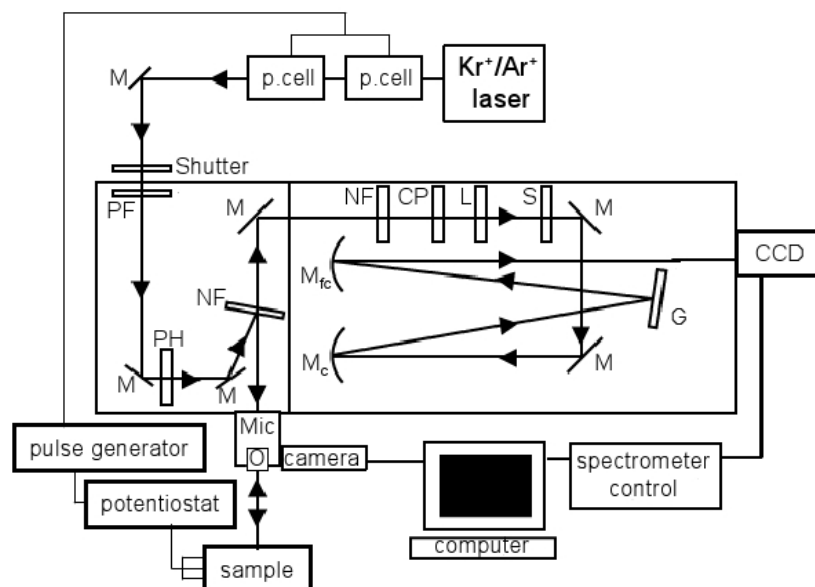


Figure 3.4 [61]: SERR spectro-electrochemical setup

p.cell – pockels cell, M – mirror, Mic – microscope, O – objective, PH – pin hole, CP – confocal pin hole, NF – notch filter, PF – plasmaline filter, G – grating, L – lens,  $M_c$  – collimating mirror,  $M_f$  – focussing mirror, S – slit.

Two different LabRam spectrometers of similar design but with different diffraction gratings were used in this study. The first spectrometer was operated with a 2400 1/mm grating and was equipped with a liquid nitrogen cooled CCD with 2048 pixels. In most cases this system was operated with a CCD binning factor 2 affording a spectral resolution of  $2\text{ cm}^{-1}$  and an increment per data point of  $0.57\text{ cm}^{-1}$  at 413 nm excitation. The second LabRam spectrometer was used with a 1200 1/mm grating and was coupled to a similar CCD with 2048 pixels. This system, however, was operated with a CCD binning factor of 1 and afforded a spectral resolution of  $1\text{ cm}^{-1}$  with an increment per data point of  $0.75\text{ cm}^{-1}$ . Both spectrometers were controlled by the LabSpec® software (version 4.07 and version 5.45.09) and calibrated prior to measurements by the strong mercury lines at 435.833 nm (in case of measurements with 413 nm excitation) and 546.074 nm (at 514 nm excitation).



## 4 Methods

### 4.1 Resonance Raman Spectroscopy of Heme Proteins

Raman and IR spectra of complex molecules such as heme proteins contain a large number of vibrational modes in the range between 200 and 1800  $\text{cm}^{-1}$ . Due to many overlapping bands in this region, an assignment of bands to certain normal modes is impossible. Since the proteins studied in this work, however, contain chromophoric heme cofactors, Raman spectroscopy can be employed in the resonance mode. With this technique, only the vibrational modes of the heme cofactor exhibit up to  $10^6$ -fold increased band intensities. As a result RR spectra contain much less bands that can be clearly assigned to specific cofactor vibrational modes [185].

Despite minor differences all heme proteins exhibit certain common features in their UV-Vis absorption and resonance Raman spectra. These are discussed in the following for human sulphite oxidase (hSO), which is a sulphite oxidising enzyme that was investigated within this work. The hSO contains a cytochrome *b5* subunit, which harbours a *b*-type heme. In figure 4.1.1 the UV-Vis absorption spectrum of hSO in the reduced and oxidised state is shown. The absorption spectrum of hSO in the visible range  $400\text{nm} < \lambda < 700$  is typical for heme proteins. No other cofactors contribute to the absorption in that region, such that all absorption bands can be ascribed to  $\pi \rightarrow \pi^*$  electronic transitions of the heme cofactor [10].

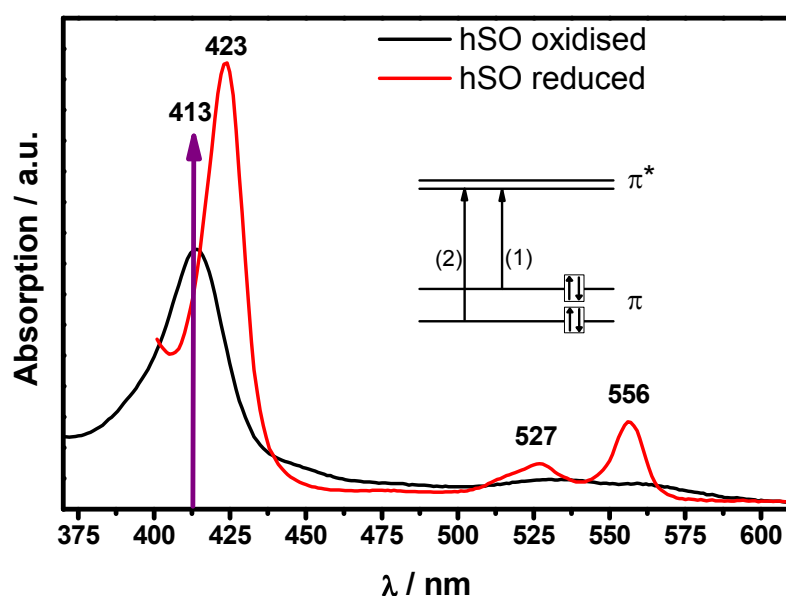


Figure 4.1.1: UV-Vis absorption spectrum of hSO oxidase in the reduced (red) and oxidised (black) state. The inset shows the underlying  $\pi \rightarrow \pi^*$  electronic transitions according to the theory by Gouterman [10].

While the  $\pi^*$ -orbitals are degenerate, the highest lying occupied  $\pi$ -orbitals have slightly different energies, leading to different electronic transitions (1) and (2). The combination of (1) and (2) may result in an addition of their transition moments leading to the strong Soret absorption at 423 nm and 413 nm in the reduced and oxidised state. In case of the so-called  $Q_0$  – absorption band at 556 nm in the reduced state (564 nm in the oxidised state), the transition moments for (1) and (2) nearly cancel out each other leading to a much weaker absorption as compared to the Soret band. Finally, there is also a weak and broad band at 527 nm (534 nm in the oxidised state). This is referred to as the  $Q_1$  – absorption band and is a result of vibronic mixing between Soret and  $Q_0$  – transitions. The wavelengths of the UV-Vis absorption bands observed for other heme proteins may be shifted by  $\pm 10$  nm. However, they are certainly located in the same regions and, more importantly, the spectra exhibit the same pattern as discussed here for the hSO. It should be noted that certain ferric heme species also exhibit weak but distinct absorption bands above 600 nm that can be attributed to charge transfer transitions from the porphyrin or an axial ligand to the central iron [185, 186].

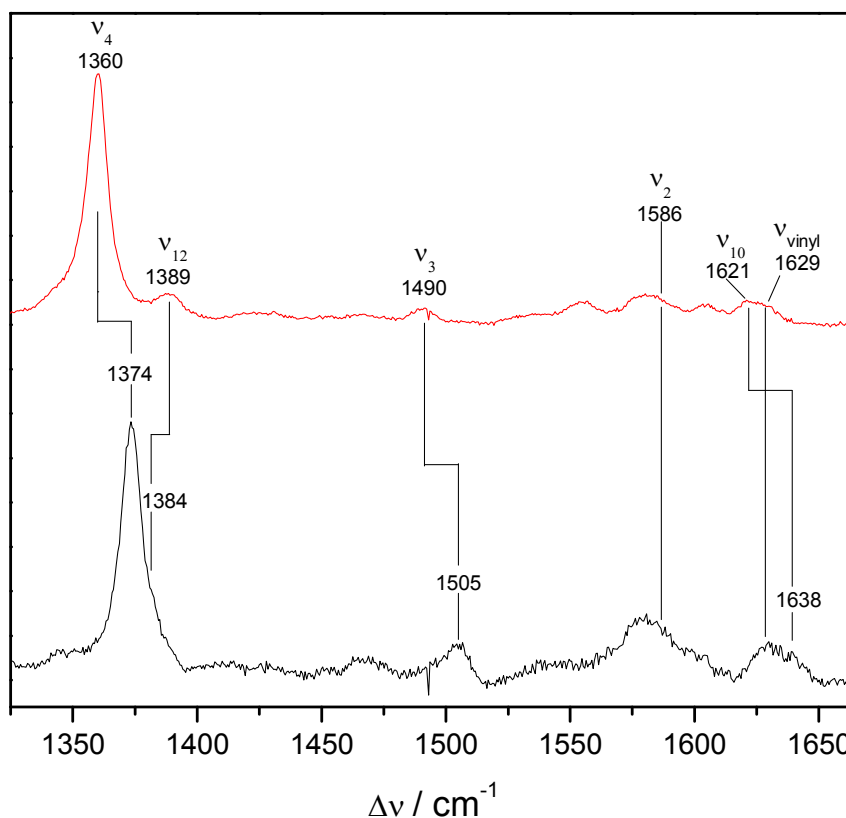


Figure 4.1.2: Resonance Raman spectra of human sulphite oxidase (hSO) in the reduced (red line) and oxidised (black line) state of the heme iron. The spectrum of the oxidised hSO was multiplied by factor of 3.4. Experimental conditions: sample concentration was  $\sim 30 \mu\text{M}$  in 5 mM Tris-HCl buffer solution, incident laser radiation of  $\lambda_{\text{exc}} = 413.138$  nm with a power on the sample 1.88 mW, a 2400/mm grating and a CCD with a binning factor 2 was used.

As indicated by the purple arrow in figure 4.1.1 RR and SERR spectra of heme proteins were in this work almost exclusively measured using the 413 nm line of a  $\text{Kr}^+$ -laser. Under resonance conditions with the Soret absorption band, primarily totally symmetric vibrational modes are greatly enhanced. The spectral properties of the heme cofactor can be discussed with reference to the  $D_{4h}$  point group. Naturally occurring heme cofactors always have lower symmetry due to different porphyrin side chains and/or deviations from the planar porphyrin structure. Nevertheless the  $D_{4h}$  point group represents a reasonable approximation for the heme symmetry. With respect to this point group hemes have nine totally symmetric modes that have  $A_{1g}$  symmetry. These are referred to as  $\nu_i$ ,  $i = 1, 2, \dots, 9$ .

The  $\nu_{\text{vinyl}}$  at  $1629 \text{ cm}^{-1}$  mainly includes the C=C stretching of the vinyl side chains and is accordingly absent in *c*-type hemes. Some other non-totally symmetric modes such as the  $\nu_{10}$ ,  $\nu_{12}$  (both with  $B_{1g}$  symmetry) also appear in the RR spectra upon Soret band excitation. The most prominent band, however, is the totally symmetric  $\nu_4$  mode at  $1360 \text{ cm}^{-1}$  and  $1374 \text{ cm}^{-1}$  in the reduced and oxidised form, respectively. Like many other modes in the so-called fingerprint region between  $1300 \text{ cm}^{-1}$  and  $1700 \text{ cm}^{-1}$ , it mainly includes stretching coordinates of the tetrapyrroles macrocycle. While the frequency of the  $\nu_4$  represents a sensitive marker for the heme oxidation state, the frequencies of other bands in this region were empirically shown to be correlated to the core size of the porphyrin  $d_{\text{Ct-N}}$ . The core size, which is defined as the distance from the center of the porphyrin core (Ct) to pyrrole nitrogens (N) sensitively depends on the axial coordination pattern and the spin- and oxidation state of the heme iron. Hence, the frequencies of these bands ( $\nu_2$ ,  $\nu_3$ ,  $\nu_{10}$  and other) contain valuable structural information.

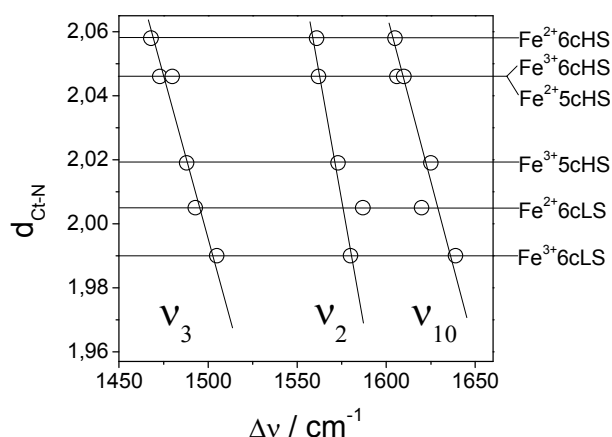


Figure 4.1.3: Vibrational band frequencies of  $\nu_2$ ,  $\nu_3$  and  $\nu_{10}$  modes and porphyrin core sizes for different heme species.

The RR spectra of hSO (figure 4.1.2) show the characteristic vibrational signature of a six-coordinated low-spin (6cLS) heme in both the ferric and the ferrous form, as expected for a *b*-type heme with bis-His axial ligation. The 6cLS conformation can be referred to as the native heme conformation in hSO. It should be noted, however, that the signal intensity, and hence the

resonance Raman cross section, of ferric and ferrous hSO are different. Since it is the most prominent band in both oxidation states the  $\nu_4$  is best suited for determining the intensity ratio under identical experimental conditions. This ratio is proportional to the ratio of the relative RR cross section  $\sigma_{relative}$  of these modes for the native ferric hSO with respect to the native ferrous species. Relative cross section parameters are needed for the evaluation of concentration ratios from RR or SERR spectra of a mixture of different heme species.

## 4.2 Surface Enhanced Resonance Raman Spectroscopy of Heme Proteins

In the study of heme proteins immobilised on rough silver surfaces molecular and surface plasmon resonance conditions are particularly well matched with 413 nm laser excitation. This excitation line provides high quality vibrational spectra of heme proteins even at submonolayer coverage within a few seconds of accumulation [3]. Therefore, surface enhanced resonance Raman (SERR) spectroscopy represents a powerful technique for the study of heme proteins. Moreover, using SAM-coated rough silver electrodes as SERR substrates opens up additional possibilities. Not only potential controlled spectroscopic measurements are possible. Also electrochemical experiments, such as protein film voltammetry, can be carried out on the same system [5, 8, 12].

### 4.2.1 Electrode preparation

Cylindrical silver electrodes were polished with polishing sheets of three different grain sizes (100  $\mu\text{m}$ , 30  $\mu\text{m}$ , 0.3  $\mu\text{m}$ ) going from rough to fine grains. The polishing sheets were purchased from 3M®. The polished electrodes were subsequently immersed in pure water and ethanol and treated in the ultrasonic bath for five minutes in each solution.

Prior to roughening, the electrode was subjected to a potential of  $E = -2$  V (vs. Ag/AgCl, 3M KCl) for 40s under stirring. The roughening procedure was employed in 0.1 M KCl electrolyte solution using the roughening cell and the CH instrument 660 C. The roughening procedure consists of three oxidation-reduction cycles at +0.32 V and -0.32 V, respectively, followed by an additional reduction step at -0.5 V for 5 minutes (figure 4.2.1).

The electrochemically roughened silver ring electrodes are first gently rinsed with water (to remove salt from the surface) and then with ethanol. They are then immersed for 8 – 16 hours in 1 – 2 M ethanol solutions of  $\omega$ -functionalised alkanethiol molecules that form self assembled monolayers (SAMs) on the roughened silver surface. In case of amino-terminated SAMs water was

added to the SAM solution in relation 1:4 (water : ethanol). The SAM-coated electrodes are thoroughly rinsed with ethanol first and then with water and are immersed for 2 – 4 hours into a solution that contains the sample protein at a concentration of  $\sim 0.5 \mu\text{M}$ . The electrode is subsequently placed into the spectro-electrochemical cell and is ready to be measured.

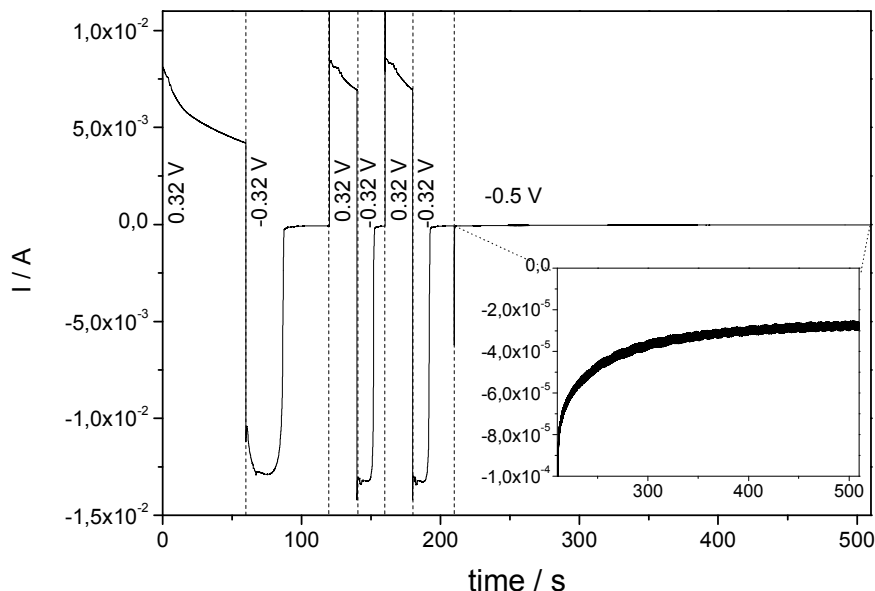


Figure 4.2.1: Current flow during the electrochemical roughening procedure. The inset shows the current flow during the last reduction step ca. 100x enlarged.

The preparation of the silver-gold hybrid device is based on 11-aminoundecanethiol-coated electrochemically roughened silver electrodes and is described in chapter 5.4.

#### 4.2.2 Stationary Potential Controlled Measurements

With stationary potential controlled SERR spectroscopy the relative concentrations of oxidised and reduced heme species for immobilised proteins are measured as a function of the applied electrode potential  $E$  (see chapter 4.3). In this way, the midpoint potential  $E_m$  and the number of transferred electrons  $n$  can be determined according to the Nernst-equation:

$$\{4.2.2\} E = E_m - \frac{RT}{nF} \ln \frac{c_{red}}{c_{ox}},$$

where  $R$ ,  $T$  and  $F$  are the universal gas constant, temperature and Faraday constant, respectively. The spectral contributions of different heme species must be clearly distinguishable and relative cross section values must be known or at least reasonably estimated. One may

approximately assume that the relative cross section parameters for different heme species as obtained with RR spectroscopy are similar in surface enhanced resonance Raman (SERR) experiments [1]. The concentration ratios can then be plotted versus the applied electrode potential and redox parameters can be extracted by fitting the Nernst-equation to the data.

#### 4.2.3 Time Resolved Potential Controlled Measurements

Information about heterogeneous electron transfer kinetics of immobilised heme proteins can be obtained with potential controlled time resolved SERR (TR-SERR) spectroscopy [1, 3, 63]. In this approach, a rapid jump of the applied electrode potential  $\Delta E$  from an initial value  $E_i$  to a final potential  $E_f$  is employed. The equilibration at  $E_i$  is perturbed by the potential jump and the kinetics of the associated relaxation process to the new equilibrium corresponding to  $E_f$  is monitored. SERR spectra are measured during the time interval  $\Delta t$  subsequent to various delay times  $\delta$  with respect to the potential jump. In order to monitor the dynamics of the relaxation process, different delay times  $\delta$  smaller than the relaxation time have to be adjusted. The accuracy of the method is higher the smaller  $\Delta t$  is with respect to  $\delta$  (typically  $\Delta t \sim 0.2 \cdot \delta$ ). Then, the measured spectrum represents the heme species composition at  $\delta' \approx \delta + \Delta t / 2$ .

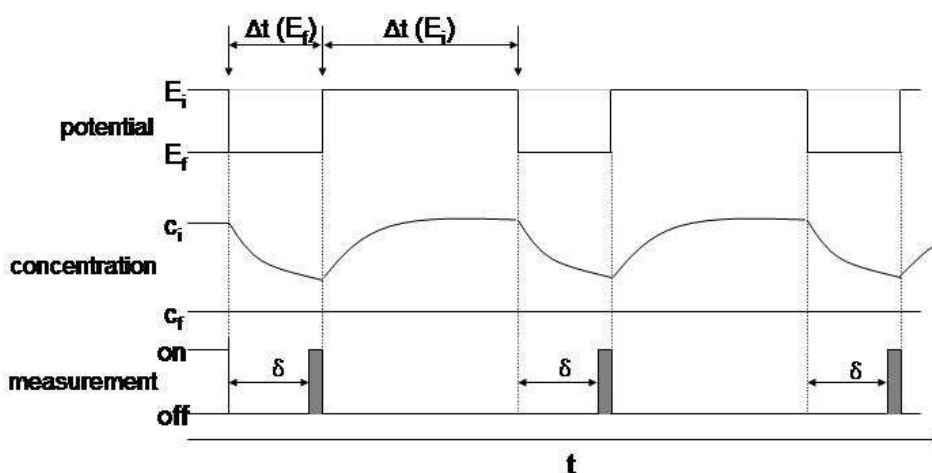


Figure 4.2.3: Schematic representation of time resolved surface enhanced resonance Raman experiments.

With this technique, the dynamics of potential jump induced processes at the heme domain can be studied. However, the signal intensity of the TR-SERR spectrum depends on the accumulation time ( $\Delta t$ ). For studying fast processes in the millisecond or microsecond time scale,  $\Delta t$  is accordingly small, such that a single shot TR-SERR spectrum would not afford a sufficiently high signal-to-noise ratio as needed for quantitative analysis. Therefore, the potential is set back to  $E_i$  after the measuring intervals in order to recover the initial equilibrium during the time interval

$\Delta t(E_i)$ , which should be distinctly larger than  $\Delta t(E_f)$ . Typically, the  $\Delta t(E_i) : \Delta t(E_f)$  ratio is around 5:1. In this way the potential jump experiment can be repeated as often ( $n$  times) as required for a satisfactory spectrum (with a total accumulation time  $n \cdot \Delta t$ ).

The potential induced (ET) process needs to be fully reversible for this procedure and the immobilised sample needs to be stable throughout the whole TR-SERR experiment. A high signal sensitivity is required in TR-SERR experiments in order to obtain good spectra while keeping the number of repetitions of the potential jump experiment ( $n$ ) as low as possible.

#### 4.2.4 SERR Spectroscopic Study of Catalytic Oxidation Processes

The reduction of the heme cofactor of immobilised heme containing enzymes during the catalytic cycle of the enzyme can be in principle monitored by SERR spectroscopy at open circuit [5, 8]. At open circuit potentials in de-aerated aqueous buffer solutions, heme cofactors are usually predominantly in the oxidised ferric form. However, the heme will get reduced upon addition of the enzyme's substrate if a catalytic oxidation process with concomitant electron transfer to the heme takes place. The kinetics of this reduction process can be determined by measuring consecutive SERR spectra after addition of the substrate. Since usually accumulation times of at least 0.5 s for each spectrum are required, only relatively slow reduction processes ( $< \sim 1.5 \text{ s}^{-1}$ ) can be studied with this approach.

The heme reduction rate obtained from such an experiment should be interpreted with care since the reduction kinetics may be limited by several parameters, some of which are difficult to control. First of all, the substrate, which can be introduced into the electrochemical cell via a syringe, has to reach the electrode surface. This depends on the final substrate concentration in the electrochemical cell after injection, the injection speed, the intrinsic diffusion behaviour of the substrate, the sample arrangement and other parameters. Since the electrode holder of the SERR setup (chapter 3.2) is rotating during measurement diffusion of small substrate molecules should probably not be the limiting step in the slow reduction processes that can be monitored with this technique.

After having reached the electrode surface, the substrate is oxidised at the active site, which could be another cofactor or the heme itself. If the heme is not the active site, the electrons from catalytic oxidation must be transferred in a second step via intramolecular electron transfer the active site to the heme center. Moreover, information on the activation rate of the enzyme is needed. It is reported in literature, that e.g. the active site of hydrogenases needs to be activated

by the substrate (hydrogen) before the enzyme exhibits catalytic activity [8, 112]. Hence, the observed heme reduction rate could be limited by the activation rate of the enzyme, the catalytic turnover or the intramolecular electron transfer rate.

In summary, with this approach the apparent rate of heme reduction associated with catalytic oxidation processes of the enzyme's substrate can be selectively monitored. This may afford valuable information about catalytic processes complementary to protein film voltammetry.

### 4.3 Component Fit Analysis

RR and SERR spectroscopy allows for quantitative determination of mixtures of heme species, which differ with respect to their oxidation, spin and/or coordination state. The contribution of each species to an observed spectrum can be disentangled by component fit analysis [69]. In this approach, 'synthetic' spectra  $X_i$  of the individual components  $i$  are generated. This can be made for each component  $i$  by fitting a set of Lorentzian bandshapes (each corresponding to a vibrational mode, e.g.  $\nu_4$ ) to the measured spectrum of a 'pure' sample containing only the component  $i$ . The Lorentzian bandshapes typically have bandwidths  $\Gamma$  in the range between 10 and 15  $\text{cm}^{-1}$ . If a pure sample of a particular component is not available, its spectrum may also be obtained and fitted by subtracting all other species from the observed spectrum of a mixture that contains this component. An observed spectrum  $O$  of a mixture of different heme species can then be simulated by the superposition of the various synthetic spectra, according to:

$$\{4.3.1\} O = \sum_i f_i X_i .$$

In the fitting process, the amplitude of each component spectrum  $X_i$  is scaled by a factor  $f_i$ . This factor will be non-zero only for those components that are present in the sample mixture giving the spectrum  $O$ . The accuracy of this technique depends on the accuracy of the synthetic component spectra and the spectral range that is fitted. Certainly, at least a part of the fingerprint region has to be covered for unambiguous assignments of component spectra to certain heme species.

In figure 4.3, a SERR spectrum of the Cyt *b* subunit of the membrane bound hydrogenase from *Ralstonia eutropha* H16 is shown [8]. As revealed by component fit analysis, four different heme species contribute to the spectrum. The amount of reduced species is distinctly lower since this spectrum was obtained under oxidising conditions. However, two different oxidised species can be clearly distinguished, especially by different  $\nu_3$  frequencies, revealing the coexistence of 6cLS and

5cHS heme species [8]. Subsequent to the fitting procedure, the spectral contributions of each component  $i$  can be converted into relative concentrations  $c_i$  [69, 70], according to:

$$\{4.3.2\} \quad \frac{c_i}{\sum_j c_j} = \frac{I_i \cdot \sigma_{relative,i}}{\sum_j I_j \cdot \sigma_{relative,j}},$$

where the summation goes over all components  $j$ . The relative RR cross section parameter  $\sigma_{relative}$  is the intensity ratio of each component with respect to a particular reference component. Usually the native ferrous species is chosen as the reference species [70], which is in this case the ferrous 6cLS species.

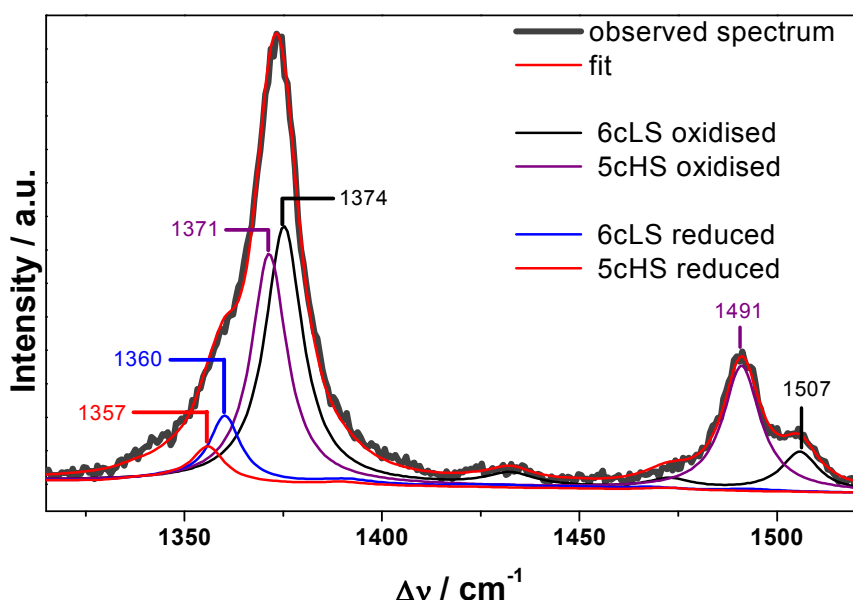


Figure 4.3: Component fit analysis of a surface enhanced resonance Raman spectrum of the Cyt  $b$  subunit of membrane bound hydrogenase from *Ralstonia eutropha* H16. Experimental conditions: immobilisation on a 5-carboxypentanethiol SAM-coated rough silver electrode, applied electrode potential was +0.1 V versus Ag/AgCl 3 M KCl, 10 mM phosphate buffer at pH 7.0, incident laser radiation of  $\lambda_{exc} = 413.138$  nm with a power on the sample of 1 mW, 1200/mm grating, CCD with a binning factor 2 .

The determination of  $\sigma_{relative}$  for the oxidised 6cLS species can be easily obtained from RR experiments. Determination of relative cross section parameters of non-native species, however, is not trivial because pure samples of non-native components can not easily be obtained. Moreover, comparison of RR intensities of different heme species can only be done under similar experimental conditions (same setup and position of the sample) and the concentration of different samples has to be known. Relative cross section parameters for many different non-native species of horse heart cytochrome  $c$  (HHCyt  $c$ ) have been determined in the extensive study by Oellerich

et al. [70]. Since similar heme species (with respect to their oxidation, spin and ligation state) of different proteins exhibit comparable spectroscopic properties the relative cross section parameter values of non-native HHCyt *c* species can be adopted in the study of other proteins [8].

In general, for component fit analysis, spectral contributions of different heme species must be clearly distinguishable and for the conversion of spectral contributions into relative concentrations the relative cross section values must be known or at least reasonably estimated.

A homemade MATLAB [62] based software (QPipsi) was used for generating synthetic component spectra. The information of different component spectra (positions, heights and widths of Lorentzian bandshapes) was stored in a fit file. These fit files were read by GNU Octave, primarily intended for numerical computations [63]. This program enables the programming of automated fitting procedures, which were employed in this work.

#### 4.4 Protein Film Voltammetry

Protein film voltammetry (PFV) is a widely used powerful electrochemical tool for the study of electronic and catalytic properties of immobilised redox-active proteins and enzymes [6, 15, 16, 19, 20]. In PFV the protein has to be immobilised on an electrode to form a (sub-)monolayer of protein, which is referred to as the protein film. Moreover, good electrical communication, i.e. efficient heterogeneous electron transfer, is required in order to perform voltammetry. Usually smooth gold or carbon electrodes are used for PFV. However, the requirements of this technique may also be met for heme proteins immobilised on SER-active SAM-coated silver electrodes. In the latter case, PFV and SERR experiments can be performed on the same electrode [5, 8].

In cyclic voltammetry (CV) the applied electrode potential  $E$  is scanned bi-directionally within a defined potential range and with a scan rate  $v_{scan}$ , which is defined as  $v_{scan} = \Delta E \cdot (\Delta t)^{-1}$ . The charge flux, i.e. the current, at the electrode is detected and plotted versus the potential. The system under study may be dissolved in the electrolyte solution or immobilised on the electrode. In the following the main concepts of PFV are presented on the example of immobilised human sulphite oxidase (hSO). CV of dissolved systems represents a conceptually different case that will not be described in this work.

In figure 4.4 two cyclic voltammograms of immobilised hSO at different conditions are shown. HSO is a sulphite oxidising enzyme, which exhibits activity also in the immobilised state [5].

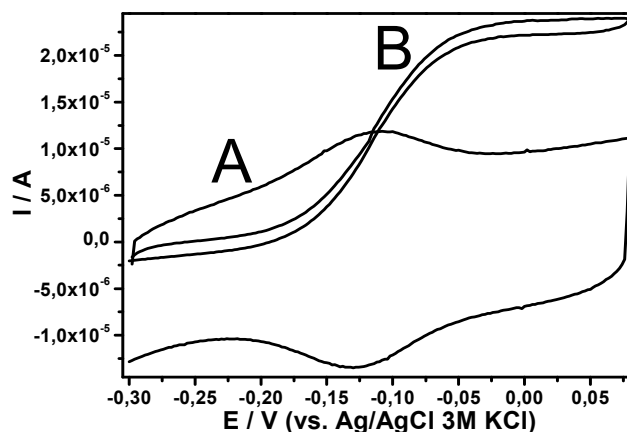


Figure 4.4: Cyclic voltammograms of human sulphite oxidase immobilised on a mixed 8-aminooctanethiole / 6-mercaptohexanol (1:3) SAM. The buffer solution was 750 mM Tris-acetate at pH 7.4. Trace A was recorded at  $v_{scan} = 0.1V/s$  in the absence of sulphite. Trace B was recorded at  $v_{scan} = 0.005V/s$  in the presence of 0.2 mM sulphite.

In PFV in general, two basically different conditions have to be discerned in the study of redox-active enzymes. Under so-called non-turnover conditions, the substrate of the enzyme is absent and hence no catalytic reaction takes place (trace A of figure 4.4). Under non-turnover conditions information about the midpoint potential  $E_m$  of redox centers, heterogeneous electron transfer rates  $k_{ET}$  and the amount of electro-active protein  $\Gamma$  can be obtained. The term turnover-conditions, in contrast, describes the situation when the substrate is present and catalytic turnover is occurring. Valuable information on the catalytic turnover rate  $k_{cat}$  and other parameters of the catalytic reaction may be obtained from PFV under turnover-conditions (trace B of figure 4.4).

#### 4.4.1 Protein Film Voltammetry under non-Turnover Conditions

If the midpoint potential of a redox center in the immobilised protein is passed in the positive scan direction (from more negative to more positive applied electrode potentials), the redox center is oxidised and may give rise to a positive anodic oxidation peak at the anodic peak potential  $E_a$  and of the height  $I_a$ . In the reverse scan direction, accordingly, the redox center is reduced and a cathodic oxidation peak at  $E_c$  with  $I_c$  is observed (figure 4.4.1). However, the redox center needs to perform efficient heterogeneous electron transfer. In case of similar heterogeneous reduction and oxidation kinetics the anodic and cathodic peaks will have similar shapes with opposite sign. The midpoint potential  $E_m$  of the ET reaction can then be obtained according to:

$$\{4.4.1.1\} \quad E_m = \frac{E_a + E_c}{2}.$$

Anodic and cathodic peaks are usually observed on top of a positive and negative linear background, respectively. The linear background in positive and negative scan direction is shifted by the value of the so-called capacitive current  $I_{cap}$ . In case of SAM-coated silver electrodes  $I_{cap}$  results from the separation of the conductive silver electrode and the conductive electrolyte solution by the insulating SAM. Therefore, the system acts as a nano-scale capacitor, which can be charged and discharged upon variation of the applied electrode potential. The capacitive current decreases with increasing SAM chain length according to the distance dependence of capacitor's conducting phases.

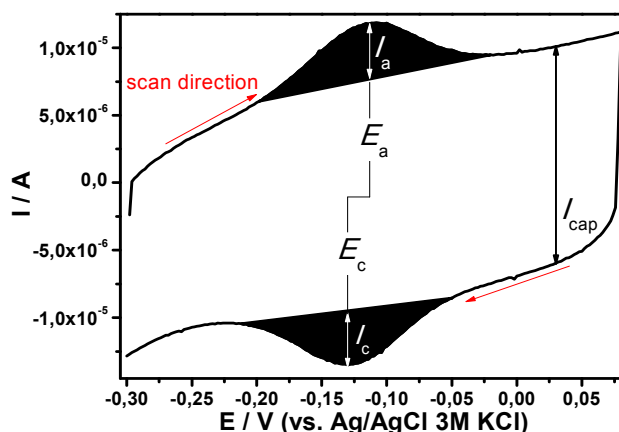


Figure 4.4.1: Cyclic voltammogram of human sulphite oxidase immobilised on a mixed 8-aminoctanethiole / 6-mercaptohexanol (1:3) SAM. The buffer solution was 750 mM Tris-acetate at pH 7.4 and contained no sulphite. The scan rate was  $v_{scan} = 0.1V/s$ .

The peak potentials are separated by  $\Delta E = |E_a - E_c|$ . The peak-to-peak separation  $\Delta E$  depends on the number of transferred electrons  $n$  at  $E_m$  ( $n=1$  for a heme unit) and is also a function of the heterogeneous ET rate  $k_{ET}$  and the scan rate  $v_{scan}$ . After a certain point,  $\Delta E$  will increase with increasing  $v_{scan}$ , because the system can respond to the potential variation only with a certain velocity, i.e the heterogeneous ET rate  $k_{ET}$ . Therefore, information about  $k_{ET}$  can be obtained by variation of  $v_{scan}$  according to [58]:

$$\{4.4.1.2\} \quad m^{-1} = \frac{RT}{nFv_{scan}} k_{ET},$$

where  $R$ ,  $T$  and  $F$  have the usual meaning and  $m^{-1}$  is an empirical parameter. This parameter

has been shown to be related to  $n$  and  $\Delta E$  as follows [58]:

nΔE[mV]	18.8	27	34.8	48.8	61.2	72.2	82.4	91.8	100.6	116.2
m <sup>-1</sup>	0.5	0.75	1	1.5	2	2.5	3	3.5	4	5

nΔE[mV]	130	142.4	153.8	164	173.4	182	190	197.6	204.6
m <sup>-1</sup>	6	7	8	9	10	11	12	13	14

Redox parameters of the heme obtained from PFV under non-turnover conditions and potential controlled SERR spectroscopy should be similar. However, some fundamental differences between these techniques that could lead to different results should be noted. SERR spectroscopy probes all scattering molecules, also the redox-inactive ones, but, as a result of a possibly different local environment, protein film subpopulations that are situated in different areas and/or are oriented differently with respect to the electrode surface may also have slightly different electronic and scattering properties. Moreover, SERR spectroscopy also probes different heme species that might be present on the surface. CV, in contrast, only probes the integrated electrochemical response of electro-active proteins.

It should also be noted that non-turnover CV is only applicable in case of sufficiently large values of  $k_{ET}$ . This is because the charge flux and hence the peak currents ( $I_a$  and  $I_c$ ) and areas ( $A_a$  and  $A_c$ , marked black in figure 4.4.1) are strongly dependent on the scan rate  $v_{scan}$ . At higher scan rates, the equilibrium between oxidised and reduced species is changed faster resulting in high peak currents. At low scan rates ( $v_{scan} < 0.01$  V/s) non-turnover currents become very small or not observable at all. Therefore, slow heterogeneous ET processes cannot be studied with PFV. In contrast, there is principally no lower detection limit for the determination of low  $k_{ET}$  with SERR spectroscopy. In summary, with respect to PFV, SERR spectroscopy is the more powerful technique for the determination of redox parameters of heme proteins, provided there are proper component spectra and values for relative RR cross sections.

On the other hand, PFV under non-turnover conditions enables the determination of the amount of electro-active proteins  $\Gamma_{hSO}$  by means of the observed peak currents according to [59]:

$$\{4.4.1.3\} \quad \Gamma_{hSO} = \frac{4 \cdot I_a \cdot RT}{A \cdot n^2 \cdot F^2 \cdot v_{scan}},$$

where  $A$  is the electrode surface area, which can be accurately determined for smooth electrode surfaces with CV [151, 152]. In case of rough SER-active surfaces, however, other techniques have to be applied for the determination of the real surface area. The roughness factor, which is

the ratio of the real and the geometric surface area, of electrochemically roughened silver electrodes is 10 – 20 [153-155].

#### 4.4.2 Protein Film Voltammetry under Turnover Conditions

The shape of the CV of a catalytically active protein film under turnover conditions widely differs from that under non-turnover conditions (figure 4.4.1). It should be noted that the scan rate of the traces in figure 4.4.1 is significantly lower in case of the turnover CV (trace B) with respect to the non-turnover CV (trace A). In general, CV under turnover conditions is performed with low  $v_{scan}$ , usually 1 – 5 mV/s [6]. Accordingly, the capacitive current is low and no peak shaped currents occur. However, an additional catalytic current  $I_{cat}^{obs}$  is observed, which starts to rise at the so-called onset potential  $E_{on}$  and reaches a plateau region, which is far above the non-catalytic current (indicated by the dotted line in figure 4.4.2.1).

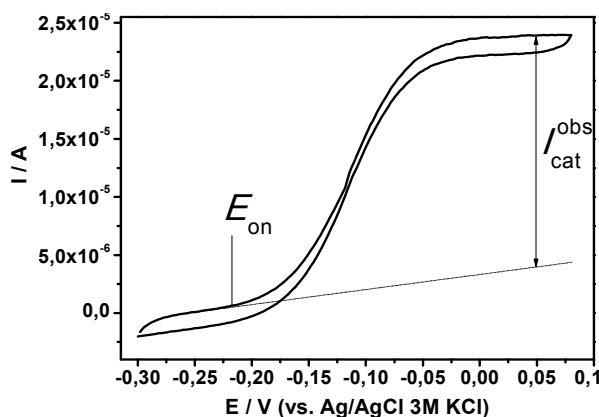


Figure 4.4.2.1: Cyclic voltammogram of human sulphite oxidase immobilised on a mixed 8-aminooctanethiole / 6-mercaptohexanol (1:3) SAM in the presence of 0.2 mM sulphite. The buffer solution was 750 mM Tris-acetate at pH 7.4 and the scan rate was  $v_{scan} = 0.005V/s$ .

In case of the hSO (figure 4.4.2.1) a positive catalytic current is observed in the presence of sulphite. This observation points towards a catalytic oxidation process at the electrode. In fact, the immobilised hSO catalyses the oxidation of sulphite to sulphate according to [15]:

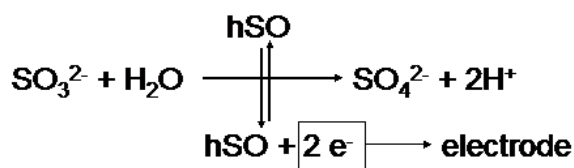


Figure 4.4.2.2: Catalytic reaction of the immobilised human sulphite oxidase.

The electrons that are generated upon oxidation of the substrate are subsequently transferred to the electrode and give rise to the positive oxidative catalytic current  $I_{cat}^{obs}$ . The onset potential  $E_{on}$  is situated in a region where the heme domain starts to get oxidised. This observation points to the involvement of the Cyt *b*5 unit in the catalytic oxidation cycle.

The observed catalytic current depends on various processes, one of which is mass transport. The substrate ( $\text{SO}_3^{2-}$ ) must reach the electrode and the product ( $\text{SO}_4^{2-}$ ) must be released back into the solution. Mass transport, in turn, depends on the substrate concentration in the surrounding electrolyte solution and the shape and rotation speed  $v_{el}$  [rpm] of the working electrode [6]. Another important variable in the electro-catalytic process is the heterogeneous electron transfer rate between the enzyme and the electrode. Only if the electro-catalytic process is not limited by mass transport and heterogeneous electron transfer kinetics, respectively, the observed catalytic current  $I_{cat}^{obs}$  represents the actual catalytic current  $I_{cat}$ . The actual catalytic current reflects the kinetics of the catalytic process according to [5, 6, 15]:

$$\{4.4.2\} \quad k_{cat} = \frac{I_{cat} \cdot v_{scan} \cdot n \cdot F}{I_a \cdot 4 \cdot RT}.$$

## 4.5 Computational Chemistry

Computational chemistry provides powerful simulation methods for the analysis of molecular observables, structures, interactions and reactions [189]. Computational methods afford very detailed information. Within this work various computational methods were employed to compute dipole moments, surface potential distributions, and structures of enzymes. Details on these studies are described in the chapters 6.3 and 7.3.



## 5 Silver-Gold Hybrid Devices for Spectro-Electrochemistry

Several studies on the synthesis of nanoparticles, consisting of a core and an ultra-thin outer layer (shell) have been reported [129-132]. These devices exhibit the surface chemistry of the outer shell layer material, which can be i.e. gold or silver [129], functionalised silica [130] or a transition metal [131], respectively. The optical enhancement properties of core-shell nanoparticles is in general determined by the plasmonically active material, which is in most cases silver [129, 130] or gold [129, 131], but can be largely influenced by the choice and geometric arrangement of the second material. Most of these devices do not provide surface enhancement of Raman scattering below 500 nm. Potential controlled spectro-electrochemistry using nanoparticles is considerably more difficult than with nanostructured solid SER-active electrodes, since particles would need to be placed onto a conductive support [131, 188].

Electrochemical deposition strategies of a direct overlayer on SER-active electrodes have been developed, e.g. using gold electrodes as optical amplifying support and transition metals as overlayer [134, 137]. A decrease in SER intensity by a factor of 2 per 1 – 2 nm of overlayer thickness has been reported for these devices [134]. Therefore, the outer layer thickness needs to be sufficiently thin (< 5 – 10 monolayers) [137]. In addition gold supports can only be utilised at excitation wavelengths above 520 nm [4].

Recently, a multilayer silver-gold hybrid device for spectro-electrochemistry was developed that aims at combining the superior optical performance of silver with the chemical and electrochemical properties of gold [11, 12, 132]. The novel silver-gold hybrid device is based on solid SER-active sub-microscopically roughened silver electrodes (chapter 3.2) and can be employed in spectro-electrochemical investigations with excitation wavelengths throughout the whole visible range.

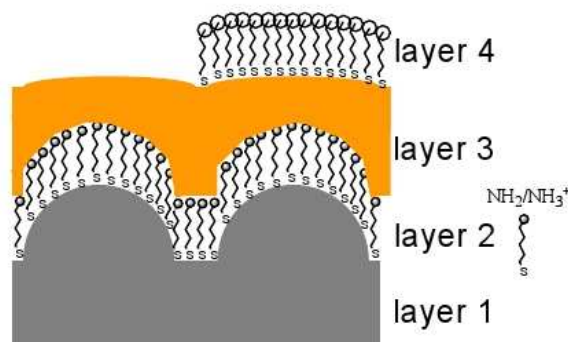


Figure 5: Schematic representation of the multilayer silver-gold electrode [adopted from Ref. 12]. Layer 1 represents the rough silver electrode, layer 2 an amino-terminated SAM [S:  $-\text{S}-(\text{CH}_2)_y\text{NH}_2$ , with  $y = 6, 8, 11$ ], layer 3 a gold film and layer 4 is another SAM layer, which might be different from layer 2 or not present at all.

In the hybrid device, the rough silver electrode, which represents the first layer, is coated by a dielectric spacer (S), which represents a second layer. On top of the spacer S, a metal island film (third layer) is deposited, which can be further functionalised with a SAM (fourth layer).

This device was first developed using different amino-terminated SAMs [S:  $-S-(CH_2)_yNH_2$ , with  $y = 6, 8, 11$ ] as dielectric spacer materials (second layer) and formation of a gold film (third layer) by electrochemical reduction of  $AuCl^-$  ions from solution [11, 12]. Strikingly, the Raman signal enhancement property of these multilayer Ag-S-Au-SAM devices, probed by the SERR signal of cytochrome *c* with 413 nm excitation immobilised on top of a fourth carboxyl-terminated SAM layer, was found to be comparable to Ag-SAM electrodes, although the silver surface was separated from the heme domain by roughly 15 nm and gold does not provide surface enhancement in this wavelength region [4]. The separation of the outer metal film by a dielectric spacer (second layer) was found to be necessary to yield high enhancements. Separation by conductive poly-electrolyte materials or direct electro-deposition of gold films yielded about four times lower SERR intensities [11].

The optical properties of the hybrid device were rationalised in terms of a long range plasmonic coupling between the underlying silver (first layer) and the gold film [11, 12, 133]. Efficient plasmonic coupling between two resonant metal nanostructures has been reported before [44, 135, 136], however, plasmonic coupling between a resonant and a non-resonant metal was first observed for the silver-gold hybrid device. This phenomenon has prompted the development of a theoretical model [133], which is discussed in the following chapter 5.1. In chapter 5.2 cytochrome *c* from horse heart and iso-1- cytochrome *c* from yeast, which were used as model proteins, are briefly introduced. In chapter 5.3 the overpotential dependence of the heterogeneous electron transfer rate of cytochrome *c* immobilised on the hybrid device is discussed and compared to pure silver and gold support materials [191]. Synthesis and further electronic properties of the silver-gold hybrid device are discussed in chapter 5.4. It should be noted that modified procedures for multilayer hybrid devices that differ either in the spacer material (second layer) [132] and/or in the material or application of the third layer have been developed [132, H. Khoa Ly (unpublished)].

## 5.1 Analytical Model for the Optical Performance

The starting point for an analytical description of the optical enhancement properties of the hybrid device is a non-concentric model, which is a simplified representation of the hybrid device geometry (figure 5.1.1) [133].

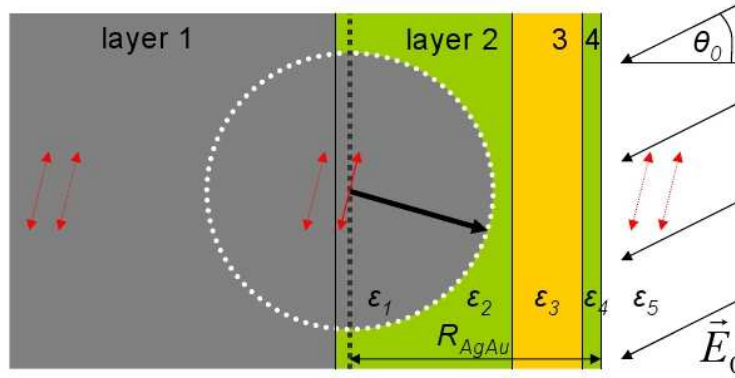


Figure 5.1.1 [adapted from reference 133]: Non-concentric model of the silver-gold hybrid device. A dipole is centered in the middle of the hemisphere of layer one, which is the silver core. The radius of the hemisphere is set to  $40 \pm 20$  nm. The dipole is depicted as a red arrow and is mirrored at each interface (exemplarily indicated by dashed red arrows). The second and fourth layers are self assembled monolayers with dielectric constants  $\epsilon_{2,4} = 2$ . Analytical expressions for the dielectric functions of silver  $\epsilon_1$  and gold  $\epsilon_3$  (third layer) can be found in literature [139, 140]. According to experimental results [11] the gold layer thickness was set to  $16 \pm 10$  nm and taken to be flat.  $R_{AgAu}$  denotes the distance from the center of the dipole to the SAM-H<sub>2</sub>O interface. The incident electric field  $\vec{E}_0$  approaches the electrode with the angle  $\theta$ . The azimuthal angle  $\phi$  (not depicted) defines the angle going out of the paper plane.

By using an image dipoles approach an expression for the electric field distribution in the multilayer system can be derived and renders the following expression for the field enhancement [133]:

$$\{5.1\} \quad F(\nu) = \frac{\vec{E}(r, \nu)}{\vec{E}_0} = \nabla_{(r, \theta, \phi)} \psi(r, \nu) R_{AgAu}.$$

In equation {5.1},  $\nabla_{(r, \theta, \phi)}$  is the divergence operator within a coordinate system defined by  $r$ , which is the distance to the core of the hemisphere, and the angles  $\theta$  and  $\phi$  (see caption of figure 5.1.1). The dimensionless potential  $\psi(r, \nu)$  is defined as:

$$\{5.1a\} \quad \psi(r, \nu) = \frac{-\Phi(r, \nu)}{\vec{E}_0 R_{AgAu}},$$

with  $\Phi(r, \nu)$  being the local electric field at position  $r$ .

In figure 5.1.2 a) the analytical results for the Raman signal enhancement  $g_0 = [F(\nu)]^2$  for the non-concentric model of the hybrid device are compared to the conventional rough silver device consisting of only the layers 1 and 2. In figure 5.1.2 b) the full spatial distribution of the signal

enhancement is depicted.

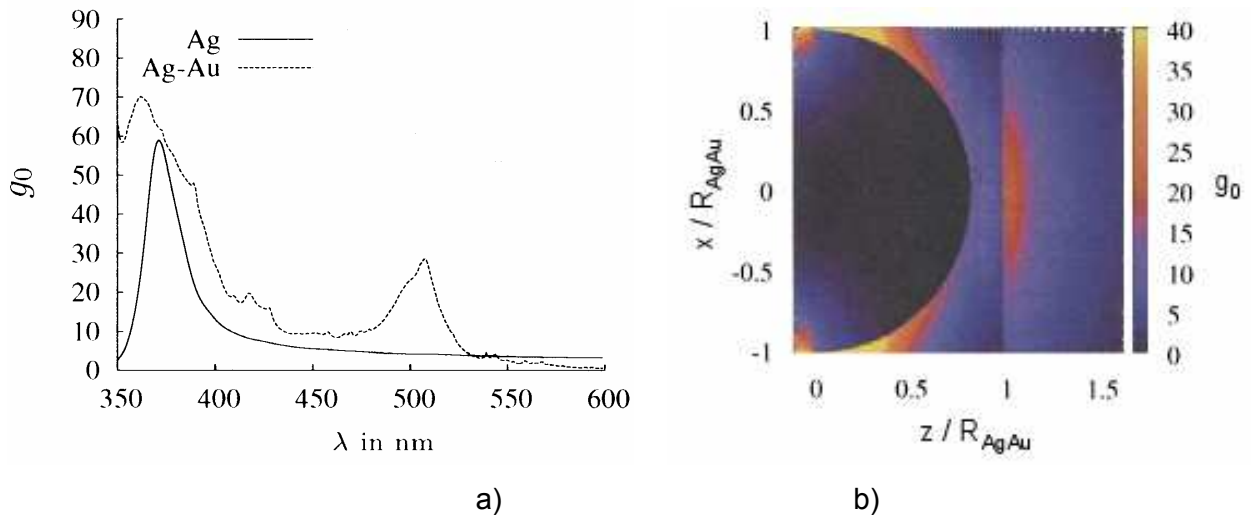


Figure 5.1.2, taken from [133]: a) Comparison of the wavelength dependent signal enhancement  $g_0 = [F(\nu)]^2$  by the hybrid device (light grey) compared to SAM-coated silver (dark grey) at the distance  $R_{AgAu}$ . b) Full spatial resolution of the signal enhancement at 413 nm excitation.

The calculations predict superior signal enhancement for the hybrid device at the distance of the Au(SAM) / H<sub>2</sub>O interface  $R_{AgAu}$  as compared to SAM-coated silver only. Another interesting finding of the analytical consideration of the hybrid model refers to the dependence of the signal enhancement with respect to the radius of the silver hemisphere  $R$  and thickness of the inner layer (figure 5.1.3).

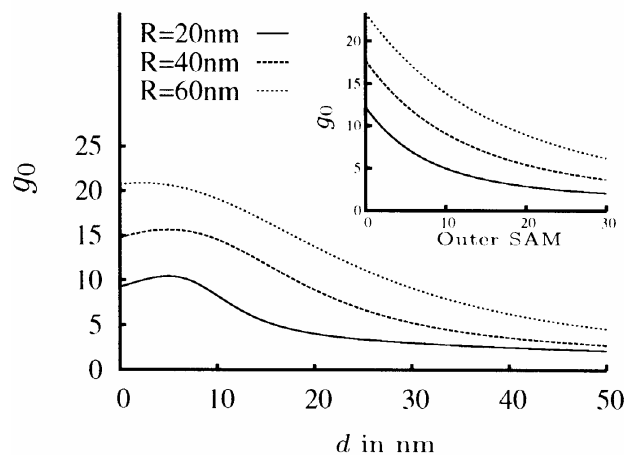


Figure 5.1.3, taken from [133]: Dependence of  $g_0 = [F(\nu)]^2$  to the thickness of the inner  $d$  and outer layer (inset) at 413 nm excitation.

While the signal enhancement is predicted to decrease with increasing outer layer thickness, it

increases first with increasing inner spacer layer thickness up to a value around 5 nm. In fact, experiments with different inner layers revealed only a weak inner spacer thickness dependence of the signal enhancement [11, 12, 132]. The inner layer thickness, however, also affects the electronic properties of the device, which are discussed in detail in chapters 5.3 and 5.4.

## 5.2 Cytochrome *c*

Cytochrome *c* is a small (~ 12 kDa), soluble *c*-type heme protein in the mitochondria of eukaryotic cells from mammals to invertebrates and yeast. This protein is primarily involved in the respiratory chain as being an electron carrier between the membrane integral enzymes complex III and complex IV [197]. Moreover, it was recently shown that cytochrome *c* is involved in different processes in the apoptosis of mammalian cells [167-169] (see chapter 8.2).

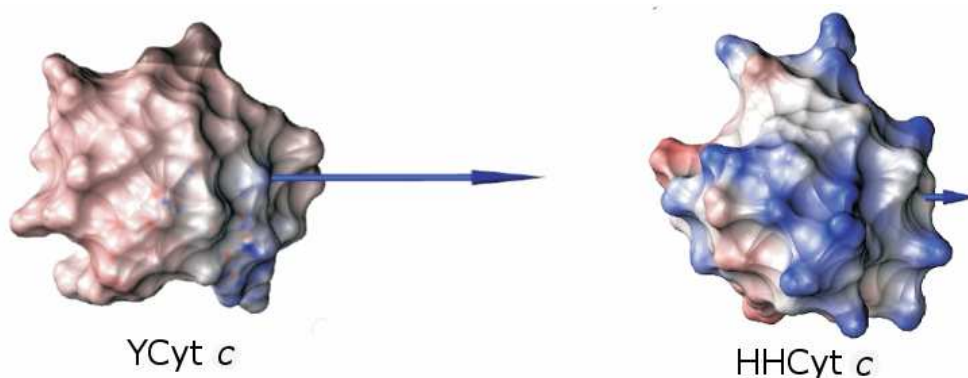


Figure 5.2, taken from [199]: Calculated surface potential distribution and dipole moment of iso-1-cytochrome *c* from yeast (YCyt *c*) compared to horse heart cytochrome *c* (HHCyt *c*) at pH 7.0. Positively charged regions are coloured blue, while red and white coloured regions are negatively charged and uncharged, respectively. The direction and strength of the dipole moment is indicated by the arrow.

In this work, cytochrome *c* from horse heart (HHCyt *c*) and iso-1-cytochrome *c* from yeast (YCyt *c*) were used as model proteins for exploring the performance of the silver-gold hybrid devices. Both, HHCyt *c* and YCyt *c* are cationic proteins with an isoelectric point  $pI > 10$ , hence, at neutral pH, both carry positive charges (+7 and +8 in the reduced and oxidised state, respectively) [199]. The lysine-rich binding patches in close proximity to the heme cofactors are positively charged. It should be noted that the dipole moment of YCyt *c* (~ 540 Debye) is more than three times larger than for HHCyt *c* (~ 170 Debye) [199]. Moreover, YCyt *c* possesses a cysteine residue at position 102 on the surface of the protein. This cysteine residue C102, which is absent in HHCyt *c*, can be utilised for covalent immobilisation of YCyt *c* onto bare gold surfaces upon formation of a strong gold-sulphur bond [200]. Both proteins can be immobilised electrostatically via lysine residues to negatively charged self assembled monolayers [201] and studied with electrochemistry [178-180] and surface enhanced vibrational spectroscopy [3, 68, 191, 197, 199].

The influence of high electric fields may induce a partial conversion to non-native species with altered coordination pattern and significantly decreased midpoint potential of the central heme iron [3, 191, 199].

### 5.3 Overpotential Dependence of Heterogeneous Electron Transfer Rates

A silver-gold hybrid device with 11-aminoundecanethiol (AUT) as spacer S (layer 2) and 16-mercaptohexadecanoic acid (MHDA) as outer SAM material (layer 4) was used for time resolved surface enhanced resonance Raman (TR-SERR) spectroscopic determination of heterogeneous electron transfer rates  $k_{ET}(\eta)$  of electrostatically immobilised horse heart cytochrome c (HHCyt c) [191]. Reduction rates were obtained as a function of the applied overpotential  $\eta$ . The overpotential dependence of the heterogeneous reduction rate using the silver-gold hybrid device is depicted in figure 5.3 and compared to pure silver [192] and gold support materials, respectively.

On MDHA-coated Ag electrodes a dramatic acceleration of the heterogeneous reduction rate with increasing overpotential is observed and analysis of the data yields a reorganisation energy of  $\lambda = 0.22$  eV for this process [56, 192] (see chapter 2.6.2). Although similar values for the reorganisation energy of heterogeneous reduction are expected for the hybrid and gold electrodes, on these electrodes  $k_{ET}(\eta)$  displays a drastically weaker increase with increasing  $\eta$ .

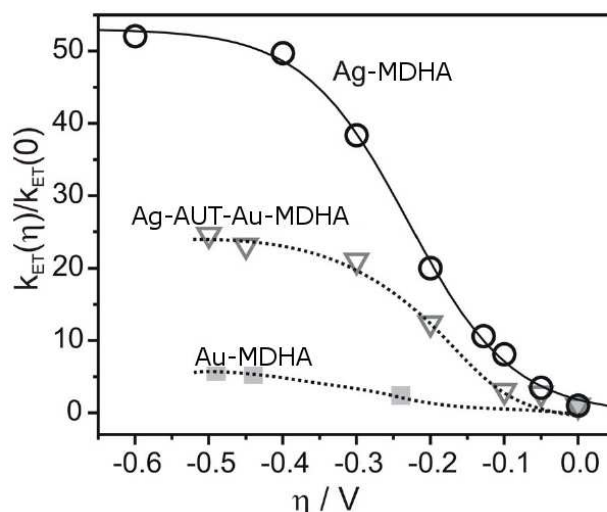


Figure 5.3 [191]: Overpotential dependence of the heterogeneous electron transfer rate constant  $k_{ET}(\eta)$  for HHCyt c immobilised on MHDA-coated electrodes. The black (open circles), dark gray (open triangles), and light gray (solid squares) symbols refer to the data obtained from an Ag (TR-SERR), Ag-AUT-Au (TR-SERR), and Au electrode (rapid scan surface enhanced infrared absorption). The solid line represents a fit of equation {2.6.2.3} (see chapter 2.6.2) to the experimental data for the Ag electrode [56, 192], whereas in the case of Au and Au-SAM-Ag, dotted lines are included to guide the eyes.

This discrepancy can be understood by taking into account different potential of zero charge ( $E_{pzc}$ ) values for the different MDHA-coated electrodes.  $E_{pzc}$  depends on the crystalline structure of the metal and the type of SAM coating and has been determined to be -0.45 and -0.2 V (vs. Ag/AgCl, 3 M KCl) for 11-mercaptoundecanoic acid (MUA) coated Ag and Ag-AUT-Au electrodes, respectively [12]. It is reasonable to assume that the values for the respective MDHA-coated electrodes are very similar [193]. According to literature data the potential of zero charge of MDHA-coated Au electrodes can be estimated to be around  $E_{pzc} = -0.05$  V [193]. The difference between the applied electrode potential  $E$  and  $E_{pzc}$  is proportional to the electric field in the MDHA / HHCyt c interface [194]. Thus, heterogeneous ET reactions of HHCyt c at Au and Ag electrodes take place under the action of opposite electric fields. Moreover, the field strength increases for Au but decreases for Ag upon increasing the driving force for reduction, i.e. with increasingly negative overpotential  $\eta = E - E_m$ , taking into account the midpoint potentials of -0.01 V and +0.04 V for HHCyt c on MDHA-coated Ag and Au electrodes, respectively [68, 194]. Accordingly, the electric field variation for the Au-AUT-Ag electrode lies in between those for the Ag and Au electrode as it first decreases until  $E = E_{pzc}$  (with  $E_{pzc} = -0.2$  V [12]) and then increases again for  $E < E_{pzc}$ .



## 5.4 Multi-layer electron transfer across nanostructured Ag-SAM-Au-SAM junctions probed by surface enhanced Raman spectroscopy

Murat Sezer,<sup>a</sup> Jiu-Ju Feng,<sup>ad</sup> H. Khoa Ly,<sup>a</sup> Yanfei Shen,<sup>b</sup> Takashi Nakanishi,<sup>bc</sup> Uwe Kuhlmann,<sup>a</sup>  
Peter Hildebrandt,<sup>a</sup> Helmuth Möhwald<sup>b</sup> and Inez M. Weidinger<sup>a\*</sup>

<sup>a</sup> Technische Universität Berlin, Institut für Chemie, Sekr. PC14, Straße des 17. Juni 135, D-10623 Berlin, Germany.

\*correspondence to E-mail: i.weidinger@mailbox.tu-berlin.de; Fax: +49 3031421122; Tel: +49 3031422780

<sup>b</sup> Max Planck Institute of Colloids and Interfaces, Research Campus Golm, D-14424 Potsdam, Germany.

<sup>c</sup> National Institute for Materials Science, 1-2-1 Sengen, Tsukuba 305-0047, Japan.

<sup>d</sup> School of Chemistry and Environmental Science, Henan Normal University, Xinxiang, Henan 453007, China.

Published in *Phys. Chem. Chem. Phys.*, 2010, **12**, 9822 – 9829.

Reproduced with permission of the PCCP Owner Societies.



# Multi-layer electron transfer across nanostructured Ag-SAM-Au-SAM junctions probed by surface enhanced Raman spectroscopy†

Murat Sezer,<sup>a</sup> Jiu-Ju Feng,<sup>ad</sup> H. Khoa Ly,<sup>a</sup> Yanfei Shen,<sup>b</sup> Takashi Nakanishi,<sup>bc</sup> Uwe Kuhlmann,<sup>a</sup> Peter Hildebrandt,<sup>a</sup> Helmuth Möhwald<sup>b</sup> and Inez M. Weidinger<sup>\*a</sup>

Received 12th February 2010, Accepted 13th April 2010

DOI: 10.1039/c003082a

We have developed a new layered Au–Ag electrode for studying interfacial electron transfer processes by surface enhanced resonance Raman (SERR) spectroscopy. The device consists of a nanostructured Ag support which is separated from a Au film *via* a thin self-assembled monolayer (SAM) of amino-terminated mercaptanes (C<sub>y</sub>-NH<sub>2</sub>, with *y* = 6, 8, 11). The Au film is biocompatibly coated to allow for binding of redox-active proteins. We have explored the performance of this device for analysing interfacial electron transfer processes by stationary and time-resolved SERR spectroscopy, using the heme protein cytochrome c (Cyt-c) as a benchmark protein. The SERRS intensity of Cyt-c on Ag-(C<sub>y</sub>-NH<sub>2</sub>)-Au electrodes and Ag electrodes was comparable when the protein was electrostatically attached to the metal coated by a SAM of carboxyl-terminated mercaptanes (C<sub>x</sub>-COOH) surface but 25 times higher upon covalent attachment *via* Cys102 to the bare Au surface. In the case of electrostatic adsorption the protein remained exclusively in its native state. Electron transfer between the protein and the Ag electrode occurred in an almost ideal Nernstian behaviour with a number of transferred electrons close to one (*n* = 0.8–0.9). Conversely, the covalent attached Cyt c showed two broad redox transitions (*n* = 0.3) and a partial conversion to a non-native species which remained redox inactive in the potential range from +0.1 to –0.3 V. For the electrostatically immobilised Cyt, apparent electron transfer rates of 0.8 and 49 s<sup>–1</sup> were obtained for *y* = 11 and *x* = 15 and 10, respectively, indicating a fast long-distance electron transfer through the multilayer with the electron tunneling through the C<sub>x</sub>-COOH SAM being the rate limiting step.

## Introduction

Hybrid materials including a conducting support and a redox-active protein are essential building blocks in many fields of modern biotechnology, including the development of biosensors, biocatalysts, or biofuel cells.<sup>1,2</sup> Regardless of the specific application, optimisation of such bioelectronic devices requires strategies for immobilising proteins on the solid support that ensure preservation of their native structure and function, and an efficient electronic coupling between the biomolecule and the inorganic material. In this respect, indispensable tools are biocompatible coatings of the solid support which may include self-assembled monolayers (SAMs) of amphiphiles, thin films of polymers, and multilayers of polyanions and polycations.<sup>3–7</sup>

In most cases, these hybrid systems are optimised empirically, guided by criteria such as fast electronic response, long life

time, or catalytic turnover number, typically screened by electrochemical methods.<sup>8–10</sup> These approaches, however, do not provide information about the underlying molecular processes which, for example, is a prerequisite for identifying factors that stabilise or destabilise the structure of the immobilised protein and thus affect its function and eventually the performance of the bioelectronic device.

In this respect, surface enhanced Raman (SER) spectroscopic techniques gain increasing importance as surface-selective and -sensitive methods that can provide molecular structure information about adsorbed species.<sup>11,12</sup> The SER effect is based on the resonant coupling of the radiation field with the surface plasmons of nanostructured metals, among which only for Au and Ag the plasmon resonances are in the visible and near-infrared region. Additional selectivity and sensitivity is introduced when the SER effect is combined with the molecular resonance Raman (RR) effect, *i.e.* surface enhanced resonance Raman (SERR), such that it is possible to probe the vibrational spectra solely of the redox centers of the immobilised proteins.<sup>13,14</sup> The applicability of SERR spectroscopy, however, meets serious constraints since it requires the match of the molecule's electronic transition with the surface plasmon resonances of the metal. The latter is typically above 600 and 400 nm for Au and Ag, respectively.<sup>15</sup> Since most of the redox centers of proteins (*i.e.*, flavins, hemes, Fe–S centers) possess electronic transitions below 500 nm, SERR spectroscopy is restricted to Ag-based materials which, on the other hand, are

<sup>a</sup> Technische Universität Berlin, Institut für Chemie, Sekr. PC14, Straße des 17. Juni 135, D-10623 Berlin, Germany. E-mail: i.weidinger@mailbox.tu-berlin.de; Fax: +49 3031421122; Tel: +49 3031422780

<sup>b</sup> Max Planck Institute of Colloids and Interfaces, Research Campus Golm, D-14424 Potsdam, Germany

<sup>c</sup> National Institute for Materials Science, 1-2-1 Sengen, Tsukuba 305-0047, Japan

<sup>d</sup> School of Chemistry and Environmental Science, Henan Normal University, Xinxiang, Henan 453007, China

† This paper contains work as a result of a collaborative research project of the German Science Foundation (DFG Sonderforschungsbereich 448) on "Mesoscopically organized composites".

of low importance for bioelectronic devices. Here, Au exhibits a superior performance specifically due to its higher chemical and electrochemical stability and its intrinsically better biocompatibility.

In our previous study, we have shown that Ag–Au hybrid electrodes may combine the advantageous (electro)chemical and optical properties of Au and Ag, respectively.<sup>16</sup> In these devices, a nanostructured Ag support is stepwise coated by a SAM of an amino-terminated mercaptane, a thin Au film, and an additional SAM for binding the redox protein. As demonstrated in the case of the heme protein cytochrome *c* (Cyt-*c*), high quality SERR spectra of the heme cofactor could be obtained with 413 nm excitation even though the protein was separated from the Ag surface by *ca.* 20 nm. This unusual enhancement was ascribed to the optical excitation of the Ag surface plasmons which are coupled to the Au surface plasmons and thus cause an enhancement of the RR scattering of the nearby heme group.

In the present work, we have extended the studies of such devices by investigating the electron transfer (ET) processes of Cyt-*c* across the multilayer Ag-SAM-Au-SAM junctions. We have focused on two types of protein binding, *i.e.*, covalent and electrostatic immobilisation, and analysed the adsorption-induced effects on the heme pocket structure and redox transitions. In addition to these stationary experiments, we have employed time-resolved SERR spectroscopy to study the interfacial ET dynamics. Finally, our experiments allow assessing the potential and limitations for utilising this device in a wide spectral range.

## Results and discussion

### Preparation of Ag-(C<sub>y</sub>-NH<sub>2</sub>)-Au hybrid devices

The preparation of Ag-(C<sub>y</sub>-NH<sub>2</sub>)-Au hybrid devices is illustrated in Fig. 1A.<sup>16</sup> After electrochemical roughening of a solid Ag electrode that leads to a coral-like surface structure on the Ag surface with a nanoscaled grain size, the electrode was incubated for 24 h in a 4 : 1 ethanol/water solution containing 1 mM C<sub>y</sub>-NH<sub>2</sub> (*y* = 6, 8, 11) until a stable monolayer was obtained. Subsequent formation of an Au film was achieved by incubating the Ag-(C<sub>y</sub>-NH<sub>2</sub>) electrode in a 1% wt AuCl<sub>4</sub><sup>-</sup> solution for 1–4 h, followed by electrochemical reduction to Au at –0.5 V vs. Ag/AgCl (3 M KCl) reference electrode in a deaerated 0.1 M KCl solution for *ca.* 5 min. The average thickness of the resultant Au film (Fig. 1A) was determined to be *ca.* 15 nm.<sup>16</sup>

For electrostatic adsorption of horse heart Cyt-*c* *via* the lysine-rich domain around the exposed heme edge, the Au surface was coated with a SAM of C<sub>x</sub>-COOH (*x* = 5, 10, 15) as described previously<sup>4,17</sup> (Fig. 1B). Immobilisation of Cyt-*c* was completed within 30 min at –0.2 V and subsequent SERRS experiments were carried out in an electrochemical cell containing a 30 mM phosphate buffer solution (pH 7.0) with a protein concentration of 0.2–0.4 μM. SERRS experiments were carried out in contact with a solution containing 12.5 mM Na<sub>2</sub>SO<sub>4</sub> and 12.5 mM phosphate buffer (pH 7.0). For binding of yeast cytochrome *c* *via* the thiol function of Cys102,<sup>18</sup> the Au–C<sub>y</sub>-NH<sub>2</sub>–Ag electrode was immersed in a 35 μM buffered

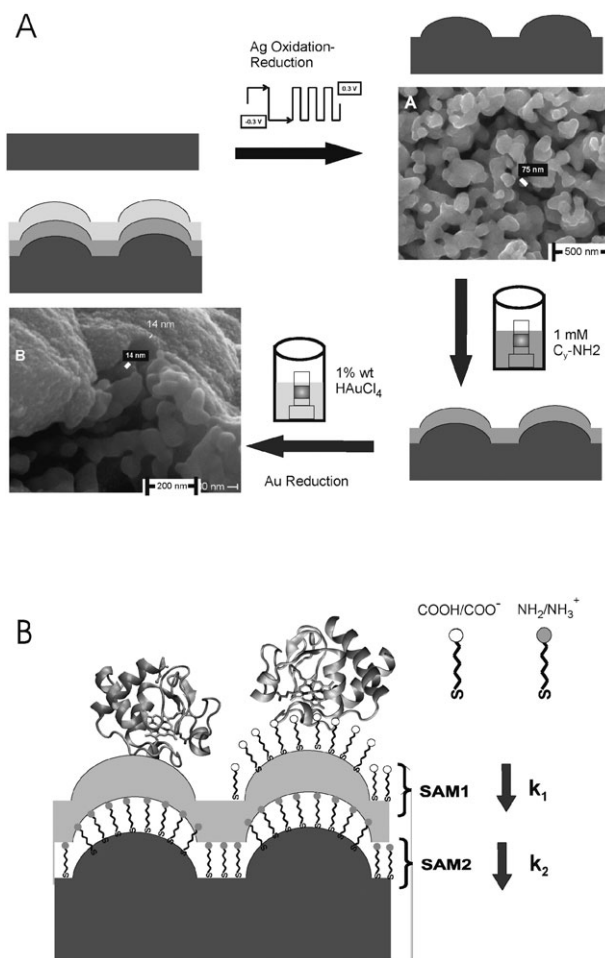


**Fig. 1** Schematic illustration of (A) the preparation of Ag-(C<sub>y</sub>-NH<sub>2</sub>)-Au electrodes and (B) the setup of the electrode with the adsorbed cytochrome *c*.

solution of Cyt-*c* for 1 h. Subsequently, the Cyt-*c* coated electrode was immersed into a 2 M KCl solution for 20 min to remove the electrostatically bound proteins. In this case, SERRS experiments were carried out with the electrode immersed into a buffered solution (pH 7.0) with an ionic strength of *ca.* 0.3 M, adjusted by addition of KCl, in order to avoid electrostatic interaction of the covalently bound protein with the metal surface.

### Preparation of Au nanoflake substrates

Au- and Ag nanoflake substrates were prepared according to our previous report.<sup>19</sup> The nanostructured template obtained by self-assembly of a fullerene derivative on a quartz support<sup>20</sup> was sputter-coated with Au or Ag of variable thickness between 10 to 100 nm. The fullerene derivative can be efficiently removed from the substrate by immersion in chloroform. After treatment with O<sub>3</sub> plasma for 2 min to remove contaminated organic species, the Au or Ag nanoflake-covered quartz substrates were immersed in ethanolic solutions containing 2 mM of 4-aminothiophenol for at least 24 h. Subsequently, the substrates were carefully rinsed with pure ethanol and dried in nitrogen gas.

### Surface enhancement on layered Ag-(C<sub>y</sub>-NH<sub>2</sub>)-Au materials

Nanostructured hybrid Ag-(C<sub>y</sub>-NH<sub>2</sub>)-Au-(C<sub>x</sub>-COOH) devices are assembled in various combinations of SAMs with different thickness that either serve for separating the Ag and Au metal (C<sub>y</sub>-NH<sub>2</sub> with  $y = 6, 8, 11$ ) or were used for electrostatic binding of Cyt-c on the Au surface (C<sub>x</sub>-COOH with  $x = 5, 10, 15$ ). The intensity of the prominent  $\nu_4$  band of ferrous Cyt c was chosen for comparing the surface enhancement of the different systems. Measurements were done at  $-0.4$  V to guarantee that the protein was present exclusively in its reduced state. SERR signals of Cyt c adsorbed on Ag-(C<sub>11</sub>-NH<sub>2</sub>)-Au-(C<sub>11</sub>-COOH) electrodes display an average SERR intensity that was only slightly lower than for Cyt c on Ag-(C<sub>x</sub>-COOH) electrodes (Fig. 2A). This surprisingly high Raman enhancement of the Ag-(C<sub>11</sub>-NH<sub>2</sub>)-Au-(C<sub>11</sub>-COOH) system can not result from direct optical excitation of surface plasmon on Au, which possesses a low optical activity below 600 nm due to  $d-d$  transitions of the metal. Instead, transfer of optical plasmon excitation from Ag to Au is assumed to be the origin for the strong Raman intensities. Long range plasmon coupling between two optically active nanostructures has been previously reported in the literature<sup>21,22</sup> for distances up to 30 nm. A similar mechanism was proposed by our group for interaction between optically active (Ag) and inactive (Au) metallic nanostructures.<sup>16,23</sup>

Upon decreasing the thickness of the inner layer, a drop in SERR intensity by a factor of 2 ( $y = 8, x = 11$ ) and 3 ( $y = 6, x = 11$ ) was observed. Presumably, this decrease is related to defects present in shorter NH<sub>2</sub>-SAMs resulting in a more discontinuous Au-film and possibly lower protein coverage.

The enhancement factor (EF) may be determined on the basis of an early study of Cyt-c adsorbed on Ag colloids<sup>24</sup> assuming that the enhancement is the same as for electrochemically roughened Ag electrodes. In that study, an EF was determined to be  $8 \times 10^4$  for 407 nm excitation which is likely to be the same as for 413 nm excitation used in this work. For Cyt-c immobilised on C<sub>x</sub>-COOH-coated Ag electrodes, a decrease in SERR intensity with increasing SAM thickness was observed,<sup>17</sup> which followed the same distance-dependence previously determined by Compagnini *et al.*<sup>25</sup> Correspondingly, for Cyt-c immobilised on an Ag electrode coated by a C<sub>10</sub>-COOH SAM, the enhancement is estimated to drop by a factor of *ca.* 2.5 as compared to Cyt-c directly adsorbed on an Ag electrode. Thus, EF for Cyt-c on an Ag-(C<sub>10</sub>-COOH) electrode is assumed to be *ca.*  $3.2 \times 10^4$ . Under the assumption that protein surface concentration does not change significantly for different C<sub>x</sub>-COOH SAMs,<sup>17</sup> EFs as a function of SAM length and hence distance to the Ag surface could be derived from the measured SERRS intensities (Fig. 2B).

To determine the EF for Cyt-c bound to Ag-(C<sub>11</sub>-NH<sub>2</sub>)-Au-(C<sub>10</sub>-COOH), however, we have to take into account the *ca.* 4 times higher surface coverage compared to Cyt-c on Ag-(C<sub>10</sub>-COOH) as determined previously.<sup>16</sup> Comparing the SERR intensities obtained from these two devices under identical conditions, the EF is then estimated to be *ca.*  $1 \times 10^4$  for Cyt-c bound to Ag-(C<sub>11</sub>-NH<sub>2</sub>)-Au-(C<sub>10</sub>-COOH). EFs derived for the Ag-(C<sub>11</sub>-NH<sub>2</sub>)-Au-(C<sub>x</sub>-COOH) system decrease with increasing number of methylene groups of the outer carboxyl-terminated SAMs; however, the decrease is much less pronounced

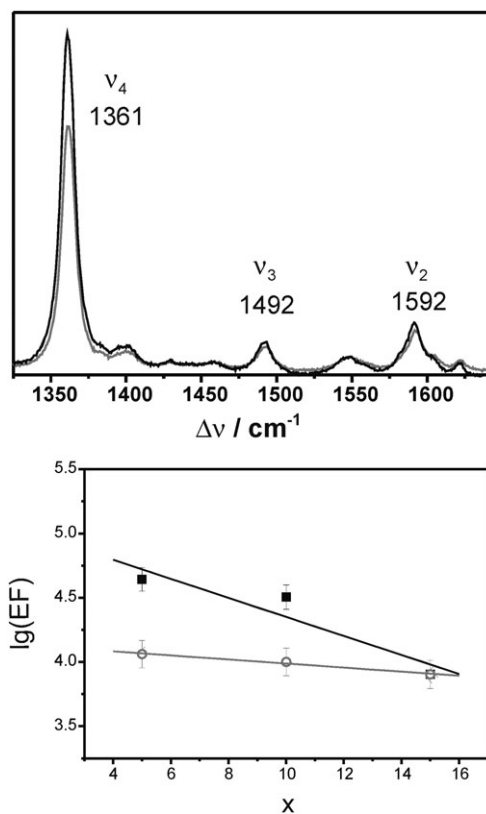


**Fig. 2** (A) SERR spectra of Cyt c on Ag (black) and Ag-(C<sub>y</sub>-NH<sub>2</sub>)-Au (grey) electrodes at  $E = -0.4$  V with 413 nm excitation. The spectra were obtained with the same laser power and accumulation time. (B) Semi-logarithmic plot of the enhancement factors for Ag-(C<sub>x</sub>-COOH) (hollow circles) and Ag-(C<sub>11</sub>-NH<sub>2</sub>)-Au-(C<sub>x</sub>-COOH) (solid squares) as a function of methylene groups of the carboxyl-terminated SAM ( $x = 5, 10, 15$ ). The error bars indicate the variation for measurements from different preparations.

than for the same SAMs directly bound to the Ag electrode (Fig. 2B).

The situation is different for excitation at wavelengths above 600 nm where direct optical excitation of Au surface plasmons becomes possible. However, with 647 nm excitation, the SER spectra of the (C<sub>10</sub>-COOH) SAM on Ag-(C<sub>11</sub>-NH<sub>2</sub>)-Au-(C<sub>10</sub>-COOH) reveal slightly lower signals than those detected from Ag-(C<sub>10</sub>-COOH) (data not shown). We thus conclude that the Au layer is too thin (*ca.* 15 nm) for an efficient direct coupling of the Au surface plasmons with the radiation field at this excitation line.

These findings imply that an efficient enhancement of the Raman scattering *via* direct optical excitation of Au surface plasmons requires a distinctly higher Au film thickness than used in the present layered Ag-(C<sub>y</sub>-NH<sub>2</sub>)-Au devices.

To test this hypothesis we have studied the effect of the Au film thickness on the EF on the basis of Au nanoflakes which have been shown to represent efficient SER-active materials for red and near-infrared excitation.<sup>19</sup> Fig. 3 displays the SER spectra of 4-aminothiophenol SAMs on Au nanoflakes of various metal film thicknesses. At 10 nm, the SER signal can hardly be detected but it strongly increases by a factor of 40 at 50 nm. For this thickness, a lower limit of the EF has been

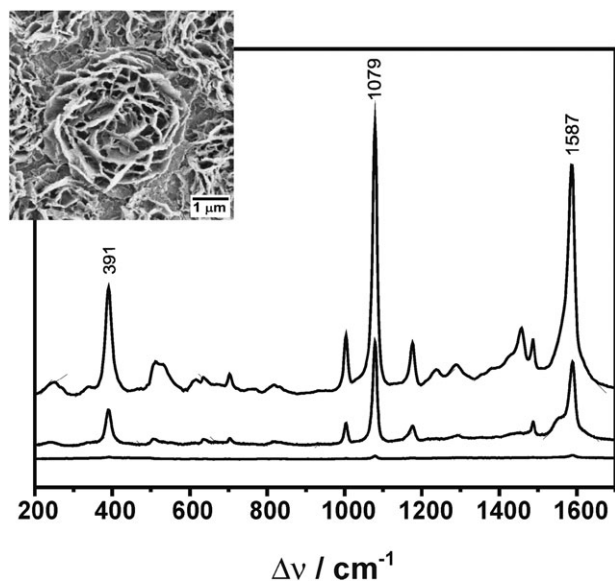


**Fig. 3** SERR spectra of 4-aminothiophenol with 1064 nm excitation on Au nanoflakes with (from bottom to top) 10, 50 and 100 nm Au thickness. The inset represents an SEM image of the Au nanoflakes with 50 nm Au thickness. The spectra were obtained with the same laser power and accumulation time.

estimated to be  $10^5$ . A further 2.5-fold increase is obtained when the thickness is increased to 100 nm. A comparably strong enhancement is also observed for Ag nanoflakes (data not shown).

However, improvement of the enhancement of the layered Ag-(C<sub>y</sub>-NH<sub>2</sub>)-Au devices also for direct optical excitation of the Au surface plasmons in the red spectral region was not possible without decreasing the performance in the violet region. Upon increasing the incubation time in the AuCl<sub>4</sub><sup>-</sup> solution and the reduction time for depositing the outer Au layer, corresponding to an increase of the Au layer thickness, the SERR signal of Cyt-c probed at 413 nm excitation decreased.<sup>16</sup> This observation can readily be understood in terms of the increased absorption of the incident light with higher Au film thickness.

### Redox equilibria of electrostatically immobilised cytochrome c

SERR spectra of the Cyt-c (horse heart) electrostatically immobilised on Ag-(C<sub>y</sub>-NH<sub>2</sub>)-Au-(C<sub>x</sub>-COOH) electrodes do not provide any indications for structural changes of the heme pocket, as compared to the protein in solution. At each electrode potential, the SERR spectra can be described by a superposition of the component spectra of the native reduced and oxidised state of Cyt-c, denoted as state B1 (Fig. 4A). In this respect, the SERR spectroscopic experiments reveal the same results as for Cyt-c bound to Ag-(C<sub>x</sub>-COOH) electrodes.

The quantitative analysis of the SERR spectra measured as a function of electrode potential allows determining the redox potentials of the immobilised proteins taking into account the relative RR/SERR cross sections of the oxidised and reduced species (Fig. 4B).<sup>17</sup> In all cases, Nernstian plots display a nearly ideal behaviour for a one-electron transfer process ( $n = 0.8 - 0.9$ ; Table 1). These relatively high values for

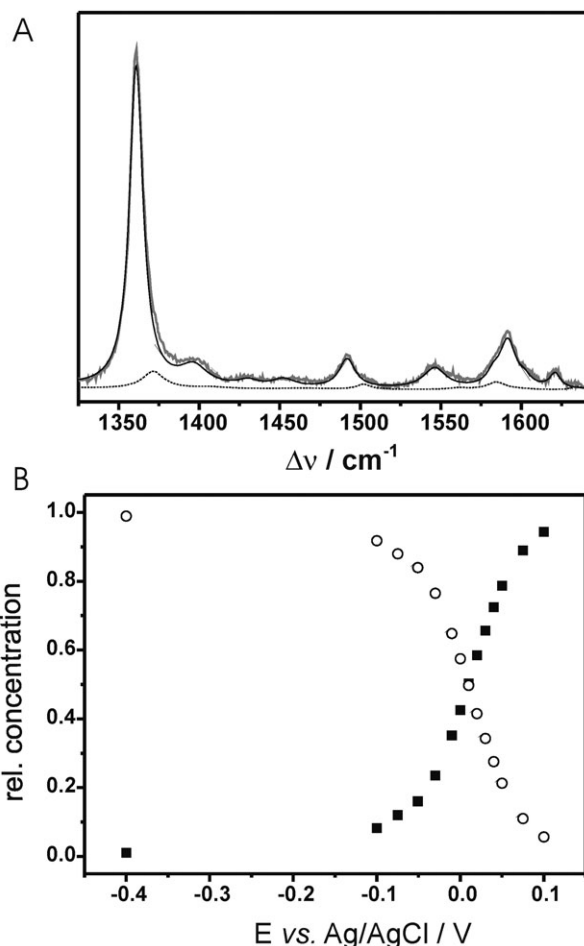


**Fig. 4** A SERR spectrum of Cyt c on Ag-(C<sub>3</sub>-NH<sub>2</sub>)-Au electrodes at  $-0.075$  V. The grey, thin solid, and dotted lines refer to the experimental spectrum and the component spectra of the reduced and oxidised Cyt c (B1), respectively. B, relative concentrations of the reduced (hollow circles) and oxidised (squares) form of Cyt c (B1) as a function of potential, as determined from the SERR experiments.

$n$  indicate a largely uniform orientational distribution of the immobilized protein. Especially for Cyt c on Ag-(C<sub>y</sub>-NH<sub>2</sub>)-Au-(C<sub>15</sub>-COOH), the  $n$  values are distinctly closer to one than for Ag-(C<sub>15</sub>-COOH) which may be due to a better packing of the SAM on Au than on Ag, particularly in view of the more pronounced surface roughness in the latter case.<sup>16</sup>

The experimentally determined redox potentials are slightly shifted with respect to the redox potential of the protein in solution. For Ag-(C<sub>11</sub>-NH<sub>2</sub>)-Au-(C<sub>10</sub>-COOH), this shift ( $E_{RC}$ ) is  $-56$  mV and therefore slightly more pronounced than for Cyt-c adsorbed on either Ag-(C<sub>10</sub>-COOH) or Au-(C<sub>10</sub>-COOH) for which  $-40$  mV and  $-20$  mV respectively has been determined. These shifts are due to the interfacial drop across the SAM and can be rationalised on the basis of simple electrostatic considerations<sup>17</sup> which suggest a relationship between the redox potential shift  $E_{RC}$  and the difference between the redox potential  $E^0$  and the potential of zero charge  $E_{pzc}$ , i.e.,  $\Delta E_{PZC} = |E^0 - E_{PZC}|$ . For Ag-(C<sub>10</sub>-COOH) and Ag-(C<sub>11</sub>-NH<sub>2</sub>)-Au-(C<sub>10</sub>-COOH),  $E_{pzc}$  has been determined to be  $-0.45$  V and  $-0.20$  V, respectively. Moreover, for Au-(C<sub>10</sub>-COOH)  $\Delta E_{PZC}$  is close to zero ( $E_{pzc} = 0.03$  V)<sup>26</sup>

**Table 1** Redox potentials ( $E^0$ ) in V and number of transferred electrons ( $n$ ) for the redox process of cytochrome c (horse heart) on various coated Ag, Au, and Ag-Au hybrid electrodes<sup>a</sup>

		C <sub>5</sub> -COOH		C <sub>10</sub> -COOH		C <sub>15</sub> -COOH	
		$E^0$	$n$	$E^0$	$n$	$E^0$	$n$
Ag	no	0.020	0.8	0.020	0.85	0.006	0.65
Ag-Au	C <sub>6</sub> -NH <sub>2</sub>	nd	nd	-0.001	0.89	nd	nd
	C <sub>8</sub> -NH <sub>2</sub>	nd	nd	0.007	0.92	nd	nd
	C <sub>11</sub> -NH <sub>2</sub>	-0.005	0.9	0.004	0.78	0.015	0.88
Au <sup>a</sup>	no	0.037	0.81	0.040	0.77	0.030	0.84

<sup>a</sup> Data determined from SEIRA spectroscopy.<sup>32</sup> Error margins for redox potentials are  $\pm 0.03$  V; nd, not determined.

such that the lack of a notable redox potential shift can readily be understood. However, this simple electrostatic model fails to account for (a) the higher redox shifts observed for Ag-(C<sub>*y*</sub>-NH<sub>2</sub>)-Au systems and (b) the increasing values for  $E_{RC}$  from  $x = 6$  (-5 mV) to  $x = 15$  (+15 mV) at Ag-(C<sub>11</sub>-NH<sub>2</sub>)-Au-(C<sub>*x*</sub>-COOH), in contrast to the opposite tendency at Ag-(C<sub>*x*</sub>-COOH).<sup>17</sup> Evidently, the underlying assumptions of the electrostatic model are too crude to provide a fully consistent description of the complex interfacial potential distribution of a metal/SAM multilayer device.

#### Redox equilibria of the covalently immobilised cytochromes

In contrast to horse heart Cyt c, iso-1 cytochrome c from yeast exhibits a single surface cysteine at position 102, which can be used for selective binding to pure metal surfaces. Upon covalent attachment of Cyt c (yeast) *via* Cys102 we have observed a significantly better performance on Ag-(C<sub>11</sub>-NH<sub>2</sub>)-Au which affords a SERR intensity that is *ca.* 25 times higher than for Ag under otherwise similar experimental conditions (Fig. 5). We attribute this effect to the higher affinity of the thiol side chain of Cys102 to Au, corresponding to a higher surface coverage. However, potential-dependent SERR spectra of the covalently bound Cyt-c on Ag-(C<sub>11</sub>-NH<sub>2</sub>)-Au reveal structural changes in the heme pocket of the protein not observed upon electrostatic immobilisation. For the covalently bound Cyt-c, the SERR spectra include spectral markers that are characteristic of a non-native ferric state of Cyt-c in which the Met80 ligand is replaced by a His residue (His33 or His26).<sup>27</sup>

In previous studies it has been shown that this species, denoted as B2 state, is induced either *via* strong electrostatic fields with lysine residues around the exposed heme edge, or by hydrophobic interactions that involve the nonpolar peptide segment 81–85. In both cases, the primary step is the removal of the Met80 ligand from the heme. This coordination site can be then occupied by His33 or His26 to yield the six-coordinated low-spin (6cLS) of B2 or remains vacant, corresponding to a five-coordinated high spin (5cHS). The 6cLS and 5cHS species of B2, which can readily be distinguished on the basis of the characteristic RR/SERR spectroscopic signature (Fig. 6A),<sup>27</sup> thus typically coexist under strong electric fields<sup>17,28</sup> and in hydrophobic environments.<sup>29</sup> Such conditions do not appear to hold for the covalently bound Cyt-c on Au and, in addition, only the 6cLS form of B2 but not the 5cHS species is detectable in the SERR spectra. We, therefore, suggest that in this case the conformational transition to the 6cLS B2 form

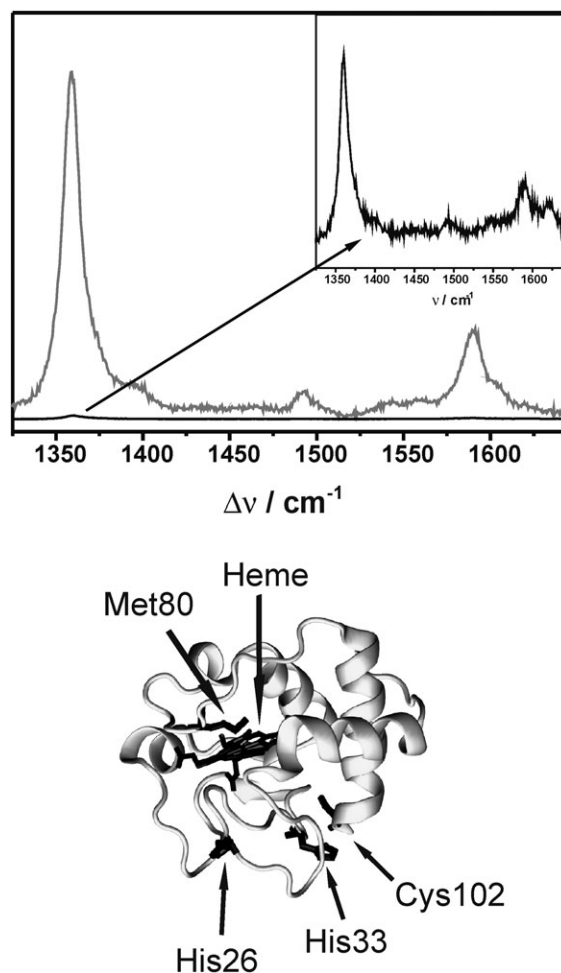


**Fig. 5** Top, SERR spectra of Cyt c covalently bound *via* Cys102 on Ag (black) and Ag-(C<sub>11</sub>-NH<sub>2</sub>)-Au (grey) electrodes. Bottom, protein structure of yeast Cyt c showing the positions of Met80, His26, His33 and Cys102.

occurs *via* a different mechanism. Taking into account that Cys102 is in close proximity to His33 (Fig. 5B), it may be that the covalent attachment to the Au surface *via* the side chain of Cys102 destabilises the region in the vicinity of His33 and eventually favours the displacement of the peptide segment involving His33 towards the heme pocket, such that this residue may effectively compete with Met80 for binding to the heme iron.

For the covalently bound Cyt-c, the relative concentration of the ferric B2(6cLS) state is potential-independent and *ca.* 40% in the potential range between +0.1 V and -0.35 V (Fig. 6B). This finding can be understood taking into account that the redox potential of this species is between -0.35 and -0.40 V.<sup>28</sup> The remaining 60% of the covalently bound Cyt-c is in the native B1 state and is fully redox-active although the redox transition appears to be more complex than for the electrostatically bound Cyt-c (*vide supra*). Here the potential-dependent distribution between the ferric and ferrous B1 state, as derived from the SERR spectra, shows two transitions associated with lower values for  $n$  (*ca.* 0.3) and more negative redox potentials (-0.1 and -0.25 V) as compared to the electrostatically immobilised protein (Fig. 4). Evidently, the

covalent linkage restricts the orientational distribution to two main pools, both of them exhibiting unfavourable electronic coupling with the metal surface, such that high overpotentials are required for interfacial ET. This result, in turn, further supports the view that fast orientational dynamics is essential for an efficient electronic communication of the protein with the electrode.<sup>30</sup>

### Electron transfer dynamics of cytochrome c

Time-resolved SERR measurements were carried out with the electrostatically immobilised Cyt-c on various Ag-(C<sub>y</sub>-NH<sub>2</sub>)-Au-(C<sub>x</sub>-COOH) electrodes, employing potential jumps to the redox potential  $E^0$  from initial potentials  $E_i = E^0 \pm 0.05$  V. The time-resolved SERR spectra could be well described by a superposition of the component spectra only of the reduced and oxidised forms of the native state B1, without any interference by other non-native states. Thus, we conclude that only two species are involved in the potential-jump relaxation process which, hence, is described by mono-exponential kinetics associated with the relaxation constant  $k_{\text{relax}}$ . If electron tunneling is the rate-determining step,  $k_{\text{relax}}$  is

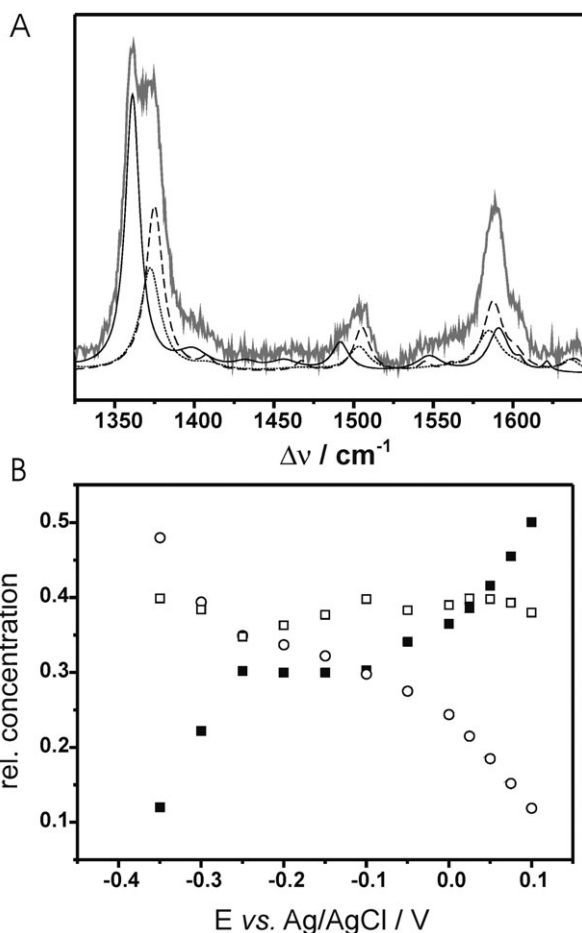


**Fig. 6** A, SERR spectrum of covalently attached yeast Cyt c at  $-0.05$  V. The grey, thin solid, dotted, and dashed lines refer to the experimental spectrum and the component spectra of the reduced B1, oxidised B1, and oxidised B2(6CLS), respectively. B, relative concentrations of the reduced (hollow circles) and oxidised (squares) B1 state and the oxidised B2(6CLS) state (hollow squares).

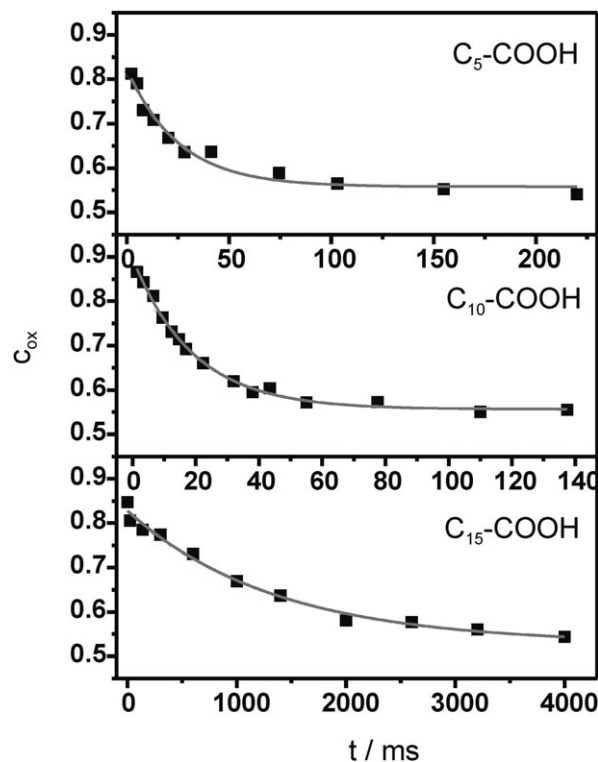


**Fig. 7** Time-dependent changes of the relative concentrations of the oxidised Cyt c (B1) following a potential-jump from  $+0.05$  V to the redox potential on Ag-(C<sub>11</sub>-NH<sub>2</sub>)-Au-(C<sub>x</sub>-COOH) electrodes ( $x = 5, 10, 15$ ). The data were obtained by time-resolved SERR spectroscopy.

related to the heterogeneous ET constant  $k_{\text{ET}}$  according to  $k_{\text{relax}} = 2 \cdot k_{\text{ET}}$ . Representative examples of the TR SERR spectra and the corresponding kinetic plots are shown in Fig. 7. All kinetic data are listed in Table 2.

To rationalise these data we distinguish the different electron transport regimes in the hybrid device (see Fig. 1) which include electron tunneling through the SAMs, *i.e.*, from Cyt-c to Au *via* the outer carboxylate-terminated SAM and from the Au film to the Ag electrode *via* the inner amino-terminated SAM. These tunneling steps primarily depend on the number of the methylene groups,<sup>31</sup> and thus should be much slower than electron transport through the conducting Au film. Accordingly, we find a value of  $0.8 \text{ s}^{-1}$  for Ag-(C<sub>11</sub>-NH<sub>2</sub>)-Au-(C<sub>15</sub>-COOH) that is comparable to that determined previously for Au-(C<sub>15</sub>-COOH) ( $0.4 \text{ s}^{-1}$ )<sup>32</sup> (Table 2), confirming the view that tunneling through the thickest SAM constitutes the rate-limiting step. Correspondingly, the rate

**Table 2** Relaxation constants (in  $\text{s}^{-1}$ ) for the interfacial redox processes of cytochrome c (horse heart) as determined by time-resolved SERR spectroscopy

		C <sub>5</sub> -COOH	C <sub>10</sub> -COOH	C <sub>15</sub> -COOH
Ag	No	$130 \pm 20$	$50 \pm 20$	$0.15^a$
Ag-Au	C <sub>6</sub> -NH <sub>2</sub>	nd	$4 \pm 2$	nd
	C <sub>8</sub> -NH <sub>2</sub>	nd	$29 \pm 4$	nd
	C <sub>11</sub> -NH <sub>2</sub>	$30 \pm 11$	$49 \pm 15$	$0.8 \pm 0.2$
Au	No	$900^b$	$90^b$	$0.4^b$

<sup>a</sup> Ref. 31. <sup>b</sup> Ref. 32; nd, not determined.

constant increase by nearly two orders of magnitude to  $49 \text{ s}^{-1}$  upon reducing the thickness of the outer SAM, *i.e.* for Ag-(C<sub>11</sub>-NH<sub>2</sub>)-Au-(C<sub>10</sub>-COOH). This value is low by a factor of *ca.* 2 compared to that measured for the Au-(C<sub>10</sub>-COOH) system, evidently due to the fact that in the hybrid device tunneling occurs *via* two SAMs of nearly the same thickness.

Correspondingly, ET through Ag-(C<sub>11</sub>-NH<sub>2</sub>)-Au-(C<sub>5</sub>-COOH) is expected to be limited by tunneling through the inner layer which seems to be confirmed since  $k_{\text{relax}}$  is similar albeit not identical to the value for Ag-(C<sub>11</sub>-NH<sub>2</sub>)-Au-(C<sub>10</sub>-COOH). Note that for Au-(C<sub>5</sub>-COOH) and Ag-(C<sub>5</sub>-COOH),  $k_{\text{relax}}$  are substantially larger and in these cases protein dynamics rather than electron tunneling represents the rate-limiting step.<sup>30</sup>

Whereas for the Ag-(C<sub>11</sub>-NH<sub>2</sub>)-Au-(C<sub>x</sub>-COOH) hybrid electrodes, ET kinetics can be largely understood in terms of the interplay between tunneling through the inner and the outer SAM, surprising kinetic data were obtained for hybrid electrodes in which the thickness of the inner SAM was varied (C<sub>y</sub>-NH<sub>2</sub> with  $x = 6, 8, 11$ ) without changing the outer SAM (C<sub>10</sub>-COOH). Here we note a steady decrease of  $k_{\text{relax}}$  with 49, 29, and  $4 \text{ s}^{-1}$  for  $y = 11, 8,$  and  $6,$  respectively (Table 1). One possible explanation may be that during the incubation of the Ag-(C<sub>y</sub>-NH<sub>2</sub>) electrode with AuCl<sub>4</sub> and the subsequent electrochemical reduction, impurities are introduced into the SAM which influence the electron transfer across the SAM.<sup>33</sup>

A possible damage of the spacer SAM could already occur during the Au reduction due to the very negative potentials and the presence of Cl<sup>-</sup> ions. This hypothesis is supported by the fact that the rate for Ag-(C<sub>6</sub>-NH<sub>2</sub>)-Au-(C<sub>10</sub>-COOH) could significantly be increased up to  $k = 35 \text{ s}^{-1}$  if during the Au reduction phosphate buffer was used instead of KCl and the reduction potential was changed to  $-0.1 \text{ V}$ . Both parameters have a direct influence on the quality and protonation state of the C<sub>y</sub>-NH<sub>2</sub> SAM but will not alter the tunneling distance between the Au-islands and the Ag electrode.

## Experimental

### Chemicals

11-Mercaptoundecanoic acid (C<sub>10</sub>-COOH), 16-mercaptohexadecanoic acid (C<sub>15</sub>-COOH), sodium tetrachloroaurate (III) dihydrate (Sigma Aldrich), 6-mercaptohexanoic acid (C<sub>5</sub>-COOH), 6-amino-1-hexanethiol hydrochloride (C<sub>6</sub>-NH<sub>2</sub>), 8-amino-1-octanethiol hydrochloride (C<sub>8</sub>-NH<sub>2</sub>) and 11-amino-1-undecanethiol hydrochloride (C<sub>11</sub>-NH<sub>2</sub>) (Dojindo) were used without further purification. Horse heart cytochrome c and yeast iso-1 cytochrome c from Sigma were purified by high performance liquid chromatography. The water used in all experiments was purified by a Millipore system and its resistivity was higher than  $18 \text{ M}\Omega \text{ cm}$ .

### Raman spectroscopic and electrochemical measurements

SER spectra of 4-aminothiophenol-coated Au nanoflakes were obtained with 1064-nm excitation using FT-Raman spectrometer (Bruker RFS 100/S). For SERR experiments with Cyt-c (413-nm excitation), a confocal Raman spectrometer (LabRam HR-800, Jobin Yvon) was used. Details of the experimental set-up including the spectroelectrochemical cell

are given elsewhere.<sup>34</sup> SERR spectra of Cyt-c were acquired with a spectral resolution of  $2 \text{ cm}^{-1}$  and an increment per data point of  $0.57 \text{ cm}^{-1}$  using a laser power  $1.5 \text{ mW}$ . The accumulation times were between 1 and 3 s. For time-resolved (TR) SERR experiments, potential jumps of variable duration and size were applied. The relaxation process of the surface bound protein was probed by measuring the SERR spectra at variable delay time ( $\delta'$ ) after each jump. Synchronization of potential jumps and measuring laser pulses was achieved with a homemade four-channel pulse-delay generator. Short laser pulses of a duration  $\Delta t$  were generated by passing the continuous wave laser beam through two consecutive laser intensity modulators (Linos). The time-dependent spectroscopic results are displayed in the following as a function of the delay time ( $\delta$ ) defined as  $\delta = \delta' + \Delta t/2$ . The working electrode was rotated at *ca.* 5 Hz to avoid laser induced sample degradation. After polynomial baseline subtraction, the measured SERR spectra were treated with homemade component analysis software.

The potential of zero-charge was determined by impedance spectroscopy as described previously.<sup>35</sup> All potentials cited in this work refer to the Ag/AgCl (3M KCl) electrode.

## Conclusions

Ag-(C<sub>y</sub>-NH<sub>2</sub>)-Au-(C<sub>x</sub>-COOH) devices are suitable substrates for SE(R)R spectroscopy, exhibiting enhancement factors and profiles that are quite comparable to Ag electrodes. Thus, it can be preferentially employed for excitation lines below 550 nm. For excitation at longer wavelengths, a distinctly increase of the Au film thickness is required which, however, would drastically lower the enhancement below 550 nm. The enhancement can be further increased by replacing a planar surface by a nanoflake-like support.

The electrodes represent an excellent platform for analysing interfacial electron transfer processes. The multilayer structure of metals and organic films causes only small potential drops. Electron transfer across these junctions is limited by electron tunneling through the organic films, specifically the outer SAM that serves for protein binding.

## Acknowledgements

The authors would like to thank Tillmann Utesch for support in preparing graphics and Diego Millo for fruitful discussions. Financial support was given by the DFG (SfB 448), the Fonds der Chemischen Industrie (M.S and I.M.W.), and the National Science Foundation of China (J.J.F.; NSFC No. 20905021).

## Notes and references

- 1 I. Willner and E. Katz, *Bioelectronics*, Wiley-VCH, Weinheim, 2005.
- 2 D. Chen, G. Wang and J. H. Li, *J. Phys. Chem. C*, 2007, **111**, 2351.
- 3 I. Willner and E. Katz, *Angew. Chem., Int. Ed.*, 2000, **39**, 1180.
- 4 M. J. Tarlov and E. F. Bowden, *J. Am. Chem. Soc.*, 1991, **113**, 1847.
- 5 D. H. Murgida and P. Hildebrandt, *Phys. Chem. Chem. Phys.*, 2005, **7**, 3773.
- 6 Y. Lvov, K. Ariga, I. Ichinose and T. Kunitake, *J. Am. Chem. Soc.*, 1995, **117**, 6117.

- 7 M. Gerard, A. Chaubey and B. D. Malhotra, *Biosens. Bioelectron.*, 2002, **17**, 345.
- 8 F. A. Armstrong, H. A. O. Hill and N. J. Walton, *Acc. Chem. Res.*, 1988, **21**, 407.
- 9 C. Léger and P. Bertrand, *Chem. Rev.*, 2008, **108**, 2379.
- 10 F. A. Armstrong and G. S. Wilson, *Electrochim. Acta*, 2000, **45**, 2623.
- 11 D. L. Jeanmaire and R. P. Vanduyne, *J. Electroanal. Chem.*, 1977, **84**, 1.
- 12 K. Kneipp, M. Moskovits and H. Kneipp, *Surface-enhanced Raman Scattering*, Springer, Berlin, 2006.
- 13 J. Siebert and P. Hildebrandt, *Vibrational Spectroscopy in Life Science*, Wiley-VCH, Weinheim, 2008.
- 14 D. H. Murgida and P. Hildebrandt, *Angew. Chem., Int. Ed.*, 2001, **40**, 728.
- 15 J. A. Sánchez-Gil and J. V. García-Ramos, *J. Chem. Phys.*, 1998, **108**, 317.
- 16 J. J. Feng, U. Gernert, M. Sezer, U. Kuhlmann, D. H. Murgida, C. David, M. Richter, A. Knorr, P. Hildebrandt and I. M. Weidinger, *Nano Lett.*, 2009, **9**, 298.
- 17 D. H. Murgida and P. Hildebrandt, *J. Phys. Chem. B*, 2001, **105**, 1578.
- 18 H. A. Heering, F. G. M. Wiertz, C. Dekker and S. de Vries, *J. Am. Chem. Soc.*, 2004, **126**, 11103.
- 19 Y. F. Shen, J. B. Wang, U. Kuhlmann, P. Hildebrandt, K. Ariga, H. Mohwald, D. G. Kurth and T. Nakanishi, *Chem.–Eur. J.*, 2009, **15**, 2763.
- 20 T. Nakanishi, N. Miyashita, T. Michinobu, Y. Wakayama, T. Tsuruoka, K. Ariga and D. G. Kurth, *J. Am. Chem. Soc.*, 2006, **128**, 6328.
- 21 L. D. Qin, S. L. Zou, C. Xue, A. Atkinson, G. C. Schatz and C. A. Mirkin, *Proc. Natl. Acad. Sci. U. S. A.*, 2006, **103**(36), 13300.
- 22 L. He, E. A. Smith, M. J. Natan and C. D. Keating, *J. Phys. Chem. B*, 2004, **108**(30), 10973.
- 23 C. David, M. Richter, A. Knorr, I. M. Weidinger and P. Hildebrandt, *J. Chem. Phys.*, 2010, **132**, 024712.
- 24 P. Hildebrandt and M. Stockburger, *J. Phys. Chem.*, 1986, **90**, 6017.
- 25 G. Compagnini, C. Galati and S. Pignataro, *Phys. Chem. Chem. Phys.*, 1999, **1**, 2351.
- 26 P. Ramirez, R. Andreu, A. Cuesta, C. J. Calzado and J. J. Calvente, *Anal. Chem.*, 2007, **79**, 6473.
- 27 S. Oellerich, H. Wackerbarth and P. Hildebrandt, *J. Phys. Chem. B*, 2002, **106**, 6566.
- 28 H. Wackerbarth and P. Hildebrandt, *ChemPhysChem*, 2003, **4**, 714.
- 29 L. Rivas, D. H. Murgida and P. Hildebrandt, *J. Phys. Chem. B*, 2002, **106**, 4823.
- 30 A. Kranich, H. K. Ly, P. Hildebrandt and D. H. Murgida, *J. Am. Chem. Soc.*, 2008, **130**, 9844.
- 31 D. H. Murgida and P. Hildebrandt, *J. Am. Chem. Soc.*, 2001, **123**, 4062.
- 32 N. Wisitruangsakul, I. Zebger, H. K. Ly, D. H. Murgida, S. Ekgasit and P. Hildebrandt, *Phys. Chem. Chem. Phys.*, 2008, **10**, 5276.
- 33 R. E. Holmlin, R. Haag, M. L. Chabinyc, R. F. Ismagilov, A. E. Cohen, A. Terfort, M. A. Rampi and G. M. Whitesides, *J. Am. Chem. Soc.*, 2001, **123**, 5075.
- 34 H. Wackerbarth, U. Klar, W. Gunther and P. Hildebrandt, *Appl. Spectrosc.*, 1999, **53**, 283.
- 35 J. J. Feng, D. H. Murgida, U. Kuhlmann, T. Utesch, M. A. Mroginski, P. Hildebrandt and I. M. Weidinger, *J. Phys. Chem. B*, 2008, **112**, 15202.

## 6 Human Sulphite Oxidase

Sulphite oxidases constitute one of three enzyme families that contain a molybdopterin cofactor (moco) (figure 6) [71]. The others are the xanthine oxidase and dimethyl sulphoxide reductase families. Moco containing enzymes are all oxidoreductases, however, they differ in their specific target molecules and the direction of their change in oxidation state. Sulphite oxidases catalyse the oxidation of sulphite to sulphate. The three enzyme families differ in the coordination pattern of the central molybdenum atom. In dimethyl sulphoxide reductases, the molybdenum is coordinated by four thiolates of two pterin molecules and additional ligands. In contrast, in sulphate oxidases and xanthine oxidases the molybdenum is coordinated by two thiolates of only one pterin and additional ligands, which are different for the different families. The chemical structure of the cofactor in sulphite oxidases is depicted in figure 6:

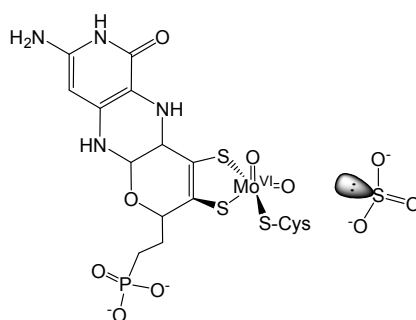


Figure 6: Chemical structure of sulphite (right) and the molybdopterin cofactor (left) of sulphite oxidases [202].

Sulphite oxidases are essential for the sulphur metabolism of many organisms. They catalyse the terminal reaction in the oxidative degradation pathway of sulphur containing amino acids cysteine and methionine [71-74]. Sulphite oxidases have attracted attention of medical research since genetic human sulphite oxidase deficiency, which can occur due to point mutations, results in profound defects, severe neonatal neurological problems and early death, with no effective therapies known [73-75]. These severe consequences occur when sulphite can not be oxidised because sulphite may disturb the tertiary structure of proteins by sulfitolysis of disulphide bridges in the protein [76]. Research on sulphite oxidases was also motivated by the fact that sulphites are widely used in food and pharmaceutical industries. They reduce or prevent microbial spoilage and prevent oxidation of foods [85-87]. However, they may cause allergic reactions and trigger asthma and many other diseases [88-89]. Hence, there is a demand for versatile and low cost quantitative sulphite sensor devices. A promising approach in this respect is the development of enzyme based bioelectronic sensor devices that take advantage of the sulphite selectivity and sensitivity of sulphite oxidases upon immobilisation and electronic coupling to conducting support materials [15, 78, 79].

## 6.1 Structure of Human Sulphite Oxidase

Human sulphite oxidase (hSO) is a homo-dimeric anionic enzyme of 110 kDa and is located in the intermembrane space of human mitochondria. With 68 % sequence identity, the structure and functioning of hSO is similar to its analogue from chicken liver (cISO), for which a crystal structure at 1.9 Å has been reported [73]. Each monomer consists of three subdomains and a loop region, which connects the relatively small cytochrome *b5* (Cyt *b5*) domain with the large moco harbouring domain. The loop region is poorly resolved in the crystal structure of cISO, pointing towards a high flexibility of this region. The third domain is the dimerisation domain at which the protein dimerises in a head-to-head arrangement. The dimer is formed via numerous hydrogen bonds and salt bridges between the dimerisation domains of the monomers.

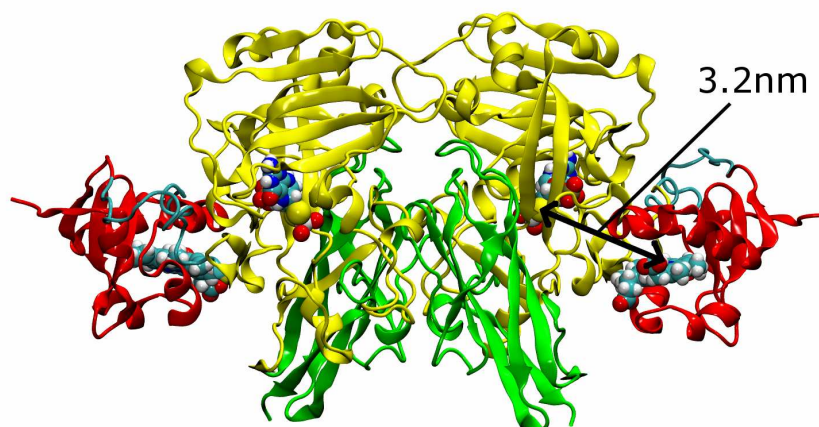


Figure 6.1: Homology structure of human sulphite oxidase (hSO) on the basis of the crystal structure of chicken liver oxidase (PDB: 1sox) and the hSO amino acid sequence (UniProtKB database entry P51687). The cytochrome *b5* (Cyt *b5*) subunit is coloured in red, molybdopterin harbouring (moco) subunit in yellow and the dimerisation domain in green. The loop region connecting the Cyt *b5* and the moco domain is coloured in cyan. The protein backbone structure is depicted in new cartoon representation and the molybdopterin and heme cofactors are depicted in van der Waals representation [77].

The distance between the molybdenum and iron metal centers of the cofactors in the hSO structure model derived from the crystal structure of cISO is 32 Å. The moco domain is deeply buried in the protein matrix of the large moco domain, whereas the heme cofactor is located close to the surface of the Cyt *b5* domain.

## 6.2 Catalytic Mechanism of Sulphite Oxidases

The mechanism of catalytic sulphite oxidation by sulphite oxidases has been investigated in detail and is depicted in figure 6.2 [13, 80 – 84, 202]. It was shown that the catalytic reaction

takes place at the molybdenum atom. Sulphite binds to an oxygen atom of the moco. The molybdenum takes up two electrons and is reduced from state +VI to +IV upon substrate binding [202]. Subsequently, the oxygen atom is transferred from the moco to the sulphite and hydroxide from a water molecule, which is involved in the catalytic reaction, binds to the molybdenum. The initial coordination and oxidation state at the molybdenum atom (figure 6) is recovered by proton release and two consecutive electron transfer processes via the Cyt *b5* domain to an external redox partner, which is cytochrome *c*. Thus, catalytic sulphite oxidation also provides electrons to the respiratory chain.

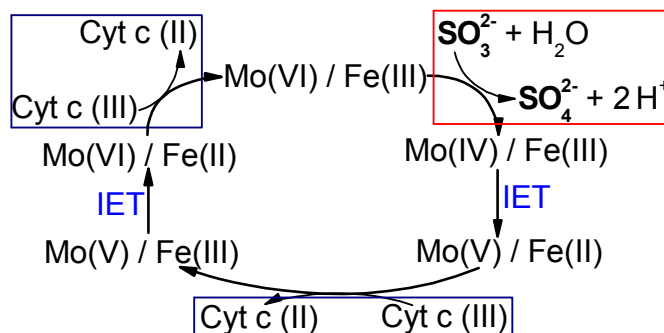


Figure 6.2: Mechanism of catalytic sulphite oxidation. IET – intramolecular electron transfer.

With the metal to metal distance of 32 Å in the homology structure, the intramolecular electron transfer step (IET) from the moco to the Cyt *b5* domain would be very inefficient [49]. The crystal structure, however, represents a static picture. It was shown that the position of the heme with respect to the moco is flexible. The flexibility is provided by the loop region and enables the heme to approach the moco thereby facilitating IET. The reduced Cyt *b5* is then removed again from the moco domain and reacts with the external redox partner. If immobilised on electrodes, cytochrome *c* can be replaced by the electrode as the external redox partner [5, 14, 15].

It was found that the performance of sulphite oxidases strongly depend on external conditions, such as the pH, ionic strength and composition of the buffer solution [13, 82-84]. It is also reported that the catalytic activity is around one order of magnitude lower in the immobilised state with respect to the value in solution [5, 13-15, 82]. The motivation of the combined SERR spectroscopic and electrochemical study of hSO (chapter 6.3) was to gain insight into the molecular processes that are responsible for these observations and to possibly improve the performance of immobilised hSO.



### **6.3 Redox properties and catalytic activity of surface-bound human sulfite oxidase studied by a combined surface enhanced resonance Raman spectroscopic and electrochemical approach**

*Murat Sezer,<sup>a</sup> Roberto Spricigo,<sup>b</sup> Tillmann Utesch,<sup>a</sup> Diego Millo,<sup>a</sup> Silke Leimkühler,<sup>b</sup> Maria A. Mroginski,<sup>a</sup> Ulla Wollenberger,<sup>b</sup> Peter Hildebrandt<sup>a</sup> and Inez M. Weidinger<sup>\*a</sup>*

<sup>a</sup> Technische Universität Berlin, Institut für Chemie, Sekr. PC14, Straße des 17. Juni 135, D-10623 Berlin, Germany.

\*correspondence to E-mail: i.weidinger@mailbox.tu-berlin.de; Fax: +49 3031421122; Tel: +49 3031422780

<sup>b</sup> Institut für Biochemie und Biologie, Universität Potsdam, Karl-Liebknecht Straße 24-25, H. 25, Golm, D-14476, Germany.

Published in *Phys. Chem. Chem. Phys.*, 2010, **12**, 7894 – 7903.

Reproduced with permission of the PCCP Owner Societies.



# Redox properties and catalytic activity of surface-bound human sulfite oxidase studied by a combined surface enhanced resonance Raman spectroscopic and electrochemical approach†

Murat Sezer,<sup>a</sup> Roberto Spricigo,<sup>b</sup> Tillmann Utesch,<sup>a</sup> Diego Millo,<sup>a</sup> Silke Leimkuehler,<sup>b</sup> Maria A. Mroginski,<sup>a</sup> Ulla Wollenberger,<sup>b</sup> Peter Hildebrandt<sup>a</sup> and Inez M. Weidinger\*<sup>a</sup>

Received 23rd December 2009, Accepted 28th April 2010

First published as an Advance Article on the web 26th May 2010

DOI: 10.1039/b927226g

Human sulfite oxidase (hSO) was immobilised on SAM-coated silver electrodes under preservation of the native heme pocket structure of the cytochrome *b5* (Cyt *b5*) domain and the functionality of the enzyme. The redox properties and catalytic activity of the entire enzyme were studied by surface enhanced resonance Raman (SERR) spectroscopy and cyclic voltammetry (CV) and compared to the *isolated* heme domain when possible. It is shown that heterogeneous electron transfer and catalytic activity of hSO sensitively depend on the local environment of the enzyme. Increasing the ionic strength of the buffer solution leads to an increase of the heterogeneous electron transfer rate from 17 s<sup>-1</sup> to 440 s<sup>-1</sup> for hSO as determined by SERR spectroscopy. CV measurements demonstrate an increase of the apparent turnover rate for the immobilised hSO from 0.85 s<sup>-1</sup> in 100 mM buffer to 5.26 s<sup>-1</sup> in 750 mM buffer. We suggest that both effects originate from the increased mobility of the surface-bound enzyme with increasing ionic strength. In agreement with surface potential calculations we propose that at high ionic strength the enzyme is immobilised *via* the dimerisation domain to the SAM surface. The flexible loop region connecting the Moco and the Cyt *b5* domain allows alternating contact with the Moco interaction site and the SAM surface, thereby promoting the sequential intramolecular and heterogeneous electron transfer from Moco *via* Cyt *b5* to the electrode. At lower ionic strength, the contact time of the Cyt *b5* domain with the SAM surface is longer, corresponding to a slower overall electron transfer process.

## Introduction

Human sulfite oxidase (hSO) is a 110 kDa enzyme in the intermembrane space of mitochondria. It catalyses the oxidation of sulfite to sulfate, which is the terminal reaction in the oxidative degradation of the sulfur-containing amino acids cysteine and methionine.<sup>1</sup> The structure of hSO is likely to be the same as its analogue from chicken liver, for which a crystal structure at 1.9 Å has been determined.<sup>2</sup> This protein is a homodimer and each monomer contains an N-terminal cytochrome *b5* (Cyt *b5*) domain, a large central domain harboring the molybdenum cofactor (Moco), and a large C-terminal dimerisation domain.<sup>2,3</sup> The Moco and Cyt *b5* domains are connected by a loop region, which provides high flexibility

between them. Catalytic sulfite oxidation takes place at the Moco domain followed by a fast intramolecular electron transfer to the heme center of the Cyt *b5* domain. The electron is subsequently transferred to an external redox partner (Fig. 1).<sup>1</sup>

When the enzyme is immobilised on a conducting support the natural external redox partner cytochrome *c* can be replaced by an electrode, which allows triggering the catalytic cycle *via* control of the potential applied at the electrode. Electrochemical studies of hSO on metal electrodes in single- and multilayer systems have shown that catalytic activity can be preserved in the immobilised state pointing to possible applications of this system as a sensitive sulfite biosensor.<sup>4-6</sup>

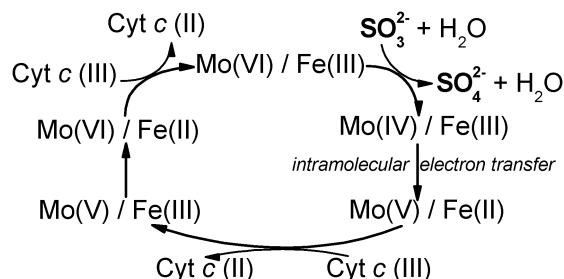


Fig. 1 Scheme of the catalytic sulfite oxidation by human sulfite oxidase.

<sup>a</sup> Technische Universität Berlin, Institut für Chemie, Sekr. PC 14, Straße des 17. Juni 135, D-10623 Berlin, Germany.

E-mail: i.weidinger@mailbox.tu-berlin.de

<sup>b</sup> Institut für Biochemie und Biologie, Universität Potsdam, Karl-Liebknecht Straße 24-25, H. 25, Golm, D-14476, Germany

† Electronic supplementary information (ESI) available: Absorption spectra of hSO and the *isolated* Cyt *b5* domain, desorption of the *isolated* Cyt *b5* domain at 50 mM buffer concentration, superposition of crystal structure of chicken liver SO and homology model of hSO, non-turnover and turnover CV signal of hSO, and effect of substrate concentration and pH on the catalytic current. See DOI: 10.1039/b927226g

For chicken liver SO it was shown that the catalytic performance of the enzyme is controlled by external parameters such as pH, ionic strength, and composition of the buffer solution.<sup>7–9</sup> Catalytic turnover rates  $k_{\text{cat}}$  of *ca.* 100 s<sup>-1</sup> are reported for the enzyme in solution,<sup>9</sup> whereas in the immobilised state values of only 2–20 s<sup>-1</sup> have been obtained.<sup>6,10</sup> Therefore, it has been suggested that a large fraction of the enzyme loses its catalytic activity but remains electroactive upon adsorption.<sup>10</sup>

In this work, we have applied a combined SERR spectroscopic and electrochemical approach to investigate electron transfer properties and catalytic activity of the surface-bound hSO. For this purpose SERR spectroscopy is an appropriate and powerful tool, since it allows probing the vibrational spectra selectively of the heme center in the Cyt *b5* domain of the immobilised protein.<sup>11–13</sup> In addition to electrochemical techniques, SERR spectroscopic investigation can also provide information on enzyme denaturation, desorption or catalytic inactivation. The high sensitivity and selective structural information afforded by SERR spectroscopy may provide deeper insight into the mechanism and performance of surface-bound hSO. In order to understand the adsorption properties of hSO on surfaces, these experimental spectroscopic and electrochemical studies are complemented by theoretical calculations of the dipole moment and the surface potential distribution of hSO.

Electrochemical and SERR spectroscopic experiments have been performed on nanostructured Ag electrodes to guarantee the best possible comparability of the results obtained by both techniques. Furthermore, these results can then be related to the kinetics of the enzyme on smooth gold substrates determined previously<sup>4–6,10</sup> and thus provide insight into the role of electrode material and surface morphology on the enzymatic processes.

## Materials and methods

### Materials

8-Amino-octanethiol hydrochloride [in the following denoted as C8(NH<sub>2</sub>)] and 11-aminoundecanethiol hydrochloride [C11(NH<sub>2</sub>)] were purchased from Dojindo. 6-Mercaptohexanol [C6(OH)] and 11-mercaptoundecanol [C11(OH)] were provided by Aldrich. His-tagged human SO was purified after expression in *E. coli* TP1000 cells containing the plasmid pTG718 as described previously.<sup>14</sup> To obtain the heme domain, a tryptic cleavage was applied (100 μg of trypsin for each mg of SO). The two proteins were incubated for 18 h at 4 °C. The two parts were afterwards separated by size exclusion chromatography. In the following we denote the heme domain contained in the integral enzyme as Cyt *b5* domain whereas the isolated heme domain is explicitly referred to as *isolated* Cyt *b5* domain. Sodium sulfite (Na<sub>2</sub>SO<sub>4</sub>) was purchased from Merck and used as substrate for catalytic reactions. The water used in all experiments was purified by a Millipore system and its resistance was higher than 18 MΩ.

### Protein immobilisation

Ag ring electrodes were mechanically polished, subjected to an electrode potential of -2 V for 40 s in 0.1 M KCl and

subsequently roughened electrochemically in the same electrolyte solution. All potentials reported here refer to a 3 M KCl Ag/AgCl reference electrode from World Precision Instruments (+204 mV *versus* NHE). The roughening consisted of three oxidation–reduction cycles at +0.3 V and -0.3 V, respectively, followed by an additional reduction step at -0.5 V for 5 min. The nanostructured Ag electrodes were immersed for 24 h into solutions of ω-substituted mercaptanes to form a self-assembled monolayer (SAM). For pure SAMs, 1 mM of C8(NH<sub>2</sub>) or C11(NH<sub>2</sub>) has been used. For the mixed SAMs, 2 mM C8(NH<sub>2</sub>) and C6(OH) at a ratio of 1 : 1 M/M, 2 mM C11(NH<sub>2</sub>) and C11(OH) at a ratio of 1 : 1 M/M, and 4 mM C8(NH<sub>2</sub>) and C6(OH) at a ratio of 1 : 3 M/M have been employed in a water/ethanol solution (1 : 4 v/v).<sup>15</sup> The presence of water in the SAM-solution favours the protonation of the amino-groups, which may otherwise interact with the electrode.<sup>16</sup> Thus, water ensures the proper binding of amino-alkanethiols to the Ag electrode *via* the sulfur atom.

Electrostatic immobilisation of the *isolated* Cyt *b5* domain and hSO was achieved within 2–4 h by immersion of the SAM-coated rough Ag electrodes into a 1 mM Tris-acetate buffer solution at pH 8.5 containing ~0.2 μM of the respective protein. Subsequently, the electrode was transferred to the buffer solution used for the SERR and electrochemical experiments. The pH of the buffer was adjusted by acetic acid to avoid possible effects of small anions on the intramolecular electron transfer.<sup>4,9</sup>

### Spectroscopic and electrochemical measurements

For RR experiments a rotating cuvette was used with a protein concentration of ~30 μM in 5 mM buffer solution at pH 8.5.

SERR and electrochemical measurements were performed using homemade spectro-electrochemical cells with a volume of about 10 mL containing the modified Ag ring as the working electrode, a 3 M KCl Ag/AgCl reference electrode and a platinum counter electrode.

Cyclic voltammetric experiments were performed with a CH instrument 660 C (Austin, USA).

SERR and RR spectra of hSO were measured using a confocal Raman spectrometer (LabRam HR-800, Jobin Yvon) with a spectral resolution of 2 cm<sup>-1</sup> and an increment per data point of 0.57 cm<sup>-1</sup>. The 413 nm laser line of a Coherent Innova 300 c Krypton cw-laser was used for excitation. The laser power on the sample was 1.9 mW for RR and 1.0 mW for SERR experiments, respectively. The laser beam was focussed by a Nikon 20× objective with a working distance of 20.5 mm and a numeric aperture of 0.35.

Accumulation times were 40 s and 1–3 s for RR and SERR spectra, respectively. For time-resolved SERR experiments, potential jumps of variable duration and size were applied on the working electrode as described previously.<sup>11,17,18</sup> The working electrode was rotated to avoid laser induced sample degradation. After polynomial baseline subtraction, the measured SERR spectra were treated by homemade component analysis software.

### Molecular modelling and theoretical calculations

The sequence identity between hSO and chicken liver sulfite oxidase is very high (67%), suggesting a similar three dimensional

(3D) structure of these two enzymes. Thus, a homology model for hSO was constructed using the chicken liver SO as template (PDB: 1SOX)<sup>2</sup> and the amino acid sequence of hSO contained in the UniProtKB database (entry P51687).<sup>19</sup> Those residues located in the loop region connecting the cytochrome *b5* and Moco domain which are missing in the template structure (A89 in chain A and E86, A87, P88, A89, A90 and P91 in chain B) were added with the CHARMM V32b<sup>20</sup> code. In the model building procedure, the hSO N-terminal transit peptides of 81 amino acids each, which are lacking in the template structure, were removed. During the modelling, the heme and molybdopterin cofactors and their linked atoms were restrained to maintain the cofactor environment of the template. The flexible loops connecting the Cyt *b5* and Moco domains were refined in order to correct for the high structural uncertainty resulting from the lack of a template in these regions. The optimisation and refinement of the 3D structure for hSO was carried out according to the dope score in MODELLER 9.5.<sup>21</sup> Validation of the predicted structure was done by calculating the root-mean-square deviation (rmsd) with respect to the template structure and by analysing the corresponding Ramachandran plots. In order to carry out dipole moment and electrostatic potential calculations with the homology model of hSO, hydrogen atoms were incorporated with CHARMM V32b.<sup>20</sup> The amino acid side chains were protonated according to pH 7 and the protonation configuration of the histidine residues were adjusted to their environment.

Dipole moment calculations were performed with VMD 1.8.6.<sup>22</sup> Partial charges of the apoprotein and the heme cofactor were taken from the CHARMM 22 force field<sup>23</sup> whereas the partial charges of the Moco cofactors were derived by quantum mechanical calculations.<sup>24</sup> The electrostatic potential of the homodimeric enzyme was calculated with the APBS program<sup>25</sup> using the PDB2PQR tool.<sup>26</sup>

## Results

### Immobilisation and characterisation of hSO

In the visible region, absorption spectra of hSO measured in solution display the characteristic electronic transitions of the heme chromophore and are found to be identical to those of the *isolated* Cyt *b5* domain (ESI<sup>†</sup>, Fig. S1), indicating that electronic transitions of the Moco do not contribute to the spectra in this region. Correspondingly, also the RR spectra of hSO (Fig. 2A) measured with 413 nm excitation exclusively display the vibrational bands of the heme *b* group and are indistinguishable from the RR spectra of the *isolated* Cyt *b5*. The spectra show the characteristic vibrational signature of a six-coordinated low-spin (6cLS) heme in both the ferric and the ferrous form, as expected for a *b*-type heme with bis-His ligation. A minor contribution from a five-coordinated high spin species might be present in the reduced form, as indicated by the weak shoulder at 1352 cm<sup>-1</sup> of the prominent  $\nu_4$  mode at 1360 cm<sup>-1</sup> (6cLS) (Fig. 2C). This finding may be rationalised in terms of the weaker binding affinity of a second His ligand towards the ferrous as compared to the ferric heme.<sup>27</sup>

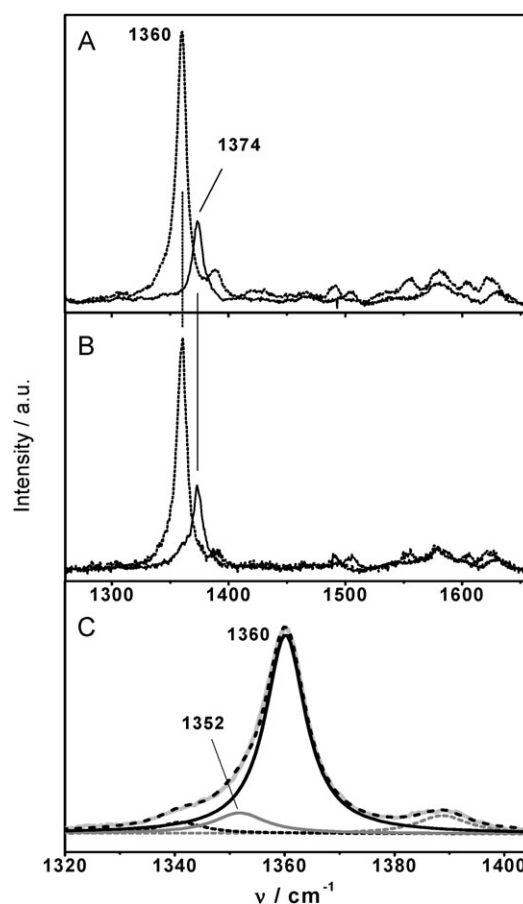


**Fig. 2** (A) RR and (B) SERR spectra of hSO in Tris-acetate buffer solution at pH 7.4. Solid lines represent the experimental spectra of the oxidised species (A: solution at aerobic atmosphere; B: at  $E = 0.15$  V). Dashed lines represent the spectra of the reduced species (A: after addition of an excess concentration of sodium dithionite; B:  $E = -0.3$  V). In B, hSO is immobilised on a rough Ag electrode coated with SAM of C8(NH<sub>2</sub>)/C6(OH) (1 : 3 M/M). (C) Component analysis in the  $\nu_4$ -region of the RR spectrum of the reduced species. The solid light grey, solid black, solid dark grey, and dashed black lines represent the experimental spectrum, the component spectrum of the 6cLS species, the component spectrum of 5cHS species, and the sum of the component spectra, respectively.

Unlike the *isolated* Cyt *b5* domain, hSO could be completely reduced in 150 mM Tris-acetate buffer solution at pH 7.4 by adding 1 mM sulfite to the sample. This result is a clear indication for the integrity and catalytic activity of hSO. However, in 5 mM Tris-acetate buffer solution at pH 8.5, only a partial hSO reduction is observed. This finding seems to be contradictive to previous results that show a decrease in catalytic activity with increasing concentration especially of certain anions such as sulfate or phosphate.<sup>7–9</sup> However, no data have been reported so far for buffer concentrations as low as 5 mM.

SERR spectra of immobilised hSO (Fig. 2B) reveal no difference in band position compared to the RR spectra. Accordingly, it is concluded that no changes of the heme pocket structure have occurred upon immobilisation.

### Heterogeneous electron transfer

Initial SERR spectroscopic and electrochemical experiments aimed at finding optimum conditions for effective heterogeneous

**Table 1** Redox parameters of hSO and *isolated* Cyt *b5* immobilised on Ag electrodes coated with different SAMs in the presence of 5 mM Tris-acetate buffer at pH 8.5. The data were determined by SERR spectroscopy

Electrode coating	Redox parameters <sup>a</sup> for hSO (Cyt <i>b5</i> )			Redox parameters <sup>a</sup> for <i>isolated</i> Cyt <i>b5</i>		
	$E^0/\text{mV}$	$n$	$k_s/\text{s}^{-1}$	$E^0/\text{mV}$	$n$	$k_s/\text{s}^{-1}$
C8(NH <sub>2</sub> )	-154	0.4	17	-122	0.6	10
C8(NH <sub>2</sub> )/C6(OH) (1 : 1)	-140	0.5	n.d. <sup>b</sup>	-120	0.5	n.d.
C8(NH <sub>2</sub> )/C6(OH) (1 : 3)	-100	0.7	15	-146 <sup>c</sup>	0.3	n.d.
C11(NH <sub>2</sub> )	-232	0.3	n.d.	-195	0.2	n.d.

<sup>a</sup> The approximate error for  $E^0$ ,  $n$ , and  $k_s$  are  $\pm 10$  mV,  $\pm 0.05$ , and  $\pm 10\%$ , respectively. <sup>b</sup> n.d., not determined. <sup>c</sup> Values were determined for 50 mM Tris-acetate buffer and pH 7.35.

electron transfer between the Cyt *b5* domain of the immobilised enzyme and the electrode. The conditions were optimised for hSO and the results were compared with those for the *isolated* Cyt *b5* domain where possible. Besides different SAM-compositions, the effect of different buffer concentration and pH was tested.

In each case, potential-dependent SERR spectra revealed that the immobilised enzyme was fully electrochemically active. The quantitative analysis of the spectra allowed determining the relative spectral contributions of the ferric and ferrous species as a function of the electrode potential *via* component analysis.<sup>12,28</sup> These spectral contributions were then converted into relative concentrations as described previously,<sup>12,28</sup> which give then, according to the Nernst equation, values for the formal potential  $E^0$  and apparent number of transferred electrons  $n$ . The results for  $E^0$  and  $n$  under different conditions are summarised in Table 1. Typical plots for a stationary potentiometric titration are shown in Fig. 3A.

For an ideal electronic communication between the Cyt *b5* domain and the electrode the value for  $n$  is expected to be equal to one. The best results in this respect are obtained for the *isolated* Cyt *b5* domain by using an C8(NH<sub>2</sub>)-SAM only and low ionic strength buffer at pH 8.5. Using a mixed SAM of C8(NH<sub>2</sub>)/C6(OH) (1 : 3 M/M) and 50 mM Tris-acetate buffer solution at pH 7.4 led to low values of  $n$  and desorption of the protein judged from SERRS intensity and CV measurements (ESI†, Fig. S2). Remarkably, this was not the case for hSO. Here only a slight reversible decrease in SERRS intensity of the heme was observed when the enzyme was exposed to higher ionic strength buffer solution. This result implies that the integral enzyme does not desorb at high ionic strength. Moreover, the values of  $n$  are much closer to one compared to those in lower ionic strength buffer solutions. Measurements of hSO could be carried out in Tris-acetate buffer solutions up to 1.5 M, *i.e.* at a much higher ionic strength than used in the experiments by Ferapontova *et al.*, who observed irreversible hSO desorption already at 300 mM Tris buffer solution.<sup>6</sup>

The formal potential  $E^0$  of the Cyt *b5* domain of chicken liver sulfate oxidase in solution was determined to be  $-128$  mV.<sup>29</sup> With respect to this value we observed a positive shift in formal potential of *ca.* 80 mV upon electrostatic adsorption of the enzyme at low ionic strength (5 mM buffer concentration). However, above a buffer concentration of 150 mM this shift is distinctly smaller and also independent of the ionic strength (Table 2). The redox potentials of the *isolated* Cyt *b5* domain determined for different SAMs at pH 8.5 were generally less negative by *ca.* 20 mV as compared to hSO.

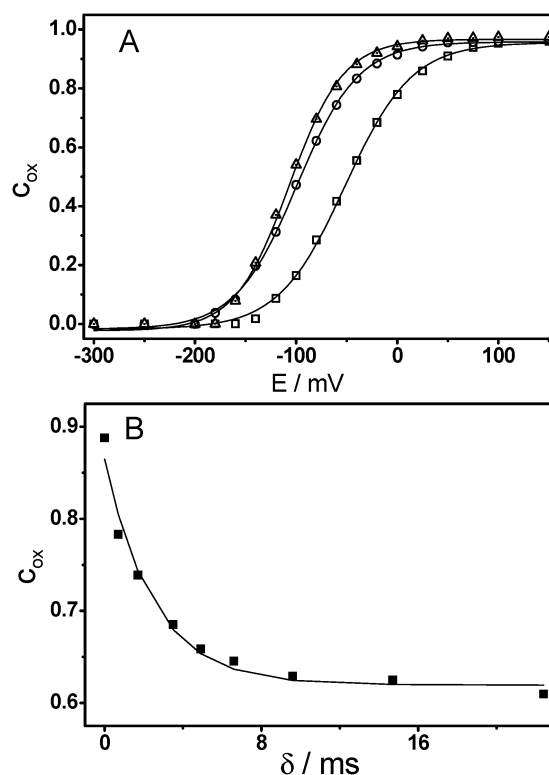


**Fig. 3** hSO immobilised on 1 : 3 M/M C8(NH<sub>2</sub>)/C6(OH) SAM in Tris-acetate buffer solutions at pH 7.4. (A) Relative concentrations of the ferric Cyt *b5* domain as a function of electrode potential in 5 mM (hollow squares), 200 mM (hollow circles), and 750 mM (hollow triangles) buffer. Sigmoidal functions have been fitted to the data. (B) Time-dependent changes of the relative concentration of the ferric Cyt *b5* domain in 750 mM buffer, following a potential jump from  $-0.01$  V to  $-0.11$  V. A mono-exponential function (solid line) has been fitted to the data (filled squares). All experimental data were determined by SERR spectroscopy.

The formal heterogeneous electron transfer rate constant ( $k_s$ ) of heme *b5* of the integral hSO was found to display a dramatic ionic strength dependence but appears to be largely unaffected by pH (7.4 and 8.5) and mixture of uncharged mercaptanes [C6(OH)] to the C8(NH<sub>2</sub>) SAM (Tables 1 and 2). Whereas at a buffer concentration of 5 mM the relaxation constant determined from the mono-exponential fit to the data was  $17$  s<sup>-1</sup>, it increases drastically with increasing buffer concentration to afford a maximum value of  $440$  s<sup>-1</sup> at 750 mM (Fig. 3B). For the *isolated* Cyt *b5* domain,  $k_s$  could only be determined at low buffer concentrations (5 mM) and was

**Table 2** Redox parameters of hSO immobilised on Ag electrodes coated with C8(NH<sub>2</sub>)/C6(OH) (1 : 3 M/M) at different pH and Tris-acetate concentrations. The data were determined by SERR spectroscopy

Solution conditions		Redox parameters <sup>a</sup>		
pH	Ionic concentration/mM	$E^0/\text{mV}$	$n$	$k_s/\text{s}^{-1}$
7.4	5	-50	0.74	17
	150	-110	0.82	220
	500	-110	0.86	340
	750	-110	0.96	440
8.5	5	-100	0.7	15
	500	-120	0.86	360

<sup>a</sup> The approximate error for  $E^0$ ,  $n$ , and  $k_s$  are  $\pm 10$  mV,  $\pm 0.05$ , and  $\pm 10\%$ , respectively.

found to be 50% smaller than for the integral enzyme under similar conditions.

### Dipole moment calculations

Superposition of the 3D homology model of hSO and the crystallographic structure of chicken liver SO yielded an rmsd for all backbone atoms of 2.5 Å (ESI†, Fig. S3). The largest structural differences refer to the loop regions whereas for the Cyt *b5* domain there are only very small deviations (rmsd *ca.* 0.65 Å) between the 3D model and the crystal structure of the Cyt *b5* domain of chicken liver SO,<sup>3</sup> reflecting the reliability of the structure prediction. Further validation of the predicted structure was based on the Ramachandran plots. The fact that more than 95% of the hSO residues lie in favoured regions of the Ramachandran plot (Ramachandran *Z*-score: -0.182)<sup>30</sup> indicates that the homology model is well defined and that there are no unusual backbone conformations.

In order to predict the preferred orientation of hSO on the coated electrode surfaces we computed surface potentials as well as dipole moments of the *isolated* Cyt *b5* domain and of the hSO monomer and dimer.

In the case of the *isolated* Cyt *b5* domain, the predicted electrostatic surface potential is in very good agreement with previous results by Rudolph *et al.*<sup>3</sup> The *isolated* Cyt *b5* domain exhibits a high negative surface charge density, which is not only relevant for electron exchange with the Moco domain as suggested previously<sup>3,7-9</sup> but it also plays an important role for protein adsorption on positively charged surfaces. The dipole moment of the *isolated* Cyt *b5* domain is determined to be 245 D and its vector forms a 72.6° angle with the porphyrin plane indicating that the heme would be oriented nearly parallel to the electrode surface as plotted in Fig. 4.

When considering the entire hSO monomer, the dipole moment of the enzyme is drastically increased to 770 D and its vector is oriented in such a way that the negative end is located at the Cyt *b5* domain and the positive end at the dimer interface as shown in Fig. 4. According to these calculations the heme cofactor would be oriented almost perpendicular to the electrode surface (the dipole moment vector forms an angle of 28.1° with respect to the porphyrin plane). However, when hSO is present as a dimer, the total dipole moment is lowered to 490 D, accompanied by an increase of the angle (69.7°) of the dipole moment vector with respect to the heme planes (Fig. 4).

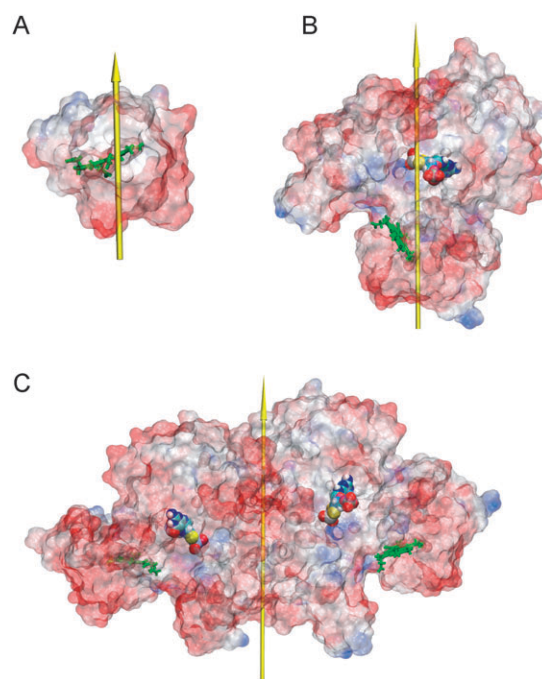


**Fig. 4** Structural models of (A) the *isolated* Cyt *b5* domain, (B) the hSO monomer, and (C) the hSO dimer. The arrows indicate the dipole moments. The surface potential is described by a color code with red and blue referring to negative and positive values, respectively. The heme group is indicated by the green color.

### Electrochemical study of enzymatic activity

CV experiments with hSO immobilised on nanostructured Ag electrodes were carried out under turnover and non-turnover conditions, *i.e.* in the presence and absence of substrate, respectively. We focused on the investigations of 1 : 3 M/M C8(NH<sub>2</sub>)/C6(OH) coatings in view of the good electrochemical response and protein adsorption. The non-turnover signal reveals two voltammetric peaks ascribed to the one-electron redox transition of the heme group of the immobilised hSO (ESI†, Fig. S4). Observation of the non-turnover signal allowed determining the amount of electroactive enzyme immobilised on the electrode according to:<sup>31</sup>

$$\Gamma_{\text{hSO}} = \frac{I_a 4RT}{Avn^2 F^2} \quad (1)$$

with  $I_a$  denoting the peak current of the non-turnover response of the immobilised enzyme at a given scan rate  $\nu$ .  $A$  is the surface area of the electrode,  $n$  is as defined before and  $R$ ,  $T$  and  $F$  have the usual meaning. Upon addition of an excess of sulfite (turnover conditions), no catalytic current was observed in 5 mM buffer solution. However, upon raising the buffer concentration up to 150 mM, a high catalytic current was detected (Fig. 5). The current intensity increased further with increasing buffer concentration up to 750 mM. The maximum value  $I_{\text{max}}$  for each buffer concentration at pH 7.4 was already reached in the presence of only  $\geq 200$   $\mu\text{M}$  sulfite. At a buffer pH of 8.5, however, a higher substrate concentration ( $> 400$   $\mu\text{M}$ ) was needed to reach  $I_{\text{max}}$  (ESI†, Fig. S5). Consequently, all further studies were carried out at pH 7.4. The Michaelis constant  $K_M$  for sulfite is by a factor of 3 lower at pH 7.4

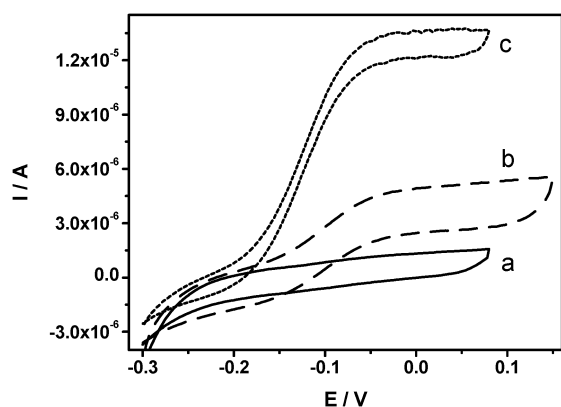


**Fig. 5** CV of hSO immobilised on an Ag electrode coated with a 1 : 3 M/M C8(NH<sub>2</sub>)/C6(OH) SAM at pH 7.4 in the presence of 200 μM sulfite but different Tris-acetate buffer concentrations. a, 5 mM, b, 150 mM, and c, 750 mM. The scan rate was 2 mV s<sup>-1</sup>.

(~60 μM) than at pH 8.5 (~170 μM) as already proposed for chicken liver sulfite oxidase in solution studies.<sup>9</sup>

However,  $K_M$  values in solution are much lower (~12 μM at pH 7.5 and ~30 μM at pH 8.5),<sup>9</sup> suggesting a better accessibility of the active site in solution. Enzymatic activity ( $k_{\text{cat,el}}$ ) can be derived according to:<sup>6</sup>

$$k_{\text{cat,el}} = \frac{I_{\text{lim}}}{\Gamma_{\text{hSO}} n F} \quad (2)$$

where  $I_{\text{lim}}$  refers to the maximum catalytic current obtained in an experiment where mass transport is not the rate limiting step.<sup>32</sup> In the present case, the effects of mass transport can be neglected due to rotation of the working electrode (*vide infra*) and thus we can set  $I_{\text{max}} = I_{\text{lim}}$ .

By combining eqn (1) and (2),  $k_{\text{cat,el}}$  can be calculated to

$$k_{\text{cat,el}} = \frac{I_{\text{lim}} n F}{I_a 4 R T} \quad (3)$$

This equation is only valid if all redox active enzymes are also catalytically active. In addition, the apparent turnover rate can only be set equal to the catalytic rate if the process is not limited by mass transport of either the substrates to or the products away from the active site.<sup>32</sup>

Turnover signals have revealed the highest catalytic current at substrate concentrations  $\geq 200$  μM in 750 mM Tris-acetate buffer solution at pH 7.4 and rotation of the Ag ring electrode at 480 rpm. In Fig. 6A the effect of rotation on the CV is illustrated. For a stationary electrode (no rotation), the catalytic current decreases rapidly and does not recover by inverting the scan direction (trace b). This behavior is indicative of substrate depletion rather than potential-induced inactivation, as reported for other enzymes.<sup>32</sup> However, substrate depletion can be minimised by fast electrode rotation, leading to the fully sigmoidal shape shown in trace c of Fig. 6A.

The CV measurements revealed an apparent turnover rate of  $k_{\text{cat,el}} = 0.85$  s<sup>-1</sup> in 100 mM Tris-acetate buffer solution (pH 7.4), which increased in 750 mM buffer to  $k_{\text{cat,el}} = 5.3$  s<sup>-1</sup> (Table 3). These rates are comparable to those for chicken liver SO reported by Elliott *et al.*, who obtained turnover rates of 2–4 s<sup>-1</sup>, using a pyrolytic graphite electrode and a C6(OH)-coated polycrystalline gold electrode.<sup>10</sup> However,

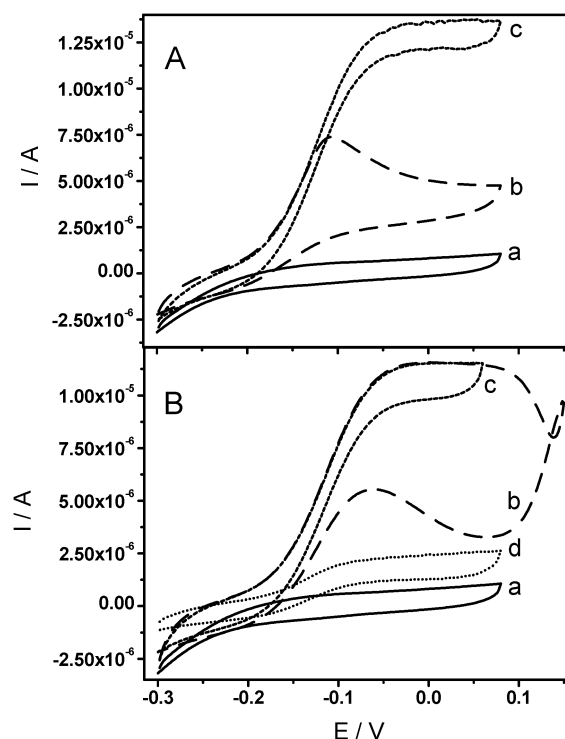


**Fig. 6** CVs of hSO immobilised on an Ag electrode with 1 : 3 M/M C8(NH<sub>2</sub>)/C6(OH) SAM in 750 mM Tris-acetate at pH 7.4. The scan rate was 2 mV s<sup>-1</sup>. (A) a, in the absence of substrate (solid line); b, in the presence of 200 μM sulfite without rotation of the electrode (dashed line); c, in the presence of 200 μM sulfite with rotation of the electrode at 480 rpm (dotted line). (B) a, without substrate (solid line); b, in the presence of 200 μM sulfite upon rotation of the electrode and sweeping to more positive potentials (dashed line); c, in the presence of 200 μM sulfite upon rotation of the electrode (dotted line), measured immediately after b; d, measured two hours after c (short dotted line).

**Table 3** Electron transfer and turnover rate constants of hSO immobilised on Ag electrodes coated with C8(NH<sub>2</sub>)/C6(OH) (1 : 3 M/M) at pH 7.4

Tris-acetate concentration/ mM	Redox parameters and apparent turnover rate constants <sup>a</sup>			
	$k_s/s^{-1}$	$k_{\text{cat,el}}/s^{-1}$	$k_{\text{cat,SERRS(1)}}/s^{-1}$	$k_{\text{cat,SERRS(2)}}/s^{-1}$
100	210	0.85	0.12	0.013
150	220	1.6	0.24	0.03
200	220	3.8	0.76	0.14
750	440	5.3	n.d. <sup>b</sup>	n.d.

<sup>a</sup> Data were determined by SERR spectroscopy except for  $k_{\text{cat,el}}$  (CV). The approximate error for  $E^0$ ,  $n$ , and the rate constants are  $\pm 10$  mV,  $\pm 0.05$ , and  $\pm 10\%$ , respectively. <sup>b</sup> n.d., not determined.

those data were obtained at much lower buffer concentrations (40 mM). On the other hand, the largest rate constant determined in the present work is yet roughly four times smaller than that reported by Ferapontova *et al.*<sup>6</sup> for chicken liver SO immobilised on a 1 : 1 C11(NH<sub>2</sub>)/C11(OH) SAM. These authors obtained turnover rates of *ca.* 20 s<sup>-1</sup> using 100 mM Tris-HCl buffer solution and smooth Au instead of a rough Ag electrode.

At 750 mM buffer concentration a decrease of catalytic activity of the immobilised enzyme with time was observed. Within two hours the enzyme was found to be irreversibly inactivated such that the catalytic current had dropped to *ca.* 20% of the initial value. This decay cannot be attributed to protein desorption or to the degradation of the heme *b* site of the enzyme since both the non-turnover signal and SERR spectra do not reveal notable changes after long term CV scanning under catalytic conditions. A similar effect has been reported also for other enzymes immobilised on similar monolayers.<sup>33</sup>

Another form of inactivation of the catalytic activity is observed at high electrode potentials above  $>0.08$  V (Fig. 6B). At that point the current decreases and the overall wave shape is indicative of an additional process. This effect is not observed in low ionic strength buffer solution.

### SERR-spectroscopic study of catalytic activity

Catalytic sulfite oxidation takes place at the Moco domain followed by an intramolecular electron transfer to the Cyt *b5* domain.<sup>1</sup> This process was monitored by SERR spectroscopy under the same conditions as used in the CV experiments except that the Ag working electrode was kept at open circuit.

Under these conditions and in the absence of sulfite, the Cyt *b5* domain of hSO is predominantly (*ca.* 90%) in the ferric state. The catalytic activity of the adsorbed hSO could then be monitored upon addition of sulfite to the electrochemical cell and subsequent monitoring of the reduction of the Cyt *b5* domain due to intramolecular electron transfer. Assuming that at open circuit the intramolecular electron transfer step is not followed by heterogeneous electron transfer to the electrode, no reoxidation of the heme domain occurs.

Due to the limited time-resolution of *ca.*  $1\text{ s}^{-1}$  for this approach, the SERR spectroscopic detection of the catalytic process is only applicable to conditions with slow turnover rates as shown for the process in 100 mM Tris-acetate at pH

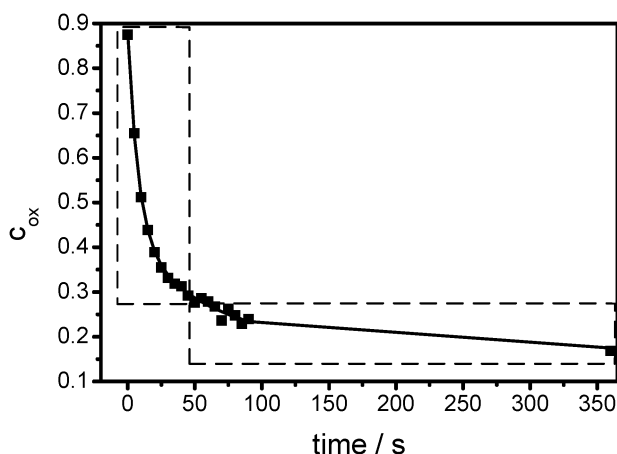


**Fig. 7** Changes of the relative concentration of the ferric Cyt *b5* domain determined by spectral component analysis<sup>12,28</sup> at open circuit as a function of time after addition of 200  $\mu\text{M}$  substrate. The data were obtained from consecutively measured SERR spectra. A bi-exponential function (solid line) has been fitted to the data (squares) (Table 3). The buffer solution is 0.1 M Tris-acetate at pH 7.4.

7.4 in Fig. 7. The data obtained for reduction of the Cyt *b5* domain can readily be described by a bi-exponential function with the fast phase comprising *ca.* 60% of the reduction (Table 3). At high buffer concentrations nearly the total amount of the immobilised protein was reduced, albeit faster than the time-resolution of the present approach. Thus, the SERR experiments demonstrate that the majority of the immobilised enzyme molecules are catalytically active.

## Discussion

### Immobilisation of hSO and the isolated Cyt *b5* domain

For the *isolated* Cyt *b5* domain desorption is observed at an ionic strength of 50 mM, whereas the integral enzyme remains adsorbed up to a buffer concentration of 1.5 M. This different adsorption behavior cannot only be attributed to a more negative binding enthalpy for the integral enzyme as suggested by the larger dipole moment. Increasing the high ionic strength may have a different effect on the electrostatic binding of small and large proteins. For larger proteins such as the integral hSO enzyme the entropic term to the free energy of adsorption gains importance since adsorption is associated with a release of counter ions from the SAM or the SAM/solution interface. Thus, the entropic term strongly increases with the size of the protein corresponding to an increasing number of released ions. This effect is known to be the driving force in polyelectrolyte adsorption<sup>34</sup> and most likely also stabilises the immobilisation of the integral enzyme at high ionic strength observed in this work. This stabilisation effect is expected to be particularly strong for the dimeric form of the enzyme since in view of the orientation of the molecular dipole moment it is expected to bind to the surface predominantly *via* the dimerisation region. Thus, we assume that the dimeric form of the enzyme is not only preserved in the adsorbed state but may be even stabilised *via* the entropic gain as discussed above. In this orientation, which is in contrast to previous suggestions,<sup>10</sup> the molecular model in Fig. 4 suggests only minor interactions of the Cyt *b5* domain with the surface. However, the present structural model as well as preliminary molecular dynamics simulations<sup>39</sup> reveal a high flexibility in the loop connecting the Moco and the Cyt *b5* domain which may allow the latter domain to swing towards the SAM surface.

### Redox potential shifts of the immobilised hSO

For immobilised hSO at buffer concentrations  $>150$  mM (pH 7.4), a potential shift  $\Delta E^0$  of *ca.* 20 mV with respect to the value in solution ( $-128$  mV)<sup>29</sup> is measured (Table 2) independent of buffer concentration. This can be explained by the interfacial potential drop  $E_{RC}$  at the SAM/protein interface as it has been observed for the anionic cytochrome *b562* on amino-terminated SAMs<sup>15</sup> and, with opposite sign, for the cationic cytochrome *c* on carboxyl-terminated SAMs.<sup>28</sup> However, at low ionic strength (5 mM)  $\Delta E^0$  increases up to 80 mV. Evidently, this high value cannot exclusively be attributed to the interfacial potential drop  $E_{RC}$ . We thus assume that, to a considerable extent,  $\Delta E^0$  also reflects the preferential stabilisation of the ferrous form of hSO (Cyt *b5*)

as compared to the ferric form.<sup>35</sup> Then  $\Delta E^0$  may be expressed according to

$$\Delta E^0 = E_{RC} - \frac{RT}{nF} \ln \frac{K_{ox}}{K_{red}} \quad (4)$$

where  $K_{ox}$  and  $K_{red}$  refer to the binding constants of the oxidised and the reduced form, respectively. At high ionic strengths adsorption occurs *via* the Moco and dimerisation domain and is therefore most likely independent of the redox state of the Cyt *b5* domain (*vide supra*) such that under these conditions  $E_{RC}$  is the leading term in eqn (4). In the low ionic strength regime also the Cyt *b5* domain interacts strongly with the SAM, thus the second term in eqn (4) becomes relevant, and can be accounted for the distinctly larger redox shift as compared to the high ionic strength regime.

At pH 8.5, however,  $\Delta E^0$  displays only a weak dependence on the ionic strength (5–25 mV; Table 2). This finding can be rationalised in terms of the largely deprotonated amino-terminated SAMs for which  $pK_a$  values between 6.5–7 have been measured.<sup>36</sup> Thus, the amount of surface charge density is lower than at pH 7 which is expected to lower  $E_{RC}$  and to attenuate the redox-state dependent modulation of the binding constant of hSO. Note that an analogous effect has also been observed for cytochrome *c* on carboxyl-terminated SAMs although, due to the inverse sign of the surface charge, with decreasing  $\Delta E^0$  upon lowering the pH.<sup>37</sup>

#### Heterogeneous electron transfer of the immobilised hSO

At low ionic strength, the rate constant for the heterogeneous electron transfer of the *isolated* Cyt *b5* domain [C8(NH<sub>2</sub>) coated electrode] is determined to be  $10 \text{ s}^{-1}$ . This small value seems to be consistent regarding the large angle (72.6°) between the molecular dipole moment and the heme plane and the long electron transfer distance from the heme to the electrode when we assume an electrostatic binding of the protein governed by the molecular dipole moment (Fig. 4). Rotational diffusion of the protein would in that case lead to orientations with shorter electron transfer distances and thus larger rate constants. Correspondingly, we assume that at such low ionic strengths the protein is rigidly fixed in the thermodynamically preferred orientation which is not the optimum electron transfer configuration. In this respect, the situation is reminiscent of the previous results on cytochrome *b562* on amino-terminated SAMs or iso-1 cytochrome *c* on carboxyl-terminated SAMs.<sup>15,37</sup> A very similar value is also determined for the Cyt *b5* domain in the integral hSO for the same low ionic strength such that it is tempting to assume that this domain, albeit connected to the Moco domain, interacts with the surface in a similar way as the *isolated* Cyt *b5* domain. As discussed above this seems to be reasonable regarding the high structural flexibility of the loop connecting the Cyt *b5* and the Moco domain.

With increasing ionic strength the electrostatic interactions of the Cyt *b5* domain with the SAM surface are attenuated such that the *isolated* Cyt *b5* domain is desorbed as reflected by the irreversible loss of SERR intensity. The integral enzyme, however, remains immobilised (*vide supra*) and the ionic-strength induced weakening of the electrostatic interactions of its Cyt *b5* domain may ensure a higher mobility and

flexibility of this subunit to adopt configurations that are more efficient for the interfacial electron transfer. This interpretation is supported by the *reversible* SERR intensity variations with increasing buffer concentrations that may reflect different distances and orientations of the heme plane with respect to the surface. Moreover, it can account for the drastic increase of the rate constant for the heterogeneous electron transfer (Table 2).

#### Catalytic mechanism of immobilised hSO

On the basis of the interpretation of the heterogeneous electron transfer process of the immobilised hSO discussed in the preceding section, we may now analyse the catalytic process of the enzyme. Here we have to take into account that the proper functioning of the enzyme requires an efficient intramolecular electron transfer from the Moco active site to the Cyt *b5* domain. In the crystal structure of chicken liver SO as well as in the present structural model of hSO the distance between the heme center and the molybdenum cofactor is 32 Å (*vide supra*<sup>2</sup>). This distance is much too large for intramolecular electron tunneling. However, a rotational movement of the Cyt *b5* domain, already proposed to be involved in the heterogeneous electron transfer, would allow for an interaction of the negatively charged binding region of the Cyt *b5* domain with the positively charged binding region of the Moco domain, corresponding to a much shorter electron tunneling distance. In this way, the flexible loop region may serve as a hinge to allow for alternate interactions of the electron exit/entry site of the Cyt *b5* domain with the Moco domain and the electrode, as schematically depicted in Fig. 8.

Upon oxidation of sulfite the Moco domain takes up two electrons. The first one is transferred to its associated Cyt *b5*

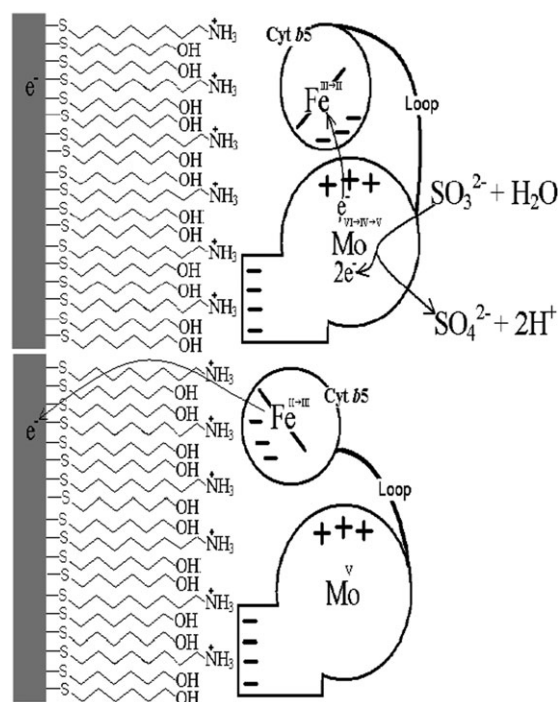


Fig. 8 Schematic presentation of the catalytic mechanism of immobilised hSO.

domain *via* an intramolecular electron transfer step. Since in the SERR experiments carried out at open circuit no re-oxidation of the heme *via* the electrode takes place, the second electron has to be transferred to another neighboring heme (intermolecular electron transfer) in order to fully reoxidise the Moco domain and enable it to react with the next substrate molecule. A similar intermolecular electron transfer mechanism has been reported by Brody and Hille<sup>9</sup> for the enzymatic reaction of chicken liver SO in solution corresponding to a dismutation reaction of two equivalents of the two-electron reduced [Mo(v)/Fe(II)] to one three-electron reduced [Mo(vI)/Fe(II)] and one one-electron reduced [Mo(IV)/Fe(II)] species.

Thus, the SERR data (Fig. 7) originate from the Cyt *b5* unit of both the catalytically active and the inactive enzyme and, in addition, reflect a complex mechanism of intra- and intermolecular electron transfer processes. Consequently, the rate constants derived from a bi-exponential fit to the experimental data cannot be directly compared with the results derived from catalytic CV experiments in which the electrode serves as the ultimate electron acceptor. However, assuming that in the kinetic SERR experiments the slower phase mainly refers to the intermolecular electron transfer between adjacent hSO molecules, the faster phase, which then predominantly reflects the intramolecular electron transfer, may be taken as a lower limit for the turnover number. In fact, the rate constants of the fast phase are lower by a factor of *ca.* 5 than the turnover rates determined by CV measurements (Table 3).

The maximum value of  $5.3 \text{ s}^{-1}$  determined by CV for the enzyme on the SAM-coated rough Ag electrodes falls in the range of values reported for different electrochemical systems ranging from  $2 \text{ s}^{-1}$  (pyrolytic graphite, SAM coated smooth Au)<sup>10</sup> to  $20 \text{ s}^{-1}$  (SAM coated smooth Au).<sup>6</sup> In none of these cases, however, turnover numbers comparable to that ( $100 \text{ s}^{-1}$ ) reported for the enzyme in solution<sup>9</sup> have been observed. The intrinsically lower enzymatic activity in the immobilised state is likely to be related to restricted protein dynamics in the adsorbed state, which may have an impact on substrate binding and product release and particularly of the mobility of the Cyt *b5* domain. This is specifically true under conditions of high interfacial electric fields which are known to affect protein and cofactor structures and dynamics.<sup>18,27,38</sup>

The increase of the local electric field may also be the origin for the reversible inactivation of the enzyme observed on Ag electrodes at potentials  $E > +0.08 \text{ V}$ . The magnitude of the electric field increases with the amount of the difference between the electrode potential and the potential of zero charge. Taking into account that the potential of zero charge is more negative for Ag than for Au,<sup>37</sup> the local electric field at electrode potentials  $> +0.08 \text{ V}$  is distinctly larger for Ag than for Au for which in fact such an inactivation was not observed. This potential-dependent inactivation may result from an electric-field dependent increase of the binding interactions of the Cyt *b5* domain with the SAM surface which slows down both the intramolecular and heterogeneous electron transfer. Correspondingly, one may also understand the weak catalytic activity and slow electron transfer at low ionic strength as an increased contact time of the electron entry/exit site of Cyt *b5* at the SAM surface.

## Conclusions

Advanced SERR-spectroscopy was applied to study the heterogeneous electron transfer of human sulfite oxidase. It has been shown that this technique is also applicable for monitoring the catalytic activity, if the turnover rate is low ( $< 1 \text{ s}^{-1}$ ). The efficiency of both the heterogeneous electron transfer and the catalytic activity strongly increases with the ionic strength of the buffer solution. This behaviour can be attributed to the increase in protein flexibility, particularly of the Cyt *b5* domain with respect to the remainder of the enzyme. This interpretation is supported by the present structural model derived for hSO on the basis of the crystal structure of the chicken liver enzyme. Dipole moment calculations suggest that the hSO dimer is immobilised *via* its dimerisation domain to the SAM surface. For the electron transfer from the Moco center to the electrode, the Cyt *b5* domain has to swing from the interaction site of the Moco domain to the SAM surface. This electron shuttling mechanism is promoted at high ionic strength which lowers the contact time of Cyt *b5* with the interaction domain of the electron donor (Moco) and electron acceptor (SAM-coated electrode). At a buffer concentration of  $750 \text{ mM}$ , a rate constant for the heterogeneous electron transfer of  $k_s = 440 \text{ s}^{-1}$  was measured, which is to our knowledge the fastest heterogeneous electron transfer rate for sulfite oxidase reported in the literature. At low ionic strength and high electric fields, the contact time of the Cyt *b5* domain with the SAM surface is strongly increased, thereby drastically slowing down the overall electron transfer process, both under catalytical and non-catalytical conditions.

We could show that a combined spectroscopic and electrochemical approach, complemented by molecular modelling and electrostatics calculations, may provide novel insight into the mechanism of enzymatic processes. The information extracted from these experiments can also be relevant for improving enzyme-based devices in bioelectronics and biocatalysis.

## Acknowledgements

Financial support was given by the Fonds der Chemischen Industrie (M.S. and I.M.W.), the DFG (Unicat) and the Alexander-von-Humboldt Foundation (D.M.).

## References

- 1 R. M. Garrett, J. L. Johnson, T. N. Graf, A. Feigenbaum and K. V. Rajagopalan, *Proc. Natl. Acad. Sci. U. S. A.*, 1998, **95**, 6394.
- 2 C. Kisker, H. Schindelin, A. Pacheco, W. A. Wehbi, R. M. Garrett, K. V. Rajagopalan, J. H. Enemark and D. C. Rees, *Cell*, 1997, **91**, 973.
- 3 M. J. Rudolph, J. L. Johnson, K. V. Rajagopalan and C. Kisker, *Acta Crystallogr., Sect. D: Biol. Crystallogr.*, 2003, **59**, 1183.
- 4 R. Spricigo, R. Dronov, F. Lisdat, S. Leimkühler, F. W. Scheller and U. Wollenberger, *Anal. Bioanal. Chem.*, 2009, **393**, 225.
- 5 R. Spricigo, R. Dronov, K. V. Rajagopalan, F. Lisdat, S. Leimkühler, F. W. Scheller and U. Wollenberger, *Soft Matter*, 2008, **4**, 972.
- 6 E. E. Ferapontova, T. Ruzgas and L. Gorton, *Anal. Chem.*, 2003, **75**, 4841.
- 7 A. Pacheco, J. T. Hazzard, G. Tollin and J. H. Enemark, *JBIC, J. Biol. Inorg. Chem.*, 1999, **4**, 390.
- 8 C. Feng, R. V. Kedia, J. T. Hazzard, J. K. Hurley, G. Tollin and J. H. Enemark, *Biochemistry*, 2002, **41**, 5816.

- 9 M. S. Brody and R. Hille, *Biochemistry*, 1999, **38**, 6668.
- 10 S. J. Elliott, A. E. McElhaney, C. Feng, J. H. Enemark and F. A. Armstrong, *J. Am. Chem. Soc.*, 2002, **124**, 11612.
- 11 F. Siebert and P. Hildebrandt, *Vibrational Spectroscopy in Life Science*, Wiley-VCH, Weinheim, 2008.
- 12 D. H. Murgida and P. Hildebrandt, *Angew. Chem., Int. Ed.*, 2001, **40**, 728.
- 13 D. Millo, A. Ranieri, W. Koot, C. Gooijer and G. van der Zwan, *Anal. Chem.*, 2006, **78**, 5622–5625.
- 14 C. A. Temple, T. N. Graf and K. V. Rajagopalan, *Arch. Biochem. Biophys.*, 2000, **383**, 281.
- 15 P. Zuo, T. Albrecht, P. D. Barker, D. H. Murgida and P. Hildebrandt, *Phys. Chem. Chem. Phys.*, 2009, **11**, 7430–7436.
- 16 I. Gallardo, J. Pinson and N. Vilà, *J. Phys. Chem. B*, 2006, **110**, 19521.
- 17 H. Wackerbarth, U. Klar, W. Gunther and P. Hildebrandt, *Appl. Spectrosc.*, 1999, **53**, 283.
- 18 D. H. Murgida and P. Hildebrandt, *J. Am. Chem. Soc.*, 2001, **123**, 4062.
- 19 A. Bairoch, *et al.*, *Nucleic Acids Res.*, 2008, **36**, W190–D195.
- 20 B. R. Brooks, R. E. Bruccoleri, B. D. Olafson, D. J. States, S. Swaminathan and M. Karplus, *J. Comput. Chem.*, 1983, **4**, 187.
- 21 A. Sali and T. L. Blundell, *J. Mol. Biol.*, 1993, **234**, 779.
- 22 W. Humphrey, A. Dalke and K. Schulten, *J. Mol. Graphics*, 1996, **14**, 33.
- 23 A. D. MacKerell, *et al.*, *J. Phys. Chem. B*, 1998, **102**, 3586.
- 24 S. Metz and W. Thiel, *J. Am. Chem. Soc.*, 2009, **131**, 14885.
- 25 N. A. Baker, D. Sept, S. Joseph, M. J. Holst and J. A. McCammon, *Proc. Natl. Acad. Sci. U. S. A.*, 2001, **98**, 10037.
- 26 T. J. Dolinsky, J. E. Nielsen, J. A. McCammon and N. A. Baker, *Nucleic Acids Res.*, 2004, **32**, W665–W667.
- 27 S. Oellerich, H. Wackerbarth and P. Hildebrandt, *J. Phys. Chem. B*, 2002, **106**, 6566.
- 28 D. H. Murgida and P. Hildebrandt, *J. Phys. Chem. B*, 2001, **105**, 1578.
- 29 E. E. Ferapontova, A. Christenson, A. Hellmark and T. Ruzgas, *Bioelectrochemistry*, 2004, **63**, 49.
- 30 R. W. W. Hoof, G. Vriend, C. Sander and E. E. Abola, *Nature*, 1996, **381**, 272.
- 31 M. I. Promdromidis, A. B. Florou, S. M. Tzouwara-Karayanni and M. I. Karayannis, *Electroanalysis*, 2000, **12**, 1498.
- 32 K. A. Vincent, A. Parkin and F. A. Armstrong, *Chem. Rev.*, 2007, **107**, 4366.
- 33 D. Millo, M. E. Pandelia, T. Utesch, N. Wisitruangsakul, M. A. Mroginski, W. Lubitz, P. Hildebrandt and I. Zebger, *J. Phys. Chem. B*, 2009, **113**, 15344–15351.
- 34 S. Y. Park, R. F. Bruinsma and W. M. Gelbart, *Europhys. Lett.*, 1999, **46**, 454–460.
- 35 J. Petrovic, R. A. Clark, H. J. Yue, D. H. Waldeck and E. F. Bowden, *Langmuir*, 2005, **21**, 6308–6316.
- 36 H. Munakata, D. Oyamatsu and S. Kuwabata, *Langmuir*, 2004, **20**, 10123.
- 37 J. J. Feng, D. H. Murgida, U. Kuhlmann, T. Utesch, M. A. Mroginski, P. Hildebrandt and I. M. Weidinger, *J. Phys. Chem. B*, 2008, **112**, 15202–15211.
- 38 H. Wackerbarth and P. Hildebrandt, *ChemPhysChem*, 2003, **4**, 714–724.
- 39 M. J. Pushie and G. N. George, *J. Phys. Chem. B*, 2010, **114**, 3266–3275.

## SUPPLEMENTARY INFORMATION

### Redox properties and catalytic activity of surface-bound human sulfite oxidase studied by a combined surface enhanced resonance Raman spectroscopic and electrochemical approach.

Murat Sezer<sup>a</sup>, Roberto Spricogo<sup>b</sup>, Tillmann Utesch<sup>a</sup>, Diego Millo<sup>a</sup>, Silke Leimkuehler<sup>b</sup>, Maria A. Mroginski<sup>a</sup>, Ulla Wollenberger<sup>b</sup>, Peter Hildebrandt<sup>a</sup>, and Inez M. Weidinger<sup>\*a</sup>

<sup>a</sup> Technische Universität Berlin, Institut für Chemie, Sekr. PC 14, Straße des 17. Juni 135, D-10623 Berlin, Germany.

<sup>b</sup> Institut für Biochemie und Biologie, Universität Potsdam, Karl-Liebknecht Straße 24-25, H. 25, Golm, D-14476, Germany.

E-mail: i.weidinger@mailbox.tu-berlin.de

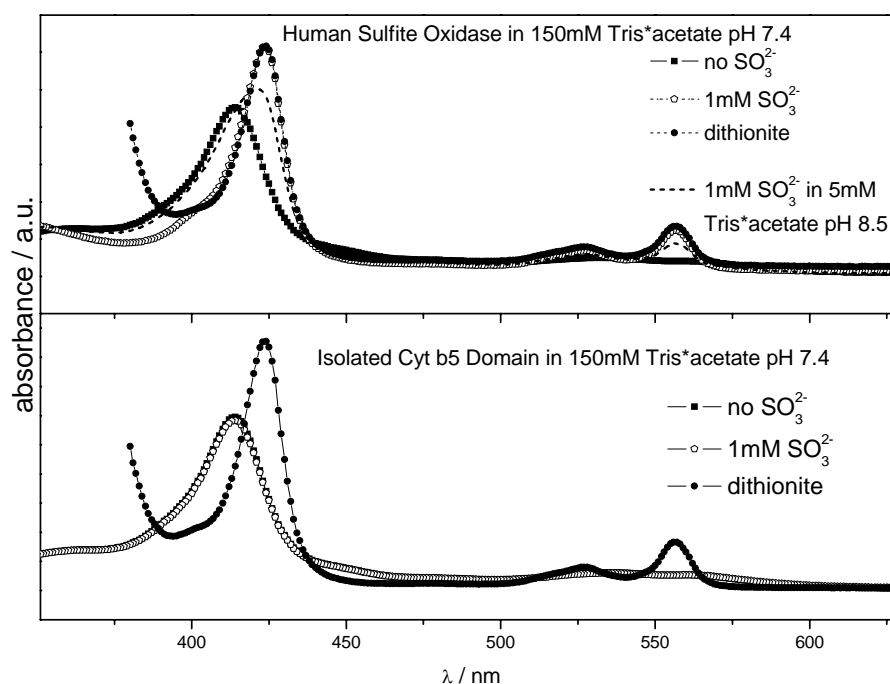


Figure S1: UV-Vis Absorption spectra of Human Sulfite Oxidase (up) and isolated cytochrome b5 domain in the absence and presence of sulfite.

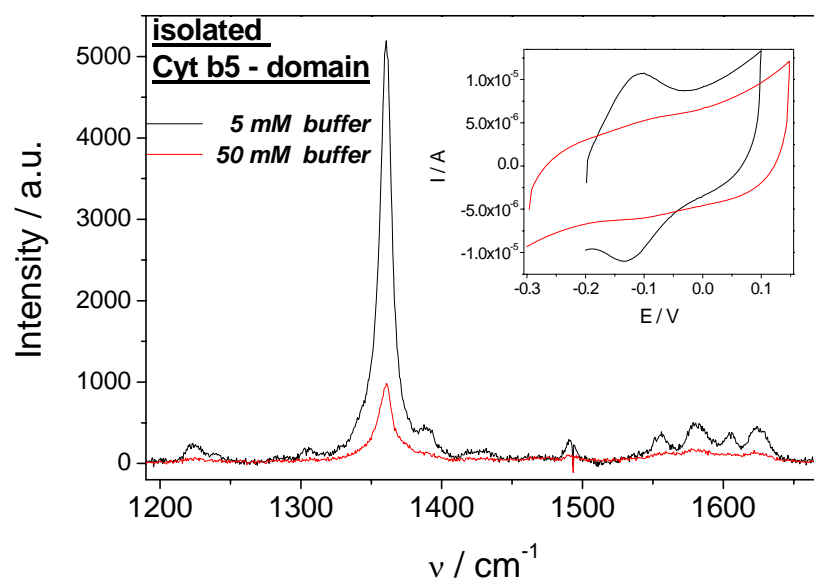


Figure S2: Desorption of the isolated Cyt b5 domain in 50 mM Tris-acetate buffer at pH 7.4 indicated by an irreversible decrease of the SERR- and CV-signal (inset).

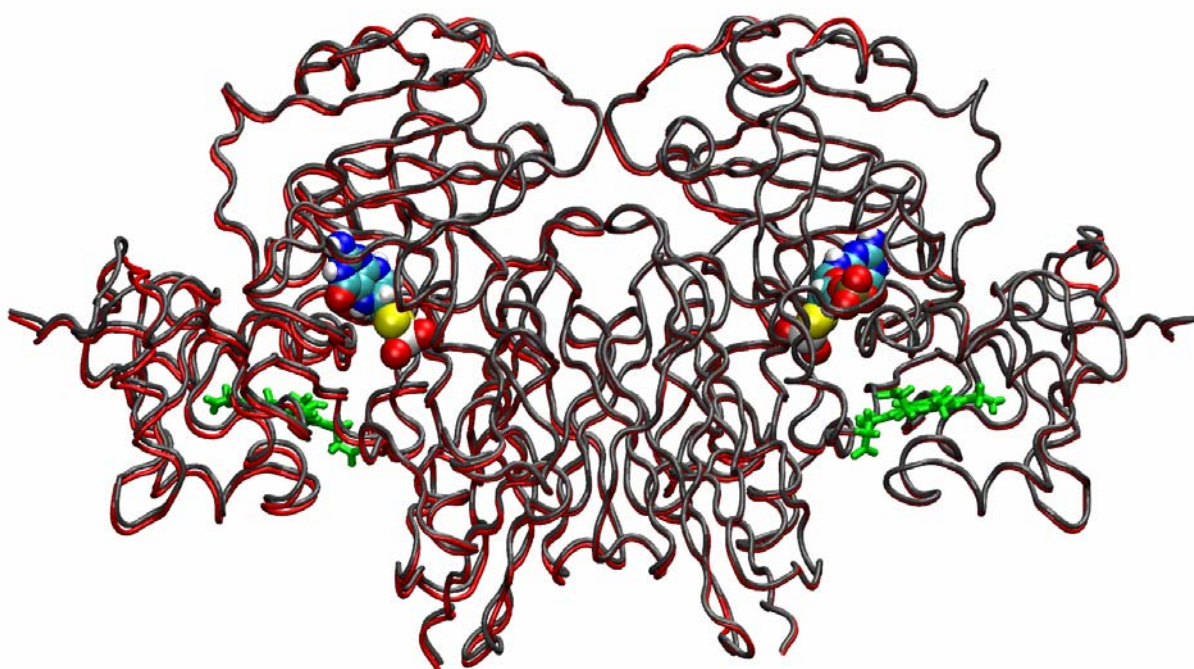


Figure S3: Superposition of crystal structure of chicken liver SO and homology model of hSO.

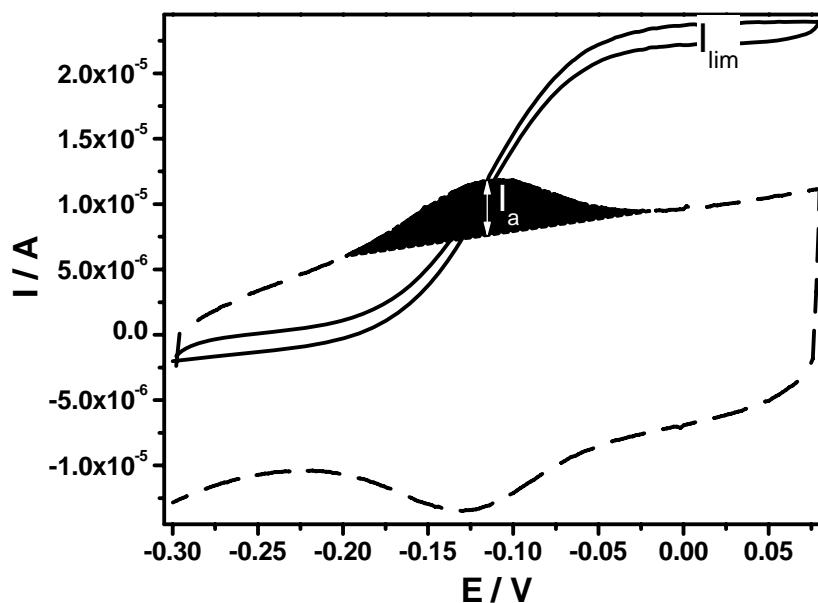


Figure S4: CV of hSO immobilized on an Ag electrode with 1:3 (M/M) C8(NH<sub>2</sub>)/C6(OH) – SAM in 750 mM Tris-acetate at pH 7.4. Dashed line, non-turnover signal at a scan rate of 100 mV/s; solid line, in the presence of 200 μM substrate at a scan rate of 2 mV/s.

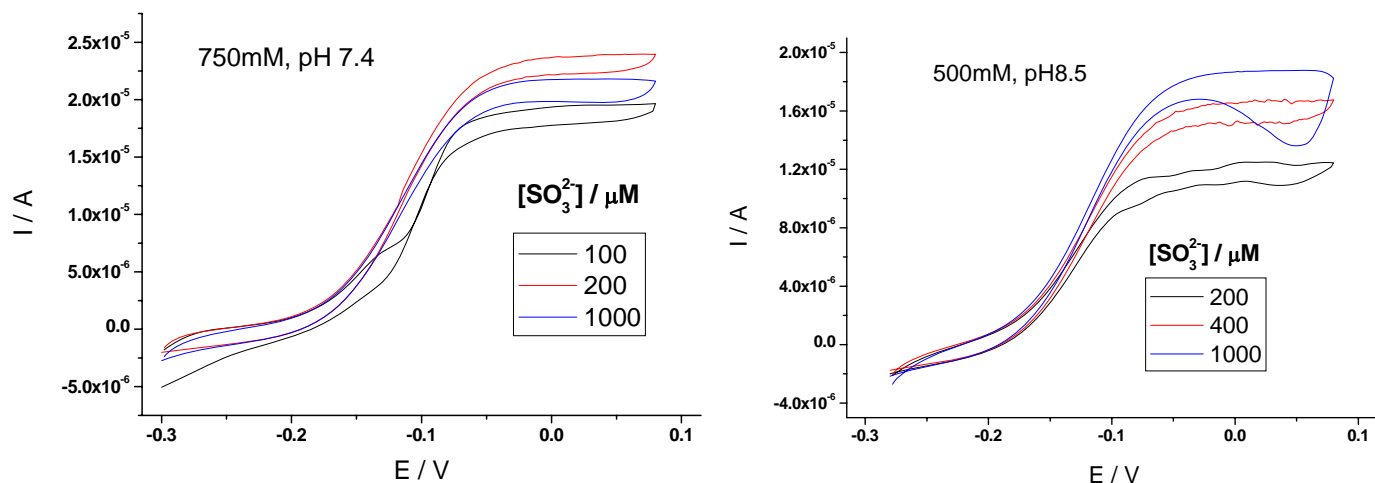
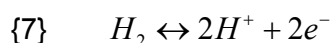


Figure S5: Cyclic voltammograms of human Sulfite Oxidase immobilized on 1:3 C8(NH<sub>2</sub>) / C6(OH) – SAM, rotation of the electrode at 480 rpm and different buffer conditions and substrate concentrations, respectively.



## 7 Membrane Bound Hydrogenase from *Ralstonia eutropha* H16

Hydrogenases enable hydrogen based energy conversion under physiological conditions and are essential in the energy metabolism of a wide variety of microorganisms [90-94]. Three phylogenetically distinct classes of hydrogenases that differ in their active site composition have been identified so far [101]: di-iron [FeFe] [98], nickel-iron [NiFe] [92, 94] and (iron-sulphur free) mono-iron [Fe] hydrogenases [93, 94]. [NiFe] and [FeFe] hydrogenases catalyse the reversible splitting of hydrogen into electrons and protons according to:



While most [NiFe] hydrogenases are more efficient in hydrogen splitting [92, 94], [FeFe] hydrogenases are usually more efficient in the opposite direction [98]. In contrast, [Fe] hydrogenases catalyse a hydride transfer reaction during the methanogenesis process in methanogens [93, 94].

In view of decreasing fossil energy resources, hydrogen-based technologies in energy storage and conversion are becoming more and more important [20, 95]. Therefore, tremendous research efforts have been made to explore the potential of hydrogenases for biotechnological applications [6, 20, 95, 96]. In this respect the oxygen sensitivity of most hydrogenases represents a serious constraint [66]. While the active site of [FeFe] hydrogenases is usually irreversibly destructed [66, 97, 98], most [NiFe] hydrogenases are inactivated by oxygen in a reversible manner [66, 97, 99, 115]. Some [NiFe] hydrogenases, however, retain activity in the presence of oxygen, such as the membrane bound [NiFe] hydrogenase I from the hyper-thermophilic bacterium *Aquifex aeolicus* [141, 142]. Except for its extraordinary thermostability it exhibits similar catalytic and electronic features as the membrane bound [NiFe] hydrogenase of the chemolithoautotrophic Knallgasbacterium *Ralstonia eutropha* H16 (MBH) [142]. Also the MBH has shown to retain considerable catalytic activity even in the presence of atmospheric oxygen concentrations [6, 18, 19, 21, 24, 97]. These hydrogenases are therefore referred to as oxygen tolerant and are of particular interest for biotechnological applications. Catalytic activity in the presence of oxygen was also shown to occur for a [Fe] hydrogenase [94, 100]. Research that is related to the elucidation of the mechanism of oxygen tolerance [103, 105] and possible biotechnological applications [6, 20, 95, 96], however, was so far mainly focussed on oxygen tolerant [NiFe] hydrogenases.

## 7.1 Structure of the Membrane Bound Hydrogenase from *Ralstonia eutropha* H16

The MBH consists of three subunits, which are denoted as HoxG, HoxK, and HoxZ. The entire complex is denoted as the HoxGKZ hetero-trimer (figure 7.1.1 a). The large hydrogenase HoxG subunit of 67.1 kDa contains the catalytic site with the bimetallic [NiFe] core that is bound to the protein via four cysteine residues. Furthermore, one CO and two CN<sup>-</sup> ligands are coordinated to the iron (figure 7.1.1 b) [24]. The small HoxK subunit (34.6 kDa) harbours three different iron sulphur clusters that act as electron relay units [24, 102, 103]. Moreover, it has a membrane integral hydrophobic C-terminal extension. The distal iron sulphur cluster is a [4Fe4S] cluster and the medial one is a [3Fe4S] cluster. Also the proximal Fe-S cluster is of the type [4Fe4S], however, it contains only three inorganic sulphur atoms, the fourth one is provided by a cysteine [103]. The HoxZ subunit is an integral membrane-bound di-heme cytochrome *b* unit, which additionally anchors the enzyme to the membrane and couples the electron transfer chain of the hydrogenase dimer HoxGK to the quinone pool of the respiratory chain [23, 24].

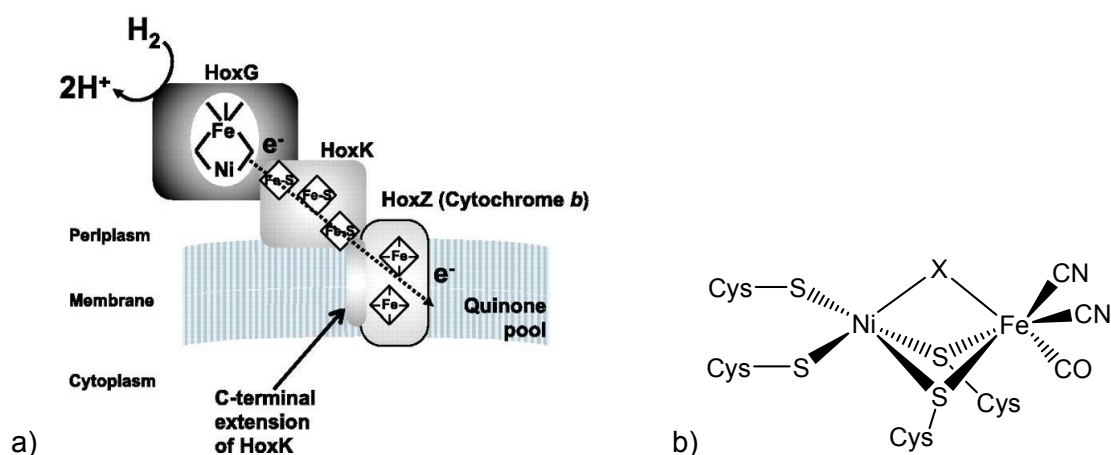


Figure 7.1.1: a) Cartoon of the membrane bound hydrogenase from *Ralstonia eutropha* H16 [adopted from reference 102]. b) Chemical structure of the [NiFe] active site [adopted from reference 6, 104]. X represents an additional bridging ligand site, which can be vacant or occupied by different ligands in different states of the active site (see chapter 7.2).

The HoxZ subunit is an essential component for the coupling between the catalytic H<sub>2</sub> conversion and the energy transduction machinery of *Ralstonia eutropha* H16, however, also the purified, isolated HoxGK hetero-dimer is catalytically fully active [6, 18, 19, 21, 24, 97]. So far, no crystal structures for MBH have been reported. The structure of the functional HoxGK hetero-dimer is therefore modelled using the crystal structure of the soluble so-called standard [NiFe] hydrogenase from *Desulfovibrio gigas* as a template. This enzyme consists only of the homologous HoxG and HoxK subdomains [103, 104] (figure 7.1.2 a). The role of the di-heme Cyt *b* unit (HoxZ) of MBH was investigated in detail in the study presented in chapter 7.3.

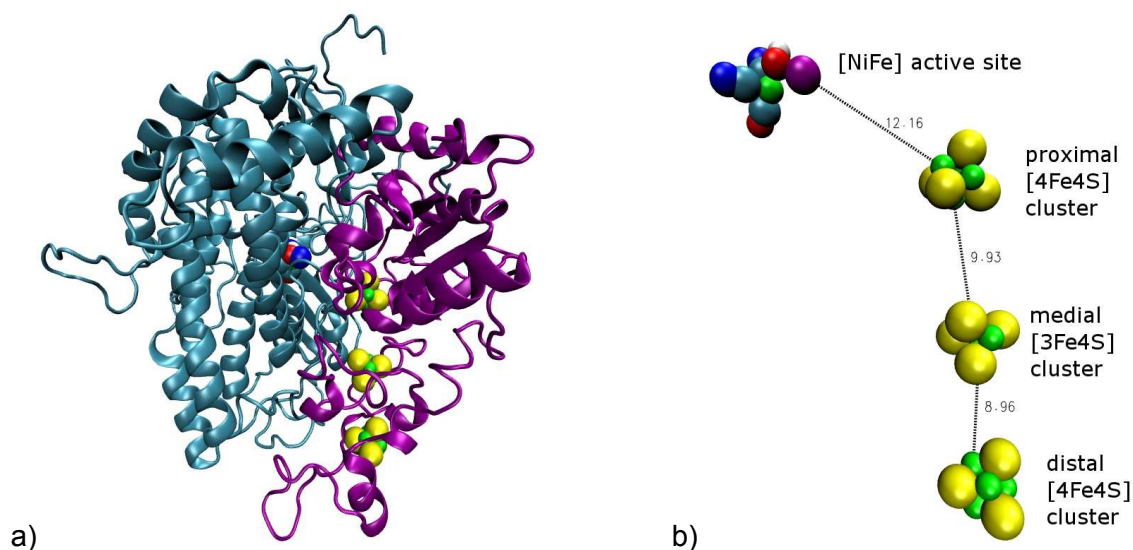


Figure 7.1.2: a) Model structure of the HoxGK heterodimer of the membrane bound hydrogenase from *Ralstonia eutropha* H16. The structure was modelled using the crystal structure of the [NiFe] hydrogenase from *Desulfovibrio gigas* as a template [104]. b) Cofactors in the HoxGK heterodimer and their distances with respect to each other (in Å).

Since an efficient purification protocol for the hetero-trimer HoxGKZ was lacking, previous studies on MBH were employed on the hetero-dimer HoxGK [6, 18, 19, 21, 25-27] or whole membrane preparations [23, 28, 102], respectively. The overall basic structure of the HoxGK hetero-dimer of oxygen tolerant MBH is similar to standard [NiFe] hydrogenases from *Desulfovibrio gigas* and *Desulfovibrio vulgaris* Miyazaki F, respectively. However, there are distinct electronic and structural differences. Redox potential values of the Fe-S clusters of the oxygen tolerant MBH and membrane bound hydrogenase I from *Aquifex aeolicus* are reported to be about 100 mV higher as compared to those of the soluble ‘standard’ oxygen sensitive [NiFe] hydrogenase from *Desulfovibrio gigas* [24-26, 108, 142, 143].

cluster \ organism	<i>Desulfovibrio gigas</i> [108]	<i>Ralstonia eutropha</i> H16 [25-26]
$E_m [4Fe4S]_{proximal}^{+2/+3}$	n.d.	+0.160 V
$E_m [4Fe4S]_{proximal}^{+1/+2}$	-0.290 V	-0.060 V
$E_m [3Fe4S]_{medial}^{+0/+1}$	-0.070 V	+0.025 V
$E_m [4Fe4S]_{distal}^{+1/+2}$	-0.340 V	-0.180 V

Table 7.1: Comparison of midpoint potential values of the Fe-S of the membrane bound hydrogenase from *Ralstonia eutropha* H16 and the standard [NiFe] hydrogenase from *Desulfovibrio gigas*. Potentials refer to SHE (-0.210 V vs.

Ag/AgCl 3M KCl).

Different electronic properties of the proximal cluster are related to structural differences. Six instead of four conserved cysteines are coordinating the proximal [4Fe4S] cluster in MBH [103]. Moreover, at high potentials the proximal Fe-S cluster in MBH most likely adopts the  $[4Fe4S]^{3+}$  oxidation state, which is not observed in standard hydrogenases [108]. Recent studies revealed

that the unusual coordination and redox behaviour of the proximal [4Fe4S] cluster of MBH is intimately related to the oxygen tolerance [103]. Replacement of the additional coordinating cysteines by other amino acids renders similar behaviour of MBH as oxygen sensitive standard [NiFe] hydrogenases.

## 7.2 Redox Chemistry and Catalytic Cycle

The reaction that is catalysed by [NiFe] hydrogenases is very simple (equation {6}), however, the underlying redox chemistry at the [NiFe] active site turned out to be quite sophisticated [110, 113]. The [NiFe] active site cycles through several redox states during catalysis involving different ligands in the third bridging position X (figure 7.2). While the iron remains always in a low spin  $\text{Fe}^{2+}$  state [114, 116, 117], the nickel adopts the  $\text{Ni}^{2+}$  and  $\text{Ni}^{3+}$  oxidation states during catalysis. The nickel carries spin density in its  $\text{Ni}^{3+}$  oxidation states, such that these states can be studied by EPR spectroscopy [113, 114, 118]. In the so-called Ni-S (EPR-silent) states the nickel is in the oxidation state  $\text{Ni}^{2+}$  and carries no spin density. The nomenclature of [NiFe] hydrogenase redox species has been developed according to the EPR signatures of the active site [113, 114].

All redox states including the Ni-S states can be studied with vibrational spectroscopy, which probes the state sensitive vibrational frequencies of the inorganic CO and  $\text{CN}^-$  ligands of the iron in the [NiFe] active site [102, 109, 113]. Figure 7.2 gives an overview over the potential dependent redox states of the Fe-S clusters and the [NiFe] active site [adopted from Ref. 102]:

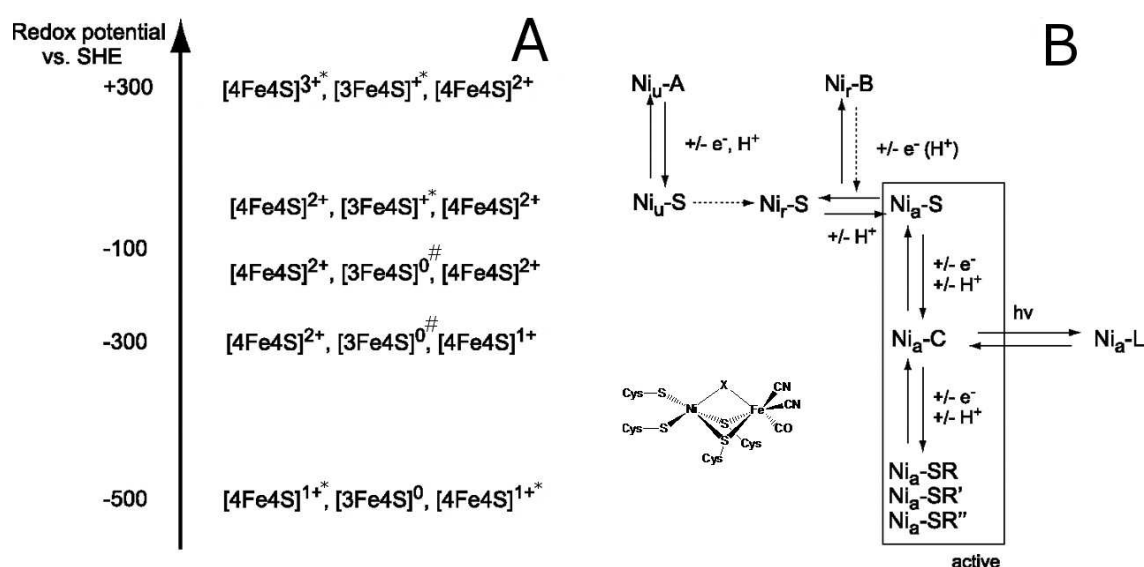


Figure 7.2: A) Redox states of the proximal (left), medial (middle) and distal (right) FeS cluster. EPR-detectable states are marked by an asterisk \* (spin of  $S = 1/2$ ) and a hash # (spin of  $S = 2$ ). All other states of the Fe-S clusters have  $S = 0$  [123, 124,]. B) Redox states of the [NiFe] active site.

A remarkable feature of oxygen tolerant [NiFe] hydrogenases is the absence of the Ni<sub>u</sub>-A state [28, 102, 109]. All other redox states that are reported for standard [NiFe] hydrogenases are observed for oxygen tolerant MBH as well [28, 102]. In the Ni<sub>u</sub>-A state the third bridging ligand position X at the active site (figure 7.1.1 b and inset of figure 7.2) is occupied by either a hydroperoxo- or hydroxide ligand [X = (O)OH<sup>-</sup>] [111]. As indicated by the index 'u' (= unready) the enzyme is not active in this state and can only be activated with very slow activation kinetics under strongly reducing conditions [66, 112, 119, 120]. The enzyme is also not active in the so-called Ni<sub>r</sub>-B state (X = OH<sup>-</sup>), however, this state is easily activated by hydrogen with fast kinetics [112, 115]. Accordingly, the index 'r' (= ready) indicates that the enzyme is ready for catalysis. The active states of the enzyme, i.e. those states that are involved in the catalytic turnover, are denoted by the index 'a'. In the Ni<sub>a</sub>-C state a hydride ion is bound to the active site in the third bridging ligand position (X = H<sup>-</sup>) [114, 121, 122]. This state is easily converted into the unphysiological Ni<sub>a</sub>-L state upon light irradiation, in which the third bridging ligand position is vacant [114]. Different Ni<sub>a</sub>-L substates (denoted as Ni<sub>a</sub>-L1, Ni<sub>a</sub>-L2 ...) were detected by EPR spectroscopy and are believed to differ slightly in the geometry of the thiol bridges at the [NiFe] site [114].

The structural features of the Ni-SR states (in some publications also denoted as Ni-R states, with R denoting reduced [142]) are yet not known. However, they can be distinguished by IR-spectroscopy and theoretical approaches are being employed to model their structure and their role in the catalytic cycle.



### **7.3 Role of the HoxZ subunit in the electron transfer pathway of the membrane-bound [NiFe]-hydrogenase from *Ralstonia eutropha* H16 immobilized on electrodes**

*Murat Sezer<sup>a</sup>, Stefan Frielingsdorf<sup>b</sup>, Diego Millo<sup>a</sup>, Nina Heidary<sup>a</sup>, Tillmann Utesch<sup>a</sup>, Maria-Andrea Mroginski<sup>a</sup>, Bärbel Friedrich<sup>b</sup>, Peter Hildebrandt<sup>a</sup>, Ingo Zebger<sup>a</sup>, Inez M. Weidinger<sup>a\*</sup>*

<sup>a</sup> Technische Universität Berlin, Institut für Chemie, Sekr. PC14, Straße des 17. Juni 135, D-10623 Berlin, Germany.

\*correspondence to E-mail: i.weidinger@mailbox.tu-berlin.de; Fax: +49 3031421122; Tel: +49 3031422780

<sup>b</sup> Humboldt-Universität zu Berlin, Chausseestraße 117, 10115 Berlin.

Reproduced with permission from *J. Phys. Chem. B*, DOI: 10.1021/jp204665r, in press.

Copyright © 2011 American Chemical Society.



## Abstract

The role of the diheme cytochrome *b* (HoxZ) subunit in the electron transfer pathway of the membrane-bound [NiFe]-hydrogenase (MBH) hetero-trimer from *Ralstonia eutropha* H16 has been investigated. The MBH in its native hetero-trimeric state was immobilized on electrodes and subjected to spectroscopic and electrochemical analysis. Surface enhanced resonance Raman spectroscopy was used to monitor the redox and coordination state of the HoxZ heme cofactors while concomitant protein film voltammetric measurements gave insights into the catalytic response of the enzyme on the electrode. The entire MBH hetero-trimer as well as its isolated HoxZ subunit were immobilized on silver electrodes coated with self-assembled monolayers of  $\omega$ -functionalized alkylthiols, displaying the preservation of the native heme pocket structure and an electrical communication between HoxZ and the electrode. For the immobilized MBH hetero-trimer, catalytic reduction of the HoxZ heme cofactors was observed upon H<sub>2</sub> addition. The catalytic currents of MBH with and without the HoxZ subunit were measured and compared with the heterogeneous electron transfer rates of the isolated HoxZ. On the basis of the spectroscopic and electrochemical results, we conclude that the HoxZ subunit under these artificial conditions is not primarily involved in the electron transfer process but plays a crucial role in stabilizing the enzyme on the electrode.

**KEYWORDS** Surface enhanced Raman spectroscopy, [NiFe]-hydrogenases, oxygen tolerance, cytochrome *b*, HoxZ, electron transfer, biocatalysis, protein film voltammetry

## Introduction

[NiFe]-hydrogenases catalyze the reversible splitting of molecular hydrogen (H<sub>2</sub>) into electrons and protons. In view of the growing importance of hydrogen-based technologies in energy storage and conversion, substantial research efforts have been made to explore the potential of these enzymes for biotechnological applications.<sup>1-4</sup> In this respect, oxygen-tolerant hydrogenases, such as the membrane-bound [NiFe]-hydrogenase (MBH) from *Ralstonia eutropha* H16 (*Re*), are of particular interest since they retain considerable catalytic activity even in the presence of atmospheric oxygen concentrations.<sup>1;5;6</sup>

MBH consists of three subunits, HoxG, HoxK, and HoxZ, and thus the entire purified complex is denoted as HoxGKZ hetero-trimer (figure 1A). The large hydrogenase subunit HoxG contains the catalytic site comprising the bimetallic [NiFe] core that is bound to the protein via four cysteine residues. Furthermore, one CO and two CN<sup>-</sup> ligands are coordinated

to the Fe. The small subunit HoxK harbors three different iron sulphur clusters acting as an electron relay unit.<sup>7;8</sup> The membrane-integral heme *b*-containing subunit HoxZ anchors the enzyme to the membrane and ensures electron transfer between the hydrogenase dimer HoxGK and the quinone pool of the respiratory chain.<sup>9;10</sup> Although HoxZ is evidently an essential component of the coupling between the catalytic H<sub>2</sub> conversion and the energy transduction machinery, it has been found that the purified, isolated hydrogenase hetero-dimer, consisting only of the subunits HoxG and HoxK, is catalytically fully active.<sup>11</sup> In fact most of the previous structural and catalytic studies on MBH were based on the hetero-dimer HoxGK,<sup>1;5-7;12-14</sup> or on intact membrane preparations.<sup>7;15</sup>

In this study the entire hetero-trimeric HoxGKZ complex was isolated and used to analyze the role of HoxZ for the overall catalytic- and electron transport processes in more detail. These studies are of particular interest for potential applications of MBH immobilized on electrodes since the optimization of the electronic communication between the catalytic center and the conducting support material is one of the crucial challenges for exploiting hydrogenases as a catalyst.

In order to elucidate the role of the HoxZ subunit in heterogeneous electron transfer between the immobilized enzyme and the electrode during the catalytic process, biocompatibly coated electrodes were employed that allow immobilization of enzyme preparations under preservation of the native structure and function as shown in previous studies of other redox enzymes.<sup>16-18</sup> To probe electric communication between enzymes and electrodes, electrochemical methods such as protein film voltammetry (PFV) are usually employed. This technique, however, monitors only the current flow from the enzyme to the electrode and *vice versa* whereas structural information on the redox cofactors cannot be obtained. This disadvantage can be overcome by employing surface sensitive vibrational spectroscopy such as surface enhanced infrared absorption (SEIRA) spectroscopy, that has been successfully used to probe CN<sup>-</sup> and CO ligands of the catalytic center under turnover and non-turnover conditions of immobilized hydrogenases.<sup>19-21</sup> To monitor the two heme *b* cofactors of HoxZ, which is in the focus of the present study, surface enhanced resonance Raman (SERR) spectroscopy is the method of choice. This technique combines the surface enhanced Raman effect, i.e. the amplification of the radiation field due to the coupling with the surface plasmons of the metallic support, with the molecular resonance Raman (RR) effect. For heme cofactors, optimum resonance conditions for both the plasmonic and the molecular electronic transitions are achieved by using excitation lines in the violet spectral region and nanostructured silver support materials. Under these conditions the SERR spectra exclusively display the vibrational bands of the cofactors solely of the immobilized

heme proteins. Thus, it is possible to selectively monitor the redox and conformational states of the cofactors of the immobilized HoxZ subunit during the catalytic cycle and to analyze the dynamics of heterogeneous electron transfer between the heme cofactors and the electrode. In combination with electrochemical and theoretical methods, the spectroscopic data provide novel insight into the involvement of the HoxZ subunit in the catalytic processes of immobilized MBH.

## Materials and Methods

### Chemicals

6-amino-1-hexanethiol hydrochloride [C6(NH<sub>2</sub>)] and 5-Carboxyl-1-pentanethiol [C5(COOH)] were purchased from Dojindo; 6-mercaptohexanol [C6(OH)] was provided from Aldrich and digitonin was purchased from Serva; n-dodecyl- $\beta$ -D-maltoside ( $\beta$ -DDM) (crystallography grade) and 7-mercaptoheptane was purchased from Applichem and Fluka, respectively. All chemicals were of highest purity grade available.

### Protein purification

In brief, the MBH hetero-trimer HoxGKZ was purified after solubilization with digitonin via a C-terminal *Strep-tag* II at the HoxZ subunit. Isolation of the HoxZ subunit was performed in a similar way but using  $\beta$ -DDM as a detergent instead of digitonin. The detailed purification protocol of the proteins used in this study will be published elsewhere.<sup>22</sup>

### Protein immobilization

Electrochemically roughened Ag electrodes were immersed for 24 h in solutions of  $\omega$ -substituted mercaptanes to form a self assembled monolayer (SAM). For pure SAMs, 1 mM of C6(NH<sub>2</sub>) or C5(COOH) was dissolved in a water/ethanol mixture (1:4 v/v) or pure ethanol. For mixed SAMs, 1 mM C6(NH<sub>2</sub>) or C5(COOH) were mixed with 3 mM C6(OH) in a water/ethanol solution (1:4 v/v) or in pure ethanol, respectively. Immobilization of the isolated HoxZ subunit, the hetero-dimer HoxGK and the entire MBH hetero-trimer HoxGKZ was

achieved by immersion (3 - 5 hours) of the SAM-coated Ag electrodes into a 10 mM potassium phosphate buffer (PB) solution containing ca. 0.4  $\mu\text{M}$  of the respective protein, as well as  $\beta$ -DDM in case of HoxZ and digitonin in case of HoxGKZ / HoxGK, respectively.

### **Spectroscopic and electrochemical measurements**

A rotating cuvette was used for RR experiments. The protein concentration was ca. 15  $\mu\text{M}$  in 50 mM PB buffer solution at pH 7.0 containing 150 mM NaCl and 0.01 % w/w  $\beta$ -DDM.

SERR and electrochemical measurements were performed using homemade spectro-electrochemical cells with a volume of about 10 mL, a rotating Ag ring with a geometrical area of  $0.75 \pm 0.05 \text{ cm}^2$  as the working electrode, an Ag/AgCl (3 M KCl) reference electrode (+0.21 V vs. SHE) and a platinum counter electrode. All potentials cited in this work refer to the standard hydrogen electrode (SHE). The buffer solutions used for the SERR spectroscopic and electrochemical experiments were adjusted to the same pH as the respective incubation buffer but did not contain any detergent.

SERR and RR spectra were measured using a confocal Raman spectrometer (LabRam HR 800, Jobin Yvon) coupled to a liquid nitrogen cooled CCD detector. The spectral resolution was  $1 \text{ cm}^{-1}$  with an increment per data point of  $0.75 \text{ cm}^{-1}$ . The 413 nm laser line of a Coherent Innova 400 Krypton cw-laser was used for excitation. The laser power on the sample was 2.0 mW for RR and 1.0 mW for SERR experiments. The laser beam was focused onto the sample by a Nikon 20x objective with a working distance of 20.5 mm and a numeric aperture of 0.35.

Accumulation times of the SERR spectra were between 1 and 10 s whereas for the RR spectra the accumulation time was 30 s. Time-resolved (TR) SERR experiments were carried out as described previously.<sup>23</sup> After polynomial baseline subtraction, the measured spectra were treated by homemade component analysis software.

UV/vis-spectroelectrochemical redox-titrations of the isolated HoxZ subunit in solution were performed using a transmission cell which has been described elsewhere.<sup>24</sup> UV-vis absorption spectra were recorded using a Cary 50 spectrometer, while the cell potential was controlled with a EG&G 263A potentiostat. The solution used for the spectroelectrochemical measurements included 100 mM PB, 150 mM NaCl and 0.01 % w/w  $\beta$ -DDM, but no additional redox mediators.

Cyclic voltammetric experiments were performed with a CH instrument 660 C (Austin, USA).

### **Molecular modelling and theoretical calculations**

Modeling was performed with the Swiss model server<sup>25</sup> using the fdnl subunit of the formate dehydrogenase-N (pdb accession code 1kqg) as a template structure.<sup>26</sup> The modeled residue range was from 26-243, the sequence identity between the model and the template is 9.174 % and the Evalue was 1.0e-38. Dipole moment calculations were carried out with VMD 1.8.7<sup>27</sup> with the partial charges of the CHARMM22 force field.<sup>28</sup> For the determination of the electrostatic potential we have utilized the APBS program<sup>29</sup> and the PDB2PQR tool.<sup>30</sup>

## **Results**

### **Calculation of the HoxZ surface potential distribution**

Due to the lack of structural information on the HoxZ subunit a homology model was generated to calculate the electrostatic potential and the dipole moment of this protein (figure 1B). The fdnl subunit of the formate dehydrogenase-N from *E. coli* served as template. A previous study reported on the basis of sequence analyses shows that these two proteins are structurally related,<sup>31</sup> such that the model is expected to represent a good approximation for HoxZ. HoxZ contains two *b*-type hemes, each of them carrying two axial His ligands. The distance between the heme irons in the model is 19.2 Å while the distance between the edges of the porphyrin  $\pi$ -electron system is 7.5 Å, enabling direct electron tunneling between the two heme groups.<sup>32</sup> According to these structural model and surface potential calculations, HoxZ possesses a cylindrical shape with a slightly negatively charged upper and a positively charged bottom side. The latter accommodates the C- and N-terminal regions and a mainly hydrophobic lateral area forming contacts with the bilayer core of the membrane (figure 1C). The dipole moment was calculated to be ca. 1100 Debye in the fully reduced state ( $\text{Fe}^{2+}/\text{Fe}^{2+}$ ).

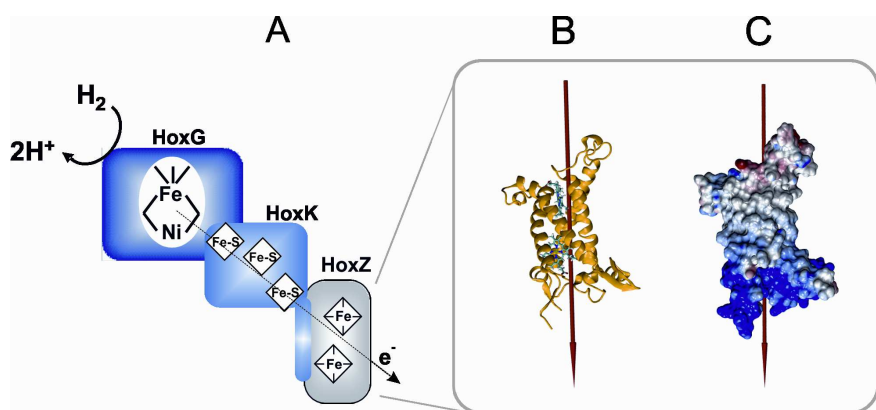


**Figure 1:** (A) Schematic representation of the whole MBH hetero-trimer HoxGKZ, (B) homology model and (C) calculated surface potential distribution of the modelled HoxZ subunit. The arrows in B and C indicate the direction of the calculated dipole moment.

### SERR spectroscopic investigation of the HoxZ subunit

The RR spectra of the isolated HoxZ subunit show the vibrational signature characteristic of six-coordinated low-spin (6cLS) hemes as expected for bis-His ligated coordination (figure 2A, E). The symmetric bandshapes point to essentially identical RR spectra of both heme groups. Upon immobilization of HoxZ on SAM-coated Ag electrodes strong SERR-signals were detected when using C6(NH<sub>2</sub>) or C5(COOH) SAMs at pH 7.0 and low ionic strength (10 mM PB). However, the SERR spectra differ from the RR spectrum, *inter alia* by a broadening of the  $\nu_4$  envelope and an additional peak in the  $\nu_3$  band region at 1491 cm<sup>-1</sup>, which is characteristic of five-coordinated high-spin (5cHS) heme (figure 2B). This conclusion is confirmed by the component analysis of the spectra that allows quantifying the relative contributions of the various species involved.<sup>33</sup>

The relative contribution of the 5cHS species is higher for C5(COOH)- than for C6(NH<sub>2</sub>)-SAMs but decreases in both cases in favor of the 6cLS species upon increasing the ionic strength and by an admixture of C6(OH) at a ratio of 3:1 [C6(OH)/C5(COOH) and C6(OH)/C6(NH<sub>2</sub>)] (Table S1 Supporting information). Both effects are accompanied by a loss of absolute intensity that reflects a partial HoxZ subunit desorption due to weakening of the electrostatic interactions between the subunit and the SAM. In the case of the carboxyl-terminated SAM, the 5cHS content was further diminished by decreasing the pH from 7.0 to 5.5. However, a similar decrease in pH in the case of C6(NH<sub>2</sub>)-SAMs led to a complete loss in signal intensity.

The structural perturbations were largely avoided upon using C5(COOH) SAMs at pH 5.5 and an ionic strength of 100 mM. These conditions represent an acceptable compromise between preservation of the structural integrity of the immobilized HoxZ and the amount of the adsorbed protein and thus were adopted for the SERR spectroscopic studies of the whole hetero-trimer HoxGKZ.

Figure 2C displays the SERR spectrum of the oxidized HoxGKZ at an electrode potential of  $E = +0.3$  V. Note that the total SERR intensity is weaker by a factor of ca. 15 as compared to the isolated HoxZ subunit under the same conditions. This is attributed to the lower surface coverage due to the significantly larger size of the whole enzyme.<sup>34</sup> Upon lowering the electrode potential to  $-0.27$  V, the heme cofactors were reduced (figure 2D). The spectra of the ferrous and ferric form of the heme included no contributions from a HS species. Furthermore, it should be noted that the cofactors of the HoxG and HoxK subunit do not contribute to the SERR spectrum of the hetero-trimer.

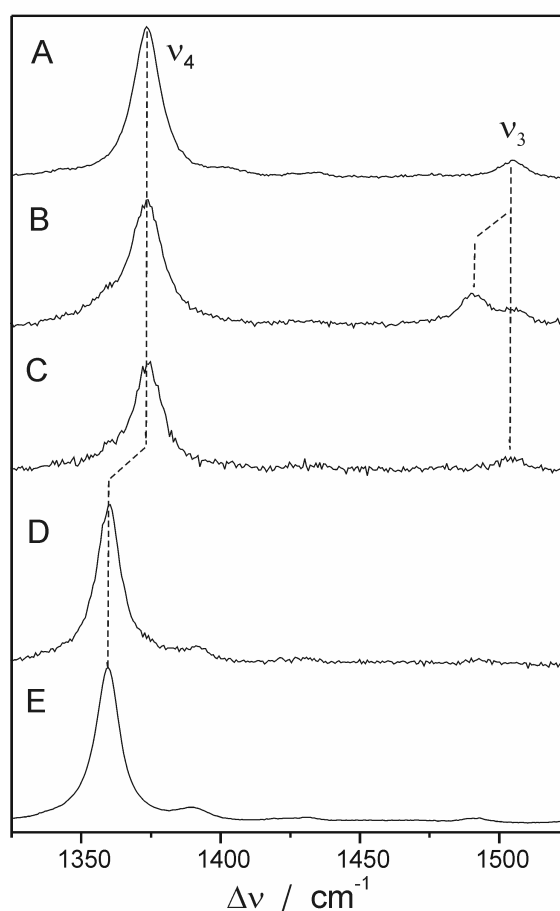


**Figure 2:** (A) RR spectrum of the isolated, fully oxidized HoxZ subunit in solution. (B) SERR spectrum of the isolated HoxZ subunit immobilized on a C5(COOH) SAM at an electrode potential  $E = +0.3$  V. Traces C and D display the SERR spectra of the whole HoxGKZ hetero-trimer immobilized on C5(COOH) SAM at  $E = +0.3$  V and  $E = -0.27$  V, respectively. (E) RR spectrum of the fully reduced HoxZ subunit. Further experimental conditions: (A, E) 50 mM PB at pH 7.0, 0.15 M KCl, and 0.01%  $\beta$ -DDM, (B) 10 mM PB at pH 7.0, (C, D) 0.1 M PB at pH 5.5.

## Redox transitions

UV-vis spectroelectrochemical redox titrations of the isolated HoxZ subunit in solution were performed by monitoring the intensity of the Soret band at 430 nm, corresponding to the maximum absorbance of the ferrous heme *b* (figure 3A). Upon variation of the applied potential, one sharp redox transition having a midpoint potential ( $E_{m,sol}$ ) at -0.086 V was detected. The transition showed an almost ideal Nernstian behavior yielding an apparent number of transferred electrons close to 1 ( $n = 0.8$ ). The redox transition of the immobilized HoxZ subunit, either isolated or as constituent of the MBH hetero-trimer, was probed by potential-dependent SERR spectroscopy. The relative spectral contributions derived from the component analysis of the spectra were converted into relative concentrations using the proportionality factors determined from the RR spectra of the isolated HoxZ subunit in solution. The corresponding factor for the 5cHS species was taken from a previous study of cytochrome *c*.<sup>33</sup>

Figure 3B shows the molar fractions of the ferric and ferrous species of the HoxZ subunit in the HoxGKZ trimer as a function of applied potential, determined under conditions that suppressed the formation of the 5cHS species (100 mM PB, pH 5.5, C5(COOH) SAM). The data show a clear redox transition with at midpoint potential at  $E_m = -0.09$  V similar to  $E_{m,sol}$  of the isolated HoxZ subunit in solution but within a significant broader potential window expressed by a smaller apparent number of transferred electrons ( $n = 0.5$ , table 1). This low value for  $n$  may reflect a broadened distribution for the midpoint potentials of the two hemes. Alternatively, it is also consistent with the superposition of the redox transitions for the two spectroscopically indistinguishable hemes exhibiting slightly different but discrete  $E_m$  values.

The redox transition was completely reversible with the majority of the immobilized proteins remaining electro-active at the surface, however a complete reduction was not possible due to the lower limit of the accessible potential range for SAM-coated electrodes<sup>20</sup> (i.e. ca. -0.3 V). The redox titration of the isolated HoxZ subunit displays essentially the same potentiometric behavior (figure S1C). This suggests that the HoxZ subunit is in both cases adsorbed similarly.

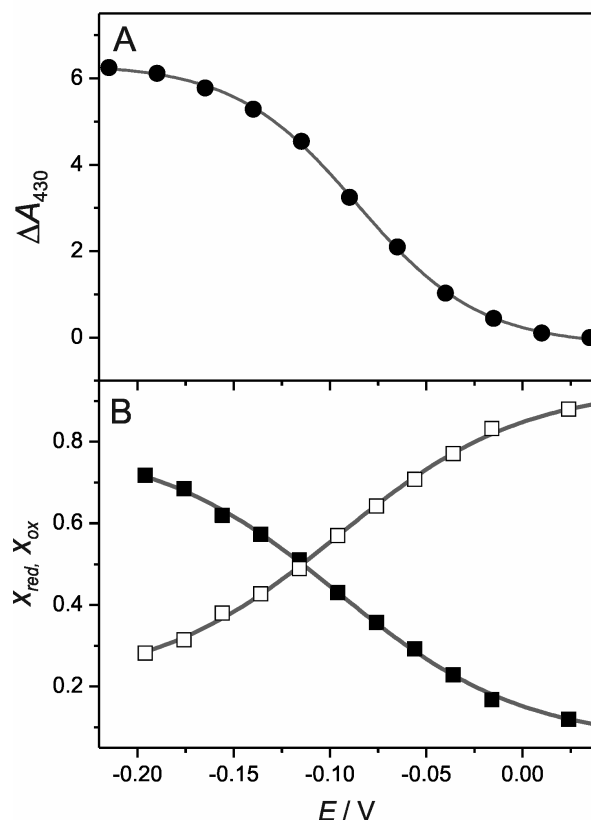


**Figure 3:** (A) Relative changes in the absorbance at 430 nm of the isolated HoxZ subunit in solution as a function of electrode potential. The reference spectrum was taken at +0.3 V. (B) Potentiometric titration of the HoxZ domain within the MBH hetero-trimer immobilized on C5(COOH)-coated electrodes at pH 5.5 (0.1 M PBS).  $x_{red}$  (solid squares),  $x_{ox}$  (open squares).

Under conditions where the 5cHS and 6cLS species coexist, redox titrations of the isolated HoxZ subunit exhibit a similar redox behavior for both species throughout the entire potential range that has been investigated (figure S1A, B). The midpoint potential of the HS species is  $E_m(\text{HS}) = -0.1$  V and thus slightly more positive than  $E_m(\text{LS}) = -0.14$  V (See Table S1, supporting information). One should note that the difference in  $E_m$  between the 5cHS and 6cLS species is the same as observed for the B2 state of cytochrome *c*.<sup>33</sup>

In all redox titrations of the isolated HoxZ, a distinct midpoint potential  $E_m$  is observed below -0.08 V.  $E_m$  is found to increase from -0.15 V (C5(COOH), pH 7.0, 10 mM PB) to more positive values with increasing ionic strength and decreasing charge density on the SAM surface (Table S1, supporting information) until, at mixed C5(COOH)/C6(OH) SAMs and pH 5.5 (100 mM PB), it approaches the value determined for the HoxZ subunit in solution ( $E_{m, sol} = -0.086$  V). No difference was noted for  $E_m$  and  $n$  values comparing the isolated and MBH-integrated HoxZ subunit (Table 1).

TR SERR spectroscopic experiments were carried out to determine the formal heterogeneous electron transfer rate constant ( $k$ , hereby obtained at  $\Delta G = 0$  eV). For both the isolated- and MBH complex integral HoxZ subunit the same value of  $0.24 \pm 0.06$  s<sup>-1</sup> was determined.

**Table 1:** Redox properties of the immobilized HoxZ subunit in its isolated form and integrated in the HoxGKZ hetero-trimer. The data refer to the 6cLS species (100 mM PB, pH 5.5).

Protein	isolated HoxZ subunit	HoxZ in the hetro-trimer
SAM	C5(COOH) / C6(OH) (1:3)	C5(COOH)
$E_m / V$	$-0.085 \pm 0.02$	$-0.09 \pm 0.01$
$n$	$0.49 \pm 0.07$	$0.52 \pm 0.02$
$k / s^{-1}$	$0.24 \pm 0.06$	$0.24 \pm 0.06$

### Electron transfer and catalytic activity of the immobilized hetero-trimer

The participation of the HoxZ subunit in the H<sub>2</sub>-dependent electron transfer process of the immobilized hetero-trimer, was investigated by SERR spectroscopy. The inset in figure 4 shows the SERR spectra of the HoxZ subunit in the hetero-trimer immobilized on the electrode at open circuit. The heme *b* cofactors are almost fully oxidized under Ar atmosphere, as revealed by the prominent band at 1374 cm<sup>-1</sup>. Purging the solution with H<sub>2</sub>, however, leads to a fast reduction of the hemes. Similar experiments performed with the isolated HoxZ subunit did not cause any heme reduction upon purging with H<sub>2</sub> (data not shown). This finding indicates that – in analogy to the electron transfer pathway under physiological conditions – also in the immobilized state the electronic communication between the catalytic center and the HoxZ subunit is largely preserved.

SERR spectra measured consecutively following H<sub>2</sub> injection allowed determining the rate of H<sub>2</sub> induced heme *b* reduction (figure 4), yielding a value of  $0.15 \pm 0.05$  s<sup>-1</sup>. Note that this value represents an apparent rate constant of the overall reduction process that may either be limited by the reductive activation of the active site in the HoxG subunit or by the electronic communication between the HoxGK hetero-dimer and the HoxZ subunit. Also

partial limitation due to incomplete H<sub>2</sub> saturation in the beginning of the experiment can not be completely ruled out. The measured rate therefore can be seen as a minimum value for intramolecular electron transfer between HoxGK and HoxZ.

However, this rate is 60 times higher than the respective value obtained from a similar experiment with the [NiFe] hydrogenase from *Desulfovibrio vulgaris* Miyazaki F.<sup>20;35</sup> It was also shown before, that activation of “standard” (i.e. oxygen-sensitive) hydrogenases is much slower as compared to oxygen-tolerant hydrogenases.<sup>6</sup> The present data, therefore, clearly indicate an intact electrical communication between the subunits characteristic for the immobilized oxygen-tolerant MBH.

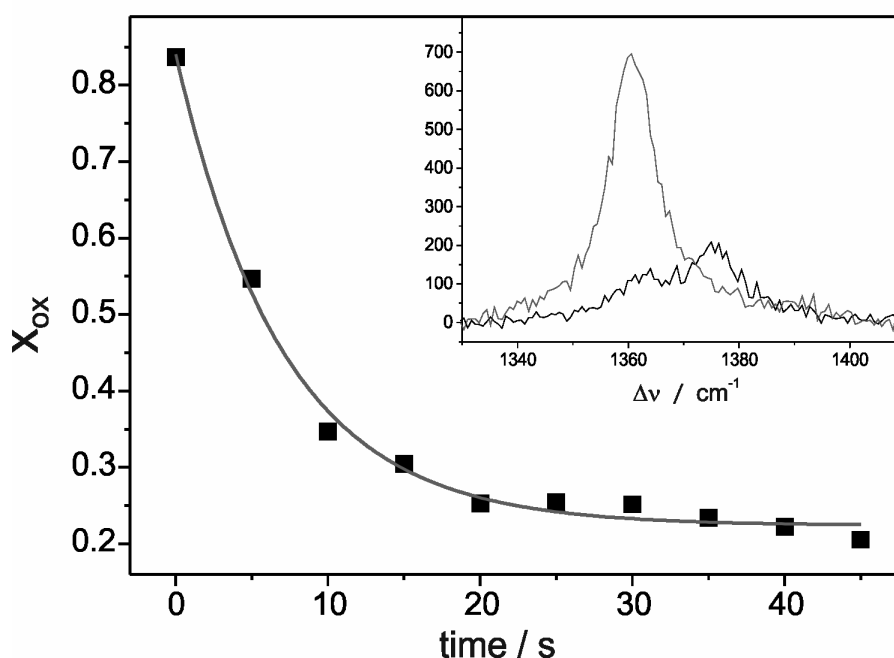


**Figure 4:** Relative concentration of the oxidized LS heme species of the immobilized hetero-trimeric at open circuit as a function of time after purging with H<sub>2</sub>. Inset: SERR spectra before (black) and 10 s after (gray) purging with H<sub>2</sub>. Experimental conditions: C5(COOH) SAM, 100 mM PB, pH 5.5.

After demonstrating the electrical communication of the HoxZ subunit with the HoxGK hetero-dimer on one hand, and with the electrode on the other hand, the overall electrochemical response of the immobilized HoxGKZ hetero-trimer was studied with PFV. The voltammetric signal recorded on a stationary electrode in solutions free of H<sub>2</sub> (Ar atmosphere) is shown in figure 5A. The negative current at -0.3 V corresponds to proton reduction. The H<sub>2</sub> produced by the enzyme at negative applied potentials, remains close to the electrode surface and is consumed in the reverse scan direction, exhibiting the sharp

catalytic oxidative peak at -0.24 V, similar to the “standard” [NiFe]-hydrogenase from *Allochromatium vinosum* adsorbed at stationary carbon electrodes.<sup>36</sup> The broad peak at -0.12 V is ascribed to the non-Faradic current of protonation-deprotonation equilibria of the SAM.<sup>37</sup>

Figure 5B shows the voltammetric trace of the immobilized HoxGKZ hetero-trimer under H<sub>2</sub> gas atmosphere. The sigmoidal-shaped plot is ascribed to enzymatic H<sub>2</sub> oxidation. This process has an onset potential of -0.26 V, which is more positive by 0.07 V than the potential of the H<sup>+</sup>/H<sub>2</sub> couple (figure 5B, vertical dotted line). Contrarily to measurements under Ar atmosphere, H<sup>+</sup> reduction was not observed for the hetero-trimer under H<sub>2</sub> atmosphere, probably because of product inhibition of this enzyme (i.e. at 1 bar H<sub>2</sub>, proton reduction is suppressed<sup>34</sup>). The arrows indicate the anaerobic inactivation and the reductive reactivation of the enzyme. The correspondent switch potential ( $E_{\text{switch}}$ ), denoted as the potential of maximum slope in the reductive reactivation direction,<sup>34</sup> is equal to 0.09 V. This value, which is related to the reactivation process,<sup>38</sup> is comparable to that obtained for the hetero-dimer on a pyrolytic graphite electrode (PGE) under similar experimental conditions, revealing comparable inflections at similar potentials.<sup>39</sup>

On the time scale of the experiments, the intensity of the catalytic current diminishes, although the overall shape of the voltammetric signal remains unchanged thus indicating reversible redox behaviour. The loss of current, quantified by comparing the loss between two consecutive scans, is about 5 – 10 % (figure S2). This behavior, already reported for the “standard” [NiFe]-hydrogenase from *Desulfovibrio vulgaris* Miyazaki F, is ascribed either to the irreversible degradation of the active site, caused by reactive oxygen species generated at the electrode during the voltammetric experiment,<sup>20</sup> or to enzyme desorption.<sup>34</sup>

To further elucidate the role of the HoxZ subunit in the catalytic electron transfer pathway, voltammetric experiments were also performed on the HoxGK hetero-dimer immobilized under the same experimental conditions as applied for the HoxGKZ hetero-trimer. Although in this case the HoxZ subunit was absent a protein film was formed affording the same voltammetric shape as the HoxGKZ hetero-trimer albeit with a much lower current (figure 5B).

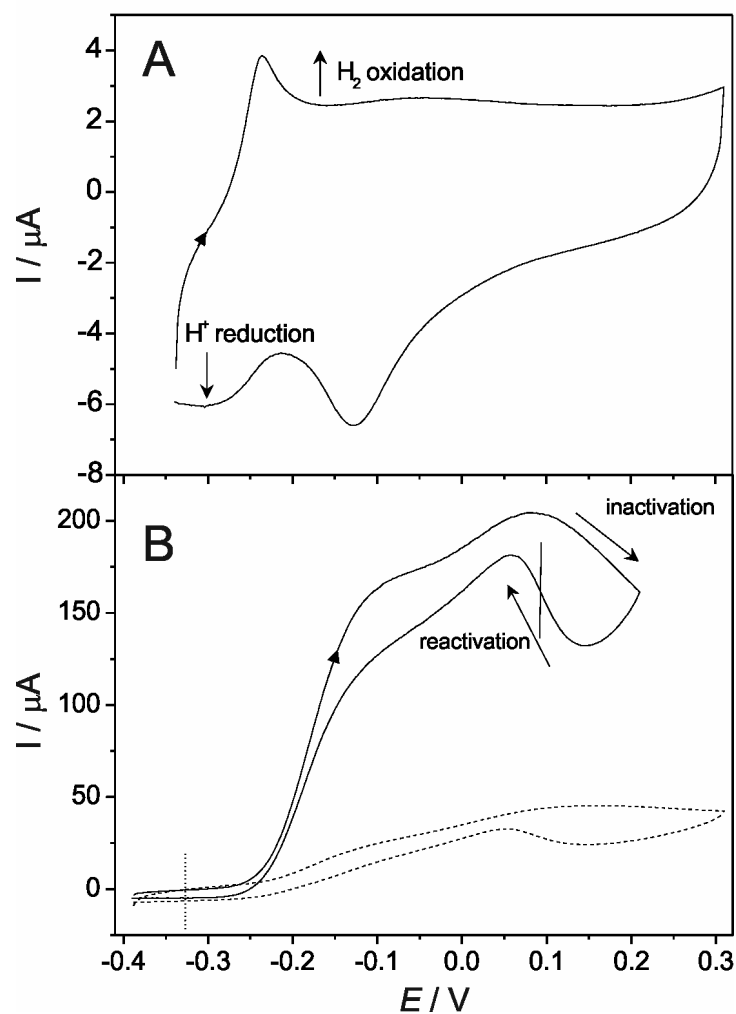


**Figure 5.** (A): Proton reduction and  $\text{H}_2$  re-oxidation by the hetero-trimer adsorbed on a stationary electrode under Ar gas atmosphere. The scan direction is indicated by an arrowhead (B): Anaerobic inactivation and reductive reactivation (marked by arrows) of the hetero-trimer (solid line) and hetero-dimer (dashed line) immobilized on a C5(COOH) SAM under  $\text{H}_2$  gas atmosphere. The scan direction is indicated by an arrowhead;  $E_{\text{switch}}$  is marked by a vertical bar. The dotted vertical line indicates the potential of the  $\text{H}^+/\text{H}_2$  couple under the experimental conditions (1 bar  $\text{H}_2$ , pH 5.5). The electrode was rotated at  $> 400$  rpm. Voltammograms were recorded at room temperature in solutions of 100 mM PB at a scan rate of  $\nu = 5 \text{ mV s}^{-1}$ .

## Discussion

### Immobilization

Surface potential calculations for the homology model of HoxZ reveal a positively charged binding domain that is likely to interact with negatively charged or polar headgroups of the SAM. This conclusion is consistent with the observation that the extent of adsorption, as reflected by the SERR intensity, decreases with lowering the charge density on carboxyl-terminated SAMs and thus weakening the electrostatic interactions with the protein either by decreasing the pH, increasing the ionic strength, or diluting the portion of carboxyl head groups via admixture of hydroxyl-terminated mercaptanes. Electrostatic interactions do not only control the adsorption equilibrium but also the structure of the cofactor sites of the immobilized protein. In analogy to previous findings for other heme proteins, strong local electrostatic fields are evidently capable to cause the dissociation of an axial ligand from the heme.<sup>16;33;40</sup> Thus, we conclude that the 5cHS species observed for the immobilized isolated HoxZ under strong electrostatic binding interactions refers to the heme *b* that is in closest proximity to the SAM surface.

A C5(COOH) SAM in 100 mM PB at pH 5.5 is associated with electrostatic interactions with the isolated- and the MBH complex-integral HoxZ subunit that are too weak to perturb the structure of the heme in closest proximity to the SAM but yet are strong enough to allow for binding of the protein to an extent that is sufficient for the spectroscopic and electrochemical characterization. Finally, the strength of the electrostatic interaction is also reflected by the redox potential shift  $\Delta E_{RC}$  defined as the difference between the redox potential of the immobilized protein ( $E_{m,SAM}$ ) and the protein in solution ( $E_{m,Sol}$ ).  $\Delta E_{RC}$  generally decreases with decreasing strength of electrostatic interactions,<sup>41</sup> which is consistent to the observed trend for  $\Delta E_{RC}$  in this work.

It is interesting to note that two separated redox potentials at +0.01 V and +0.16 V were reported for the HoxZ subunit of MBH in membrane fragments<sup>9</sup> whereas spectro-electrochemical titrations of the isolated and MBH complex-integral HoxZ subunit carried out in this work display only one redox transition around -0.09 V.

Attempts to immobilize HoxZ via the weakly negatively charged top side did not lead to unambiguous conclusions. Immobilizing the isolated HoxZ subunit on C6(NH<sub>2</sub>) SAMs in neutral solutions afforded essentially the same redox potential as determined for C5(COOH)

SAMs. Under these conditions HoxZ might be immobilized via the cationic bottom side, possibly via hydrogen bonding interactions to the non-protonated amino groups of the SAM. This conclusion is supported by the fact that decreasing the pH, corresponding to an increasing degree of protonation of the SAM, causes a decrease of the amount of adsorbed proteins such that at pH 5.5 no SERR spectrum can be obtained anymore.

### **Electrical communication and catalytic activity of the immobilized HoxGKZ heterotrimer**

It was shown that the immobilized heterotrimer is able to catalytically oxidize hydrogen and deliver electrons from its active site in HoxG to the HoxZ subunit. However, it is very unlikely that the HoxZ subunit is primarily involved in the transfer of these electrons to the electrode as observed in PFV experiments. On one hand, the onset potential of the catalytic current is around -0.26 V, which is far below the redox potential of the HoxZ. Therefore, both hemes of the subunit should be reduced at this electrode potential and, hence, not be able to accept electrons. On the other hand, the heterogeneous electron transfer rate determined by TR SERR spectroscopy ( $k = 0.24 \pm 0.06 \text{ s}^{-1}$ ) is too small to account for the strong catalytic current observed in PFV experiments, considering a turnover number of  $k_{\text{cat}} = 250 \text{ s}^{-1}$  estimated for the heterodimer on PGE.<sup>6</sup> The poor electron transfer from HoxZ to the electrode might be due to sterical hindrances caused by the detergent surrounding hydrophobic patches of HoxZ. Based on these considerations, the voltammetric signal shown in figure 5B is not mainly attributable to a heterotrimer shuttling electrons through the HoxZ subunit. On the first sight, the CV signal might be attributed to a fraction of heterodimer dissociated from the heterotrimer upon immobilization. This assumption, however, can be excluded since a voltammetric film consisting of the heterodimer revealed a lower catalytic current. Although this finding shows that the heterodimer alone may bind to the electrode upon retention of catalytic activity, further stabilization of the enzyme on the electrode is achieved by the HoxZ subunit.

It has to be noted at this point that in its biological context the HoxZ subunit unambiguously fulfills two functions, i.e. (i) anchoring the hydrogenase module to the membrane and (ii) transferring electrons to the quinone pool.<sup>9;42</sup> On the electrode HoxZ mainly performs a stabilizing function that could be related to its anchoring function in biological systems. Also an additional stabilizing function as an electron sink or supply should be considered.

Accordingly, we propose that immobilization preserves essentially the heterotrimer structure but opens two different electron pathways for electronic communication with the

electrode (figure 6): a slow one, transferring electrons from the distal Fe-S cluster to HoxZ and finally to the electrode, and a fast one, transferring electrons directly from the distal FeS cluster to the electrode. Whereas the slow HoxZ-mediated electron transfer is exclusively probed by SERR spectroscopy by monitoring heme reduction, PFV mainly probes the bypass from HoxK to the electrode. These two electron pathways are drawn schematically in figure 6. Further studies will be done to quantify this mechanism in more detail.

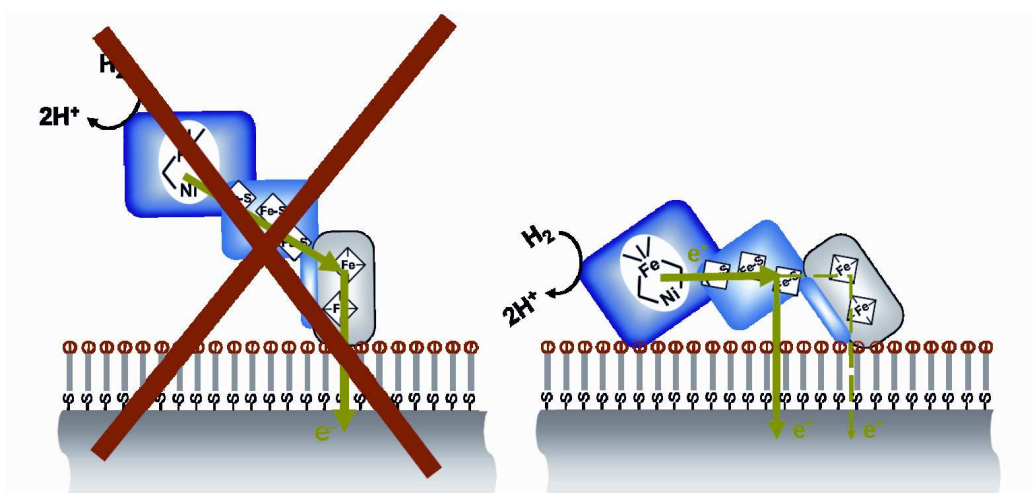


**Figure 6:** Schematic representation of the proposed orientation and electron transfer pathways for the HoxGKZ hetero-trimer on electrodes.

## Conclusions

Combined electrochemistry and SERR techniques were used to characterize the membrane-bound [NiFe]-hydrogenase hetero-trimer HoxGKZ and its isolated HoxZ subunit. Comparing the behavior of the whole enzyme with that of the HoxZ subunit, a model was derived to rationalize enzyme/electrode interactions. This model suggests that the hetero-trimeric unit is immobilized on the SAM-coated electrode via the positively charged side of the HoxZ subunit. The native heme pocket structure and the electrical communication between the HoxZ and the HoxGK units are largely preserved upon immobilization. However, due to a presumably close vicinity of the distal Fe-S cluster of the HoxGK hetero-dimeric module to the electrode, the electrons may be transferred from the active site of the enzyme to the electrode via two independent pathways: a route associated with a slow overall rate proceeding via the HoxZ subunit, and a faster pathway via the HoxGK module. In this scenario the role played by the HoxZ subunit is not crucial for the electron transfer process, but it contributes to the stabilization of the enzyme on the electrode.

**ACKNOWLEDGMENT:** The authors would like to thank the DFG (Cluster of excellence, UniCat), the Fonds der Chemischen Industrie (I.W.), and the Alexander von Humboldt Foundation (D.M).

**SUPPORTING INFORMATION:** Additional data on the different immobilization strategies and the potentiometric titration of the isolated HoxZ subunit.

## References

- (1) Vincent, K. A.; Cracknell, J. A.; Lenz, O.; Zebger, I.; Friedrich, B.; Armstrong, F. A. *Proc. Nat. Acad. Sci. USA* **2005**, *102*, 16951-16954.
- (2) Cammack, R; Frey, M.; Robson, R. *Hydrogen As a Fuel: Learning From Nature*, Taylor & Francis: London, 2001.
- (3) Krassen, H.; Schwarze, A.; Friedrich, B.; Ataka, K.; Lenz, O.; Heberle, J. *ACS Nano* **2009**, *3*, 4055-4061.
- (4) Friedrich, B.; Fritsch, J.; Lenz, O. *Curr. Opin. Biotech.* **2011**, *22*, 358-364.
- (5) Ludwig, M.; Cracknell, J. A.; Vincent, K. A.; Armstrong, F. A.; Lenz, O. *J. Biol. Chem.* **2009**, *284*, 465-477.
- (6) Cracknell, J. A.; Wait, A. F.; Lenz, O.; Friedrich, B.; Armstrong, F. A. *Proc. Nat. Acad. Sci. USA* **2009**, *106*, 20681-20686.
- (7) Saggu, M.; Zebger, I.; Ludwig, M.; Lenz, O.; Friedrich, B.; Hildebrandt, P.; Lenzian, F. *J. Biol. Chem.* **2009**, *284*, 16264-16276.
- (8) Goris, T.; Wait, A. F.; Saggu, M.; Fritsch, J.; Heidary, N.; Stein, M.; Zebger, I.; Lenzian, F.; Armstrong, F. A.; Friedrich, B.; Lenz, O. *Nat. Chem. Biol.* **2011**, *7*, 310-318.
- (9) Bernhard, M.; Benelli, B.; Hochkoepler, A.; Zannoni, D.; Friedrich, B. *Eur. J. Biochem.* **1997**, *248*, 179-186.
- (10) Lenz, O.; Ludwig, M.; Schubert, T.; Burstel, I.; Ganskow, S.; Goris, T.; Schwarze, A.; Friedrich, B. *ChemPhysChem* **2010**, *11*, 1107-1119.

- (11) Schink, B.; Schlegel, H. G. *Biochim. Biophys. Acta* **1979**, *567*, 315-324.
- (12) Knuttel, K.; Schneider, K.; Erkens, A.; Plass, W.; Muller, A.; Bill, E.; Trautwein, A. X. *Bull. Pol. Acad. Sci. Chem.* **1994**, *42*, 495-511.
- (13) Saggiu, M.; Teutloff, C.; Ludwig, M.; Brecht, M.; Pandelia, M. E.; Lenz, O.; Friedrich, B.; Lubitz, W.; Hildebrandt, P.; Lenzian, F.; Bittl, R. *Phys. Chem. Chem. Phys.* **2010**, *12*, 2139-2148.
- (14) Schneider, K.; Patil, D. S.; Cammack, R. *Biochim. Biophys. Acta* **1983**, *748*, 353-361.
- (15) Saggiu, M.; Ludwig, M.; Friedrich, B.; Hildebrandt, P.; Bittl, R.; Lenzian, F.; Lenz, O.; Zebger, I. *ChemPhysChem* **2010**, *11*, 1215-1224.
- (16) Murgida, D. H.; Hildebrandt, P. *J. Phys. Chem. B* **2001**, *105*, 1578-1586.
- (17) Feng, J. J.; Murgida, D. H.; Kuhlmann, U.; Utesch, T.; Mroginski, M. A.; Hildebrandt, P.; Weidinger, I. M. *J. Phys. Chem. B* **2008**, *112*, 15202-15211.
- (18) Sezer, M.; Spricigo, R.; Utesch, T.; Millo, D.; Leimkuehler, S.; Mroginski, M. A.; Wollenberger, U.; Hildebrandt, P.; Weidinger, I. M. *Phys. Chem. Chem. Phys.* **2010**, *12*, 7894-7903.
- (19) Wisitruangsakul, N.; Lenz, O.; Ludwig, M.; Friedrich, B.; Lenzian, F.; Hildebrandt, P.; Zebger, I. *Angew. Chem. Int. Ed.* **2009**, *48*, 611-613.
- (20) Millo, D.; Pandelia, M. E.; Utesch, T.; Wisitruangsakul, N.; Mroginski, M. A.; Lubitz, W.; Hildebrandt, P.; Zebger, I. *J. Phys. Chem. B* **2009**, *113*, 15344-15351.
- (21) Millo, D.; Pandelia, M. E.; Lubitz, W.; Hildebrandt, P.; Zebger, I. *Angew. Chem. Int. Ed.* **2011**, *50*, 2632-2634.
- (22) Frielingsdorf et al. *unpublished*
- (23) Wackerbarth, H.; Klar, U.; Gunther, W.; Hildebrandt, P. *Appl. Spec.* **1999**, *53*, 283-291.
- (24) Moss, D.; Nabedryk, E.; Breton, J.; Mantele, W. *Eur. J. Biochem.* **1990**, *187*, 565-572.
- (25) Arnold, K.; Bordoli, L.; Kopp, J.; Schwede, T. *Bioinformatics* **2006**, *22*, 195-201.
- (26) Jormakka, M.; Tornroth, S.; Byrne, B.; Iwata, S. *Science* **2002**, *295*, 1863-1868.
- (27) Humphrey, W.; Dalke, A.; Schulten, K. *J. Mol. Graphics* **1996**, *14*, 33-&.

- (28) MacKerell et al *J. Phys. Chem. B* **1998**, *102*, 3586-3616.
- (29) Baker, N. A.; Sept, D.; Joseph, S.; Holst, M. J.; McCammon, J. A. *Proc. Nat. Acad. Sci. USA* **2001**, *98*, 10037-10041.
- (30) Dolinsky, T. J.; Nielsen, J. E.; McCammon, J. A.; Baker, N. A. *Nucleic Acid. Res.* **2004**, *32*, W665-W667.
- (31) Berks, B. C.; Page, M. D.; Richardson, D. J.; Reilly, A.; Cavill, A.; Outen, F.; Ferguson, S. J. *Mol. Microbiol.* **1995**, *15*, 319-331.
- (32) Page, C. C.; Moser, C. C.; Chen, X. X.; Dutton, P. L. *Nature* **1999**, *402*, 47-52.
- (33) Wackerbarth, H.; Hildebrandt, P. *ChemPhysChem.* **2003**, *4*, 714-724.
- (34) Vincent, K. A.; Parkin, A.; Armstrong, F. A. *Chem. Rev.* **2007**, *107*, 4366-4413.
- (35) To avoid confusion: Only the reductive activation rate of the Ni<sub>i</sub>-B state in ref. 20 is taken into account for comparison.
- (36) Léger, C.; Jones, A. K.; Roseboom, W.; Albracht, S. P. J.; Armstrong, F. A. *Biochemistry* **2002**, *41*, 15736-15746.
- (37) Millo, D.; Bonifacio, A.; Ranieri, A.; Borsari, M.; Gooijer, C.; van der Zwan, G. *Langmuir* **2007**, *23*, 9898-9904.
- (38) Fourmond, V.; Infossi, P.; Giudici-Ortoni, M. T.; Bertrand, P.; Léger, C. *J. Am. Chem. Soc.* **2010**, *132*, 4848-4857.
- (39) Vincent, K. A.; Parkin, A.; Lenz, O.; Albracht, S. P. J.; Fontecilla-Camps, J. C.; Cammack, R.; Friedrich, B.; Armstrong, F. A. *J. Am. Chem. Soc.* **2005**, *127*, 18179-18189.
- (40) Weidinger, I. M.; Murgida, D. H.; Dong, W. F.; Möhwald, H.; Hildebrandt, P. *J. Phys. Chem. B* **2006**, *110*, 522-529.
- (41) Petrović, J.; Clark, R. A.; Yue, H. J.; Waldeck, D. H.; Bowden, E. F. *Langmuir* **2005**, *21*, 6308-6316.
- (42) Gross, R.; Pisa, R.; Sanger, M.; Lancaster, C. R. D.; Simon, J. *J. Biol. Chem.* **2004**, *279*, 274-281.



## Supporting Information

### Role of the HoxZ subunit in the electron transfer pathway of the membrane-bound [NiFe]-hydrogenase from *Ralstonia eutropha* immobilized on electrodes

Murat Sezer<sup>a</sup>, Stefan Frielingsdorf<sup>b</sup>, Diego Millo<sup>a</sup>, Nina Heidary<sup>a</sup>, Tillman Utesch<sup>a</sup>, Maria-Andrea Mroginski<sup>a</sup>, Bärbel Friedrich<sup>b</sup>, Peter Hildebrandt<sup>a</sup>, Ingo Zebger<sup>a</sup>, Inez M. Weidinger<sup>a\*</sup>

<sup>a</sup>Technische Universität Berlin, Insitut für Chemie, Straße des 17. Juni 135, 10623 Berlin. <sup>b</sup>Humboldt-Universität zu Berlin, Chausseestraße 117, 10115 Berlin.

**Table S1:** Redox properties of the immobilized isolated Cyt *b* domain under different conditions. The data refers to the 6c LS species.

SAM	C6(NH <sub>2</sub> )	C6(NH <sub>2</sub> )/ C6(OH) (1:3)		C5(COOH)			C5(COOH)/ C6(OH)(1:3)
		10mM pH7.0	100m pH7.0	10mM pH7.0	100mM pH7.0	100mM pH6.0	
PB- buffer	10mM pH7.0	10mM pH7.0	100m pH7.0	10mM pH7.0	100mM pH7.0	100mM pH6.0	100mM pH5.5
E <sub>m</sub> /V	-0.15 ±0.01	-0.125 ±0.02	-0.12 ±0.02	-0.14 ±0.02	-0.130 ±0.02	-0.11 ±0.01	-0.085 ±0.02
n	0.42 ±0.05	0.48 ±0.07	0.51 ±0.05	0.42 ±0.03	0.47 ±0.05	0.44 ±0.03	0.49 ±0.07
5cHSox [E=0.3V]	~ 20 %	~ 10 %	~0%	~ 40 %	~ 25 %	~ 15 %	0 - 10 %

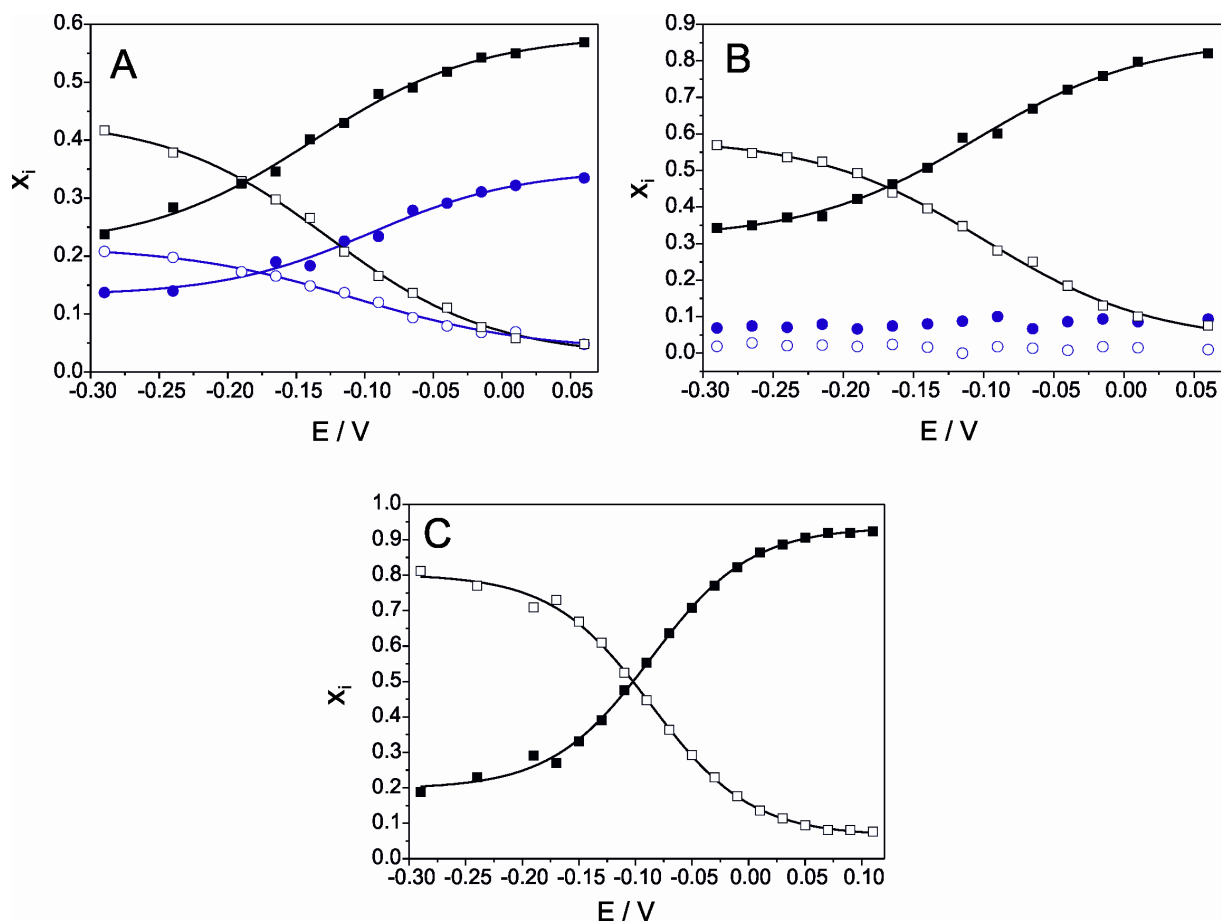


Figure S1: Potentiometric titration of the isolated HoxZ domain immobilized on (A) C5(COOH) (10 mM PB, pH 7.0) (B) C6(NH<sub>2</sub>) (10 mM PB, pH 7.0) and (C) C5(COOH)/C6OH (100 mM, pH 5.5) SAMs.  $x_{ox}(6cLS)$  (solid black squares),  $x_{red}(6cLS)$  (open black squares),  $x_{ox}(5cHS)$  (solid blue circles), and  $x_{red}(5cHS)$  (open blue circles).

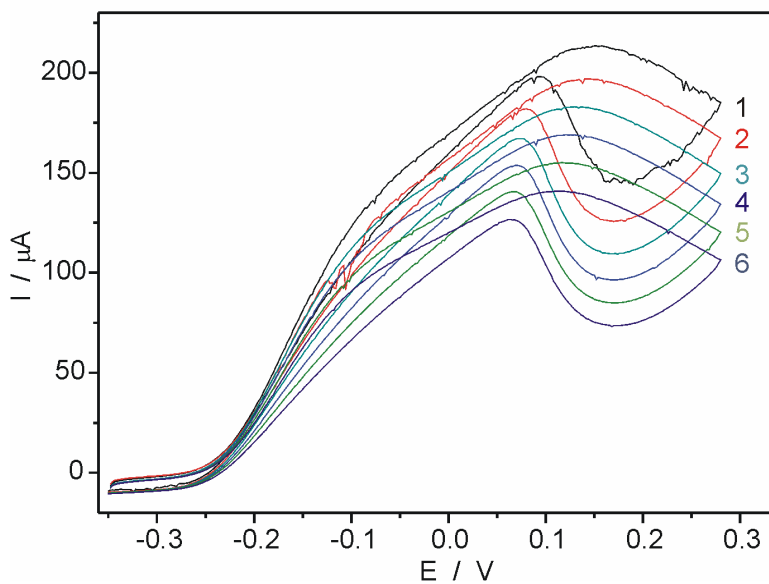


Figure S2: Voltammetric signal of HoxGKZ on C5(COOH) SAMs for consecutive scans.

## 8 Other Projects

During my PhD period I have also worked on projects which did not result in publications in scientific journals. Two of these projects are briefly presented in this chapter.

### 8.1 Surface Enhanced Resonance Raman Spectroscopic Investigations on Xenobiotic Reductase A

Xenobiotic reductase A (XenA) from *Pseudomonas Putida* 86 is a homo-dimeric enzyme with a subunit size of 39.8 kDa (for the apoprotein) [157]. It is involved in the metabolism of quinoline, which is a soluble, carcinogenic pollutant that is released to the environment in the course of coal mining [158]. *Pseudomonas Putida* 86 can grow using quinoline as the only source of carbon, nitrogen and energy, whereby XenA is assumedly catalysing a specific reduction of 8-hydroxycoumarin or coumarin, which are intermediates in the degradation pathway of quinoline [157]. The reaction center is a flavin-mononucleotide (FMN) cofactor.

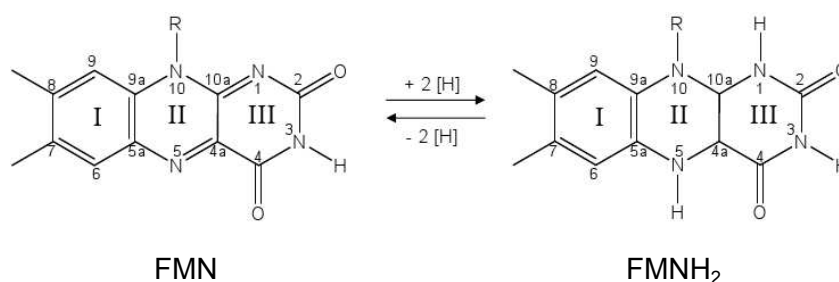


Figure 8.1.1: Reaction at the isoalloxazine motif of flavins. For flavin-monocleotide (FMN), the side chain R =  $-\text{CH}_2-\text{[CH(OH)]}_3-\text{CH}_2-\text{O}-\text{PO}_3^{2-}$ . The numbering is adopted from reference [160].

In the oxidised state, the FMN cofactor of XenA has a strong absorption in the blue region of the visible spectrum with a maximum at 464 nm [157, 159]. The absorption was used for spectrometric investigation of the catalytic reaction kinetics [159]. Our aim was to immobilise and to characterise XenA by surface enhanced resonance Raman spectroscopy. Theoretical calculations on the dimer revealed a very weak dipole moment of only  $\sim 55$  debye and a rather homogeneous surface potential distribution without a distinct charged binding patch around the cofactor region [164].

Upon 413 nm excitation at pH 6.0 – 6.5 strong SERR signals of the FMN cofactor were observed using amino-terminated SAMs on rough silver (figure 8.1.1.1 and 8.1.2.1). No signal was observed at pH 8.0 and/or using carboxyl-terminated SAMs, indicating the necessity of positive

surface charge density for adsorption.

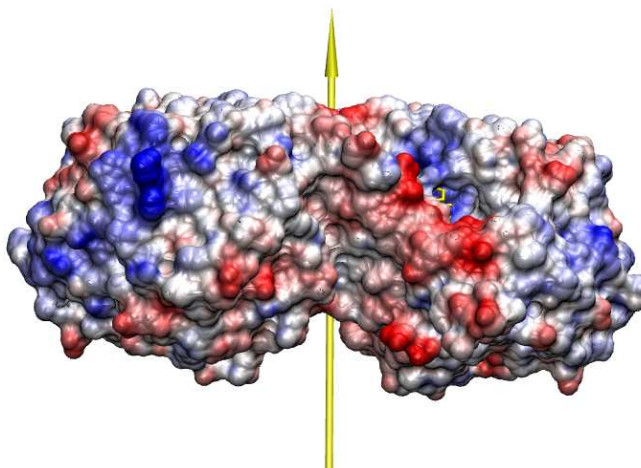


Figure 8.1.2 [164]: Dipole moment and surface potential distribution of the XenA dimer. A small part of the FMN cofactor of one monomers can be seen in yellow (top right).

As reported for many other proteins [160-163] and also observed in this work upon immobilisation on 6-aminohexanethiol (AHT) and 8-aminooctanethiol (AOT), the fluorescence of flavoproteins can be effectively oppressed upon immobilisation on silver substrates. Silver acts as an effective fluorescence quencher and may also provide vibrational surface enhancement. However, a huge fluorescence background was observed on silver coated with 11-aminoundecanethiol, indicating that for this SAM the separation of the fluorescent cofactor from the silver surface is too large for efficient quenching (not shown).

### 8.1.1 RR and SERR Spectra Using 8-Aminooctanethiol Coating

Obviously, either the whole enzyme, or the extracted cofactor only, interact with positively charged surfaces. Extraction of the cofactor was shown to occur for many flavoproteins in SERR experiments using silver colloids [163]. To figure out whether the SERR signal originates from the cofactor that is still incorporated in the enzyme or extracted, a similar experiment was carried out using only the isolated FMN cofactor (figure 8.1.1.1 c).

The band at  $1629\text{ cm}^{-1}$  in the RR spectrum of XenA can be designated as band I according to the nomenclature introduced by Bowman and Spiro [160]. No significant frequency changes upon adsorption onto AOT-coated electrodes is observed for this band, which consists of stretching modes of aromatic C-C bonds in ring I of the isoalloxazine motif (figure 8.1.1) [160]. On the contrary, a considerable downshift of  $\sim 9\text{ cm}^{-1}$  is observed for band II at  $1589\text{ cm}^{-1}$ . Band II mainly consists of C-N stretching modes in ring II and III [160]. A large shift of this band upon

immobilisation is reported also for other flavoproteins and is believed to be caused by an interaction of the N(3) heteroatom in ring III with the SERRS substrate [161, 162]. Other remarkable downshifts of  $\sim 7\text{ cm}^{-1}$  upon adsorption are observed for bands IV and VII at  $1500\text{ cm}^{-1}$  (RR:  $1506\text{ cm}^{-1}$ ) and  $1350\text{ cm}^{-1}$  (RR:  $1357\text{ cm}^{-1}$ ), respectively. Both bands contain contributions of  $\text{CH}_3$  deformation modes in ring III [160], hence a shift of these bands also points towards a strong SAM-cofactor interaction via ring III.

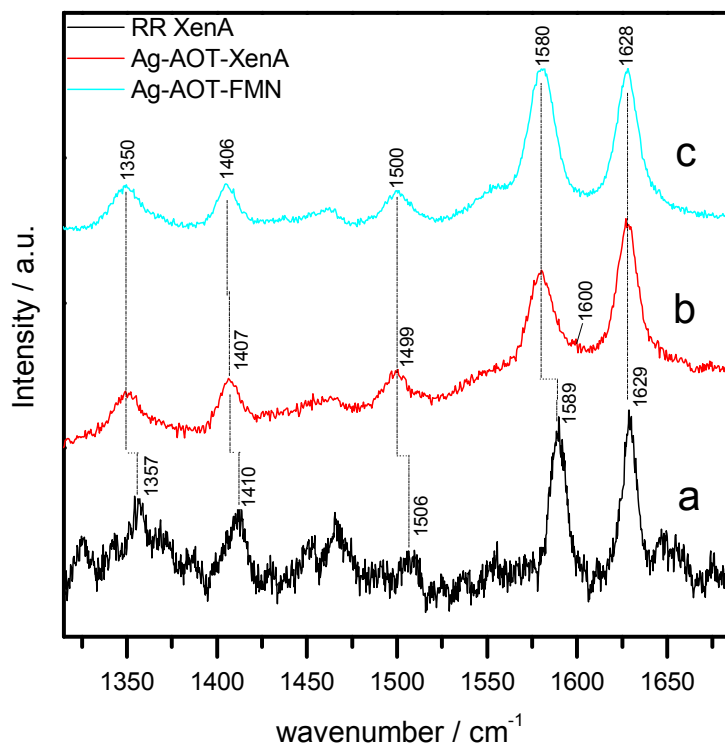


Figure 8.1.1.1: (a) Resonance Raman spectrum of XenA in 50mM Tris-HCl at pH 8.0 [7.4 mW, 20 s / 50 Acc]. (b) Surface enhanced resonance Raman spectrum of XenA and (c) the isolated FMN cofactor on 8-aminoactanethiol-coated electrodes at open circuit. The buffer solution for (b) and (c) was 10 mM Tris-HCl at pH 6.5 and the laser power was 2.5 mW. The spectra are normalised.

In the crystal structure of the XenA dimer reported by Griese et al. [157] an opening on the protein surface is present at the cofactor region (figure 8.1.2). However, in this structure the FMN cofactor is not oriented towards the opening with its ring III but rather with its ring I. An interaction of the N(3) heteroatom with the surface would therefore imply either a dramatic conformational change of the FMN binding site with respect to the crystal structure. In view of quite similar SERR band frequencies and spectral patterns of XenA and the isolated FMN cofactor (figure 8.1.1.1 b and c) another possibility, namely extraction of the cofactor, is more likely. On the other hand, the broad feature at  $1600\text{ cm}^{-1}$  in the SERR spectra of XenA is absent for the isolated FMN. This feature becomes more prominent during the SERR experiment and finally dominates the spectrum. It may be caused by impurities or degradation of the sample and was sometimes present to a

considerable extend even in the beginning of the SERR experiment. Hence, the reproducibility and signal stability was found to be insufficient for this system. Nevertheless, since the broad feature at  $1600\text{ cm}^{-1}$  is completely absent in the SERR spectra of the isolated FMN it is also a sign for an interaction of the protein matrix with the surface.

Because the reduced FMN does not absorb light in the visible range [157, 159], no SERR signal was expected to appear for reduced species due to the lack of resonance enhancement at 413 nm laser excitation. However, the signal was not diminished at  $-0.5\text{ V}$  (vs. Ag/AgCl 3M KCl). In solution measurements a value of  $-0.47\text{ V}$  was determined for the midpoint potential for the FMN / (FMN-H) $^{-1}$  couple at pH 8.0 [159]. Since the midpoint potential of the FMN is expected to increase at lower pH values [165] and adsorption onto positively charged surfaces [12], we would expect a fully reduced protein film at  $-0.5\text{ V}$ . However, potential controlled SERR using AOT coating only revealed a continuous irreversible decrease of the signal intensity with time, regardless of the applied electrode potential. This finding indicates poor electrochemical communication and potential and/or laser induced degradation of the immobilised XenA. Remarkably a similar irreversible decrease of the signal was observed for the isolated FMN cofactor.

### 8.1.2 SERR Spectra Using 6-Aminohexanethiol Coating

The SERR spectra on AHT clearly prove the existence of two different species, one of which has a similar spectrum as on AOT and reversibly diminishes at negative potentials. Despite the fact that the redox active species on AHT seems to be similar to the species observed on AOT, there was no electronic communication on AOT, which might be related to the slightly greater thickness of the AOT coating. The other species observed on AHT exhibits a different spectral pattern (band II at  $1593\text{ cm}^{-1}$ , band VII at  $1359\text{ cm}^{-1}$ ) and is inactive with respect to the electrode potential (figure 8.1.2.1). During the SERRS experiment the spectrum of this species, which is in the following denoted as the inactive form, gain more and more intensity. Obviously, the initially redox active XenA immobilised on AHT-coated electrodes undergoes an irreversible change into the inactive form. This process seems to be accelerated when a potential is applied on the electrode.

The broad feature at  $1600\text{ cm}^{-1}$  appears and gains more intensity during the experiment also on AHT coatings. Apart from this, only the inactive form contributes to the SERR spectrum at negative potentials. Remarkably, the frequencies of band I, II and VII for the inactive form are quite similar to the respective positions in the RR spectrum of XenA (figure 8.1.1.1 a). From this observation it may be concluded that the FMN cofactor in the inactive form does not interact with the AHT coating via the N(3) heteroatom, at least not in a similar manner as in the active form. Direct contact between N(3) and silver was shown to be required for SERRS at colloidal silver

[162]. Obviously, this does not apply for the system presented here. However, the data can be interpreted in a way that this interaction, together with a sufficiently short separation from the electrode surface, is required for electronic communication between the electrode and the FMN cofactor.

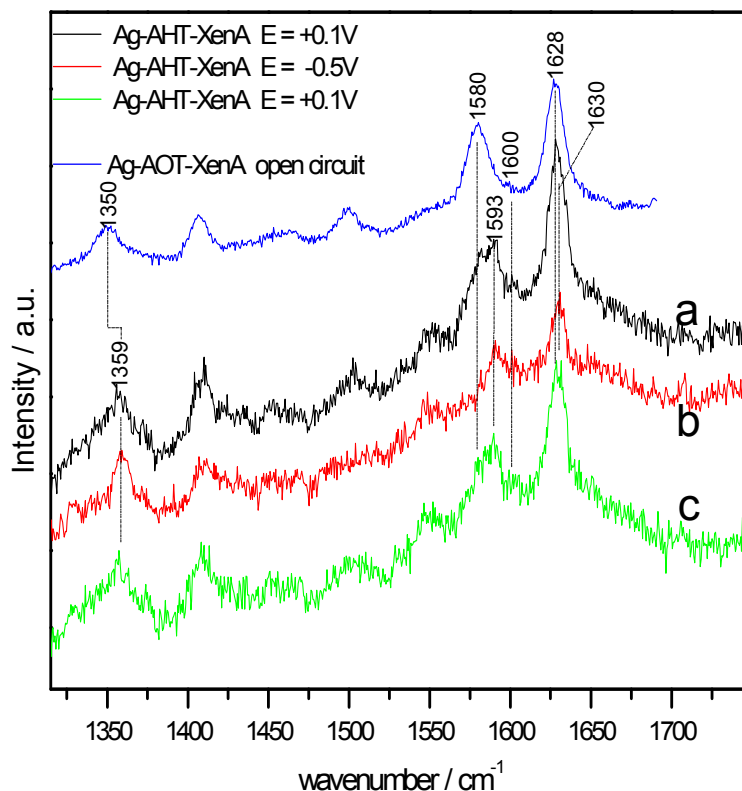


Figure 8.1.2.1: SERR spectra of XenA on AHT coating at different electrode potentials. The spectra were collected chronologically in alphabetical order from (a) to (c). The SERR spectrum of XenA on AOT coatings is also included for comparison. The buffer solution was 10 mM Tris-HCl pH 6.5 and the laserpower was  $\sim 2.5$  mW. Potentials are reported vs. Ag/AgCl 3M KCl. The spectra are normalised.

In summary, the SERR spectra of XenA indicate the presence of FMN that is not bound to the protein. This might be due to extraction of FMN from the enzyme and/or to sample impurities. The samples that were used for experiments contain traces of free FMN, which was used for the reconstitution of the holoenzyme and specifically binds to the SAM surface. Nevertheless, a SERR spectrum that resembles the RR spectrum was observed using AHT coating and is most likely related to protein-bound FMN. However, an advanced purification protocol is required for unambiguous assignment and further SERR spectroscopic investigations only make sense if samples that do not contain free FMN can be provided.

## 8.2 Resonance Raman Spectroscopic Investigations of Mitochondria Preparations from Mouse Pancreas

The aim of this project was to examine the conformational state of cytochrome *c* in intact and caerulein exposed mitochondria preparations. Caerulein is a specific decapeptide obtained from the skin of hila caerulea, an Australian amphibian. It is known to induce necrotizing pancreatitis in mice [166]. It was recently shown that cytochrome *c* (Cyt *c*) is involved in different processes in the apoptosis of mammalian cells [167-169]. Apoptosis is the biochemically regulated program for the physiological elimination of irreversibly damaged or unwanted cells. During this process, Cyt *c* is released from the mitochondria into the cytosol, where it binds to the outer membrane and undergoes structural alterations resulting in a significantly decreased midpoint potential and enhanced peroxidase activity [167-171]. The most crucial structural alteration that is associated with increased peroxidase activity is the rupture of the Fe-S bond to the axial met80-ligand leading to a 5c high spin state [170]. This state was observed in carboxymethylated Cyt *c* [174] and upon adsorption of native Cyt *c* on cardiolipin [170], other negatively charged surfaces and on electrodes [172, 173]. Since this state, also denoted as state B2 [3], occurs upon binding to the outer mitochondria membrane after release of Cyt *c* to the cytosol [170], mitochondria samples prepared under different conditions are expected to contain different contents of state B2. In fact, different B2 contents were previously shown with resonance Raman spectroscopy for mitochondria preparations from bovine heart and rat liver [174].

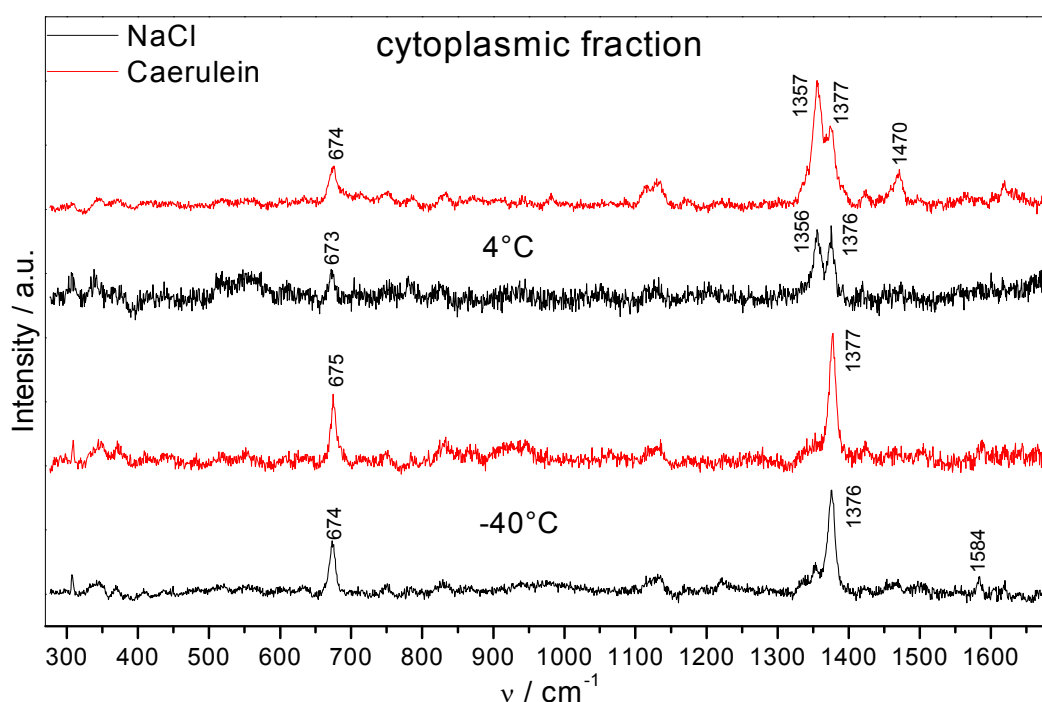


Figure 8.2.1: Resonance Raman spectra of the cytoplasmic fraction of mitochondria preparations from sodium chloride and caerulein exposed mice pancreas at different temperatures.

In figure 8.2.1 resonance Raman spectra from the cytoplasmic fraction of different mitochondria sample preparations are shown. These samples are obtained from differential centrifugation which allows for separation of the cytoplasmic fraction (containing dissolved Cyt c) from the microsomal fraction (containing vesicles/vacuoles) and a heavy fraction (containing membrane fragments with membrane bound Cyt c). The spectra of the frozen sample at  $-40\text{ }^{\circ}\text{C}$  clearly show the presence of an oxidised heme species, however, the spectra are not attributable to Cyt c. In the liquid phase at  $+4\text{ }^{\circ}\text{C}$  a partial reduction of the heme species is observed due to photoreduction [175]. In figure 8.2.2 the spectra of the microsomal fraction and 'heavy' fraction are shown.

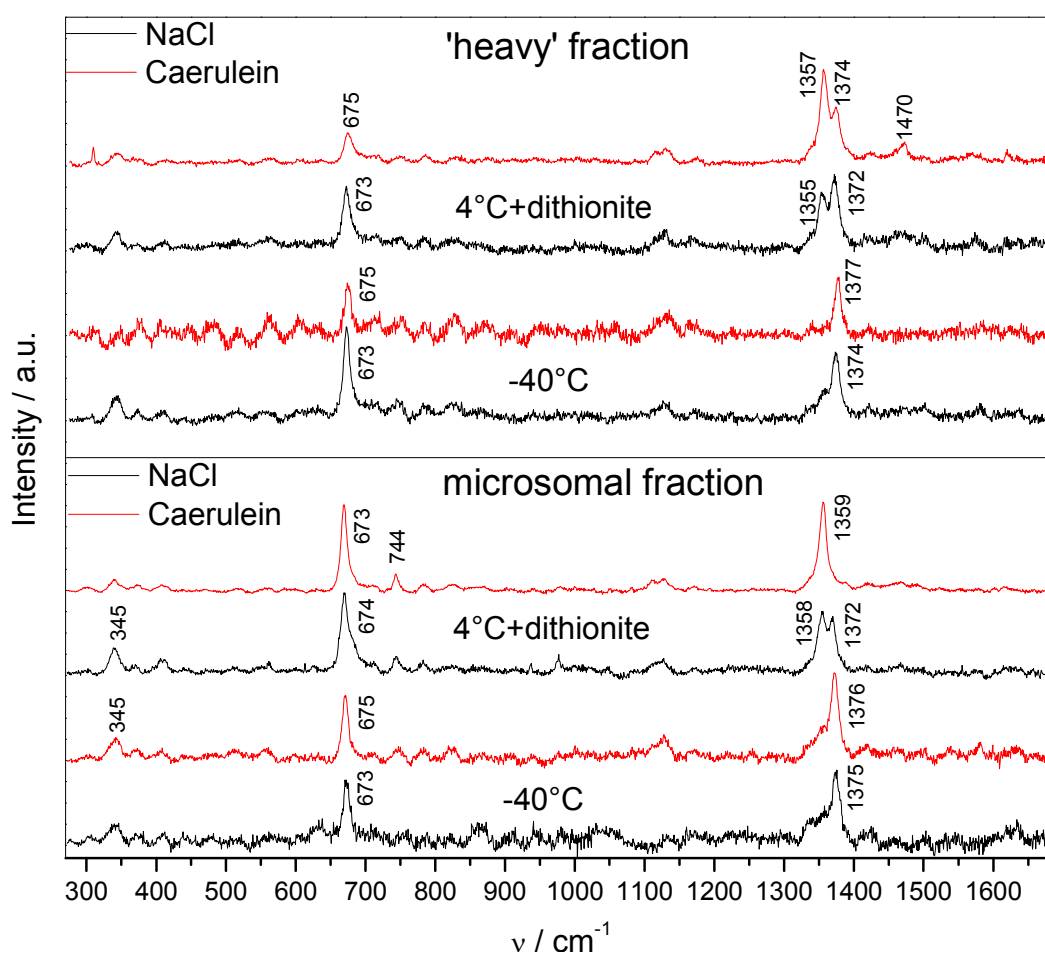


Figure 8.2.2: Resonance Raman spectra of the microsomal and heavy fraction of mitochondria preparations from sodium chloride and caerulein exposed mice pancreas at different temperatures.

A significantly lower extent of photoreduction was found for the more viscose microsomal and heavy mitochondria fractions. Therefore, dithionite was added to the samples at  $+4\text{ }^{\circ}\text{C}$  in order to obtain vibrational signals from the respective reduced species. However, here again, none of the spectra is attributable to any form of Cyt c, which was actually expected to dominate the spectra of these sample preparations.



## 9 Conclusion and Outlook

This work contributed to two different aspects within the research field of resonance Raman (RR) and surface enhanced resonance Raman (SERR) spectroscopy of chromophore containing proteins. One aspect was related to the development of advanced functional support materials for potential controlled surface enhanced (resonance) Raman spectroscopy. The optical and electrochemical performance of recently developed silver-gold hybrid devices as support materials was explored. Other projects within this work were related to the analysis of interfacial processes of heme enzymes. The study of human sulphite oxidase and membrane bound hydrogenase from *Ralstonia eutropha* H16 substantially contributed to the understanding of immobilised enzymes and the parameters that determine their structural integrity, stability, catalytic performance and electronic communication with conductive support materials.

### 9.1 Silver-Gold Hybrid Devices

The electrochemical and optical performance of novel silver-gold hybrid devices was explored. In these devices a thin gold island film is separated by amino-terminated self assembled monolayers (spacer SAMs) from an electrochemically roughened silver support. The devices were found to exhibit optical enhancement factors and profiles that are comparable to pure silver supports. At the same time they exhibit the surface chemistry and biocompatibility of gold.

Heterogeneous electron transfer (ET) between immobilised HHCyt *c* and the multilayer device was found to be limited by electron tunnelling through the spacer SAM or an outer SAM deposited on the outer gold film. Surprisingly, decreasing ET rates with decreasing spacer SAM thickness were found and rationalised in terms higher amounts of impurities and/or defects in shorter spacer SAMs. The potential of zero charge of an Ag-AUT-MDHA hybrid device was determined to be in between of MDHA-coated silver and gold supports and, accordingly, the magnitude of acceleration of heterogeneous reduction rates with increasing overpotential was found to lie between those of silver and gold.

Silver-gold hybrid devices represent excellent support materials for SE(R)R spectro-electrochemistry. In principle, the concept of separating an island film by an insulating spacer material from a rough silver surface in order to obtain optical enhancement properties of the

underlying silver and the surface chemistry of the overlying island film material should also work for different spacer and island film materials, respectively. In fact, silica coatings as spacer materials can be applied in the synthesis of modified silver-gold hybrid devices with improved long-term stability and reusability [132]. Also different metal film materials, e.g. platinum, can be applied. This opens up the possibility of designing functional materials with interesting surface chemistry that can be monitored and controlled by SER(R) spectro-electrochemistry.

## 9.2 Human Sulphite Oxidase

Potential controlled surface enhanced resonance Raman (SERR) spectroscopy was applied to monitor the cytochrome *b5* (Cyt *b5*) domain of human sulphite oxidase (hSO) immobilised on amino-terminated self assembled monolayer (SAM) coated rough silver electrodes. Structural and electronic properties of the Cyt *b5* domain and its role during catalysis were studied. Protein film voltammetry was applied on the same electrode/enzyme system and provided additional information on the catalytic performance of hSO in the immobilised state.

An increased heterogeneous ET rate, up-shifted midpoint potentials of the Cyt *b* domain, and increased catalytic activity of the immobilised enzyme were observed upon increasing the ion concentration of the buffer solution, thus weakening of electrostatic interaction forces of the enzyme with the SAM. Experimental results, theoretical calculations on the surface potential distribution, and comparative studies of the isolated Cyt *b5* domain suggest that at high buffer concentrations the Cyt *b5* is not bound to the surface and the enzyme is immobilised exclusively via its dimerisation domain to the SAM. This finding, together with improved catalytic performance and electronic communication at higher buffer concentrations, suggests that high flexibility of the Cyt *b5* domain is required for catalysis. This is in accordance with previous studies on analogous sulphite oxidases in solution.

The combined SERR spectroscopic and electrochemical study of hSO provided insight into fundamental enzymatic processes at the SAM/protein interface. Knowledge about these processes may not only be relevant for further studies on hSO but also for improving enzyme based bio-electronic devices in general.

### 9.3 Membrane Bound Hydrogenase from *Ralstonia eutropha* H16

A combined electrochemical and potential controlled surface enhanced resonance Raman (SERR) spectroscopic study of the entire HoxGKZ hetero-trimer and the isolated HoxZ domain of the membrane bound hydrogenase from *Ralstonia eutropha* H16 (MBH) was performed. The HoxZ domain, which is a di-heme cytochrome *b* (Cyt *b*) unit, could be immobilised onto negatively charged and polar SAM surfaces and electronic communication with the silver electrode was observed. The heterogeneous ET kinetics between the heme cofactor(s) and the silver electrode was found to be slow ( $k = 0.24 \text{ s}^{-1}$ ).

At high negative surface charge densities, partial spin conversion from the native 6cLS to a 5cHS state was observed. The spin states were found to be in an equilibrium that was shifted towards the native species upon weakening of electrostatic interaction forces by decreasing the negative surface charge density and/or increasing the buffer concentration. However, weakening of electrostatic interaction forces resulted in decreased SERR signal intensities. In SERR spectroscopy of proteins, structural integrity on the one hand, and strong interaction with the surface, corresponding to high signal intensities on the other hand, often represent a dichotomy that needs to be balanced out for each biomolecule.

Experimental conditions at which the native heme pocket structure of the HoxZ domain was preserved were adopted in the study of the entire HoxGKZ hetero-trimer. In the immobilised state, the HoxZ domain of the entire hetero-trimer exhibited similar structural and electronic features as the isolated HoxZ. In case of the immobilised HoxGKZ low enzymatic hydrogen evolution at negative potentials under inert gas atmosphere and high hydrogen oxidation activity at higher potentials under hydrogen supply was observed with protein film voltammetry. As proven by SERR spectroscopy, electrons from enzymatic hydrogen oxidation are transferred to hemes of the HoxZ domain. The observed rate of the catalytic heme reduction is low ( $k = 0.15 \text{ s}^{-1}$ ) and includes transport of hydrogen to the electrode, reductive activation of the enzyme and intramolecular electron transfer.

On the basis of these findings, a model was derived to rationalise SAM/enzyme interactions. Further studies are required to support this model. While SERR spectroscopy was shown to be appropriate to monitor the heme cofactor(s) in the HoxZ domain, surface enhanced infrared absorption spectroscopy can be applied to monitor the [NiFe] active site in the HoxG of immobilised MBH. In addition, further Raman and EPR spectroscopic investigations can be performed to monitor and characterise the FeS clusters in the HoxK domain.



## 10 References

- [1] F. Siebert and P. Hildebrandt, *Vibrational Spectroscopy in Life Sciences*, WILEY-VCH, Weinheim, 2008.
- [2] D. H. Murgida and P. Hildebrandt, *Acc. Chem. Res.*, 2004, **37**, 854 – 861.
- [3] D. H. Murgida and P. Hildebrandt, *Phys. Chem. Chem. Phys.*, 2005, **7**, 3773 – 3784.
- [4] J. A. Sánchez-Gil and J. V. Garcia-Ramos, *J. Chem. Phys.*, 1998, **108**, 317.
- [5] M. Sezer, R. Spricigo, T. Utesch, D. Millo, S. Leimkübler, M. A. Mroginski, U. Wollenberger, P. Hildebrandt and I. M. Weidinger, *Phys. Chem. Chem. Phys.*, 2010, **12**, 7894 – 7903.
- [6] K. A. Vincent, A. Parkin and F. Armstrong, *Chem. Rev.*, 2007, **107**, 4366 – 4413.
- [7] D. H. Murgida and P. Hildebrandt, *Angew. Chem. Int. Ed.*, 2001, **40**, 728.
- [8] M. Sezer, S. Frielingsdorf, D. Millo, N. Heidary, T. Utesch, M. A. Mroginski, B. Friedrich, P. Hildebrandt, I. Zebger and Inez M. Weidinger, *J. Phys. Chem. B*, 2011, accepted.  
DOI: 10.1021/jp204665r
- [9] J. C. Love, L. A. Estroff, J. K. Kriebel, R. G. Nuzzo, G. M. Whitesides, *Chem. Rev.*, 2005, **105**, 1103–1170.
- [10] M. Gouterman, 'Optical spectra and electronic structure in porphyrins and related rings' in 'The Porphyrins', pp 1 – 156, D. Dolphin (Ed.), Vol. III, part A, Academic Press, New York, 1979.
- [11] J.-J. Feng, U. Gernert, M. Sezer, U. Kuhlmann, D. H. Murgida, C. David, M. Richter, A. Knorr, P. Hildebrandt and I. M. Weidinger, *Nano Lett.*, 2009, **9**, 298 – 303.
- [12] M. Sezer, J.-J. Feng, H. K. Ly, Y. Shen, T. Nakanishi, U. Kuhlmann, P. Hildebrandt, H. Möhwald and I. M. Weidinger, *Phys. Chem. Chem. Phys.*, 2010, **12**, 9822 – 9829.
- [13] M. S. Brody and R. Hille, *Biochemistry*, 1999, **38**, 6668 – 6677.
- [14] S. J. Elliott, A. E. McElhaney, C. Feng, J. H. Enemark and F. A. Armstrong, *J. Am. Chem. Soc.*, 2002, **124**, 11612 – 11613.
- [15] E. E. Ferapontova, T. Ruzgas and L. Gorton, *Anal. Chem.*, 2003, **75**, 4841 – 4850.
- [16] I. Willner and E. Katz, *Bioelectronics*, Wiley-VCH, Weinheim, 2005.
- [17] D. Chen, G. Wang and J. H. Li, *J. Phys. Chem. C*, 2007, **111**, 2351.
- [18] M. Ludwig, J. A. Cracknell, K. A. Vincent, F. A. Armstrong and O. Lenz, *Journal of Biological Chemistry*, 2009, **284**, 465 – 477.
- [19] J. A. Cracknell, A. F. Wait, O. Lenz, B. Friedrich, F. A. Armstrong, *P. Natl. Acad. Sci. USA*, 2009, **106**, 20681 – 20686.
- [20] R. Cammack, M. Frey, R. Robson, *Hydrogen As a Fuel: Learning From Nature*, Taylor & Francis, London, 2001.
- [21] K. A. Vincent, J. A. Cracknell, O. Lenz, I. Zebger, B. Friedrich and F. A. Armstrong, *P. Natl. Acad. Sci. USA*, **2005**, *102*, 16951 – 16954.

- [22] B. Bowien and H. G. Schlegel, *Annu. Rev. Microbiol.*, 1981, **35**, 405 – 452.
- [23] M. Bernhard, B. Benelli, A. Hochkoeppler, D. Zannoni and B. Friedrich, *European Journal of Biochemistry*, 1997, **248**, 179 – 186.
- [24] O. Lenz, M. Ludwig, T. Schubert, I. Bürstel, S. Ganskow, T. Goris, A. Schwarze and B. Friedrich, *CHEMPHYSICHEM*, 2010, **11**, 1107 – 1119.
- [25] K. Knüttel, K. Schneider, A. Erkens, W. Plass, A. Muller, E. Bill and A. X. Trautwein, *Bulletin of the Polish Academy of Sciences-Chemistry*, 1994, **42**, 495 – 511.
- [26] K. Schneider, D. S. Patil and R. Cammack, *Biochimica et Biophysica Acta*, 1983, **748**, 353 – 361.
- [27] N. Wisitruangsakul, O. Lenz, M. Ludwig, B. Friedrich, F. Lenzian, P. Hildebrandt and I. Zebger, *Angew. Chem. Int. Ed.*, 2009, **48**, 611 – 613.
- [28] M. Saggiu, M. Ludwig, B. Friedrich, P. Hildebrandt, R. Bittl, F. Lenzian, O. Lenz and I. Zebger, *CHEMPHYSICHEM*, 2010, **11**, 1215 – 1224.
- [29] The purification procedure was developed by Dr. Stefan Frielingsdorf at the Humboldt University Berlin and will be published soon.
- [30] S. J. George, S. Kurkin, R. N. F. Thorneley and S. P. J. Albracht, *Biochemistry*, 2004, **43**, 6808 – 6819.
- [31] S. Kurkin, S. J. George, R. N. F. Thorneley and S. P. J. Albracht, *Biochemistry*, 2004, **43**, 6820 – 6831.
- [32] E. B. Wilson, J. C. Decius, P.C. Cross, *Molecular Vibrations: The Theory of Infrared and Raman Vibrational Spectra*, McGraw-Hill, New York, 1995.
- [33] H. A. Kramers and W. Heisenberg, *Z. Phys.*, 1925, **31**, 681 – 708.
- [34] P. A. M. Dirac, *Proc. Roy. Soc. Lond. A*, 1927, **114**, 243 – 265.
- [35] P. A. M. Dirac, *Proc. Roy. Soc. Lond. A*, 1927, **114**, 710 – 728.
- [36] G. Breit, *Rev. Mod. Phys.*, 1932, 504–576.
- [37] A. C. Albrecht, *J. Chem. Phys.*, 1961, **34**, 1476 – 1484.
- [38] A. Warschel and P. Dauber, *J. Chem. Phys.*, 1977, **66**, 5477 – 5488.
- [39] R. S. Czernuszewicz and T. G. Spiro, *IR, Raman, and Resonance Raman Spectroscopy*, in *Inorganic Electronic Structure and Spectroscopy*, Vol. 1, John Wiley & Sons, Inc, 1999.
- [40] D. A. Long, *The Raman Effect: A Unified Treatment of the Theory of Raman Scattering by Molecules*, John Wiley & Sons Ltd, 2002.
- [41] H. Miyake, S. Ye and M. Osawa, *Electrochem. Commun.*, 2002, **4**, 973 – 977.
- [42] Y. Hirai, H. Yabu, Y. Matsuo, K. Ijiro and M. Shimomura, *Chem. Commun.*, 2010, 46, 2298 – 2300.
- [43] P. Hildebrandt and M. Stockburger, *J. Phys. Chem.*, 1984, **88**, 5935 – 5944.
- [44] S. J. Lee, Z. Guan, H. Xu and M. Moskovits, *J. Phys. Chem. C*, 2007, **111**, 17985 – 17988.
- [45] M. Moskovits, *Rev. Mod. Phys.*, 1985, **57**, 783 – 826.

- [46] D. K. Schwartz, *Annu. Rev. Phys. Chem.*, 2001, **52**, 107 – 137.
- [47] P. E. Laibinis, G. M. Whitesides, D. L. Allara, Y. T. Tao, A. N. Parikh and R. G. Nuzzo, *J. Am. Chem. Soc.*, 1991, **113**, 7152 – 7167.
- [48] R. A. Marcus, *J. Chem. Phys.*, 1956, **24**, 966 – 978.
- [49] R. A. Marcus and N. Sutin, *Biochimica et Biophysica Acta*, 1985, **811**, 265 – 322.
- [50] J. Jortner, *J. Chem. Phys.*, 1976, **63**, 4358 – 4368.
- [51] L. D. Zusman, *Z. Phys. Chem.*, 1994, **186**, 1.
- [52] M. D. Newton, N. Sutin, 1984, *Annu. Rev. Phys. Chem.*, 35, 437.
- [53] E. Fermi, *Nuclear Physics*, University of Chicago Press, 1950.
- [54] J. R. Bolton and M. D. Archer, *Basic Electron-Transfer Theory*, in *Electron Transfer in Inorganic, Organic, and Biological Systems*, American Chemical Society, 1991.
- [55] T. M. Nahir, R. A. Clark and E. F. Bowden, *Anal. Chem.*, 1994, **66**, 2595 – 2598.
- [56] P. Hildebrandt and D. H. Murgida, *Bioelectrochemistry*, 2002, **55**, 139 – 143.
- [57] L. D. Zusman, *Chem. Phys.*, 1980, **49**, 295.
- [58] E. Laviron, *J. Electroanal. Chem.*, 1979, **101**, 19 – 28.
- [59] M. I. Promdromidis, A. B. Florou, S. M. Tzouwara-Karayanni and M. I. Karayannis, *Electroanalysis*, 2000, **12**, 1498 – 1501.
- [60] R. Goldstein, *Pockels Cell primer*, in *Laser Focus Magazine*, 1968.  
<http://www.fastpulse.com/pdf/pcp.pdf>
- [61] Figure 3.4 is based on: <http://www.raman.re.kr/technote/image/LabRam-HR.gif>
- [62] MATLAB is a product of Mathworks®.
- [63] <http://www.gnu.org/software/octave/>
- [64] H. Wackerbarth, U. Klar, W. Gunther and P. Hildebrandt, *Appl. Spec.*, 1999, **53**, 283 – 291.
- [65] Scanning electron microscope images were recorded by Dipl.-Ing. Ulrich Gernert at the 'Zentraleinrichtung Elektronenmikroskopie' at the Technical University Berlin.
- [66] A. L. De Lacey, V. M. Fernandez, M. Rousset and R. Cammack, *Chem. Rev.*, 2007, **107**, 4304 – 4330.
- [67] A. Kranich, H. K. Ly, P. Hildebrandt and D. H. Murgida, *J. Am. Chem. Soc.*, 2008, **130**, 9844 – 9848.
- [68] N. Wisitruangsakul, I. Zebger, H. K. Ly, D. H. Murgida, S. Ekgasit and P. Hildebrandt, *Phys. Chem. Chem. Phys.*, 2008, **10**, 5276 – 5286.
- [69] S. Döpner, P. Hildebrandt, A. G. Mauk, H. Lenk and W. Stempfle, *Spectrochim Acta A*, 1996, **51**, 573 – 584.
- [70] S. Oellerich, H. Wackerbarth and P. Hildebrandt, *J. Phys. Chem. B*, 2002, **106**, 6566 – 6580.
- [71] R. Hille, *Chem. Rev.*, 1996, **96**, 2757 – 2816.
- [72] U. Wollenberger, R. Spricigo, S. Leimkühler and K. Schröder, *Adv. Biochem. Eng. Biotechnol.*, 2008, **109**, 19 – 64.

- [73] C. Kisker, H. Schindelin, A. Pacheco, W. A. Wehbi, R. M. Garrett, K. V. Rajagopalan, J. H. Enemark and D. C Rees, *Cell*, 1997, **91**, 973 – 83.
- [74] R. M. Garrett, J. L. Johnson, T. N. Graf, A. Feigenbaum and K. V. Rajagopalan, *Proc. Natl. Acad. Sci. USA*, 1998, **95**, 6394 – 6398.
- [75] J. L. Johnson, *Prenat Diagn*, 2003, **23**, 6 – 8.
- [76] D. B. Menzel, D. A. Keller and K. H. Leung, *Adv. Exp. Med. Biol.*, 1986, **197**, 477 – 492.
- [77] The homology model and structure representation was created by Tillmann Utesch. The designations of representation modes (new cartoon and van der Waals, respectively) refer to the terminology of the VMD software.
- [78] R. Spricigo, C. Richter, S. Leimkühler, L. Gorton, F. W. Scheller and U. Wollenberger, *Colloids and Surfaces A: Physicochemical and Engineering Aspects*, 2010, **354**, 314 – 319.
- [79] R. Spricigo, R. Dronov, F. Lisdat, S. Leimkühler, F. W. Scheller and U. Wollenberger, *Anal. Bioanal. Chem.*, 2009, **393**, 225 – 233.
- [80] R. Hille, *Biochimica et Biophysica Acta*, 1994, **1184**, 143 – 169.
- [81] R. C. Bray, S. Gutteridge, M. T. Lamy and T. Wilkinson, *Biochem. J.*, 1983, **211**, 227 – 236.
- [82] H. L. Wilson and K. V. Rajagopalan, *J. Biol. Chem.*, 2004, **279**, 15105 – 15113.
- [83] A. Pacheco, J. T. Hazzard, G. Tollin and J. H. Enemark, *J. Biol. Inorg. Chem.*, 1999, **4**, 390 – 401.
- [84] C. Feng, R. V. Kedia, J. T. Hazzard, J. K. Hurley, G. Tollin and J. H. Enemark, *Biochemistry*, 2002, **41**, 5816 – 5821.
- [85] T. F. Chichester DF, (1972). *Sulfur Dioxides and Sulfites. Handbook of Food Additives*.
- [86] M. A. Joslyn and J. B. Braverman, *Adv. Food Res.*, 1954, **5**, 97 – 160.
- [87] R. Walker, *Food Addit. Contam.*, 1985, **2**, 5 – 24.
- [88] D. D. Stevenson and R. A. Simon, *Journal of Allergy and Clinical Immunology*, 1981, **68**, 26 – 32.
- [89] W. H. Yang and E. C. R. Purchase, *Canadian Medical Association Journal*, 1985, **133**, 865 – 867.
- [90] M. Stephenson and L. H. Stickland, *Biochem J.*, 1931, **25**, 205 – 214.
- [91] P. M. Vignais and A. Colbeau, *Curr. Issues Mol. Biol.*, 2004, **6**, 159 – 188.
- [92] P. M. Vignais and B. Billoud, *Chem. Rev.*, 2007, **107**, 4206 – 4272.
- [93] R. K. Thauer, A.-K. Kaster, H. Seedorf, W. Buckel and R. Hedderich, *Nat. Rev. Microbiol.*, 2008, **6**, 579 – 591.
- [94] R. K. Thauer, A.-K. Kaster, M. Goenrich, M. Schick, T. Hiromoto and S. Shima, *Annu. Rev. Biochem.*, 2010, **79**, 507 – 536.
- [95] J. A. Cracknell, K. A. Vincent and F. A. Armstrong, *Chem. Rev.*, 2008, **108**, 2439 – 2461.
- [96] H. Krassen, A. Schwarze, B. Friedrich, K. Ataka, O. Lenz and J. Heberle, *ACS Nano*, 2009, **3**, 4055 – 4061.

- [97] K. A. Vincent, A. Parkin, O. Lenz, S. P. J. Albracht, J. C. Fontecilla-Camps, R. Cammack, B. Friedrich and F. A. Armstrong, *J. Am. Chem. Soc.*, 2005, **127**, 18179 – 18189.
- [98] M. W. W. Adams, *Biochimica et Biophysica Acta*, 1990, **1020**, 115 – 145.
- [99] R. Cammack, V. M. Fernandez and K. Schneider, *Biochimie*, 1986, **68**, 85 – 91.
- [100] S. Shima and R. K. Thauer, *Chem. Rec.*, 2007, **7**, 37 – 46.
- [101] P. M. Vignais, B. Billoud and J. Meyer, *FEMS Microbiol. Rev.*, 2001, **25**, 455 – 501.
- [102] M. Saggiu, I. Zebger, M. Ludwig, O. Lenz, B. Friedrich, P. Hildebrandt and F. Lendzian, *J. Biol. Chem.*, 2009, **284**, 16264 – 16276.
- [103] T. Goris, A. F. Wait, M. Saggiu, J. Fritsch, N. Heidary, M. Stein, I. Zebger, F. Lendzian, F. A. Armstrong, B. Friedrich and O. Lenz, *Nat. Chem. Biol.*, 2011, **7**, 310 – 318.
- [104] A. Volbeda, M. H. Charon, C. Piras, E. C. Hatchikian, M. Frey and J. C. Fontecilla-Camps, *Nature*, 1995, **373**, 580 – 587.
- [105] P.-P. Liebgott, S. Dementin, C. Léger and M. Rousset, *Energy Environ. Sci.*, 2011, **4**, 33 – 41.
- [106] M. Jormakka, S. Törnroth, B. Byrne and S. Iwata, *Science*, 2002, **295**, 1863 – 1868.
- [107] B. C. Berks, M. D. Page, D. J. Richardson, A. Reilly, A. Cavill, F. Outen and S. J. Ferguson, *Mol. Microbiol.*, 1995, **15**, 319 – 331.
- [108] M. Teixeira, I. Moura, A. V. Xavier, J. J. Moura, J. LeGall, D. V. DerVartanian, H. D. Peck, Jr. and B. H. Huynh, *J. Biol. Chem.*, 1989, **264**, 16435 – 16450.
- [109] F. Germer, I. Zebger, M. Saggiu, F. Lendzian, R. Schulz and J. Appel, *J. Biol. Chem.*, 2009, **284**, 36462 – 36472.
- [110] M. J. Maroney and P. A. Bryngelson, *J. Biol. Inor. Chem.*, 2001, **6**, 453 – 459.
- [111] M. Van Gastel, *Appl. Magn. Reson.*, 2010, **37**, 207 – 218.
- [112] D. Millo, M. E. Pandelia, T. Utesch, N. Wisitruangsakul, M. A. Mroginski, W. Lubitz, P. Hildebrandt and I. Zebger, *J. Phys. Chem. B*, 2009, **113**, 15344 – 15351.
- [113] M.-E. Pandelia, H. Ogata and W. Lubitz, *ChemPhysChem*, 2010, **11**, 1127 – 1140.
- [114] W. Lubitz, E. Reiherse and M. van Gastel, *Chem. Rev.*, 2007, **107**, 4331 – 4365.
- [115] V. M. Fernandez, K. K. Rao, M. A. Fernandez and R. Cammack, *Biochimie*, 1986, **68**, 43 – 48.
- [116] A. Volbeda and J. C. Fonticella Camps, *Dalton Trans.*, 2003, 4030 – 4038.
- [117] J. E. Huyett, M. Carepo, A. Pamplona, R. Franco, I. Moura, J. J. G. Moura and B. M. Hoffman, *J. Am. Chem. Soc.*, 1997, **119**, 9291 – 9292.
- [118] J. J. G. Moura, M. Teixeira, I. Moura, J. Le Gall, *The Bioinorganic Chemistry of Nickel*, Ed.: J. R. J. Lancaster, Wiley & Sons, 1988, p. 191.
- [119] V. M. Fernandez, E. C. Hatchikian and Richard Cammack, *Biochimica et Biophysica Acta*, 1985, **832**, 69 – 79.
- [120] A. G. Agrawal, M. van Gastel, W. Gärtner and W. Lubitz, *J. Phys. Chem. B*, 2006, **110**, 8142 – 8150.

- [121] M. Brecht, M. van Gastel, T. Buhrke, B. Friedrich, W. Lubitz, *J. Am. Chem. Soc.*, 2003, **125**, 13075 – 13083.
- [122] S. Foerster, M. van Gastel, M. Brecht and W. Lubitz, *J. Biol. Inorg. Chem.*, 2005, **10**, 51 – 62.
- [123] H. Beinert, *FASEB J.*, 1990, **4**, 2483 – 2491.
- [124] D. C. Johnson, D. R. Dean, A. D. Smith and M. K. Johnson, *Annu. Rev. Biochem.*, 2005, **74**, 247 – 81.
- [125] M. E. Abdelsalam, S. Mahajan, P. N. Bartlett, J. J. Baumberg and A. E. Russell, *J. Am. Chem. Soc.*, 2007, **129**, 7399 – 7406.
- [126] M. F. Mrozek, Y. Xie and M. J. Weaver, *Anal. Chem.*, 2001, **73**, 5953 – 5960.
- [127] Z.-Q. Tian, Z.-L. Yang, B. Ren, J.-F. Li, Y. Zhang, X.-F. Lin, J.-W. Hu and D.-Y. Wu, *Faraday Discuss.*, 2006, **132**, 159 – 170.
- [128] P. L. Stiles, J. A. Dieringer, N. C. Shah, and R. P. Van Duyne, *Annu. Rev. Anal. Chem.*, 2008, **1**, 601 – 626.
- [129] S. Pande, S. K. Ghosh, S. Praharaj, S. Panigrahi, S. Basu, S. Jana, A. Pal, T. Tsukuda and T. Pal, *J. Phys. Chem. C*, 2007, **111**, 10806 – 10813.
- [130] G. Maduraiveeran and R. Ramaraj, *Anal. Chem.*, 2009, **81**, 7552 – 7560.
- [131] S. Park, P. Yang, P. Corredor and M. J. Weaver, *J. Am. Chem. Soc.*, 2002, **124**, 2428 – 2429.
- [132] J.-J. Feng, U. Gernert, P. Hildebrandt and Inez M. Weidinger, *Adv. Funct. Mater.*, 2010, **20**, 1954 – 1961.
- [133] C. David, M. Richter, A. Knorr, I. M. Weidinger and P. Hildebrandt, *J. Chem. Phys.*, 2010, **132**, 024712.
- [134] S. Zou and M. J. Weaver, *Anal. Chem.*, 1998, **70**, 2387 – 2395.
- [135] L. Qin, S. Zou, C. Xue, A. Atkinson, G. C. Schatz and C. A. Mirkin, *Proc. Natl. Acad. Sci. USA*, 2006, **103**, 13300 – 13303.
- [136] L. He, E. A. Smith, M. J. Natan and C. D. Keating, *J. Phys. Chem. B*, 2004, **108**, 10973 – 10980.
- [137] M. F. Mrozek, Y. Xie and M. J. Weaver, *Anal. Chem.*, 2001, **73**, 5953 – 5960.
- [138] R. A. Marcus, *J. Chem. Phys.*, 1965, **43**, 679 – 701.
- [139] a) P. G. Etchegoin, E. C. Le Ru and M. Meyer, *J. Chem. Phys.*, 2006, **125**, 164705. b) P. G. Etchegoin, E. C. Le Ru and M. Meyer, *J. Chem. Phys.*, 2007, **127**, 189901.
- [140] P. B. Johnson and R. W. Christy, *Phys. Rev. B*, 1972, **6**, 4370 – 4379.
- [141] M. Guiral, P. Tron, V. Belle, C. Aubert, C. Léger, B. Guigliarelli and M.-T. Giudici-Ortoni, *International Journal of Hydrogen Energy*, 2006, **31**, 1424 – 1431.
- [142] M.-E. Pandelia, V. Fourmond, P. Tron-Infossi, E. Lojou, P. Bertrand, C. Léger, M.-T. Giudici-Ortoni and W. Lubitz, *J. Am. Chem. Soc.*, 2010, **132**, 6991 – 7004.
- [143] M.-E. Pandelia, W. Nitschke, P. Infossi, M.-T. Giudici-Ortoni, E. Bill and W. Lubitz, *Proc.*

- Natl. Acad. Sci. USA*, 2011, **108**, 6097 – 6102.
- [144] H. Munakata, D. Oyamatsu and S. Kuwabata, *Langmuir*, 2004, **20**, 10123 – 10128.
- [145] K. Shimazu, T. Teranishi, K. Sugihara and K. Uosaki, *Chem. Lett.*, 1998, **27**, 669 – 670.
- [146] K. Sugihara and K. Shimazu, *Langmuir*, 2000, **16**, 7101 – 7105.
- [147] E. W. van der Vegte and G. Hadziioannou, *J. Phys. Chem. B*, 1997, **101**, 9563 – 9569.
- [148] D. V. Vezenov, A. Noy, L. F. Rozsnyai and C. M. Lieber, *J. Am. Chem. Soc.*, 1997, **119**, 2006 – 2015.
- [149] T. Kakiuchi, M. Iida, S. Imabayashi and K. Niki, *Langmuir*, 2000, **16**, 5397 – 5401.
- [150] M. L. Wallwork, D. A. Smith, Jin Zhang, Jennifer Kirkham, and Colin Robinson, *Langmuir*, 2001, **17**, 1126 – 1131.
- [151] S. Trasatti and O. A. Petrii, *J. Electroanal. Chem.*, 1992, **327**, 353 – 376.
- [152] G. Jarzqbek and Z. Borkowska, *Electrochim. Acta*, 1997, **42**, 2915 – 2918.
- [153] D. Millo, A. Ranieri, P. Gross, H. K. Ly, M. Borsari, P. Hildebrandt, G. J. L. Wuite, C. Gooijer and G. van der Zwan, *J. Phys. Chem. C*, 2009, **113**, 2861 – 2866.
- [154] D. Millo, A. Bonifacio, M. R. Moncelli, V. Sergo, C. Gooijer and G. van der Zwan, *Colloid Surface B*, 2010, **81**, 212 – 216.
- [155] J. T. Hupp, D. Larkin and M. J. Weaver, *Surf. Sci.*, 1983, **125**, 429 – 451.
- [156] G. Smulevich and T. G. Spiro, *J. Phys. Chem.*, 1985, **89**, 5168 – 5173.
- [157] J. J. Griese, R. P. Jakob, S. Schwarzingler and H. Dobbek, *J. Mol. Biol.*, 2006, **361**, 140 – 152.
- [158] S. Fetzner, *Appl. Microbiol. Biotechnol.*, 1998, **49**, 237 – 250.
- [159] O. Spiegelhauer, F. Dickert, S. Mende, D. Nicks, R. Hille, M. Ullmann and H. Dobbek, *Biochemistry*, 2009, **48**, 11412 – 11420.
- [160] W. D. Bowman and T. G. Spiro, *Biochemistry*, 1981, **20**, 3313 – 3318.
- [161] N. S. Lee, R. Sheng, M. D. Morris and L. M. Schopfer, *J. Am. Chem. Soc.*, 1986, **108**, 6179 – 6183.
- [162] R. A. Copeland, S. P. A. Fodor and T. G. Spiro, *J. Am. Chem. Soc.*, 1984, **106**, 3872 – 3874.
- [163] N. S. Lee, Y. Z. Hsieh, M. D. Morris and L. M. Schopfer, *J. Am. Chem. Soc.*, 1987, **109**, 1358 – 1363.
- [164] Calculations were performed by Tillmann Utesch.
- [165] P. A. O'Farrell, M. A. Walsh, A. A. McCarthy, T. M. Higgins, G. Voordouw and Stephen G. Mayhew, *Biochemistry*, 1998, **37**, 8405 – 8416.
- [166] C. Niederau, L. D. Ferrell and J. H. Grendell, *Gastroenterology*, 1985, **88**, 1192 – 1204.
- [167] X. Liu, C. N. Kim, J. Yang, R. Jemmerson and X. Wang, *Cell*, **86**, 147 – 157.
- [168] X. Jiang and X. Wang, *Annu. Rev. Biochem.*, 2004, **73**, 87 – 106.
- [169] V. E. Kagan, V. A. Tyurin, J. Jiang, Y. Y. Tyurina, V. B. Ritov, A. A. Amoscato, A. N. Osipov, N. A. Belikova, A. A. Kapralov, V. Kini, I. I. Vlasova, Q. Zhao, M. Zou, P. Di, D. A. Svistunenko, I. V. Kurnikov and G. G. Borisenko, *Nat. Chem. Biol.*, 2005, **1**, 223 – 232.

- [170] N. A. Belikova, Y. A. Vladimirov, A. N. Osipov, A. A. Kapralov, V. A. Tyurin, M. V. Potapovich, L. V. Basova, J. Peterson, I. V. Kurnikov and V. E. Kagan, *Biochemistry*, 2006, **45**, 4998 – 5009.
- [171] L. V. Basova, I. V. Kurnikov, L. Wang, V. B. Ritov, N. A. Belikova, I. I. Vlasova, A. A. Pacheco, D. E. Winnica, J. Peterson, H. Bayir, D. H. Waldeck and V. E. Kagan, *Biochemistry*, 2007, **46**, 3423 – 3434.
- [172] P. Hildebrandt and M. Stockburger, *Biochemistry*, 1989, **28**, 6710 – 6721.
- [173] P. Hildebrandt and M. Stockburger, *Biochemistry*, 1989, **28**, 6722 – 6728.
- [174] S. Berezhna, H. Wohlrab and P. M. Champion, *Biochemistry*, 2003, **42**, 6149 – 6158.
- [175] Y. Gu, P. Li, J. T. Sage and P. M. Champion, *J. Am. Chem. Soc.*, 1993, **115**, 4993 – 5004.
- [176] K. L. Davis, B. J. Drews, Hongjun Yue, D. H. Waldeck, K. Knorr and R. A. Clark, *J. Phys. Chem. C*, 2008, **112**, 6571 – 6576.
- [177] K. L. Davis and D. H. Waldeck, *J. Phys. Chem. B*, 2008, **112**, 12498 – 12507.
- [178] A. El Kasmi, J. M. Wallace, E. F. Bowden, S. M. Binet and R. J. Linderman, *J. Am. Chem. Soc.*, 1998, **120**, 225 – 226.
- [179] J. Petrović, R. Clark, H. Yue, D. H. Waldeck and E. D. F. Bowden, *Langmuir*, 2005, **21**, 6308 – 6313.
- [180] T. M. Nahir and E. F. Bowden, *J. Electroanal. Chem.*, 1996, **410**, 9 – 13.
- [181] E. J. Zeman and G. C. Schatz, *J. Phys. Chem.*, 1987, **91**, 634 – 643.
- [182] S. Link and M. A. El-Sayed, *J. Phys. Chem. B*, 1999, **103**, 8410 – 8426.
- [183] K. L. Kelly, E. Coronado, L. L. Zhao and G. C. Schatz, *J. Phys. Chem. B*, 2003, **107**, 668 – 677.
- [184] A. Sivanesan, H. K. Ly, J. Kozuch, M. Sezer, U. Kuhlmann, A. Fischer and I. M. Weidinger, *Chem. Commun.*, 2011, **47**, 3553 – 3555.
- [185] S. Hu, I. K. Morris, J. P. Singh, K. M. Smith and T. G. Spiro, *J. Am. Chem. Soc.*, 1993, **115**, 12446 – 12458.
- [186] W. A. Eaton and R. M. Hochstrasser, *J. Chem. Phys.*, 1967, **46**, 2533.
- [187] Z.-Q. Tian, B. Ren and D.-Y. Wu, *J. Phys. Chem. B*, 2002, **106**, 9463 – 9483.
- [188] R. G. Freeman, K. C. Grabar, K. J. Allison, R. M. Bright, J. A. Davis, A. P. Guthrie, M. B. Hommer, M. A. Jackson, P. C. Smith, D. G. Walter and M. J. Natan, *Science*, 1995, **267**, 1629 – 1632.
- [189] C. J. Kramer, *Essentials of Computational Chemistry, 2<sup>nd</sup> Ed.*, John Wiley & Sons, Ltd, West Sussex, England, 2004.
- [190] C. E. D. Chidsey, *Science*, 1991, **257**, 919 – 922.
- [191] H. K. Ly, N. Wisitruangsakul, M. Sezer, J.-J. Feng, A. Kranich, I. M. Weidinger, I. Zebger, D. H. Murgida and P. Hildebrandt, *J. Electroanal. Chem.*, 2010, in Press.
- [192] D. H. Murgida and P. Hildebrandt, *J. Phys. Chem. B*, 2002, **106**, 12814 – 12819.
- [193] P. Ramírez, R. Andreu, Á. Cuesta, C. J. Calzado and J. J. Calvente, *Anal. Chem.*, 2007, **79**,

6473 – 6479.

- [194] D. H. Murgida and P. Hildebrandt, *J. Phys. Chem. B*, 2001, **105**, 1578 – 1586.
- [195] S. Trasatti, in H. Gerischer and Ch. W. Tobias (Eds.), *Advances in Electrochemistry and Electrochemical Engineering*, Vol. 10, 1977, p. 213.
- [196] A. Hamelin, L. Stoicoviciu, L. Doubova and S. Trasatti, *Surf. Sci.*, 1988, **201**, L498 – L506.
- [197] F. Lemberg and J. Barrett, *Cytochromes*, ACADEMIC PRESS INC. (LONDON) LTD, 1973.
- [198] H. K. Ly, M. Sezer, N. Wisitruangsakul, J.-J. Feng, A. Kranich, D. Millo, I. M. Weidinger, I. Zebger, D. H. Murgida and P. Hildebrandt, *FEBS J.*, 2011, **278**, 1382 – 1390.
- [199] J.-J. Feng, D. H. Murgida, U. Kuhlmann, T. Utesch, M. A. Mroginski, P. Hildebrandt and I. M. Weidinger, *J. Phys. Chem. B*, 2008, **112**, 15202 – 15211.
- [200] H. A. Heering, F. G. M. Wiertz, C. Dekker and S. de Vries, *J. Am. Chem. Soc.*, 2004, **126**, 11103 – 11112.
- [201] J. Xu and E. F. Bowden, *J. Am. Chem. Soc.*, 2006, **128**, 6813 – 6822.
- [202] R. Hille, J. Rétey, U. Bartlewski-Hof, W. Reichenbecher and B. Schink, *FEMS Microbiol. Rev.*, 1999, **22**, 489 – 501.



## 11 List of Publications

### Articles in Scientific Journals

M. Sezer, J. J. Feng, H. K. Ly, Y. Shen, T. Nakanishi, U. Kuhlmann, H. Möhwald, P. Hildebrandt, I. M. Weidinger, „Multi-layer electron transfer across nanostructured Ag-SAM-Au-SAM junctions probed by surface enhanced Raman spectroscopy”, *Phys. Chem. Chem. Phys.*, 2010, **12**, 9822 – 9829.

M. Sezer, R. Spricigo, T. Utesch, D. Millo, S. Leimkuehler, M. A. Mroginski, U. Wollenberger, P. Hildebrandt, I. M. Weidinger, „Redox properties and catalytic activity of surface-bound human sulfite oxidase studied by a combined surface enhanced resonance Raman spectroscopic and electrochemical approach“, *Phys. Chem. Chem. Phys.*, 2010, **12**, 7894 – 7903.

M. Sezer, D. Millo, R. Spricigo, U. Wollenberger, T. Utesch, M. A. Mroginski, P. Hildebrandt, I. M. Weidinger, „A Combined SERR Spectroscopic And Electrochemical Approach To Study Enzymes On Electrodes”, *XXII INTERNATIONAL CONFERENCE ON RAMAN SPECTROSCOPY. AIP Conference Proceedings*, 2010, **1267**, 1033 – 1034.

M. Sezer, S. Frielingsdorf, D. Millo, I. Zebger, T. Utesch, M. A. Mroginski, N. Heidary, B. Friedrich, P. Hildebrandt, I. M. Weidinger, „Role of the HoxZ subunit in the electron transfer pathway of the membrane-bound [NiFe]-hydrogenase from *Ralstonia eutropha* H16 immobilized on electrodes”, *J. Phys. Chem. B.*, 2011, accepted.

---

I. M. Weidinger, J. J. Feng, M. Sezer, U. Kuhlmann, D. H. Murgida, P. Hildebrandt, „Electron transfer dynamics of cytochrome c immobilised on coated silver and silver-gold hybrid electrodes studied by SERR spectroscopy“, *Proc. XXIst Int. Conf. Raman Spectrosc.*, 2008, IM Pub., Chichester, 358 – 359.

J. J. Feng, U. Gernert, M. Sezer, U. Kuhlmann, D. H. Murgida, C. David, M. Richter, A. Knorr, P. Hildebrandt, I. M. Weidinger, „A Novel Au-Ag hybrid device for surface enhanced (resonance) Raman spectroscopy”, *Nano Lett.* 2009, **9**, 298-303.

I. M. Weidinger, J. J. Feng, M. Sezer, H.K. Ly, U. Kuhlmann, P. Hildebrandt, „Electron transfer Dynamics of cytochrome c on novel nanostructured Au-Ag supports probed by surface enhanced Raman spectroscopy“, *J. Biol. Inorg. Chem.*, 2009, **14** (Suppl.1), 95.

H. K. Ly, N. Wisitruangsakul, M. Sezer, J.-J. Feng, A. Kranich, I. M. Weidinger, I. Zebger, D. H. Murgida, P. Hildebrandt, „Electric-field effects on the interfacial electron transfer and protein dynamics of cytochrome c“, *J. Electroanal. Chem.*, 2010, in Press.

A. Sivanesan, H. K. Ly, J. Kozuch, M. Sezer, U. Kuhlmann, A. Fischer and I. M. Weidinger, „Functionalized Ag nanoparticles with tunable optical properties for selective protein analysis“, *Chem. Commun.*, 2011, **47**, 3553 – 3555.

H. K. Ly, M. Sezer, N. Wisitruangsakul, J.-J. Feng, A. Kranich, D. Millo, I. M. Weidinger, I. Zebger, D. H. Murgida and P. Hildebrandt, „Surface-Enhanced vibrational spectroscopy for probing transient interactions of proteins with biomimetic interfaces: electric field effects on structure, dynamics and function of cytochrome c“, *FEBS J.*, 2011, **278**, 1382 – 1390.

### **Book Chapters**

P. Hildebrandt, J. J. Feng, A. Kranich, H. K. Ly, M. Martí, D.F. Martín, D. H. Murgida, D. A. Paggi, M. Sezer, N. Wisitruangsakul, I. M. Weidinger, I. Zebger, „Electron transfer of proteins at membrane models“, in *Surface Enhanced Raman Spectroscopy – Analytical, Biophysical and Life Science Applications* (Schlücker, S., Ed.), Wiley-VCH, 2010.

### **Oral Presentations**

#### **Sep 19, 2008**

oral presentation at the Institute for Technology, Biology and Chemistry (ITQB) in Oeiras, Portugal: "Gated electron transfer of iso-1-cytochrome c from yeast"

#### **Nov 23, 2009**

oral presentation at the Workshop on Bioanalysis 2009, Luckenwalde, Germany: "Combined electrochemical and SERR-spectroscopic study of human Sulfite Oxidase"

## **Poster Presentations**

### **Sep 2008**

poster presentation at the German Biophysical Society Meeting, Berlin, Germany: "Electron transfer dynamics of cytochrome c on coated electrodes measured with SERR spectroscopy"

### **Aug 2009**

poster presentation at the European Conference on the Spectroscopy of Biomolecules, Palermo, Italy: "Combined surface enhanced resonance Raman spectroscopic and electrochemical study of human Sulfite Oxidase"

### **Aug 2010**

poster presentation at the International Conference on Raman spectroscopy (ICORS), Boston, USA: "A Combined SERR Spectroscopic And Electrochemical Approach To Study Enzymes On Electrodes"



## Danksagung

Ich möchte mich vor allem bei zwei Personen bedanken,

- bei meinem Doktorvater **Prof. Dr. Peter Hildebrandt**, der mir diese Promotion und somit eine sehr spannende und lehrreiche Zeit meines Lebens ermöglicht hat,
- und bei **Dr. Inez Weidinger**, die stets ein offenes Ohr für mich hatte, mich intensiv unterstützt hat und einen sehr großen Anteil am Erfolg dieser Arbeit trägt.

Außerdem danke ich

- meinem Kollegen **Dr. Diego Millo** für die produktive Zusammenarbeit, Unterstützung in unzähligen wissenschaftlichen Fragen und für die Leitung der ‚Hilde-Band‘,
- **Tillmann Utesch** für ergänzende computergestützte Studien,
- **Dr. Ingo Zebger** für die tolle Zusammenarbeit und viele anregende Diskussionen,
- **Dipl.-Ing. Ulrich Gernert** für Messungen am Rasterelektronenmikroskop,
- ganz herzlich meinem alten Weggefährten **Khoa Ly** und den weiteren Kollegen **Sara Bruun, Dr. Jiu-Ju Feng, Jacek Kozuh, Nina Heidary, Marius Horch, Philipp Hummel, Wiebke Meister, Yvonne Rippers, Johannes Salewski, Elisabeth Siebert, Dr. Arumugam Sivanesan** und **Francisco Velazquez Escobar**, die alle auf ihre Art wunderbar sind und mich wissenschaftlich, menschlich und musikalisch (!) sehr bereichert haben,
- **Dr. Uwe Kuhlmann** und **Lars Paasche** für geduldige und kompetente Unterstützung in vielen technischen Fragen,
- **Marina Böttcher, Jürgen Krauss, Norbert Michael, Prof. Dr. Maria Andrea Mroginski, Dr. Hendrik Naumann, Dr. Miguel Saggi, Claudia Schulz, Dr. David von Stetten**, die alle auf die eine oder andere Weise Anteil am Gelingen dieser Arbeit hatten, **Dr. Steve Kaminski, Gal Schkolnik** und allen weiteren **Mitgliedern des MVL** für eine nette Arbeitsatmosphäre,
- meinen Kooperationspartnern vom Max-Planck-Institut für Kolloid- und Grenzflächenforschung **Prof. Dr. Helmuth Möhwald, Yanfei Shen** und **Takashi Nakanishi**,
- meinen Kooperationspartnern an der Universität Potsdam **Dr. Roberto Spricigo, Prof. Dr. Silke Leimkühler** und **Prof. Dr. Ulla Wollenberger**,
- meinen Kooperationspartnern aus der Humboldt Universität Berlin **Dr. Stefan Frielingsdorf** und **Prof. Dr. Bärbel Friedrich**,
- den Arbeitskreisen von **Prof. Dr. Holger Dobbek** und **Prof. Dr. Walter Halangk** für die Bereitstellung von Proben.

Ich möchte mich an dieser Stelle auch ganz herzlich bei **Franziska** und allen weiteren **Freunden** bedanken, die hier nicht aufgelistet sind.

Natürlich danke ich auch meiner Familie, und zwar auf Türkisch:

Beni her zaman destekleyen aileme çok teşekkür ediyorum. Özellikle annem **Yüksel**, babam **Şevki**, vede abilerim **Alper** ve **Sadettin**'e çok teşekkür ediyorum. Yenlerim **Emre** ve **Cihan**'ı gözlerinden öpüyorum.

Vielen Dank.

